Optimalisering van gecombineerde compacte warmtewisselaars met lamellen en wervelgeneratoren

Optimisation of Compound Louvred Fin and Vortex Generator Heat Exchangers

Bernd Ameel

Promotoren: prof. dr. ir. M. De Paepe, prof. dr. ir. J. Vierendeels
Proefschrift ingediend tot het behalen van de graad van
Doctor in de Ingenieurswetenschappen: Werktuigkunde-Elektrotechniek

Vakgroep Mechanica van Stroming, Warmte en Verbranding
Voorzitter: prof. dr. ir. J. Vierendeels
Faculteit Ingenieurswetenschappen en Architectuur
Academiejaar 2013 - 2014

UNIVERSITEIT GENT

ISBN 978-90-8578-697-9
NUR 961
Wettelijk depot: D/2014/10.500/43

Universiteit Gent
Faculteit Ingenieurswetenschappen en Architectuur
Vakgroep Mechanica van Stroming, Warmte en Verbranding

Promotoren: prof. dr. ir. Michel De Paepe
prof. dr. ir. Jan Vierendeels

Universiteit Gent
Faculteit Ingenieurswetenschappen en Architectuur

Vakgroep Mechanica van Stroming, Warmte en Verbranding
Sint-Pietersnieuwstraat 41, B-9050 Gent, België

Tel.: +32-9-264.32.88
Fax.: +32-9-264.35.75

Dit werk kwam tot stand in het kader van een doctoraatsmandaat van het Bijzonder Onderzoeksfonds van de Universiteit Gent.

Department of Flow, Heat and Combustion Mechanics

Proefschrift tot het behalen van de graad van
Doctor in de Ingenieurswetenschappen:
Werktuigkunde-Elektrotechniek
Academiejaar 2013-2014

Dankwoord

Graag wil ik enkele mensen bedanken die mij direct of indirect geholpen hebben tijdens de vier jaar die geresulteerd hebben in dit boek.

Eerst en vooral dank aan mijn promotoren Michel De Paepe en Jan Vierendeels om mij de kans te geven om te doctoreren en voor hun begeleiding tijdens het onderzoek.

Joris Degroote en Christophe T'Joen, bedankt voor het nalezen en verbeteren van mijn papers. Joris, ook bedankt voor de vele hulp met Gambit en Fluent!

Bedankt aan mijn collega's voor de aangename sfeer op het werk. Peter wil ik graag extra bedanken voor de vele leerrijke discussies en om mijn boek te willen nalezen. Henk, bedankt om mijn papers na te lezen en om met jouw werk een goede basis te vormen waar ik kon van beginnen.

Yves Maenhout verdient mijn dank om de rekenservers steeds aan de praat te houden en om mijn quota te verhogen wanneer ik de fileserver op mijn eentje probeerde vol te krijgen.

Griet Blondé, Patricia Vande Voorde en Annie Harri wil ik graag bedanken voor de administratieve ondersteuning.

Mijn huisgenoten, Ellen en Timothy, bedankt onder andere voor het gezelschap. Ook bedankt aan de harde kern van het pastateam, Mieke.

Bedankt aan de vrienden van de skiteams, ardennenteams, quizteams, pastateams, barbecueteams, het fietsteam en iedereen die ik hier nog niet mee heb opgesomd voor de toffe tijden samen. Bedankt aan Kenny om te luisteren naar mijn gezaag wanneer het eens wat minder ging.

Ten slotte, bedankt aan mijn grootouders, mijn ouders en mijn zus voor hun steun en interesse.

Gent, juni 2014
Bernd Ameel

Table of Contents

List of Figures

List of Tables

Nomenclature

A	area	m^2
A_{front}	frontal area	m^2
A_c	minimum flow area	m^2
A_s	heat transfer surface area	
C	heat capacity rate (= $\dot{m} \cdot c_p$)	W/K
C^*	heat capacity ratio	-
c_p	specific heat capacity	J/kgK
C_f	skin friction coefficient	-
D_o	tube outer diameter	m
D_h	hydraulic diameter	m
E	relative error	-
f	Fanning friction factor	-
F	cross-flow factor used in the LMTD method	-
F	pumping power factor	-
F_p	fin pitch	m
G	mass flux	kg/m^2s
G_c	mass flux in the minimum flow area	kg/m^2s
h	convective heat transfer coefficient	W/m^2K
h	grid spacing	m
h	enthalpy	kJ/kg
h	vortex generator height	m
h^*	dimensionless vortex generator height (= h/s)	-
j	Colburn j-factor (unmodified in chapter 2, modified elsewhere)	-
j^*	modified Colburn j-factor	-
J	heat transfer performance factor	-
k	thermal conductivity	W/mK
K	minor loss coefficient	-
K	covariance matrix	-
L	length	m
L_p	louvre pitch	m
$\dot{m}$	mass flow rate	kg/s
$\vec{n}$	normal vector	-
N	number of tube rows	-
Nu	Nusselt number	-

P	pressure	Pa
$\mathcal{P}$	pumping power	W
P_l	longitudinal tube pitch	m
P_t	transversal tube pitch	m
Pe	Peclet number	-
Pr	Prandtl number	-
$\vec{q}$	heat flux vector	W/m^2
$\dot{Q}$	heat transfer rate	W
r	radial coordinate	m
r	refinement ratio	-
R	radius	m
R	ideal gas constant	J/kgK
Re	Reynolds number	-
R_f	fouling resistance	K/W
s	fin spacing ($F_p - t_f$)	m
St	Stanton number	-
St	Strouhal number	-
T	temperature	K
T	period	s
t_f	fin thickness	m
u	x-component of the velocity vector	m/s
u_c	velocity in the minimum cross-sectional flow area	m/s
U	thermal transmittance	W/m^2K
V	heat exchanger volume	m^3
Vc	heat exchanger core volume	m^3
x, y, z	cartesian coordinates	m

Greek symbols

α	thermal diffusivity	m^2/s
α	vortex generator angle of attack	$degrees$
δ	boundary layer thickness	m
Δ	difference	-
ϵ	effectiveness	-
η	flow efficiency	-
η_f	fin efficiency	-
η_o	surface efficiency	-
Λ	vortex generator aspect ratio	-
μ	dynamic viscosity	Pas
μ	mean	-

ν	kinematic viscosity	m^2/s
ϕ	viscous dissipation	W/m^3
θ	louvre angle	$degrees$
θ	activity parameter of the correlation function	-
ρ	density	kg/m^3
σ	contraction ratio	-

Subscripts

$_{accel}$	due to acceleration
$_{avg}$	average
$_{c}$	cold
$_{cond}$	conductive
$_{conv}$	convective
$_{e}$	exit
$_{f}$	fin
$_{h}$	hot
$_{i}$	inner
$_{i}$	inlet
$_{m}$	mean
$_{o}$	outer
$_{ref}$	reference
$_{w}$	wall
$_{\infty}$	free stream

Acronyms

CFD	computational fluid dynamics
EGO	efficient global optimisation
COP	coefficient of performance
GCI	grid convergence index
HVAC&R	heating, ventilation, air-conditioning & refrigeration
LMTD	logarithmic mean temperature difference
NTU	number of transfer units
PEC	performance evaluation criterion
VG	vortex generator
VG-1	variable geometry criterion 1

Nederlandse Samenvatting –Summary in Dutch–

Compacte buis-vin warmtewisselaars worden veelvuldig gebruikt bij toepassingen van verwarming, ventilatie en koeling (HVAC). Door gebruik te maken van speciale vinstructuren zoals de gelammeleerde vin, kunnen warmtewisselaars gemaakt worden die minder materiaal vereisen en een lager ventilatorvermogen nodig hebben. Omdat grondstoffen schaars zijn, is er al veel onderzoek gebeurd naar het optimaliseren van de vinstructuren om de performantie van warmtewisselaars nog te verbeteren. Uit dit onderzoek is onder andere gebleken dat het opwekken van wervels in de stroming een interessante aanpak is, wat geleid heeft tot de vin met wervelgeneratoren. Er zijn veel geometrische parameters die de vorm van deze vin bepalen. Om met de vin met wervelgeneratoren een beter resultaat te bekomen dan met de hedendaagse vinstructuren moeten deze geometrische parameters geoptimaliseerd worden. Heel recent werk heeft aangetoond dat er een aanzienlijk potentieel is als gelammeleerde vinnen gecombineerd worden met vortexgeneratoren. De optimale afmetingen en positionering van de wervelgeneratoren is echter nog een open vraag, die in dit werk zal bestudeerd worden.

Het eerste probleem dat hiervoor dient beantwoord worden is hoe de optimalisatie van een vinstructuur dient te gebeuren. Elke vingeometrie heeft verschillende drukval- en warmteoverdrachtskarakteristieken. Over het algemeen is er een afweging tussen deze karakteristieken, aanpassingen die de warmteoverdracht verbeteren resulteren in toenames van de drukval en dus het ventilatorvermogen. Om te bepalen hoe goed een vingeometrie zijn er verschillende performantieevaluatiecriteria (PEC) beschikbaar in de wetenschappelijke literatuur. Wanneer een dergelijk criterium gebruikt wordt als doelfunctie in een optimalisatieroutine is het belangrijk om goed te weten wat de fysische betekenis is van dat criterium om te begrijpen op welke manier de oplossing optimaal is. Uit de literatuurstudie zal blijken dat bij een aanzienlijk aantal recente studies criteria worden gebruikt die geen duidelijke fysische betekenis hebben. Door de bestaande methoden aan te passen wordt er een nieuwe aanpak ontwikkeld in dit werk die wel een duidelijke fysische betekenis heeft. Deze methode wordt toegepast op de optimalisatie van een gelammeleerde vin en van een gecombineerde vin. Dit resulteert in een vingeometrie die voor eenzelfde volume en massadebiet van de warmtewisselaar met een lager ventilatorvermogen kan werken. Onder deze voorwaarden blijken grotere lammelhoeken betere resultaten te geven dan een geometrie met een kleinere lammelhoek.

De performantiecriteria maken gebruik van een aantal veronderstellingen om eenvoudige analytische vergelijkingen te verkrijgen. Dit maakt ze zeer handig om snelle vergelijkingen te maken tussen sterk verschillende vingeometrieën. Die eenvoud is onbelangrijk wanneer die criteria gebruikt worden om vingeometriën te optimaliseren met behulp van computersimulaties (numerieke stromingsmechanica). In dat geval is de nauwkeurigheid veel belangrijker dan de eenvoud van de vergelijkingen, omdat er sowieso toch computers dienen gebruikt te worden om de dataverwerking te doen. De gevolgen van het achterwege laten van enkele van de veronderstellingen wordt daarom bekeken. Een voorbeeld van een dergelijke aanname is dat twee kritische warmtewisselaarsparameters, the Colburn j-factor en de frictiefactor, onafhankelijk zijn van de lengte van de warmtewisselaar. Het resultaat van deze aanname is dat er voorspeld wordt dat het volume van een warmtewisselaar kan verkleind worden door de frontale snelheid en de lengte te verhogen. Echter, wanneer deze aanname niet gemaakt wordt en de impact van de lengte op deze parameters in rekening gebracht wordt, blijkt dat deze voorspelling niet klopt.

Er wordt aangetoond dat als de lengte van de warmtewisselaar wordt vastgelegd en het massadebiet wordt gevarieerd, dat de optimale geometrie dan afhankelijk is van het aantal warmtewisselingseenheden van de warmtewisselaar. Als deze parameter groot is, geeft een gewone vlakke vin betere resultaten dan de gelammeleerde vin. Als deze parameter klein is, resulteert de gelammeleerde vin in een betere afweging tussen het volume en het ventilatorvermogen. Een andere optie om de lengte van de warmtewisselaar vast te houden is om de hydraulische diameter te laten variëren en het massadebiet constant te houden. Onder deze voorwaarden kunnen hebben warmtewisselaars met kleinere lammelhoeken kleinere ventilatorvermogens nodig dan warmtewisselaars met grotere lammelhoeken. Het is duidelijk dat de optimale vingeometrie afhangt van de preciese randvoorwaarden die gebruikt worden. Het is dus zeer belangrijk dat er een duidelijke fysische interpretatie is van het optimalisatiecriterium, om te weten op welke manier een bepaalde vingeometrie precies optimaal is.

Omdat er aanzienlijk aantal geometrische parameters zijn, moet een groot aantal verschillende geometrieën geëvalueerd worden. Omdat elke computersimulatie veel rekenkracht en tijd vereist, is het niet mogelijk om de invloed van elke parameter voor een groot aantal waarden te bekijken. De theorie van experimenteel ontwerpen (design of experiments, DoE) laat toe om veel informatie te halen uit een zeer beperkte hoeveelheid gegevens. Met name de Taguchi methode wordt in de literatuur zeer vaak gebruikt omdat deze methode zeer flexibel is en grote reductie in de hoeveelheid gegevens toelaat. Een essentiële voorwaarde om deze methode zonder speciale voorzorgen te mogen gebruiken is dat er geen interacties zijn tussen de verschillende parameters. Of dit wel klopt is nog nooit gecontroleerd in de wetenschappelijke literatuur voor de vin met wervelgeneratoren of voor de gecombineerde vin. In dit werk wordt aangetoond dat deze interacties wel degelijk bestaan en belangrijk zijn. De optimale waarden voor parameters van de wervelgenerator hangen af van de andere parameters van de wervelgenerator en van de gelammeleerde vin. Mits een goede keuze van alle parameters is het mogelijk om warmtewisselaars te bouwen die 7% kleiner zijn dan moest een huidige gelamme-

leerde vin gebruikt worden, zonder hiervoor een hoger ventilatorvermogen nodig te hebben. Hierbij is ook de keuze van de parameters essentieel.

Om te begrijpen waarom de nieuwe gecombineerde vingeometrie een beter resultaat geeft dan de huidige gelammeleerde vin is het nodig om dieper te kijken naar het gedrag van de vin. Een nieuwe methode wordt ontwikkeld om de vinefficiëntie uit te rekenen op basis van beschikbare computersimulaties, zonder dat er hiervoor extra simulaties nodig zijn. Door deze methode toe te passen op de gecombineerde vin, wordt het duidelijk dat de gecombineerde vin beter is omdat de vinefficiëntie groter is. Dit toont aan dat de optimale geometrie beïnvloed wordt door de keuze om effecten van de vinefficiëntie mee te rekenen of niet. Bovendien betekent dit dat de wervelgeneratie op zich niet beter is dan de techniek van oppervlakteonderbreking die toepast wordt in de gelammeleerde vin. Door het stromingspatroon van verschillende vingeometrieën in detail te bekijken, wordt aangetoond dat er in de gewone gelammeleerde vin ook al wervels aanwezig zijn. Dit verklaart waarom het toevoegen van enkele extra wervels met een wervelgenerator niet spectaculair beter is dan het toevoegen van oppervlakteonderbrekingen zoals gelammeleerde vinnen.

English Summary

Compact fin and tube heat exchangers are extensively used in heating, ventilation, air-conditioning and refrigeration (HVAC&R) applications. Specialised fin geometries such as the louvred fin allow the construction of heat exchangers with less material use and low fan powers. Due to the scarcity of resources, many investigations of the fin geometry have been conducted to improve heat exchanger performance even further. These investigations revealed that the use of vortices was an interesting approach, resulting in the vortex generator fin design. However, there are many degrees of freedom regarding the geometry of these vortex generators. In order to obtain a better performance than the fin geometries which are already commonly used, optimisation of the vortex generator geometry is required. Very recent work has showed that the combination of louvres with vortex generators has significant potential. The optimal geometry of the vortex generator geometry and positioning in these types of fins is an open question, which is dealth with in this work.

The first issue which needed to be resolved was how to perform optimisation of fin geometries. Every fin geometry has different pressure drop and heat transfer characteristics. In general, there is a trade-off between these two characteristics, increases in the heat transfer tend to result in increases in the pressure drop. Many different performance evaluation criteria are available in the open literature. When one of these criteria is used as a goal function in an optimisation routine, it is important to be aware of the physical significance of these criteria to understand just in what way the obtained fin geometry is optimal. Several recent studies have used criteria which have no clear physical meaning to perform the optimisation. By modifying the existing approaches, a new method was developed which has a clear physical interpretation. This method was used to optimise the louvred fin and round tube geometry for low velocity HVAC applications, resulting in a geometry which required a lower fan power for the same volume or a lower volume for the same fan power and mass flow rate. Geometries with larger louvre angles were found to outperform geometries with lower louvre angles.

The performance evaluation criteria use specific assumptions to result in simple analytic equations, allowing them to be used for quick comparisons between vastly different fin geometries. However, their simplicity is of no particular value if they are used to optimise geometries using computational fluid dynamics (CFD) simulations. In this case, accuracy is far more important than the simplicity of the equation. The impact of relaxing these assumptions on the predicted heat exchanger performance was therefore investigated. One such assumption was that

two critical heat exchanger parameters, the Colburn j-factor and the friction factor were independent of the heat exchanger length. This assumption resulted in the prediction that the heat exchanger volume could be reduced by increasing the frontal velocity and increasing the heat exchanger length. If this assumption was abandoned and the effect of the length on these parameters was taken into account, it became apparent that this prediction was erroneous.

It was shown that if the heat exchanger length was constrained and the mass flow was varied, the optimal geometry depended on the number of transfer units of the heat exchanger. For a large number of transfer units, the plain fin geometry outperformed the enhanced fin designs, whereas for a low number of transfer units, the enhanced fin designs performed better than the plain fin. In contrast, if the mass flow rate was constrained and the length was allowed to vary, the enhanced fin geometries always outperformed the plain fin. Another option was to constrain both the mass flow rate and the heat exchanger length and to allow the hydraulic diameter to vary. This resulted in louvre geometries with larger louvre angles requiring larger hydraulic diameters and therefore also a larger volume for the same fan power. Clearly the optimal fin geometry depends on the constraints, which shows the importance of having a clear physical interpretation to determine when a certain geometry is optimal.

Due to the relatively large number of geometrical parameters, the number of different geometries which need to be evaluated is quite large. Since the simulations are computationally expensive, it is not possible to investigate the entire behaviour of every parameter of interest. The design of experiments methodology allows obtaining virtually the same information with a vastly reduced amount of data under certain conditions. The Taguchi method in particular is quite popular due to its impressive reduction in required data and large flexibility. However, an essential requirement for this method is that there are no interactions between different parameters. Whether this is valid or not was not investigated for the compound louvres and vortex generator fin. It is revealed in this work that interaction effects between the louvre angle and the vortex generator parameters are very important. An interaction between four different parameters was generated as a result of the interaction between the position of the trailing edge of the vortex generator and the tube wake. A performance screening of the compound fin showed that it was possible to do better than the current state-of-the art X-shaped louvred fin, reducing the required heat exchanger volume by 7%. The way the vortex generator geometry is parametrised is essential to obtain good performance.

In order to understand why this compound geometry performed better than the X-shaped louvred fin, it was necessary to further investigate the behaviour of the fin. A new method was developed to obtain the fin efficiency from CFD simulations as a post-processing step. By applying this method to the geometries of interest, it was revealed that the main reason for the difference in performance between the X-shaped louvred fin and the compound design was due to the superior fin efficiency of the compound design. This showed that the optimal fin geometry depended on whether fin efficiency effects were taken into account for the evaluation or not. Furthermore, the generation of the vortex was not more effective than

the louvre geometry which was already used. By studying the flow field of the different geometries in detail, it was revealed that vortices were already present in the regular louvred fin. The addition of an additional vortex by means of the vortex generator was therefore not more efficient than adding more louvred surfaces.

1 Introduction

1.1 Introduction

Heat exchangers exist in many forms, shapes and sizes. From small liquid central processing unit (CPU) coolers to huge cooling towers for power plants, all these heat exchangers have several things in common. For given mass flow rates and inlet temperatures of the fluids, a certain heat transfer rate must be achieved. This must be done with as little material, volume and pressure drops as possible. Since these requirements are contradictory, a trade-off must be made. Some heat exchanger types are still clearly more superior for a given application than others. Criteria have been developed to quantitatively evaluate and compare different heat exchanger geometries. These criteria are called performance evaluation criteria (PECs). These PECs allow a quick selection of a heat exchanger geometry for a given application [1].

One particular application of interest where heat exchangers are used extensively is heating, ventilation and air-conditioning (HVAC). HVAC accounts for approximately 40% of the energy use in buildings, and around 11% of the total energy use in Europe. In these applications, heat must often be exchanged between a carrier fluid and air. Fin and tube heat exchangers are particularly suited for this type of application. Figure 1.1 shows an example of a fin and tube heat exchanger. The fluid (e.g. water or a refrigerant) flows inside copper tubes and aluminium fins are used to extend the heat transfer surface area. In order to reduce the material and energy use of these heat exchangers, several different fin types have been de-

veloped. The 2020 targets of the EU provide incentives to further improve the fin geometry in order to further reduce energy use by HVAC installations.

Figure 1.1: Compact fin and tube heat exchanger

Thanks to the power of computational fluid dynamics (CFD), it has become feasible to evaluate many different fin geometries. Using one of the aforementioned PECs as a goal function of an optimisation algorithm, many different authors have studied the optimisation of heat exchanger fins numerically. Two specific geometries in particular have been investigated in this study, the louvred fin and the vortex generator fin. A typical louvred fin geometry is shown in figure 1.2.

The main idea behind the louvred fin is illustrated in figure 1.3. The plain fin surface is interrupted by separating it into smaller strips of fin material. These strips are oriented at an angle to the inlet flow and are called the louvres. Ideally, the flow should align itself with the louvers once it enters the heat exchanger core. This increases the path length for a fluid particle from the inlet to the exit of the heat exchanger, so it encounters more fin surface than it would if it would pass through the heat exchanger without deflection. As a result the heat transfer rate can be increased. A second reason for the increase in heat transfer rate for louvred fin is the interruption of the fin surface. This will become clear during the discussion in Chapter 2.

Another option to improve the heat transfer rate is to introduce vortices into the flow in the heat exchanger core, by adding vortex generators. Very recently,

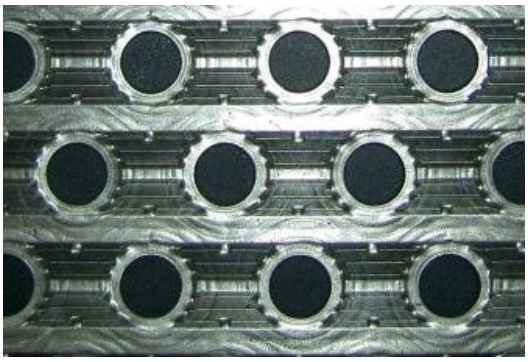

Figure 1.2: Louvred fin geometry [2]

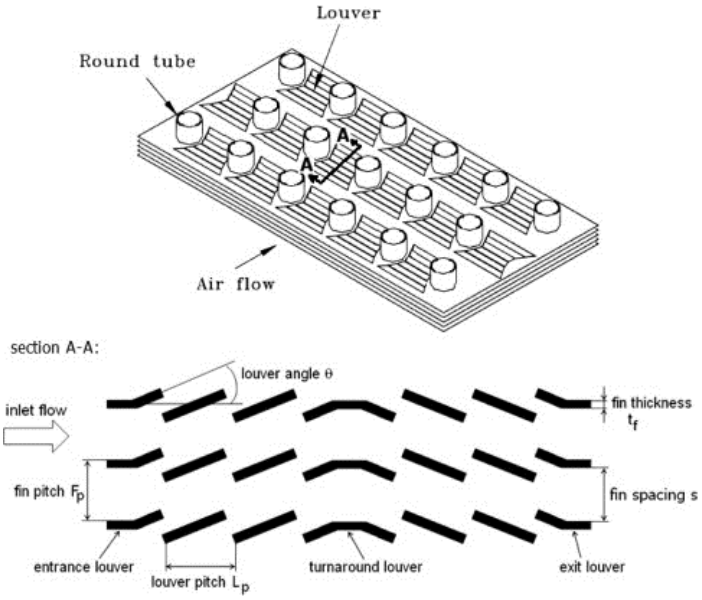

Figure 1.3: Schematic representation of the louvred fin geometry [3]

the combination of louvres with vortex generators has been shown to have some potential, mainly for low-velocity applications [4]. By optimising the geometrical parameters of the vortex generators, the performance of this fin geometry can be increased further.

However, due to several underlying assumptions of the PECs, special care must be taken if they are to be applied in optimisation routines.

1.2 Objective of the study

The objective of this work is to determine how the fin geometry of a compact fin and tube heat exchanger can be optimised, resulting in a universally better geometry. The PEC methods which are commonly used for this purpose involve several assumptions. The physical implications of these assumptions will be identified. Applicable optimisation routines will be implemented to optimise the louvred fin and round tube geometry. It will be investigated how much the performance can be improved further by combining the louvres with vortex generators. The study will be limited to the low frontal air velocities often encountered in HVAC applications, as opposed to higher velocities encountered e.g. in automotive applications.

1.3 Outline

In Chapter 2, the background to the design and optimisation of heat exchangers is given. First, the basic principles behind heat transfer are discussed, introducing the concepts of conductive heat transfer, as well as convective heat transfer and boundary layers for external flow over a flat plate. These concepts are then applied to wall-bounded flow by studying the flow in a heated cylindrical channel. Fully developed flow is introduced and the similarity between heat transfer and surface friction is explained. By introducing a second fluid on the other side of the wall of the cylindrical channel, a simple heat exchanger is then obtained. The theory of the thermal characterisation of heat exchangers is explained. In general, the pressure drop in heat exchangers is more complicated than just channel friction. In the next section, the different components of the pressure drop in a generic heat exchanger are discussed. Heat exchangers must meet several objectives, such as pressure drop, volume and heat transfer rate. Performance evaluation criteria (PEC), which are commonly used to evaluate the performance of heat exchangers, are then discussed. Finally, a brief overview of several optimisation tools, which are commonly used in the scientific literature to optimise heat exchangers, is given.

In Chapter 3, the current state of the art in heat exchanger optimisation is discussed. An overview of experimental and numerical studies regarding louvred fins, vortex generator fins and the combination of both is presented. Four main topics are investigated, namely the geometries of interest, the velocity range, the numerical models used to evaluate the heat exchangers and the optimisation tools which were used. As it is revealed that the Taguchi method is quite a popular optimisation tool, some extra attention is given to the use of this method in the heat exchanger literature.

In Chapter 4, the numerical model which is used in this work is presented. The geometry of interest is defined and the construction of the computational grid is discussed, as well as the boundary conditions of the computational domain. It is

shown that the physical flow in the selected geometry and velocity range of interest is unsteady. A steady-state approximation is used to reduce the computational effort. It is discussed why this approximation is necessary and justified. It is then discussed how to obtain the required data for the performance evaluation from the simulations. An estimate of the error due to the finite discretisation of the continuum problem is given.

The optimisation of heat exchangers is discussed in Chapter 5. First it is discussed how the existing performance evaluation criteria must be used in the context of optimisation methods. It is shown that many recent authors did this incorrectly and the correct method is developed. An efficient algorithm is proposed to perform the optimisation, by combining existing optimisation tools. This algorithm is applied to optimise the X-shaped louvred fin. It is shown that PEC-based optimisation is equivalent to multi-objective optimisation. The impact of some of the underlying assumptions in the PEC methodology is revealed. This is followed by a performance screening of the compound louvres and vortex generators fin. Special attention is paid to the presence of interactions between the various geometrical parameters. Finally, a new fin geometry is proposed which performs slightly better than the X-shaped louvred fin.

In Chapter 6 the concept of fin efficiency is investigated in detail. Even though this is a well-known and often used concept, it will be shown that nevertheless some authors applied it incorrectly when using CFD to evaluate heat exchangers. The physical meaning of fin efficiency is discussed and a method is proposed, which is capable of obtaining the fin efficiency as a post-processing step from CFD data.

Chapter 7 explains why some fin designs perform better than others. In order to achieve this, the pressure drop and the thermal conductance are decomposed into separate contributions. The local distribution of the heat transfer coefficient on the fin surface is discussed for several geometries. Finally, the flow field is investigated to determine whether the vortices disappear as the flow enters the louvre banks.

2

Fundamentals of Heat Exchangers and Optimisation

2.1 Introduction

As the name indicates, the purpose of a heat exchanger is to exchange heat. This is, however, not the only consideration. Many other quantities are also of interest, such as the volume, the cost, the propensity to fouling and the ability to handle high-pressure fluids. Therefore, it comes as no surprise that many different heat exchanger types exist, each with particular advantages. For example, shell and tube heat exchangers consist of a tube bundle in a shell. One fluid flows in the shell around the tubes, the other fluid flows inside the tubes. The advantage of this design is that high pressures can be achieved, especially on the tube side. Another common design is the plate-fin heat exchanger. In this heat exchanger, plates separate both fluids and fins increase the total surface area. This heat exchanger is mainly used for low-pressure fluids and is quite popular for ventilation applications. Both of these vastly different heat exchanger designs operate using the same basic principles of heat transfer. In this chapter, some background to the basic physics behind the design of heat exchangers will be given.

Three main heat transfer modes can be identified: conductive heat transfer, convective heat transfer and heat transfer due to radiation. In most heat exchangers, radiatiative heat transfer is not important and will therefore be neglected. First, conductive heat transfer will be discussed.

2.2 Conductive heat transfer

Conductive heat transfer is determined by Fourier's law (2.1). The law states that the conductive heat transfer rate per unit surface area $\vec{q}$ (also called the heat flux vector) is proportional to the temperature gradient $\vec{\nabla}T$. The factor of proportionality is called the thermal conductivity k and is a material property. Heat flows from high-temperature regions to low-temperature regions, as indicated by the minus sign.

$$\vec{q} = -k\vec{\nabla}T \tag{2.1}$$

The analogy can be made with electrical systems, where the current density is proportional to the electric field. The proportionality constant is equal to the electrical conductivity. As by definition the electrical field is equal to the negative of the gradient of the voltage, the same form of the equation (2.1) is obtained. The current density can be identified with the heat flux and the voltage can be identified with the temperature. For electrical systems, in order to avoid having to compute the electrical field in every point in a component, a relation between current and voltage is established at a component level. The current through a component is proportional to the voltage difference over the component, with the factor of proportionality equal to the electrical conductance. Following the analogy, the same can be done for thermal systems. By integrating Fourier's law for a component, a relation between the heat transfer rate through the component and the temperature difference over the component can be established. The factor of proportionality in this case is called the thermal conductance.

As an example, the thermal conductance for a hollow cylinder of length L will be derived. This corresponds to conductive heat transfer through a tube wall. As heat flows radially through the tube, a temperature difference will be observed between the inner- and the outer-tube wall. The heat transfer rate $\dot{Q}$ through a surface is obtained by integrating the heat flux $\vec{q}.\vec{n}$ over the surface. This is most easily done using cylindrical coordinates. Since both the normal vector and the heat flux vector are aligned with the radial unit vector, the inner product resolves to a single term, as shown by equation 2.2.

$$\dot{Q} = -\int k\vec{\nabla}T.\vec{n}dA = -\iint k\frac{\partial T}{\partial r}rdzd\theta \tag{2.2}$$

As the first law of thermodynamics states that energy is conserved, the heat transfer rate $\dot{Q}$ must be independent of the radius. By integrating equation (2.2) over the radius from the inner to the outer wall, an expression linking the heat transfer rate through the tube wall and the temperature difference over the tube wall is obtained.

$$\dot{Q} = \frac{2\pi Lk}{ln(\frac{r_o}{r_i})}\Delta T \tag{2.3}$$

In order to obtain the connection between the fluid temperatures on both sides of the tube wall and the heat transfer rate, a relation between the fluid temperature and the temperature of the adjacent wall is required.

2.3 Convective heat transfer and boundary layers

2.3.1 Introduction

The required relation between the fluid temperature, the temperature of the adjacent wall and the heat transfer rate is given by the heat transfer coefficient. The heat transfer rate per unit surface area is proportional to the temperature difference between wall and fluid, with the proportionality constant given by the heat transfer coefficient h.

$$\dot{Q} = hA(T_{wall} - T_{fluid}) \tag{2.4}$$

Note that for finite values of the heat transfer coefficient, the equation implies that there is a temperature difference between the wall and the temperature of the fluid if the heat transfer rate is different from zero. As the fluid temperature field must be continuous, it is necessary to be more careful with the definition of the concept of fluid temperature when defining the heat transfer coefficient. Clearly, there must be a region where the fluid temperature varies with the distance from the wall, so it is necessary to specify what is meant with the fluid temperature appearing in the equation. Furthermore, a physical justification for equation (2.4) needs to be provided. This will be done for the problem of forced convection over a flat plate at fixed temperature.

2.3.2 Laminar flow over a heated plate

The flow infinitely far from the plate can be considered to have a constant temperature and a constant velocity. These quantities are called the temperature at infinity T_∞ and the velocity at infinity u_∞. In the limit infinitesimally close to the wall, the velocity must be equal to the wall velocity and the temperature must be equal to the wall temperature, due to continuity of the fields.

This problem was studied by Prandtl [5], who introduced the concept of boundary layers. Only close to the wall, the flow is influenced by the presence of the wall. The region where the wall influences the flow is called the boundary layer. Everything outside the boundary layer is the bulk flow, which is undisturbed by the wall. Since the velocity and temperature fields are continuous, there is no

sudden transition between the bulk flow and the boundary layer. The velocity boundary layer is therefore defined as the location where the flow achieves 99% of the bulk flow velocity. Similarly, the temperature boundary layer is determined by the location where the temperature difference between the wall and the fluid is 99% of the temperature difference between the wall and the bulk flow temperature. By making some simplifications to the Navier-Stokes equations in the region of the wall-influenced flow, Blasius developed the boundary layer equations [6] for a semi-infinite flat plate. By solving the boundary layer equations for laminar flow over a heated flat plate, approximate equations for the temperature profile and velocity profile in the boundary layer are obtained. The velocity profile is well approximated by a third-order polynomial, given by equation (2.5), where δ is the boundary layer thickness and y is the distance from the wall [7].

$$\frac{u}{u_\infty} = \frac{3}{2}\frac{y}{\delta} - \frac{1}{2}(\frac{y}{\delta})^3 \tag{2.5}$$

The velocity boundary layer thickness is a function of the distance from the leading edge to the plate. As the distance from the leading edge increases, the boundary layer thickness also grows. It also depends on the Reynolds number, which expresses a ratio between momentum flux of the flow and frictional stress in the flow. The Reynolds number for flow over a flat plat is given by equation (2.6), where ν is the kinematic viscosity and x is the distance from the leading edge of the plate.

$$Re_x = \frac{u_\infty x}{\nu} \tag{2.6}$$

The boundary layer thickness as a function of x and the Reynolds number is given by equation (2.7) [7].

$$\delta = 4.92 x Re_x^{-\frac{1}{2}} \tag{2.7}$$

The thermal boundary layer has exactly the same shape as the velocity boundary layer. The approximate profile of the dimensionless temperature is given by equation (2.8).

$$\frac{T_{wall} - T}{T_{wall} - T_\infty} = \frac{3}{2}\frac{y}{\delta_T} - \frac{1}{2}(\frac{y}{\delta_T})^3 \tag{2.8}$$

The thermal boundary layer thickness δ_T is proportional to the velocity boundary layer thickness. The proportionality constant is a function of the Prandtl number, which expresses the ratio of the kinematic viscosity (diffusivity of momentum) ν and thermal diffusivity $\alpha = \frac{k}{\rho c_p}$. The temperature and velocity profiles are shown in figure 2.1.

$$\delta_T = \delta Pr^{-\frac{1}{3}} \tag{2.9}$$

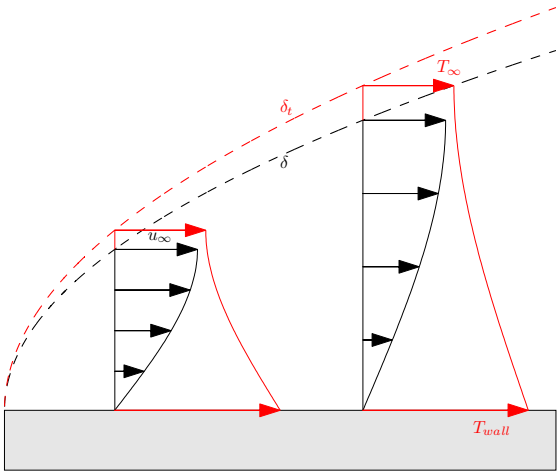

Figure 2.1: Velocity and temperature profile according to the approximated Blasius solution

$$Pr = \frac{\nu}{\frac{k}{\rho c_p}} \tag{2.10}$$

It has now been shown that there is in fact a temperature difference between the wall temperature and the fluid temperature infinitely far from the wall. It still needs to be shown that the heat transfer rate from the heated plate to the fluid is proportional to the temperature difference between the plate and the fluid.

The heat transfer rate from the plate to the fluid can be evaluated at the plate surface. Since the velocity of the fluid at the plate surface is zero, the local heat flux is purely given by conduction through the fluid. The heat flux can be evaluated by using Fourier's law 2.1, since the temperature profile of the fluid near the surface is known from equation (2.8).

$$\vec{q}|_{y=0} = -k\vec{\nabla}T|_{y=0} = \frac{3}{2}k\frac{(T_{wall} - T_\infty)}{\delta_T}\vec{n} \tag{2.11}$$

Equation (2.11) shows that the heat transfer rate is proportional to the temperature difference between the wall and the fluid infinitely far from the wall. The fluid temperature to be used in equation (2.4) is T_∞, the heat transfer coefficient h can readily be identified from equation (2.11).

$$h = \frac{3}{2}\frac{k}{\delta_T} \tag{2.12}$$

Therefore, if high heat transfer rates are desired for a given temperature difference and fluid, the thickness of the thermal boundary layer must be kept small. Another conclusion which follows from equation (2.12) is that the heat transfer coefficient is not constant over the surface of the plate. As the thermal boundary layer thickness increases with the distance from the leading edge of the plate, the heat transfer coefficient decreases. By integrating the local heat transfer coefficient over the surface of the plate, the average heat transfer coefficient is obtained. It can be shown that the average heat transfer coefficient over a finite length of the plate is equal to twice the value at the end of the plate.

2.3.3 Similarity between heat flux and friction stress

An analogy can be drawn between heat transfer and momentum transfer. For so-called Newtonian fluids, the friction stress is proportional to the strain rate. At the surface of a flat plate, the friction stress τ_{wall} for an incompressible Newtonian fluid is given by equation (2.13).

$$\tau_{wall} = \nu \frac{\partial \rho u}{\partial y}|_{y=0} \tag{2.13}$$

This is clearly the same form as equation (2.11). A momentum flux $\vec{\tau}$ is associated with a gradient in momentum ρu in much the same way that a heat flux $\vec{q}$ is associated with a gradient in temperature T. Since the velocity and temperature profiles are also similar, some kind of relation between the heat transfer rate and the friction stress can be expected. In order to obtain this relation, the velocity profile equation (2.5) is substituted into equation (2.13), resulting in equation (2.14).

$$\tau_{wall} = \frac{3}{2}\frac{\nu}{\delta}\rho u_\infty \tag{2.14}$$

As expected, this is exactly the same form as 2.11, with the exception that now the momentum difference between the bulk flow and the wall is used instead of the temperature difference. In order to obtain a dimensionless expression, the skin friction coefficient C_f is defined as the ratio between viscous stress at the wall and the dynamic pressure of the flow infinitely far from the plate.

$$C_f = \frac{\tau_{wall}}{\frac{1}{2}\rho u_\infty^2} \tag{2.15}$$

The relation between the thermal and velocity boundary layers (2.9) is now substituted.

$$C_f = \frac{\frac{3}{2}\frac{\nu}{\delta_T Pr^{\frac{1}{3}}}\rho u_\infty}{\frac{1}{2}\rho u_\infty^2} = 2\frac{\frac{3}{2}\frac{k}{\delta_T}\frac{\nu\rho c_p}{k}}{u_\infty \rho c_p} Pr^{-\frac{1}{3}} = 2\frac{h}{u_\infty \rho c_p} PrPr^{-\frac{1}{3}} = 2StPr^{\frac{2}{3}} \tag{2.16}$$

The Stanton number St expresses the heat transfer coefficient dimensionlessly by normalising it with the heat capacity rate of the fluid. The product of the Stanton number with the Prandtl number to the power two thirds is called the Colburn j-factor (2.17).

$$j = StPr^{\frac{2}{3}} \tag{2.17}$$

$$C_f = 2j \tag{2.18}$$

Just like the Stanton number, the Colburn j-factor is a dimensionless representation of the heat transfer coefficient. Equation 2.18 is a very important result. For laminar flow over a flat plate, the dimensionless viscous stress and the dimensionless heat transfer coefficient are proportional. This result is called the Reynolds analogy. This indicates that in a heat exchanger, modifications which increase the local heat transfer coefficient by locally reducing the thermal boundary layer will also locally increase the skin friction. Increased skin friction will result in an overall increased pressure drop over the heat exchanger, which will be shown in section 2.3.4.2.

2.3.4 Wall-bounded flow

2.3.4.1 Introduction

In a heat exchanger, the flow is bounded by walls on all sides. Therefore, it is not possible to use the concepts of velocity and temperature at an infinite distance from the wall. From the previous discussion, it is clear that the flow is influenced by the presence of the walls and that this influence is a function of the distance from the entrance. In what follows, the case of forced flow through a pipe of radius R with heated walls at a constant temperature will be considered. The fluid enters the tube with a uniform velocity and temperature profile. Just like in the flat-plate case, velocity and thermal boundary layers develop as the flow comes into contact with the walls. Since the flow is now bounded by walls, the boundary layer can no longer grow to an arbitrary thickness with increasing distance from the starting position. Eventually, the entire flow field is adapted to the presence of the walls and the flow is said to be fully developed. For laminar flow over a flat plate, it is known that the thermal and the hydrodynamic boundary layers do not have the same thickness, unless the Prandtl number of the fluid is equal to unity. Therefore,

it can be expected that the length required before a fully developed temperature profile is obtained differs from the hydrodynamic development length.

2.3.4.2 Hydrodynamically fully developed flow

Assuming an initial uniform velocity profile, boundary layers start developing as the fluid comes into contact with the tube walls. As the fluid near the walls is slowed down due to the wall friction, conservation of mass requires that the fluid near the centre line of the tube increases in velocity. As the velocity boundary layers develop, the velocity profile over the entire cross-section of the tube changes. Eventually, fully developed flow is obtained, which means that the velocity profile no longer changes as the distance from the tube entrance increases. This equilibrium velocity profile can be obtained analytically.

The problem is most easily solved using cylindrical coordinates. The radial coordinate is chosen to be zero at the centre line of the tube. Firstly, the Navier-Stokes equations which express the conservation of momentum in continuum mechanics are evaluated for an incompressible Newtonian fluid. The symbol μ represents the dynamic viscosity, $\mu = \rho\nu$.

$$\rho\frac{D\vec{v}}{Dt} = -\vec{\nabla}P + \mu\Delta\vec{v} \tag{2.19}$$

In this form, the Navier-Stokes equation shows that as one fluid parcel with infinitesimal volume is followed, the mass times the acceleration of the parcel is equal to the forces on the parcel. It can be shown that the negative gradient of the pressure is the pressure force per unit volume, whereas the second term is the friction force per unit volume. The term on the left-hand side is the mass (mass per unit volume is the density ρ) times the acceleration of the parcel. Hydrodynamically developed flow is defined as a flow where the velocity of any fluid parcel remains constant as it is followed. Mathematically, this is equivalent to stating that the total derivative of the velocity $\frac{D\vec{v}}{Dt}$ is zero. In this case, the pressure forces exactly balance the friction forces.

It is now assumed that the flow is axisymmetrical and aligned along the centre line: $\vec{v} = u_z\vec{e_z}$. Equation 2.19 is expressed in cylindrical coordinates (r, θ, z). For axisymmetrical fully developed flow, the velocity is only a function of the radial coordinates. Partial derivatives with respect to other coordinates vanish.

$$\frac{1}{\mu}\frac{\partial P}{\partial z} = \frac{\partial^2 u_z}{\partial r^2} + \frac{1}{r}\frac{\partial u_z}{\partial r} + \cancel{\frac{1}{r^2}\frac{\partial u_z}{\partial \theta}} + \cancel{\frac{\partial^2 u_z}{\partial z^2}} \tag{2.20}$$

Just as in the case of the flat plate, the velocity at the tube-wall surfaces is equal to zero: $u_z(R) = 0$. Furthermore, the velocity should be finite for every value of the radial coordinate. Equation (2.20) is a second-order ordinary differential

equation with respect to r and can be solved using these two boundary conditions. The result is given by equation (2.21), D is the inner diameter of the tube.

$$u_z(r) = (\frac{r^2}{R^2} - 1)\frac{D^2}{16\mu}\frac{\partial P}{\partial z} \tag{2.21}$$

The resulting equation (2.21) shows that the velocity profile for fully developed laminar flow in a circular tube is parabolic. This type of flow is called Poiseuille flow. The area-averaged velocity u_{avg} is a useful reference quantity and can be obtained from the velocity profile (2.21) by integrating over the cross-sectional area of the tube. The equation is rearranged to show the pressure drop per unit length as a function of the average velocity.

$$\frac{\partial P}{\partial z} = -\mu\frac{32}{D^2}u_{avg} \tag{2.22}$$

As previously mentioned, in fully developed laminar flow, the pressure forces exactly balance the friction forces. This fact can be used to derive the link between skin friction and pressure drop. For an infinitesimal slice of the tube, the balance is given by equation (2.23).

$$-A_{cross}dP = \tau_{wall}L_{wet}dz \tag{2.23}$$

The left-hand side represents the net pressure force on the slice, whereas the right-hand side is equal to the net force due to friction at the tube wall. L_{wet} is the wetted perimeter and A_{cross} is the cross-sectional area of the tube. By definition, four times the ratio of the cross-sectional flow area to the wetted perimeter is called the hydraulic diameter. For a circular tube, this is equal to the inner diameter of the tube. The friction force per unit length is proportional to the pressure drop per unit length, with the proportionality constant given by the tube diameter divided by four. For fully developed flow in a heat exchanger, the same balance between pressure forces and viscous forces applies. Therefore, increased skin friction in a heat exchanger will also lead to higher pressure drop.

$$\tau_{wall} = -\frac{D}{4}\frac{\partial P}{\partial z} \tag{2.24}$$

Both the skin friction τ_{wall} and the pressure drop ΔP over a finite length L of tube can be represented non-dimensionally. The area-averaged velocity is used as the reference velocity for both quantities.

$$C_f = \frac{\tau_{wall}}{\frac{1}{2}\rho u_{avg}^2} = \frac{\mu\frac{32}{D^2}u_{avg}\frac{D}{4}}{\frac{1}{2}\rho u_{avg}^2} = 16\frac{\nu}{u_{avg}D} = \frac{16}{Re_D} \tag{2.25}$$

$$f = \frac{\Delta P}{\frac{1}{2}\rho u_{avg}^2}\frac{L}{D} = \frac{4\tau_{wall}}{\frac{1}{2}\rho u_{avg}^2} = 4C_f = \frac{64}{Re_D} \tag{2.26}$$

The skin friction coefficient defined in equation (2.25) is also called the Fanning friction factor. In equation (2.26), the Darcy friction factor is defined. In the rest of this work, the term 'friction factor' refers to the Fanning friction factor.

It has been shown that as flow with a uniform velocity profile enters a wall-bounded region, boundary layers develop. The skin friction decreases as the boundary layers grow. Eventually, a hydrodynamically fully developed flow is obtained and the velocity profile does not change any more with increasing distance from the entrance. Since the skin friction is determined by the velocity profile, it therefore also becomes constant. The friction factor is determined for fully developed laminar flow and is shown to be inversely proportional to the Reynolds number.

2.3.4.3 Thermally fully developed flow

Next, the temperature profile is investigated. As long as there is a temperature difference over the cross-section of the flow, heat will flow in accordance with Fourier's law. Because of the conservation of energy, this implies the temperature of the fluid must change until thermal equilibrium is obtained and no temperature gradients are present infinitely far from the tube entrance. Demanding that the temperature profile must be constant in analogy with the velocity profile is therefore not a useful definition, as it only occurs in complete thermal equilibrium. Therefore, the first issue that needs to be resolved is how to define thermally fully developed flow.

This will again be done by considering the case of laminar flow through a tube with walls at a constant and higher temperature than that of the fluid. For hydrodynamically fully developed flow, it was shown that the friction factor was constant. For flow over a flat plate, it is known that the friction factor is proportional to the Colburn j-factor, which is proportional to the heat transfer coefficient. This suggests defining thermally fully developed flow as a flow for which the heat transfer coefficient is constant. As there is no longer a temperature at infinity to use as a reference for the heat transfer coefficient, a sensible reference temperature needs to be chosen.

For the velocity profile, the average velocity was used as a characteristic velocity representing the velocity profile. In the same manner, some kind of average temperature will be used to represent the temperature profile. The reference temperature which is chosen is the adiabatic mixing cup temperature (2.27), also called the bulk temperature. It is the temperature which would be obtained if the flow through a certain cross-section would be allowed to mix adiabatically and without friction until a uniform velocity and temperature are obtained. If the heat capacity of the fluid is constant, the numerator is equal to the heat capacity rate of the flow. In this case the bulk temperature can also be interpreted as the mass-averaged temperature over the cross-section. In order to simplify the analysis, it will be assumed that the flow has a constant density ρ and a constant specific heat

capacity c_p.

$$T_{bulk} = \frac{\int T \rho c_p \vec{v}.\vec{n} dA}{\int \rho c_p \vec{v}.\vec{n} dA} \tag{2.27}$$

The local heat transfer coefficient is now defined with respect to the temperature difference between the wall temperature and the bulk temperature. The heat flux vector and the bulk temperature are both a function of the distance from the inlet of the tube.

$$h = \frac{\vec{q}.\vec{n}}{T_{wall} - T_{bulk}} \tag{2.28}$$

As heat is transferred from the tube walls to the fluid, the temperature of the fluid changes according to the principle of conservation of energy. L_{heated} is the heated perimeter, which is equal to the perimeter of the tube if heat is transferred by the entire tube surface.

$$\vec{q}.\vec{n} L_{heated} dz = u_{avg} \rho c_p dT_{bulk} \tag{2.29}$$

Assuming hydrodynamically fully developed flow, it will now be shown that the heat transfer coefficient indeed approaches a fully developed value asymptotically, just like the friction factor. This follows from the temperature field associated with the Poiseuille velocity field. Calculating this is known as the Graetz problem. For a given velocity field, the temperature field can be calculated from equation (2.30) expressing conservation of internal energy, where h now indicates the enthalpy.

$$\rho \frac{Dh}{Dt} - \frac{DP}{Dt} = \cancel{\varphi} - \vec{\nabla}.\vec{q} \tag{2.30}$$

In HVAC heat exchanger applications, the viscous dissipation term φ is negligible. If the density and the specific heat capacity are additionally assumed to be constant and Fourier's law for a fluid with constant thermal conductivity is introduced, the simplified equation (2.31) is obtained. This equation allows determining the temperature field if the velocity field is known. It is valid more generally as well, the interested reader is referred to section B.1.

$$\rho c_p \frac{DT}{Dt} = k \Delta T \tag{2.31}$$

Equation (2.31) is expressed in cylindrical coordinates and the Poiseuille velocity profile 2.21 is substituted. By additionally imposing steady-state flow, equation (2.32) is obtained.

$$2u_{avg}(\frac{r^2}{R^2} - 1)\frac{\partial T}{\partial z} = \alpha(\frac{1}{r}\frac{\partial}{\partial r}(r\frac{\partial T}{\partial r}) + \frac{\partial^2 T}{\partial z^2}) \tag{2.32}$$

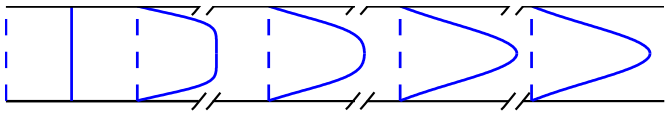

Figure 2.2: Dimensionless temperature profiles at several positions

The equation is made dimensionless by introducing the Peclet number $Pe = \frac{2Ru_{avg}}{\alpha}$ and dimensionless coordinates $Z = \frac{z}{RPe}$ and $Y = \frac{y}{R}$.

$$(Y^2 - 1)\frac{\partial T}{\partial Z} = \frac{1}{Y}\frac{\partial}{\partial Y}(Y\frac{\partial T}{\partial Y}) + \frac{1}{Pe^2}\frac{\partial^2 T}{\partial z^2} \tag{2.33}$$

This shows that the last term in the equation which represents axial conduction becomes negligible if the Peclet number is sufficiently large. For most heat exchanger problems, this condition is satisfied and axial conduction in the fluid can be neglected. In this case, the equation can then be solved analytically through separation of variables. Once the temperature profile is calculated, the dimensionless temperature can be calculated, given by equation (2.34). The reference is now T_{bulk} instead of T_∞ as in equation (2.8). The analytical solution is in the form of a combination of infinite sums as no closed-form solution exists, it is therefore not shown.

$$\Theta = \frac{T_{wall} - T}{T_{wall} - T_{bulk}} \tag{2.34}$$

It can be shown that the dimensionless temperature becomes dependent only on the radial coordinate after a sufficient distance from the entrance. The dimensionless temperature profile therefore exhibits the same behaviour as the velocity profile. For several positions, the dimensionless temperature profile is shown in figure 2.2. It is clear that unlike in the case of external flow, the dimensionless temperature profile is not geometrically similar to the velocity profile. The fully developed velocity profile is parabolic, the fully developed dimensionless temperature profile clearly is not.

Since the temperature profile can be calculated analytically, the heat transfer coefficient can be derived from the temperature profile.

$$h(T_{wall} - T_{bulk}) = \frac{\dot{Q}}{A} = \vec{q}.\vec{n}|_{wall} = -k\frac{\partial T}{\partial r}|_{wall} = -(T_{wall} - T_{bulk})k\frac{\partial \Theta}{\partial r}|_{wall} \tag{2.35}$$

$$h = -k\frac{\partial \Theta}{\partial r}|_{wall} \tag{2.36}$$

Since the dimensionless temperature Θ becomes asymptotically independent of the radial coordinate, the partial derivative with respect to r evaluated at the wall $\frac{\partial \Theta}{\partial r}|_{wall}$ also converges to an asymptotic value. The same is therefore valid for the heat transfer coefficient.

By introducing the analytically determined fully developed temperature profile into equation (2.36), the heat transfer coefficient can be calculated. It is represented non-dimensionally in the form of the Nusselt number given by equation (2.37).

$$Nu_D = \frac{hD}{k} = 3.66 \tag{2.37}$$

It is interesting to note that the Nusselt number for fully developed laminar flow is constant. As a consequence, the heat transfer coefficient for laminar flow is inversely proportional to the diameter. For heat exchanger applications, this means that small flow channels are preferable from a heat transfer coefficient point of view. The Colburn j-factor is obtained from the Nusselt number and given by equation (2.38). The j-factor depends only on the Prandtl and the Reynolds number, not on the distance from the entrance of the pipe. The heat transfer coefficient is independent of the average velocity of the flow.

$$j = \frac{Nu_D}{Re_D Pr^{\frac{1}{3}}} = \frac{3.66}{Re_D Pr^{\frac{1}{3}}} \tag{2.38}$$

Heat transfer between a wall and a fluid can always be expressed as a heat transfer coefficient multiplied by a driving temperature difference. However, the heat transfer coefficient is constant only if the driving temperature difference is chosen as the difference between the adiabatic mixing cup temperature and the wall temperature. Other choices for the driving temperature difference could be made, for instance the temperature difference at the inlet of the tube. However, in that case the heat transfer coefficient is not constant for thermally fully developed flow. In this work, the heat transfer coefficient will always be defined using the adiabatic mixing cup temperature as the reference temperature of the flow.
It comes as no surprise that equation (2.38) for the j-factor is similar to the equation of the friction factor (2.26). Like the friction factor, the Colburn j-factor is inversely proportional to the Reynolds number. The ratio between the Colburn j-factor and the friction factor is now dependent on the Prandtl number, as opposed to the flat-plate case. The proportionality constant is also different for both cases. Still, the fundamental linkage between friction and heat transfer is also valid for wall-bounded flow.

2.4 Thermal characterisation of a heat exchanger

2.4.1 Thermal transmittance

Up until now, the discussion has been limited to heat transfer of a single fluid with a wall at a constant temperature. However, in most engineering applications heat is exchanged between two fluids. Both of these fluids can have a different temperature in every position of the heat exchanger. To evaluate the total heat transfer rate, it is necessary to know the local heat transfer rate everywhere, given the local temperatures of both fluids. The theory of heat exchanger calculation can be found in many textbooks, among others, it was discussed by Shah and Sekulic [8].

As is known from the previous discussion, the temperature profiles of both fluids are non-trivial functions of the position. However, the heat transfer rate between each fluid and the adjacent wall can be expressed as a linear function of the bulk temperature and the wall temperature. Temporarily assuming that the wall temperature and the bulk temperature are constant, a thermal resistance can be introduced. In equation (2.39), the symbol h_1 represents the heat transfer coefficient between fluid 1 and the adjacent wall, A_1 is the total surface area of the adjacent wall.

$$R_{conv,1} = \frac{T_{wall,1} - T_{bulk,1}}{\dot{Q}} = \frac{1}{h_1 A_1} \tag{2.39}$$

A similar relationship is obtained for the second fluid. The connection between both wall temperatures is given by the conductive temperature difference, given by an integrated version of Fourier's law such as equation (2.3) for a tube. If the heat conduction along the streamlines of the fluid is negligible (valid for sufficiently high Peclet numbers), the heat transfer rate $\dot{Q}$ is the same through all thermal resistances. Therefore, an equivalent total thermal resistance can be introduced.

$$R_{tot} = \frac{T_{bulk,1} - T_{bulk,2}}{\dot{Q}} = R_{conv,1} + R_{cond} + R_{conv,2} \tag{2.40}$$

The inverse of the thermal resistance is called the thermal conductance UA.

$$UA = \frac{\dot{Q}}{T_{bulk,1} - T_{bulk,2}} = \frac{1}{\frac{1}{h_1 A_1} + R_{cond} + \frac{1}{h_2 A_2}} \tag{2.41}$$

Now the thermal transmittance U can be introduced by dividing the thermal conductance by an area. Either the area heating fluid 1 or fluid 2 can be chosen, leading to thermal transmittance based on side 1 or based on side 2. It is assumed that the thermal transmittance U is constant throughout the entire heat exchanger. This is guaranteed if the flow for both fluids is fully developed, since the heat transfer coefficients are then constant.

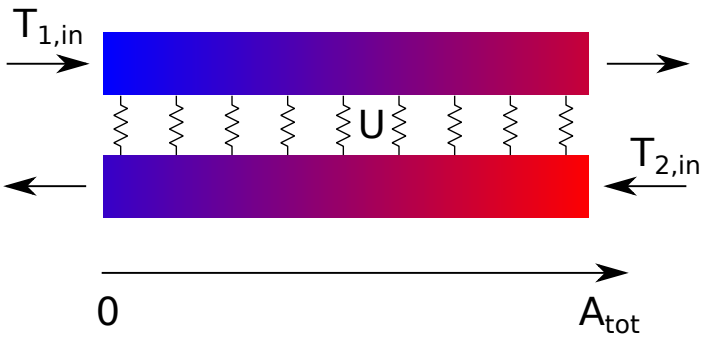

Figure 2.3: Counter flow configuration, the colours indicate the adiabatic mixing cup temperature

The local heat transfer rates can then be calculated by using equation (2.42), where the index i can refer to either fluid 1 or fluid 2. In what follows, the index i will be removed from the group $U_i dA_i$ as this group is independent of the fluid index (equation (2.41)).

$$d\dot{Q} = U_i(T_{bulk,1} - T_{bulk,2})dA_i \tag{2.42}$$

2.4.2 Logarithmic mean temperature difference

The objective of this section is to establish a connection between the bulk temperatures of both fluids at the entrance and the exit of the heat exchanger and the heat transfer rate. This will be done by integrating the equation for the local heat transfer rate (2.42) over the entire heat exchanger. For simple one-dimensional flow only two configurations are possible: counterflow and parallel flow. Assuming constant specific heat capacities and a counterflow configuration, the relationship between the local heat transfer rate and the local change in bulk temperature is given by equation (2.43). In this equation, $\dot{m}_i$ refers to the mass flow rate of stream i.

$$d\dot{Q} = \dot{m}_1 C_{p1} dT_1 = -\dot{m}_2 C_{p2} dT_2 \tag{2.43}$$

Equations (2.42) and (2.43) now form a coupled set of ordinary differential equations. As the dependent variables, the heat transfer rate $\dot{Q}$ and the temperature difference $T_1 - T_2$ are chosen. Since there are two dependent variables, two boundary conditions are required. The boundary conditions are determined by the flow configuration. Figure 2.3 sketches the situation for counterflow. Note that the colours represent the adiabatic mixing cup temperature, the real temperature distribution is much more complicated.

For counterflow, the boundary conditions are given by equation (2.44).

$$T_1(0) = T_{1,in} \quad \text{and} \quad T_2(A_{tot}) = T_{2,in} \tag{2.44}$$

Now let the indices a and b refer to the sides of the heat exchanger. For counterflow a corresponds to $A = 0$ and b to $A = A_{tot}$. It can then be shown that equation (2.45) is valid for both counterflow and parallel flow. It defines the logarithmic mean temperature difference $LMTD$.

$$\dot{Q} = UA\frac{\Delta T_a - \Delta T_b}{ln(\frac{\Delta T_a}{\Delta T_b})} = UA\,LMTD \tag{2.45}$$

If the difference between the bulk temperatures of the fluids is known at both sides of the heat exchanger, the LMTD can be calculated and the heat transfer rate follows from equation (2.45).

In real-life cases, more complicated flow patterns such as cross-flow occur. This can be dealt with in a similar manner, with the exception that the governing equations now become partial differential equations in two dimensions. They can also be solved analytically in several cases. It can be shown that for fixed boundary conditions and area, the counterflow configuration has a greater heat transfer rate. Therefore, the heat transfer rates of other flow configurations are expressed as a cross-flow factor F times the counterflow heat transfer rate. The cross-flow factor is bounded between 0 and 1.

$$\dot{Q} = F\,UA\,LMTD \tag{2.46}$$

2.4.3 Effectiveness-NTU method

It is also possible to choose the temperatures as the dependent variables in equation (2.43) and eliminate the heat transfer rate. Dimensionless temperatures are introduced by equation (2.47).

$$\theta_i = \frac{T_i - T_{i,in}}{T_{1,in} - T_{2,in}} \tag{2.47}$$

The thermal capacity of a flow C_i is defined as $C_i = \dot{m}_i C_{pi}$. For the flow with the smallest thermal capacity, equation (2.47) evaluated at the exit has a clear physical interpretation. The denominator is the maximum possible temperature difference, whereas the numerator is the actually occurring temperature difference for the fluid. The maximum temperature difference occurs for the flow with the smallest thermal capacity C_{min} in an infinitely large counterflow heat exchanger. By multiplying denominator and numerator with the heat capacity rate, the ratio between the actual heat transfer rate and the heat transfer rate in an infinitely large counterflow heat exchanger is obtained. Therefore the dimensionless temperature

at the exit of the fluid with the smallest thermal capacity is also called the effectiveness ϵ of the heat exchanger.

$$\dot{Q}_{max} = C_{min}(T_{1,in} - T_{2,in}) = C_{min}\Delta T_{max} \tag{2.48}$$

Additionally, the number of transfer units NTU and the heat capacity ratio C^* are introduced.

$$NTU = \frac{UA}{C_{min}} \tag{2.49}$$

$$C^* = \frac{C_{min}}{C_{max}} = \frac{min(\dot{m}_1 C_{p1}, \dot{m}_2 C_{p2})}{max(\dot{m}_1 C_{p1}, \dot{m}_2 C_{p2})} \tag{2.50}$$

Using these dimensionless variables, equations (2.43) and (2.42) can be rewritten as the set (2.51) for a counterflow configuration. It is assumed that the fluid 1 is the fluid with the smallest thermal capacity rate. In order to make the temperature differences dimensionless, both sides of the equations are divided by the maximum possible temperature difference $\frac{dT_1}{T_{1,in}-T_{2,in}}$.

$$\begin{cases} C_{min}\frac{dT_1}{T_{1,in}-T_{2,in}} = \frac{T_1-T_2}{T_{1,in}-T_{2,in}} U dA \\ \frac{C_{min}}{C^*}\frac{dT_2}{T_{1,in}-T_{2,in}} = -\frac{T_1-T_2}{T_{1,in}-T_{2,in}} U dA \end{cases} \tag{2.51}$$

Rearranging the equations results in the set (2.52), where the group $\frac{UdA}{C_{min}}$ has been called $dNTU$. As the surface area is integrated from 0 to A_{tot}, the NTU varies from 0 to the total number of transfer units of the heat exchanger, which is indicated with the symbol NTU.

$$\begin{cases} d\theta_1 = dNTU(\theta_1 - \theta_2) \\ d\theta_2 = -C^* dNTU(\theta_1 - \theta_2) \end{cases} \tag{2.52}$$

The corresponding boundary conditions for a counterflow heat exchanger are given by equation (2.53).

$$\theta_1(0) = 1 \quad \text{and} \quad \theta_2(NTU) = 1 \tag{2.53}$$

This is again a set of coupled ordinary differential equations which can be solved. Evaluating the dimensionless temperature of the fluid with the smallest heat capacity at the NTU value of the heat exchanger, the heat exchanger effectiveness ϵ is obtained. It depends only on the number of transfer units NTU and the heat capacity ratio C^*, not on the fluid temperatures.

$$\epsilon = \theta_{min}(NTU) = \frac{1 - exp(-NTU(1 - C^*))}{1 - C^* exp(-NTU(1 - C^*))} \tag{2.54}$$

For evaporating or condensing flow, the temperature of one of the fluids is constant. The thermal capacity of the fluid is essentially infinite, therefore, the

heat capacity ratio is zero. Substituting this value into equation (2.54) results in the effectiveness relation (2.55).

$$\epsilon = 1 - exp(-NTU) \tag{2.55}$$

For other flow configurations such as cross flow or parallel flow, other relations can be developed. In general, the effectiveness is a function of the flow configuration, the heat capacity rate ratio C^* and the number of transfer units NTU.

2.4.4 Fin efficiency

2.4.4.1 Thermal analysis of finned surfaces

In many applications, fins are used to extend the surface area available for heat transfer. As heat flows through the fin, a conductive temperature drop occurs between fin base and fin tip. Due to this temperature drop, the temperature difference between the local wall temperature and the fluid bulk temperature is reduced. Therefore, the heat transfer rate will be smaller than if the fin temperature were constant. A single fluid in contact with a finned base surface is considered. In order to determine the thermal transmittance in this case, it is again assumed that the temperature of the base surface and the bulk temperature are constant as was done for the derivation of equation (2.39). For this constant base temperature, the fin temperature varies over the surface of the fin. The total heat transfer rate can be obtained by integrating the local heat transfer rate over the fin surface.

$$\dot{Q}_{fin} = \int_{A_{fin}} h_{fin}(T_{fin} - T_{bulk})dA \tag{2.56}$$

The problem in evaluating equation (2.56) is that the local fin temperatures are not a priori known. This is solved by expressing the actual fin heat transfer rate as a fin efficiency times the theoretical heat transfer rate if the fin would entirely be at the local base temperature.

$$\dot{Q}_{fin} = \eta_f \int_{A_{fin}} h_{fin}(T_{base} - T_{bulk})dA = \eta_f h_{fin}(T_{base} - T_{bulk})A_{fin} \tag{2.57}$$

Now the total heat transfer rate is equal to the sum of the convective heat transfers from the base surface and the fin surface. The additional simplifying assumption is made that the heat transfer coefficient on the fin surface is equal to the heat transfer coefficient on the base surface. This allows writing the thermal conductance between the wall temperature and the fluid bulk temperature as in equation (2.58). In case two fluids would be used, the thermal resistance of the material

separating the two fluids and the thermal resistance of the other fluid also appear in the thermal conductance.

$$UA = \frac{\dot{Q}_{fin} + \dot{Q}_{base}}{T_{base} - T_{bulk}} = \eta_f h_{fin} A_{fin} + h_{base} A_{base} = h_{fin} \eta_o (A_{fin} + A_{base}) \tag{2.58}$$

In the final step, the surface efficiency is introduced, which is only valid if $h_{base} = h_{fin}$.

$$\eta_o = 1 - \frac{A_{fin}}{A_{fin} + A_{wall}} (1 - \eta_f) \tag{2.59}$$

Therefore, in order to incorporate a finned surface into the thermal transmittance equation (2.41), the total surface area adjacent to the fluid needs to be multiplied with the surface efficiency η_o.

2.4.4.2 Determining the fin efficiency

The fin efficiency can be calculated analytically if several simplifying assumptions are made. This was first done by Gardner [9]. The assumptions are as follows:

1. The problem is steady-state.
2. The thermal conductivity is a constant.
3. The heat transfer coefficient is a constant.
4. The surrounding bulk temperature is a constant.
5. One-dimensional radial conduction along the length of the fin.
6. The temperature at the base of the fin is a constant.
7. There is no internal heat generation.
8. The heat transfer through the fin tips is negligible.
9. The cross-sectional area of the fin is constant.

With these assumptions, the one-dimensional equation expressing the conservation of energy is given by equation (2.60). The fin thickness is represented by the symbol t_f. The situation is sketched in figure 2.4. Different boundary conditions are possible at the fin tip, such as adiabatic, convective or constant temperature conditions. Here the adiabatic (zero heat flux) condition $\frac{\partial T}{\partial x} = 0$ is used, which is valid when the fin tip surface is much smaller than the total surface area of the fin. The interested reader is referred to section B.2 for an explanation.

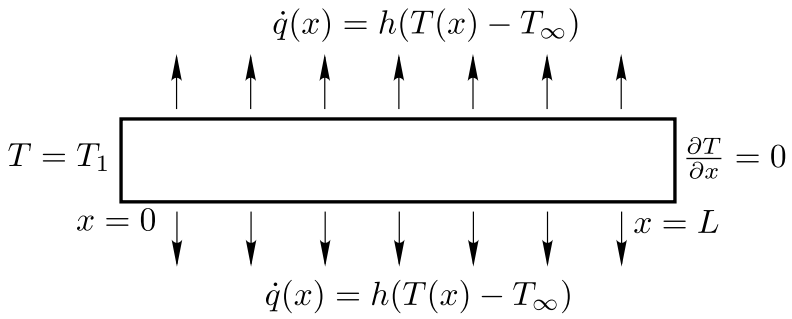

Figure 2.4: One-dimensional fin efficiency problem

$$\frac{\partial^2 T}{\partial x^2} = \frac{2h}{kt_f}(T - T_\infty) \tag{2.60}$$

This is a second-order ordinary differential equation, which requires two boundary conditions. The first condition is that at the base of the fin, the temperature is equal to the temperature of the wall. The second condition is that the gradient of the temperature at the fin tip $x = L$ is zero, corresponding to the neglected heat flux through the tip. The problem is now fully defined and the equation with its boundary conditions can be solved for the temperature distribution over the fin. The solution is given by equation (2.62) in which the fin parameter m was introduced, given by equation (2.61).

$$m = \left(\frac{2h}{kt_f}\right)^{\frac{1}{2}} \tag{2.61}$$

$$T = T_\infty + \frac{cosh(m(L-x))}{cosh(mL)}(T_{base} - T_\infty) \tag{2.62}$$

By substituting the fin temperature profile given by equation (2.62) into equation (2.56), the actual heat transfer rate from the fin is obtained. The fin efficiency is then obtained by taking the ratio of the actual heat transfer rate to the ideal heat transfer rate if the entire fin would be at the base temperature.

$$\eta_f = \frac{\dot{Q}_{fin}}{\dot{Q}_{fin,ideal}} = \frac{tanh(mL)}{mL} \tag{2.63}$$

Now the fin efficiency is determined analytically, it can be used in the equation for the thermal transmittance. Assuming that the second fluid is in contact with a finned surface, equation (2.41) is modified to become equation (2.64).

$$UA = \frac{1}{\frac{1}{h_1 A_1} + \frac{1}{R_{cond}} + \frac{1}{h_{2,base}A_{2,base} + h_{2,fin}\eta_f A_{2,fin}}} \tag{2.64}$$

Again, it is assumed that the thermal transmittance U derived from equation (2.64) is constant for the entire fin surface and remains valid when used in cases where the bulk temperatures are not constant.

The previous analysis can be easily extended to circular fins by posing the problem in cylindrical coordinates. An equivalent fin length, which can be used in equation (2.62) to give the fin efficiency, is provided. Schmidt [10] extended the theory further for continuous fins. He found that a good approximation of performance of continuous fins can be found by introducing an equivalent fin length in the equations for a fin with adiabatic boundary conditions. This equivalent fin length is a function of the geometrical parameters of the fin and the tubes.

2.5 Pressure drop in a heat exchanger

2.5.1 Introduction

Whereas the pressure drop for laminar flow in a cylindrical channel is easy to evaluate, this is not the case for flow in a heat exchanger. Shah [8] identifies four main pressure drop contributions for a compact heat exchanger. The first contribution is due to the change in velocity profile of the flow as it enters the heat exchanger core, which is called the entrance loss. This is followed by the pressure drop in the heat exchanger core, called the core friction term. As the temperature of the fluid changes due to the heat transfer, changes in density can result in a pressure change due to acceleration or deceleration of the flow. Finally, there is change in the pressure as the flow exits from the heat exchanger core. These different contributions will be discussed in more detail in this section.

2.5.2 Entrance loss

Two main pressure drops can be associated with the entrance of the flow into the heat exchanger core.

Firstly, as the flow enters the heat exchanger core, the average velocity is increased due to the decreased area available for the flow. According to Bernoulli's law, a (reversible) pressure drop is associated with this increase in average velocity (and therefore in momentum).

Secondly, as the flow passes through the heat exchanger core, the shape of the velocity profile changes until it is fully developed. As the velocity profile changes, so does the momentum of the flow. As indicated by Newton's second law, this change in momentum must be compensated for by another force, which is the pressure force in this case. The change in velocity profile from a uniform profile towards fully developed flow in the heat exchanger core is accompanied by an increase in momentum and therefore a pressure drop. As this change in velocity

profile is caused by the viscous forces, this is accompanied by a loss in the total pressure.

Finally, a minor loss is associated with flow contractions and expansions. This is also an irreversible pressure drop, resulting in a decrease of the total pressure. Due to the inertia of the flow, the flow contraction starts occurring in front of the heat exchanger core.

The flow contraction is treated theoretically by defining a minimum flow area A_c. For a fin and tube heat exchanger, it is obtained by projecting the heat exchanger material on the frontal plane. The projected area, which is not occupied by material and which is free for fluid flow, is the minimum flow area. The ratio of the minimum flow area to the frontal surface area is the contraction factor σ.

$$\sigma = \frac{A_c}{A_{front}} \tag{2.65}$$

Using the contraction factor, it is possible to define the mass flux at the minimum flow area G_c. This is an estimate for the average mass flux in the heat exchanger core. The frontal mass flux is notated with the symbol G.

$$G_c = \frac{\dot{m}}{A_c} = \frac{\dot{m}}{\sigma A_{front}} = \frac{G}{\sigma} \tag{2.66}$$

The pressure drop associated with the entrance of the flow into the heat exchanger core is then given by equation (2.67) [8]. The index i refers to the entrance conditions. The first term is the reversible part of the pressure drop, the second term is the irreversible part of the pressure drop. K_i is the minor loss coefficient associated with the sudden contraction from the frontal area to the minimum flow area and the change in momentum due to the change in velocity profile.

$$\Delta P_{entrance} = \frac{(1-\sigma^2)G_c^2}{2\rho_i} + K_i \frac{G_c^2}{2\rho_i} \tag{2.67}$$

2.5.3 Core friction

The second and most important contribution to the overall pressure drop over the heat exchanger core is given by the core friction. As was the case for fully developed flow in a pipe, friction at the wetted walls is responsible for an irreversible pressure drop $\Delta P_{friction}$. In general there can also be wake zones in a heat exchanger due to flow separation from surfaces such as tube walls. This is associated with a form drag on the heat exchanger surface, which results in an irreversible pressure drop ΔP_{form}. This pressure drop due to form drag in the heat exchanger core is also incorporated into the core friction term of the pressure drop. According to Shah and Sekulic [8], the core friction typically accounts for 90% of the total pressure drop over the heat exchanger core.

For the friction factor of a heat exchanger, the same relation as for fully developed flow in a pipe is used, given by equation (2.26). The reference velocity is the theoretical mean velocity in the heat exchanger core v_c , given by $v_c = \frac{G_c}{\rho}$, where ρ is the arithmetic mean density.

$$\Delta P_{core} = \Delta P_{friction} + \Delta P_{form} = f\frac{1}{2}\rho v_c^2 \frac{L}{D_h} \tag{2.68}$$

Since compact heat exchangers can have a very complicated internal geometry, the hydraulic diameter is not defined as four times the flow area divided by the wetted perimeter as was done for pipe flow. Both the flow area and the wetted perimeter change in the interior of the heat exchanger. Therefore, the hydraulic diameter is defined as four times the heat exchanger fluid core volume divided by the heat transfer surface A_s. The fluid core volume is calculated theoretically as $A_c L$, where L is the length of the heat exchanger.

$$D_h = 4\frac{A_c L}{A_s} \tag{2.69}$$

2.5.4 Flow acceleration

For single-phase fluids, as heat is transferred to the fluid, the temperature changes. If the fluid density depends on the temperature, as is the case for gases, the average velocity changes due to conservation of mass. This change in the average velocity corresponds to an acceleration of the flow, which must be balanced by the pressure force to satisfy the momentum balance.

$$\Delta P_{accel} = G_c(u_i - u_e) \tag{2.70}$$

$$\Delta P_{accel} = G_c^2(\frac{1}{\rho_e} - \frac{1}{\rho_i}) \tag{2.71}$$

2.5.5 Exit loss

Finally, as the flow leaves the heat exchanger core, the velocity profile changes again to a different flow profile infinitely far behind the heat exchanger. There is again an irreversible pressure drop associated with the sudden expansion. As the available area for the flow is increased, the average velocity decreases again, resulting in a reversible increase in the pressure.

$$\Delta P_{exit} = -\frac{(1-\sigma^2)G_c^2}{2\rho_e} + K_e\frac{G_c^2}{2\rho_e} \tag{2.72}$$

2.6 Performance evaluation of fin geometries

2.6.1 Multiple objectives of a heat exchanger design

A good heat exchanger must meet many different objectives. First and foremost, for given mass flow rates and temperatures of the incoming fluids, the required heat transfer rate must be achieved. This requires a sufficiently large surface area A_s, which is limited by the material cost. The surface area to volume ratio is also limited due to manufacturability constraints, imposing a further restriction on the available surface area for a given heat exchanger volume. In many cases, a small heat exchanger volume is also desired to achieve a compact design. Assuming the heat transfer coefficient is independent of the flow velocity as in equation (2.38) for the pipe flow, the required heat transfer surface does not change as the flow velocity is increased. An increased flow velocity in the heat exchanger corresponds to a smaller frontal surface area due to the mass flow rate constraint. For a fixed surface area to volume ratio, the required volume is determined by the heat transfer coefficient and the heat exchanger length then follows from the choice of the flow velocity in the heat exchanger. In real interrupted fin heat exchangers, the heat transfer coefficient is not independent of the flow velocity, but increases with increasing flow velocity as in equation (2.7) due to the thinner boundary layers at higher flow velocities. The required surface area to meet the heat transfer rate constraint can then be reduced by increasing the velocity through the heat exchanger core.

However, increased flow velocity results in a higher pressure drop through the heat exchanger core. This pressure drop must be suitable for the fan or pump which is used to pass the fluid over the heat exchanger core. Additionally, the forced flow over the heat exchanger core requires mechanical power, which is proportional to the pressure drop if the mass flow rate is fixed. This is a second reason to strive for low pressure drops over the heat exchanger core. The easiest way to reduce the pressure drop is using lower flow velocities, but this is directly at odds with the requirement for a high heat transfer coefficient and therefore leads to an increased heat exchanger volume.

From this brief discussion, it is clear that there are several objectives which are at odds and are strongly interconnected. For a heat exchanger where mass flow rate, inlet temperatures of the fluids and the required heat transfer rate are kept fixed, two independent control parameters have been identified so far. These two parameters are the frontal velocity of the heat exchanger and surface area to volume ratio. By changing the surface area to volume ratio, for instance by changing the distance between the fins, the heat exchanger volume can be varied independently from the required heat transfer surface area.

In the previous discussion, it was assumed that in order to vary the velocity of the flow in the heat exchanger core, it was necessary to vary the frontal flow

velocity in an equal measure. Actually, it is possible to vary the flow velocity in the heat exchanger core independently of the frontal flow velocity by varying the contraction factor σ. This forms the third degree of freedom.

The fourth and final degree of freedom is given by the shape of the fin geometry. The global characteristics of the heat exchanger depend on the small scale flow in the heat exchanger core. This small-scale flow is determined by the fin geometry. Different fin designs have different heat transfer and pressure drop characteristics, allowing for different heat exchanger designs.

2.6.2 Performance evaluation criteria according to Cowell

Figure 2.5 shows a schematic representation of an interrupted fin-and-tube heat exchanger. If it is approached from a black box point of view, the heat exchanger is an object where air enters at a specific mass flow rate, velocity and temperature. Due to the flow resistance caused by the heat exchanger, the air stream is subject to a pressure drop. Due to the heat transfer with the fluid, the temperature of the air flow also changes. Several important characteristics can now be identified. First, there is the heat transfer rate between both fluids. Secondly, the characteristics of the flows are essential to the behaviour of the heat exchanger: the fluid, mass flow rate, velocity and temperature. The pressure drop of the air stream must be compensated for by a fan, the required fan power is therefore also an important quantity. Finally, there are the geometric characteristics of the heat exchanger. It has a certain frontal area and a length; the volume of the heat exchanger is determined by the product of the frontal area and the length. The fan power, frontal area, pressure drop and the heat transfer rate are all important objectives which need to be taken into account in order to evaluate the performance of a heat exchanger.

The performance of heat exchangers is intrinsically a multi-objective problem. For example, there is a clear trade off between the volume of the heat exchanger and the mechanical power requirement to drive the fan or pump. Quite small volumes can be obtained when very high velocities are used, but the result is that the pressure drop and therefore the mechanical power also, is very high. However, it is possible to achieve designs which are fundamentally better, by achieving a smaller volume and a smaller or equal pressure drop than another design. This is done by making use of the freedom offered by changing the fin geometry.

One possible option to optimise a heat exchanger design is therefore to apply multi-objective optimisation methods. Another option is to introduce a performance evaluation criterion (PEC), which is a single scalar value representing the performance of the heat exchanger in some metric. For a given fin geometry, it is possible to design fictitious heat exchangers under certain constraints. By fixing several degrees of freedom to the same value for two heat exchangers with different fin geometries, the difference in one of the objectives can be compared.

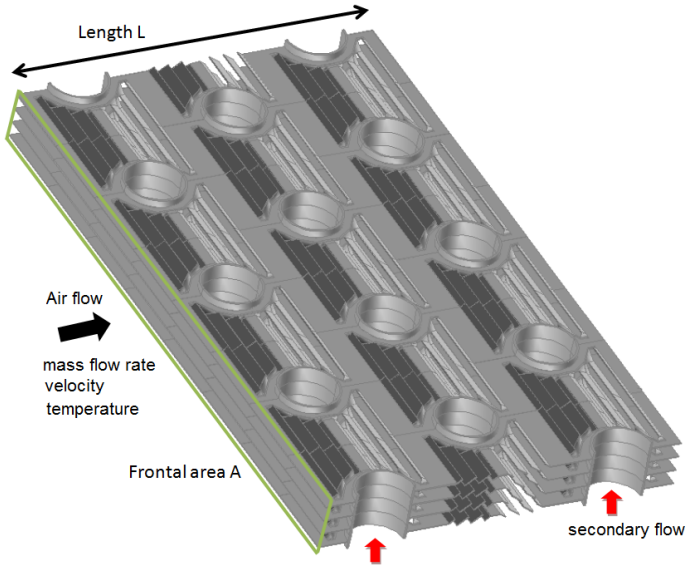

Figure 2.5: Schematic representation of a fin and tube heat exchanger

This allows using a single criterion for comparing two different fin geometries. The PEC can then be used as the goal function for a single-objective optimisation routine. Many different performance criteria exist, based either on the first or second law of thermodynamics. Cowell [1] presented a theory which unified a large number of PECs based on the first law.

It is assumed that the thermal resistance is completely determined by the convective resistance on the fin side. The fin-side fluid changes temperature, whereas the other fluid is supposed to have a constant temperature. This allows comparing different fin geometries independent of parameters which are not influenced by the fin design, such as the heat transfer coefficient of the other flow which is not in contact with the fin. This also has practical applications, namely if the secondary flow is a condensing or evaporating refrigerant, such as in condensers or evaporators. In that case, the refrigerant temperature is constant and the heat transfer coefficient is sufficiently large to justify the approximation of neglecting the convective thermal resistance on the refrigerant side.

The hydraulic diameter is defined as in equation (2.69), using the heat exchanger core volume and the heat transfer surface area. The heat exchanger fluid core volume is a theoretical concept and is equal to the product of the minimum free flow area A_c and the heat exchanger length. The relationship between the heat exchanger volume V and the core volume V_c is given by the contraction factor σ.

$$\sigma = \frac{A_c L}{A_{front} L} = \frac{V_c}{V} \tag{2.73}$$

By introducing the contraction factor into equation (2.69), it becomes apparent that the hydraulic diameter is inversely proportional to the surface area to volume ratio as shown by equation (2.74). Small hydraulic diameters correspond to dense fin spacings.

$$D_h = 4\sigma \frac{V}{A_s} \tag{2.74}$$

The Reynolds number is defined on the hydraulic diameter and on the core velocity v_c, which is the same reference which was used for the definition of the friction factor in equation (2.26). The Reynolds number is given by equation (2.75).

$$Re_{Dh} = \frac{v_c D_h}{\nu} = \frac{\rho}{\mu} \frac{\dot{m}}{A_c \rho} D_h = \frac{\dot{m} D_h}{\mu \sigma A_{front}} \tag{2.75}$$

Now it is assumed that the Colburn j-factor and the friction factor of the fin geometry are known as function of the Reynolds number. The frontal surface area, volume and fan power of the heat exchanger will now be calculated. The fluid inlet temperature, mass flow rate and the heat transfer rate are constants. The physical properties are also assumed to be constant to simplify the analysis.

The frontal area can easily be calculated from the mass flow rate constraint as a function of the Reynolds number, the result is shown by equation (2.76). Independent variables, which are not fixed by the constraints are indicated in bold. This equation can easily be interpreted physically if the hydraulic diameter and contraction factor are held constant. In that case, the Reynolds number is proportional to the frontal velocity. Since the mass flow rate and density are also constant, the frontal velocity must vary inversely proportionally to the frontal area.

$$A_{front} = \frac{\mathbf{1}}{\mathbf{Re_{Dh}}} \frac{\mathbf{D_h}}{\boldsymbol{\sigma}} \frac{\dot{m}}{\mu} \tag{2.76}$$

As the inlet temperature, mass flow rate and heat transfer are constant, the conservation of energy shows that the exit temperature is also constant. Since the temperatures are constant, the logarithmic mean temperature difference is also constant. From equation (2.45), it then follows that the thermal conductance UA is also constant. Finally, because the mass flow rate and specific heat capacity are constant, the number of transfer units NTU is also a constant.

Using the definition of NTU (2.49), the relation for UA for a finned surface (2.64), the definition of the Reynolds number (2.75) and the Colburn j-factor (2.17), the NTU can be written as in equation (2.77). The reference velocity for the Colburn j-factor is again the core velocity v_c.

$$NTU = \frac{h\eta_o A_s}{\dot{m}C_p} = \frac{h\eta_o}{\dot{m}C_p}\frac{4\sigma V}{D_h} = \frac{\eta_o j}{Pr^{\frac{2}{3}}}\frac{4V}{D_h}\frac{\sigma Re_{Dh}\mu}{D_h\dot{m}} \tag{2.77}$$

Equation (2.77) can be rearranged to give the heat exchanger volume as a function of the other degrees of freedom, which are indicated in bold, and the constants, shown in equation (2.78). The product of the surface efficiency and the Colburn j-factor is notated as the modified Colburn j-factor $j^* = \eta_o j$.

$$V = \frac{\mathbf{D_h^2}}{\boldsymbol{\sigma}\mathbf{Re_{Dh}j^*}}\frac{\dot{m}NTUPr^{\frac{2}{3}}}{4\mu} \tag{2.78}$$

A physical interpretation can again be obtained by considering the case in which the hydraulic diameter is constant. Since the thermal conductance UA is constant, the heat exchanger surface area A must vary inversely proportionally with the thermal transmittance U. Since the hydraulic diameter is constant, the heat exchanger volume is proportional to the surface area. If the Prandtl number is also held constant, the product of the Reynolds number and the modified Colburn j-factor is proportional to the Nusselt number and hence to the thermal transmittance U. The heat exchanger volume is then inversely proportional to the thermal transmittance.

The fan power can be computed by using the Bernoulli equation.

$$\mathcal{P} = \dot{m}\int\frac{dP}{\rho} = \dot{m}\frac{\Delta P}{\rho} \tag{2.79}$$

The entrance, exit and acceleration loss are all neglected. This is necessary because these losses are independent of the flow length, which would greatly complicate the equations if they were included. As mentioned in paragraph 2.5.3, in most cases, the core friction dominates the total pressure drop, making this a reasonable assumption. By substituting equations (2.76) and (2.78), the fan power can be written as in equation (2.80). The independent degrees of freedom are indicated in bold.

$$\mathcal{P} = \frac{\mathbf{f}}{\mathbf{j^*}}\frac{\mathbf{Re_{Dh}^2}}{\mathbf{D_h^2}}\frac{\dot{m}\mu^2 NTUPr^{\frac{2}{3}}}{2\rho^2} \tag{2.80}$$

The heat exchanger length is simply the ratio between the volume (2.78) and the frontal area (2.76) and is given by equation (2.81). Again, the independent degrees of freedom are indicated in bold. The physical interpretation of the fan power, if the hydraulic diameter is held constant, follows from the pressure drop, which is proportional to the friction factor, the square of the Reynolds number and the heat exchanger length, which is inversely proportional to the modified j-factor. Since the mass flow rate is constant, the fan power is proportional to the pressure drop. Equation (2.80) shows that by increasing the modified Colburn j-factor, the required fan power is reduced because the length of the heat exchanger is reduced.

$$L = \frac{\mathbf{D_h}}{\mathbf{j}^*} \frac{NTUPr^{\frac{2}{3}}}{4} \tag{2.81}$$

Each of the previous global characteristics of the heat exchanger can be expressed as a group indicated in bold and a function of some constants. By dividing the characteristic by the characteristic of a reference heat exchanger, these relative values are then only a function of the respective groups indicated in bold. This reference heat exchanger can be chosen arbitrarily.

Now that several heat exchanger characteristics have been expressed as a function of the four degrees of freedom, scalar PECs can be established by setting three quantities to a fixed value. The remaining quantities are then a function of the remaining degree of freedom, which is chosen to be the fin geometry. For example, the hydraulic diameter D_h, the contraction factor σ and the fan power $\mathcal{P}$ can be held fixed and the frontal surface area A_{front} or the heat exchanger volume V can be examined for different fin designs. The constraint that the fan power is equal to the fan power of some fictitious reference heat exchanger $\mathcal{P} = \mathcal{P}_{ref}$ is expressed by equation (2.82) and follows from equation (2.80).

$$\frac{f}{j^*} \frac{Re_{Dh}^2}{D_h^2} = \frac{f_{ref}}{j_{ref}^*} \frac{Re_{Dh,ref}^2}{D_{h,ref}^2} \tag{2.82}$$

Equation (2.82) can be solved for the Reynolds number of the heat exchanger, resulting in equation (2.83).

$$Re_{Dh} = \sqrt{\frac{f_{ref}}{f} \frac{j^*}{j_{ref}^*}} \frac{D_h}{D_{h,ref}} Re_{Dh,ref} \tag{2.83}$$

By evaluating (2.76) for the heat exchanger under consideration and for the reference heat exchanger and substituting equation (2.83), the ratio of the frontal area of the heat exchanger A_{front} to the frontal area of the reference heat exchanger $A_{front,ref}$ is obtained. It is given by equation (2.84).

$$\frac{A_{front}}{A_{front,ref}} = \frac{1}{\sqrt{\frac{f_{ref}}{f} \frac{j^*}{j_{ref}^*}}} \frac{\sigma_{ref}}{\sigma} \tag{2.84}$$

Since the contraction factor σ was also held fixed, it is equal to the contraction factor of the reference σ_{ref}. Equation (2.84) is the well-known j/f factor criterion established by Kays and London [11].
The Reynolds number (2.83) can also be substituted into the ratio of the volume of the heat exchanger V to the volume of the reference heat exchanger V_{ref}, resulting in equation (2.85).

$$\frac{V}{V_{ref}} = \left(\frac{j_{ref}^*}{j^*}\right)^{\frac{3}{2}} \left(\frac{f}{f_{ref}}\right)^{\frac{1}{2}} \frac{D_h}{D_{h,ref}} \frac{\sigma_{ref}}{\sigma} \tag{2.85}$$

Equation (2.85) shows that to achieve a compact heat exchanger without the penalty of a higher fan power, it is a good idea to reduce the hydraulic diameter D_h. This corresponds to a high surface area to volume ratio. Furthermore, flow contraction should be avoided as much as possible, the contraction factor σ should be as close to one as possible. This explains why in many commercial compact heat exchangers, very high fin densities are used (small D_h), whereas the fin thickness is kept as small as possible (reduced flow contraction, increased σ). These results are independent of the shape of the fin geometry.

When the contraction factor and the hydraulic diameter are kept fixed, the VG-1 criterion by Webb [12] is obtained, given by equation (2.86). When comparing two fin geometries, the fin geometry with the smaller value for VG-1 results in a more compact heat exchanger design without requiring a higher fan power to force the flow over the heat exchanger core.

$$VG\text{-}1 = \frac{V}{V_{ref}} = \left(\frac{j^*_{ref}}{j^*}\right)^{\frac{3}{2}} \left(\frac{f}{f_{ref}}\right)^{\frac{1}{2}} \tag{2.86}$$

Since VG-1 should be as small as possible, this means that the modified Colburn j-factor should be large and the friction factor should be small. As discussed in paragraphs 2.3.3 and 2.3.4.3, both for flow over a plate and wall-bounded flow, increases in the j^* factor are linked with increases in f. For many modifications to a basic fin geometry, the result will be that as the j^*-factor increases, so does the friction factor f. The trade-off between both factors which results in better (with respect to VG-1) heat exchangers is represented by the exponents for the factors in equation (2.86). Clearly, improvements in the modified Colburn j-factor are more important that the accompanying increase in the friction factor.

2.6.3 Other first law performance criteria

Many other first law-based criteria can be derived from this framework. For example, the heat transfer performance factor J and the pumping power factor F proposed by LaHaye et al. [13] can both be obtained from the Cowell method. J is proportional to the heat transfer per unit volume (equation (2.87)) and F is proportional to the fan power per unit volume (equation (2.88)).

$$J = jRe_{Dh} \tag{2.87}$$

$$F = fRe^3_{Dh} \tag{2.88}$$

Since the heat transfer rate in the Cowell method is constant, the required heat exchanger volume given by equation (2.78) is inversely proportional to the J-factor. The F-factor is obtained by dividing the fan power equation (2.80) by the equation

for the volume (2.78) and ignoring the constant non-bold factors. Plotting the J-factor as a function of the F-factor contains the same assumptions and information as plotting the heat exchanger volume as a function of the fan power.

Another example of a first-law based PEC is the JF criterion established by Yun and Lee [14]. The JF criterion expresses the ratio between the heat transfer coefficient and the cube root of the friction power per unit surface area. It is a "the-larger-the-better" criterion, as friction power per unit surface should be as small as possible and the heat transfer coefficient should be as large as possible. It can be derived by dividing the J-factor (2.87) by the cube root of the F-factor (2.88) if the hydraulic diameter is constant, since the unit surface area is proportional to unit volume. By taking the cube root of the fan power per unit surface area the Reynolds number is eliminated from the fraction. However, since the j- and f-factors are a function of the Reynolds number, the fraction is still implicitly dependent on the Reynolds number. There is no fundamental difference between taking the ratio of the J-factor with the cube root of F, or any other combination of powers of these dimensionless quantities.

$$JF = \left(\frac{j^*}{j^*_{ref}} \right)^1 \left(\frac{f_{ref}}{f} \right)^{\frac{1}{3}} \tag{2.89}$$

Clearly, the JF criterion (2.89) is very similar to the VG-1 criterion (2.86), differing only in the value of the exponents. The qualitative result that the j^*-factor should be large and the f-factor should be small is the same. However, the weighting of the relative importance between the increase in j^* and the increase in f due to a modification in fin geometry is now different. While the VG-1 criterion has a clear physical interpretation in terms of fan power and heat exchanger volume, this is not the case for the JF criterion. For the VG-1 criterion, there is a single degree of freedom due to the constraint on the fan power, for the JF criterion there are two degrees of freedom if the hydraulic diameter is constant, as no extra constraints are imposed. If the hydraulic diameter is not constant, there are three degrees of freedom with respect to fan power and volume. Several fin designs with different fan powers and volumes can all correspond to the same JF factor, even if the hydraulic diameter is held constant. For this reason and because the exponents in the JF-factor are essentially arbitrary, the JF factor will not be considered further in this work.

2.6.4 Other heat exchanger objectives

In real-life applications, other objectives can be as important or even more so than the considered fan power, volume and frontal area. For instance, the pressure drop over the heat exchanger could be limited by the chosen fan. In that case, the value of the pressure drop is not important, as long as it remains below a certain thresh-

old. This could be treated by checking the pressure drop for every geometry under study and excluding those designs where the pressure drop does not meet the requirement.
In many cases, the heat exchanger is just a means to an end, a component which is a part of a larger system. For instance, in a heat pump system, heat exchangers are used, but the quantity of interest is the overall coefficient of performance (COP) of the entire heat pump system. Even though the fan or pumping power of the heat exchanger form a significant contribution to the COP of the system, the thermodynamic irreversibilities associated with heat transfer over a finite temperature difference strongly influence the power of the compressor and therefore also the overall COP. Second law-based performance evaluation criteria exist, which attempt to take the effect of irreversibilities in the heat exchanger on the overall system efficiency into account. This allows optimising the heat exchanger with respect to the overall system performance, which is ultimately of much more interest. The difficulty in using these criteria is in effectively choosing the constraints for the heat exchanger, such as the fluid temperature and mass flow rate. If these are not well chosen, the result of the actual optimisation of the entire system and the result of optimising the heat exchanger with respect to the second law criterion can be very different. In this work, second law criteria will not be considered.

Other objectives are the propensity of the fin geometry to fouling, heat exchanger performance under frosting conditions, the frequency and power of the noise which is generated due to unsteady phenomena in the heat exchanger core, manufacturing cost and robustness. These are even more difficult to treat in a generally valid manner and will not be considered further in this work. The parameters of interest which will be considered are the heat exchanger volume and the fan power. The hydraulic diameter will be kept constant for most cases, because the effect of the hydraulic diameter can readily be obtained theoretically from the Cowell method equations.

2.7 Optimisation tools

2.7.1 Single-objective optimisation methods

2.7.1.1 Introduction

Different optimisation tools are available. In this section, a very brief overview will be given of the methods which are commonly used in heat exchanger optimisation, as well as the methods which will be used in this work. Heat exchangers can be optimised with respect to a single objective, such as the area goodness factor, JF factor or VG-1 criterion. In this case, a single-objective optimisation method can be used. Two types will be discussed, gradient-based methods and heuristic approaches. An optimisation problem can be constrained or unconstrained. In

constrained problems, an optimum for the objective function is required, where the optimum point also satisfies one or more constraint functions. The constraint functions can either be equalities or inequalities.

2.7.1.2 Gradient-based methods

Gradient-based methods find a local optimum by using information about the gradient of the function to move towards the optimum, starting from a given starting location. These methods are only guaranteed to find a local optimum. It is only under certain conditions, it can be guaranteed that a gradient-based method converges to a global optimum. Constrained problems can be reformulated as unconstrained problems by using the methodology of Lagrange multipliers. The necessary and sufficient conditions which need to be satisfied for a given point to be a local optimum are called the Karush-Kuhn-Tucker conditions. It can be shown that if the problem space is convex, this is also the global optimum.

Two main issues can be identified in a gradient-based optimisation method. The first issue is to determine the direction along which will be searched to find a better point, the second issue is to determine how far to travel in this direction. A very simple method is the steepest descent method, where the gradient in the current test point is used as the search direction. A new one-dimensional optimisation problem is then solved to find the optimal magnitude of the step along this direction. This method tends to converge rather slowly and more efficient methods exist. The conjugate gradient method determines a new search direction based on the gradient in the current test point and the gradients of all previously visited test points. This is done by taking the weighted average of the gradient in the current point and the previous search direction as the new search direction. The weights are selected based on the magnitude of the gradient in previous iterations.

In order to mitigate the drawback of convergence to a local optimum, multistart optimisation can be used. Several starting locations in the design space are used and the method is performed for each starting point. Finally, the best point is selected out of all local optima.

Gradient-based methods are deterministic. For a given objective function and a given starting point, the algorithm always returns the same result.

2.7.1.3 Heuristic methods: genetic algorithms

Other methods are probabilistic, such as the genetic algorithm heuristic. It is possible to obtain a different result by running the heuristic repeatedly.

Genetic algorithms are based on evolutionary selection. A population of different designs is initialised and this population is evolved over several generations. A fitness function determines how likely a certain design is to propagate to the next generation. Propagation to the next generation can occur directly, where the same

design reoccurs in the next generation. Another option is that two designs produce children, which are inserted into the next generation. Children are new designs which incorporate features of both parent designs. This requires a function which generates a new design from two given parent designs. The selection of which parents combine to produce children is done probabilistically based on the fitness value of the parents. From one generation to the next, mutation of the population also occurs, which corresponds to small changes in the design. The population contains a fixed number of individual designs. Designs with low fitness tend to die off and not propagate their features into the next generation. New generations are produced and evaluated until a certain stopping criterion is met. This could be because the average fitness of the population is no longer changing with increasing generations, or because some arbitrary limit on the number of generations is met. The best individual design in the final population is then the optimal design returned by the heuristic.

When compared with gradient-based methods, the main advantage of heuristics such as genetic algorithms is that they are much less likely to get stuck in a local optimum as they tend to explore the design space more. The downside is that they are likely to require much more function evaluations.

2.7.2 Surrogate models

2.7.2.1 Introduction

Another useful tool in optimisation problems are surrogate models. A surrogate model is a simplified model which is used as a surrogate for a more complicated and more accurate model. A surrogate model is much cheaper to evaluate computationally and can therefore be used to explore the design space much more thoroughly. This is of course only of any use if the surrogate model well approximates the actual model. A distinction can be made between regression and interpolation surrogate models. A regression model allows for a mismatch between the result of the accurate model and the surrogate model in the points where the result of the accurate model is known. This is useful in the case of measurement uncertainty on the accurate model, which is modelled as random noise. The surrogate model needs to predict the underlying physics of the accurate model and not the noise itself. If the accurate model is provided by deterministic numerical simulations, there is no noise. In this case, the surrogate model needs to interpolate the accurate model, which means that there can be no error between the surrogate and the accurate model in the data points. In this work, all data will be provided by numerical simulations, regression models are therefore not discussed. The two interpolating surrogate models which are used in this work will be discussed.

2.7.2.2 Polynomial models

A very simple but ubiquitous surrogate model is the polynomial model. Each dimension of the design vector can have a different degree of the polynomial. For example, equation (2.90) shows a polynomial model for a two-dimensional design space. The variable of the first dimension is indicated with x, the second dimension with y. The degree of the polynomial for x is one, for y, the degree is two. The coefficients of the polynomial are indicated with $a_{i,j}$ where the first index refers to the degree of the first factor x and the second to the degree of the second factor y.

$$f(x,y) = a_{0,0} + a_{1,0}x + a_{0,1}y + a_{0,2}y^2 + \underline{a_{1,1}xy} + \underline{a_{1,2}xy^2} \tag{2.90}$$

The underlined terms with mixed variables are also called the interaction terms. In total, there are $(1+1)*(1+2) = 6$ coefficients which need to be determined from the data. In general, the number of coefficients is equal to the product of the number of levels. The level for a dimension is equal to the degree of the polynomial incremented by one. As the number of dimensions increases, the number of data points required to fit the model increases exponentially.

Polynomial models are called parametric models, because there are a finite number of parameters a which are determined from the data. The number of data points is exactly equal to the number of parameters. For a given polynomial with fixed degrees for the variables, it is not possible to add more data than required by the number of parameters.

2.7.2.3 Gaussian process models

The prior

Other models such as Gaussian process models are non-parametric. No explicit parametrisation is imposed, there is therefore no limit to the number of data points which can be used to fit the model without needing to change the assumptions. In what follows, the broad principles of the function space view of Gaussian process models will be explained. A more detailed and mathematical approach is given by Rasmussen and Williams [15].

A Gaussian process is a distribution of functions. A sample of a Gaussian distribution is a single number, whereas a sample from a Gaussian process is a single function. Just as some numbers are more likely than others for a Gaussian distribution, some functions are more likely than others for the Gaussian process. The model is called a *Gaussian* process model because of the special property of the functions which are obtained by sampling from this distribution. For any choice of a finite number of input vectors, the corresponding ordinates of the sampled function form a finite dimensional multivariate Gaussian distribution. This means that

the Gaussian process can be described as a Gaussian distribution with an average function $\mu(x)$ and a covariance function $k(x, x')$.

The functions which are obtained by sampling from the Gaussian process can now be described further by imposing a correlation function. For a given finite dimensional sampling of any function, there is some correlation between the obtained ordinates. If the sampled input vectors are very close together, the ordinates will also be close together. This is expressed mathematically by the correlation between the ordinates, which will be close to one. For input vectors which are very far removed in the design space, the correlation will be close to zero. Note that for an interpolating model, the correlation function must be exactly one if the distance between the input vectors is zero. If the same input vector is entered into the surrogate repeatedly, the same answer needs to be returned each time, corresponding to a correlation of unity.

The possible functions are now specified by imposing a certain shape for the correlation function. For an arbitrary function y obtained by sampling from the Gaussian process and two input vectors x and x', one possible choice for the correlation function is given by equation (2.91). The index i refers to the component of the input vector. The so-called hyperparameters Θ_i determine how fast the correlation between two points decreases along a certain dimension. The covariance function $k(x, x')$ is obtained by multiplying the correlation function with the variance on the ordinates.

$$corr(x, x') = \frac{k(x, x')}{\sigma_y^2} = exp(-\sum \Theta_i (x_i - x_i')^2) \tag{2.91}$$

Consider now the multivariate Gaussian distribution which follows by evaluating the sampled function in a certain set of input vectors. The vector of corresponding ordinates is given by the vector y. The covariance matrix K is obtained by evaluating the correlation between the different input vectors and multiplying by a constant variance. The covariance matrix is a sampling of the covariance function $k(x, x')$ where each entry corresponds to the covariance between the two input vectors associated with the position in the matrix. Likewise, the average vector μ is a sampling of the average function $\mu(x)$. The multivariate Gaussian distribution is then given by equation (2.92).

$$\mathcal{N}(\mu, K) = (2\pi)^{-k/2} \, |K|^{-1/2} \, exp(-\frac{1}{2} \, (y - \mu)^T \, K^{-1} \, (y - \mu)) \tag{2.92}$$

In order to fully define the Gaussian process, the average function and the covariance functions need to be fully defined. As an example, a Gaussian process will be constructed for a one-dimensional input. By fixing the root of the variance σ_y to 0.5 and the activity parameter Θ to 20 in equation (2.91), the covariance function is now known. For the average function $\mu(x)$ the choice of a constant

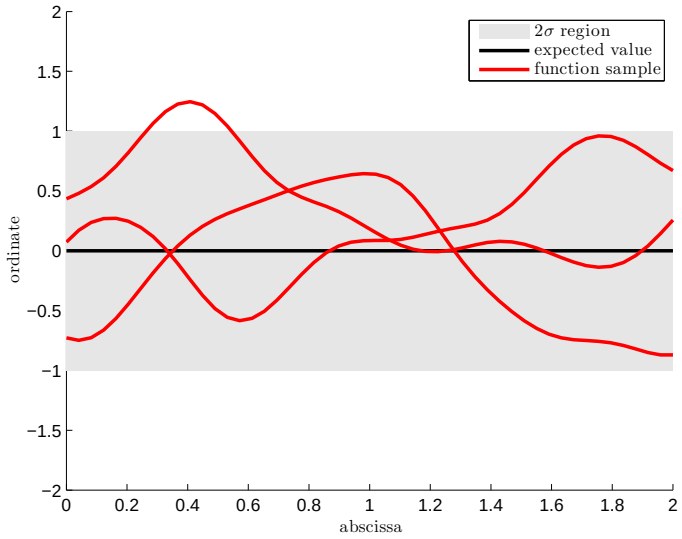

Figure 2.6: Three representations of sampled functions from the Gaussian process

function equal to zero is made. Using equation (2.92) for a set of 50 abscissa linearly spaced from 0 to 2, finite dimensional representations of the functions can be sampled from the Gaussian process. The result is shown in figure 2.6.

Several observations can be made about the types of functions which are generated from the Gaussian process. The observations are as follows:

1. The functions are smooth.
2. The behaviour of the functions is not dependent on the location of the design space
3. The functions fluctuate around the mean.
4. Fluctuations occur with a single characteristic length scale.

The properties are direct consequences from the choice of the covariance function. It can be shown that for the given choice of an exponential correlation function, the sampled functions are infinitely smooth. This means that the functions and any derivative of any order is continuous. Secondly, the correlation function is only dependent on the distance between the input vectors, and not on the actual value of the components. This results in what is called stationarity. The behaviour of the sampled functions does not change as the input vectors are translated

in the design space. The third point is explained by noting that the correlation function approaches zero as the distance between two input vectors approaches infinity. This means that if a certain section of the function is known, infinitely far away from this known section, the function values have no correlation with that section. As such, function values in that region are just as likely to be above the mean as below the mean, since the Gaussian distribution is symmetrical around the mean. Far away from any known data, the sampled functions will therefore fluctuate around the mean. The final observation is caused by the correlation function. A single hyperparameter Θ determines the rate of change of the correlation with the distance. It is therefore not possible to have both long-scale and short-scale behaviour.

As the distribution on functions discussed in this paragraph is independent from any data, it is called the prior. It is the assumed behaviour of the sampled functions prior to any data being known.

The a posteriori distribution

Once some data is known, a conditional distribution on functions can be determined. It is the distribution on functions, given the model and given the observed data for a certain set of input vectors. The stochastic variable describing the data for these input vectors is written as the vector Y_1. Sampling the Gaussian process for the known input vectors and the test input vectors results in a multivariate Gaussian distribution on the vector Y_1 and on the unknown test data Y_2. The realisation of a specific sampling or observation of the Gaussian process is notated with lower case y_1 and y_2. It is known that the variable Y_1 is equal to the realisation y_1.

Samples from the conditional distribution could be obtained by sampling from the joint distribution, and rejecting all sampled functions which do not match the observed data y_1. It is much more efficient to determine and directly sample from the conditional distribution instead. The conditional distribution on Y_2 given $Y_1 = y_1$ is given by equation (2.93).

$$f_{Y_2}(y_2|Y_1 = y_1) = \frac{f_{Y_1,Y_2}(y_1, y_2)}{f_{Y_1}(y_1)} \tag{2.93}$$

The conditional probability density is equal to the joint probability density normalised by the marginal density for Y_1. The marginal density does not depend on the variable y_2 and is therefore just a normalising constant. The conditional distribution can therefore be written as equation (2.94). This is exactly the same equation as equation (2.92), with the exception that all constants have been lumped into a single constant C. The constant is defined by the requirement that the total probability is equal to unity. The inverse of the covariance matrix has been written out in block matrix form, which allows separating terms which depend on the test

points (i.e. A_2 and B) and terms which only depend on the data and are therefore constant with respect to Y_2 (i.e. A_1 and y_1). For the sake of clarity, the mean function has been assumed to be the constant zero function.

$$f_{Y_2}(y_2|Y_1 = y_1) = Cexp(-\frac{1}{2}\begin{bmatrix} y_1^T & y_2^T \end{bmatrix}\begin{bmatrix} A1 & B \\ B^T & A2 \end{bmatrix}\begin{bmatrix} y_1 \\ y_2 \end{bmatrix}) \quad (2.94)$$

This equation can be rewritten into the standard form for a Gaussian distribution as shown in equation (2.95). Through parameter identification, the a posteriori expected value $\overline{y}_2$ and the a posteriori covariance matrix K_{y_2} can be obtained.

$$f_{Y_2}(y_2|Y_1 = y_1) = C'exp(-\frac{1}{2}(y_2 - \overline{y}_2)^T K_{y_2}^{-1}(y_2 - \overline{y}_2)) \quad (2.95)$$

$$\overline{y}_2 = -A_2 B^T y_1 \quad (2.96)$$

$$K_{y_2} = A_2^{-1} \quad (2.97)$$

With these two parameters, the conditional distribution is fully characterised. Figure 2.7 shows three sampled functions from the conditional distribution, as well as the expected value function and the standard deviation function of the conditional distribution.

The expected value function can now be used as a prediction of the accurate model in points where data is unknown. The standard deviation function gives an estimate of the uncertainty associated with this prediction. The uncertainty estimate is zero in points where data is available and it increases as the distance from the data points increases. It should also be noted that the prediction tends to converge towards the average function as the distance from the data increases.

Estimation of the hyperparameters

At this point, the Gaussian process model can be used to perform predictions. For a given prior and given observed data, the a posteriori conditional distribution can be determined. The expected value of the conditional distribution is used to predict data for test points. If a single test point is used, the covariance matrix of the conditional distribution reduces to the variance. This variance gives an indication of the uncertainty on the prediction.

However, the results depend on the selection of the prior distribution, which is defined by a mean function and a covariance function. It is necessary to select reasonable functions for this, based on the data which has been observed. These

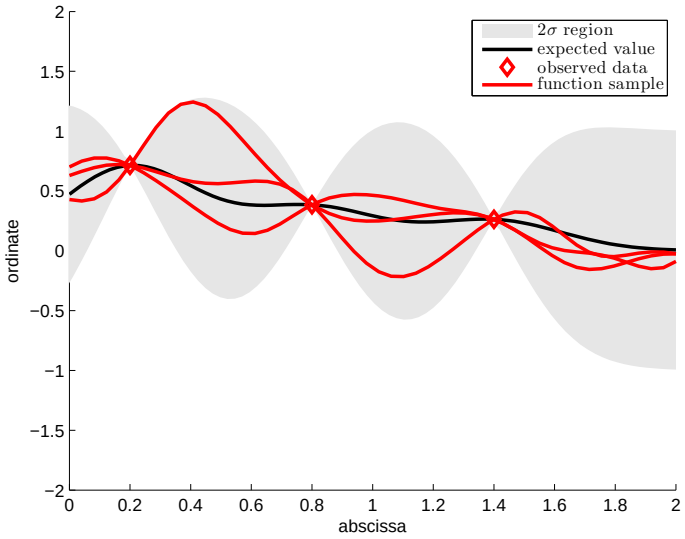

Figure 2.7: Three representations of sampled functions from the conditional Gaussian process

functions form the parameters of the Gaussian process model. These functions are themselves parametrised using so-called hyperparameters. For the choice of the exponential correlation function, the hyperparameters for the covariance function are the variance σ_y and activity vector Θ. For the mean function, there are also several possible choices, for example, it could be parametrised using a polynomial of a certain degree. In this work, a zero degree polynomial is used, which corresponds to a constant mean function.

The problem is now reduced to finding good values for the hyperparameters. This can be done by using a maximum likelihood estimation. By entering the known data into the probability distribution (2.92), the likelihood to sample the observed data from a given distribution is obtained. By assuming the hyperparameters to be variable, they can be optimised to obtain the largest likelihood for the prior to generate the observed data. The logarithm of the likelihood is given by equation (2.98), the hyperparameters appear implicitly in the covariance matrix K and the mean vector μ.

$$ln(\mathcal{L}) = -\frac{1}{2}\left(y-\mu\right)^T K^{-1}\left(y-\mu\right) - \frac{1}{2}ln(|K|) - \frac{k}{2}ln(2\pi) \tag{2.98}$$

In the special case where the exponential correlation function (2.91) is used and the hyperparameters Θ, σ and a constant mean μ are obtained by maximum

likelihood estimation, the Gaussian process model is also called an ordinary Kriging model.

2.7.3 Sampling plans

2.7.3.1 Introduction

All surrogate models require some data in order to make predictions. The problem of choosing which inputs to evaluate in order to obtain the maximum amount of information from a given complicated model or experiment is treated by the theory of the design of experiments (DOE). A series of inputs which needs to be evaluated is called a sampling plan. The best choice for the sampling plan depends on the properties of the accurate model or experiment. Many different sampling plans exist, each with its own assumptions. Some of these sampling plans will be briefly discussed in this section.

The first problem which needs to be solved is to determine which variables are important for the problem to be studied. In case there are many variables which might all have some impact, a screening method can be useful. Screening allows efficiently evaluating which input variables definitely have some impact on a given output variable and which input variables have negligible effect. In this work, parameters will be selected based on physical intuition about the problem.

2.7.3.2 Full factorial sampling

Full factorial sampling plans are used if a polynomial model is assumed as underlying behaviour of the accurate model. In the case of experiments, measurements are assumed to be the result of some physical reality which follows a polynomial model compounded with some noise due to measurement error. It is necessary to determine the degree of the polynomial for each variable. In the terminology of full factorial sampling plans, this is usually done by selecting the number of levels for each variable. The degree of the polynomial is the number of levels reduced by one.

For a full factorial sampling plan, the total number of sampling points is equal to the product of the levels. This corresponds to the number of parameters which need to be fitted in the polynomial model. The sampling plan is then constructed by imposing a uniform distribution for each variable.

The advantage of full factorial sampling plans is that all interaction terms are modelled in the polynomial model. The only additional assumption which is made is the degree of the polynomial for each variable. It is observed that in general, higher-order terms tend to be smaller in the polynomial model. This is why taking relatively few levels for the variables can still result in a good model for the overall qualitative effect of the different variables on the output.

2.7.3.3 Fractional factorial designs

In the fractional factorial model, some more additional assumptions are made. Higher-order interaction terms between the high-degree terms of different variables are often small. In a fractional factorial design they are assumed to be exactly zero, which reduces the number of parameters in the polynomial model. Correspondingly, the number of data points required to fit the model is also reduced. Under the assumption that the interaction terms are negligible compared with the other terms, the fractional factorial design results in the same information for a fraction of the calculations. On the other hand, if interaction terms are in actuality significant, severe errors are made. The effect of the interaction is contributed to one of the other parameters in the polynomial model. This is called confounding or aliasing.

In order to illustrate the problem, a fractional factorial design will be constructed for a problem with three variables with each two levels. The general polynomial model is then given by equation (2.99).

$$\begin{aligned} f(x,y,z) =& a_{0,0,0} + a_{1,0,0}x + a_{0,1,0}y + a_{0,0,1}z + \\ & \underline{a_{1,1,0}xy} + \underline{a_{1,0,1}xz} + \underline{a_{0,1,1}yz} + \underline{a_{1,1,1}xyz} \end{aligned} \tag{2.99}$$

There are four main effects and four interaction effects, the latter of which are underlined in the equation. The values for the variables are represented non-dimensionally by letting them vary between -1 and +1, -1 corresponds to the lowest setting of the variable and +1 to the highest setting. The fractional factorial design can then be generated by choosing a generator function. For example, the choice could be made that the interaction term xyz is aliased with the constant term. The settings for the variables will be chosen such that the product of all variables is constant. There are two possible choices, either ensure that $xyz = +1$ or that $xyz = -1$.

This results in two choices for the fractional factorial sampling plan, given by tables 2.1 and 2.2.

x	y	z
1	1	1
-1	-1	1
1	-1	-1
-1	1	-1

Table 2.1: Fractional factorial sampling plan for three variables and two levels with generator xyz=1

There are now four data points to determine the eight parameters of a full factorial model. This is an under-defined system. The system is fully defined by

x	y	z
-1	1	1
1	-1	1
-1	-1	-1
1	1	-1

Table 2.2: Fractional factorial sampling plan for three variables and two levels with generator xyz=-1

assuming that the interaction effects are negligible. The four underlined terms in equation (2.99) therefore vanish, the number of data points can be reduced from 2^3 to 2^{3-1}. If the interaction effects are in reality not negligibly small, aliasing will occur. If two variables are aliased, it means that the effect of both variables on the output cannot be distinguished from one another.

It can be shown that the aliasing pattern can be obtained by multiplying the generator function with a variable on both sides of the equation and equating the second power of any variable to the identity. This results in the relations $yz = x$, $xy = z$ and $xz = y$, which indicates that the main effect of the x-parameter is aliased with the interaction effect yz, y is aliased with xz and z with xy.

This can also be seen by introducing the sampling plan into the equation of the fractional factorial polynomial model and solving for the parameters. The function evaluations are performed using the full factorial model. This gives the parameters of the fractional factorial model X, Y, Y and I as a function of the parameters of the full factorial model $a_{i,j,k}$.

$$f(x, y, z) = I + Xx + Yy + Zz \tag{2.100}$$

Using the design corresponding to the generator $xyz = 1$, the result is given by equation (2.101).

$$\begin{aligned} I &= a_{0,0,0} + a_{1,1,1} \\ X &= a_{1,0,0} + a_{0,1,1} \\ Y &= a_{0,1,0} + a_{1,0,1} \\ Z &= a_{0,0,1} + a_{1,1,0} \end{aligned} \tag{2.101}$$

With the other choice of the generator $xyz = -1$, the obtained coefficients are given by equation (2.102).

$$\begin{aligned} I &= a_{0,0,0} - a_{1,1,1} \\ X &= a_{1,0,0} - a_{0,1,1} \\ Y &= a_{0,1,0} - a_{1,0,1} \\ Z &= a_{0,0,1} - a_{1,1,0} \end{aligned} \tag{2.102}$$

Using a fractional factorial sampling plan and polynomial model to evaluate a system where in reality two-factor interaction terms are present results in incorrect values for the coefficients. The coefficients of the interaction terms are added to or subtracted from the actual coefficients, depending on the specific choice of the fractional factorial sampling plan. The main effects are aliased with two-factor interactions. This type of design is known as a resolution III design.

The resolution summarises the aliasing pattern. Resolution II designs result in aliasing between the main factors. There are more main factor coefficients than there are data points. This kind of design is therefore completely useless. Resolution IV designs contain enough data to determine the main factors accurately. There is no aliasing between the main factors and two-factor interactions (only with three-factor and higher interaction terms). Two-factor interactions are aliased with other two-factor interactions. Resolution V designs exhibit no aliasing between main factors and three-factor or lower interaction terms. Two-factor interaction terms can be determined without aliasing with other two-factor interactions. If two-factor interaction and higher interaction effects are negligible, a resolution III design suffices.

For a larger number of factors, it is possible to choose which interaction effects will be aliased. For example, a resolution III design for five factors of two levels consists of $2^{5-2} = 8$ data points. This is enough to determine the constant term and the five linear coefficients of the polynomial model. The additional two data points can be used to eliminate the effect of some interaction terms. For example, consider the case where the generators are chosen to be $D = AB$ and $E = AC$. The aliasing structure is then given by equation (2.103), where the equals sign indicates aliasing. This design corresponds to four equivalent polynomial models. The two data points result in the determination of the terms $BC = DE$ and $BE = DE$. It does not matter whether the terms BC and DE are included in the polynomial model, or BC and BE or one of the other two combinations. They all result in the same values for the coefficients, since it is not possible to distinguish BC from DE or BE from DE for the given sampling plan. The combination BC is equal to the combination DE for every point in the sampling plan. It does not matter whether the term BC or DE is used in the polynomial model, the equations for the coefficients resulting from substituting the sampling plan into the polynomial model are identical. Furthermore it is apparent that the combinations BC, BE, CD and DE do not appear in the aliasing pattern of equation (2.103). If it would be known a priori that these interactions are the only interactions which occur physically, then this resolution III design gives just as much information as the full factorial design with respect to the main factor effects. It is not possible to estimate these interactions, as they are aliased with each other ($BC = DE$ and $BE = DE$).

$$\begin{aligned} A &= BD, CE \\ B &= AD \\ C &= AE \\ D &= AB \\ E &= AC \end{aligned} \tag{2.103}$$

The problem is that it is often problematic to establish a priori which interaction effects will be negligible or not. For several cases in this work, significant two-factor interaction effects will be observed. Using a fractional factorial sampling plan which assumes certain interaction effects to be negligible can give absurd results if this assumption is not valid. The interaction effect could result in completely unimportant parameters to be assigned a significant impact. Another option is that the interaction and the main effect could cancel, causing important variables to be considered unimportant. According to the sparsity of effects principle of Wu et al. [16], interaction effects between three or more variables tend to be rare. Therefore, it is often enough to account for main effects and two-factor interactions. Still, it is important to check which terms are assumed to be negligible in the sampling plan. If two-factor interactions are neglected, it is necessary to provide a physical reason why this would be justified.

It is also possible to use three levels for the factors. This significantly complicates the aliasing pattern, as a two-factor interaction effect between, for example, x and y now consists of several terms, namely xy, x^2y, xy^2 and x^2y^2. It is again possible to construct fractional factorial sampling plans by making assumptions on the interaction terms.

2.7.3.4 Orthogonal arrays

If more than two levels are used, other sampling plans than fractional factorial designs are more common, such as orthogonal arrays. The factorial designs discussed in paragraphs 2.7.3.2 and 2.7.3.3 are special cases of orthogonal array designs. Consider a sampling plan consisting of N entries and m variables. Each variable has s_i levels. This sampling plan is orthogonal with strength t if for any t variables, each possible combination of the level occurs equally often in the sampling plan. An example of a strength 2 array for four variables with three levels is given by table 2.3. This orthogonal array is known as the L9 array. If any pair ($t = 2$) of columns are chosen, all combinations occur just once. The advantage of orthogonal arrays over fractional factorial designs is that different levels can be used for different variables, which allows for more flexibility. This results in quite complicated aliasing patterns. An orthogonal design of insufficient strength results in some main factors to be aliased with some two-factor interactions. It can be shown that a fractional factorial sampling plan with resolution R is equivalent

to an orthogonal array with strength $R-1$ if all factors have the same levels [16]. Orthogonal arrays are the sampling plans that are used in the Taguchi method, which will be discussed later.

A	B	C	D
0	2	2	0
0	0	0	1
2	2	0	2
1	0	2	2
2	1	2	1
2	0	1	0
0	1	1	2
1	2	1	1
1	1	0	0

Table 2.3: L9 orthogonal array

2.7.3.5 Latin hypercube sampling

A Latin hypercube sampling plan is a special case of an orthogonal array of strength 1, where each level occurs only once in every column. An orthogonal array of strength 1 is also called a fully stratified sampling plan. If the entire design space is projected on a single dimension, the result is an equidistant set of points.

This does not uniquely specify the sampling plan, it can be shown that there are $s!^{N-1}$ possibilities for a sampling plan with N variables and s levels. The maximin criterion is used to select the best sampling plan out of all the possibilities. The criterion specifies that the smallest distance between any two points in the design space should be maximised, which ensures a good filling of the design space. The criterion requires a distance metric and is therefore dependent on the dimensions of the variables. It is therefore recommended to non-dimensionalise all variables so they vary over the same range. In this work, the euclidean distance will be used, even though other metrics such as the Manhattan distance are also possible. The distance metric should be interpreted as a measure of similarity between the designs in the design space, rather than a real physical distance.

Latin hypercube sampling plans are useful to initialise Gaussian process models, because of their space-filling properties. With relatively little data, an idea can be given of the behaviour of the design space, even though aliasing will occur between main factors. The Gaussian process prediction of the uncertainty can then be used to update the model in interesting regions in order to fully resolve the impact of the variables on the output quantity of interest in those regions.

2.7.4 Taguchi method

The Taguchi method is a design of experiments method which combines orthogonal arrays with a specific data reduction method. It was developed for an industrial context. The general idea is that if something is produced, there is always some variation on this produced quantity, due to uncontrolled factors such as ambient humidity, temperature and variations in human actions. Taguchi contends that the controllable factors should not just be chosen to obtain optimal expected behaviour, but that the impact of the control factors on the variation should also be taken into account. In other words, the choice of control factors should lead to a robust behaviour, which is not strongly influenced by noise due to uncontrolled quantities.

Two main types of Taguchi analyses can be identified, namely dynamic and static analysis. For a dynamic analysis, there is a system which transforms some kind of input signal into some kind of output signal. The quantities of interest are then characteristic parameters of the transformation, such as linearity or gain. A temperature measurement device is an example, where a temperature signal needs to be transformed linearly into a voltage signal, with as little influence of noise factors such as humidity as possible. This type of analysis is not applicable to the optimisation of heat exchangers and will not be discussed further.

The optimisation of heat exchangers is an example which can be treated with the static Taguchi analysis. In a static analysis, there are quantities of the system which need to be optimised, such as the volume of a heat exchanger. This is independent from some kind of input signal. In order to incorporate the effect of uncontrolled factors, a signal to noise ratio is defined. For a single setting of the controllable factors, a fluctuation in the output quantities will be observed due to the noise. The signal to noise ratio transforms this set of measurements corresponding to a single design setting to a single value. Different signal to noise ratios are available, depending on whether the quantity of interest should be as large/small as possible, or instead should ideally reach a target value. The noise is modelled as uncorrelated Gaussian noise.

In numerical simulations, there are no uncontrollable factors which can be treated as Gaussian noise. Numerical simulations are deterministic, a single choice of the controlled factors will always result in the same solution. The signal to noise ratio idea is therefore not necessary, as there is no stochastic noise. Each measurement set consists of a single value.

The data reduction of the orthogonal array will be treated using an example of an L9 array, shown in table 2.4. This is an orthogonal array of strength 2 for four variables of three levels. This corresponds to a full factorial design of resolution III, which consists of $3^{4-2} = 9$ entries. The underlying assumption is that there are no interactions between the factors. The polynomial model which corresponds to this orthogonal array has nine parameters, namely four quadratic terms, four linear terms and one constant term. These nine parameters of the quadratic model

can be solved for by using the nine known signal to noise ratios. Alternatively, it is possible to express the observed signal to noise ratios in the table as a function of the parameters of the underlying polynomial model.

A	B	C	D	SN
1	**1**	**1**	**1**	**SN1**
1	2	2	2	SN2
1	3	3	3	SN3
2	1	2	3	SN4
2	2	3	1	SN5
2	**3**	**1**	**2**	**SN6**
3	1	3	2	SN7
3	**2**	**1**	**3**	**SN8**
3	3	2	1	SN9

Table 2.4: L9 Taguchi array

Taguchi now defines average signal to noise levels for each factor level. These are obtained by taking the average of the signal to noise ratios of every row where the factor takes the correct value. For example, the average signal to noise ratio for factor C at level 1 corresponds to the rows which are indicated in bold in the table. The corresponding average signal to noise levels for the factor C are given by equation (2.104). The optimal level for each factor is now obtained by choosing the factor level which corresponds to the maximum value for this average signal to noise level.

$$\begin{aligned} SN_{C1} &= \frac{1}{3}(SN1 + SN6 + SN8) \\ SN_{C2} &= \frac{1}{3}(SN2 + SN4 + SN9) \\ SN_{C3} &= \frac{1}{3}(SN3 + SN5 + SN7) \end{aligned} \tag{2.104}$$

Why this optimisation method is correct will be shown by using the underlying polynomial model. The variables of this model are chosen such that the value -1 corresponds to the lowest level and 1 to the largest level. A parameter curve corresponding to variations in parameter C and all other parameters held constant is then given by equation (2.105). For the sake of brevity, neither the equation for the entire polynomial model nor that for the other parameter curves is given.

$$f = c_2 C^2 + c_1 C + constant \tag{2.105}$$

Now the observed signal to noise values are solved for the parameters of the entire polynomial model. These values are then substituted into the relation for the

average signal to noise ratio of every factor level (equation 2.104). The result of the procedure for the factor C in equation is given by equation (2.106), where the constant term of the polynomial model is indicated with a_0.

$$\begin{aligned} SN_{C1} &= c_2 - c_1 + (a_0 + \frac{2}{3}(a_2 + b_2 + d_2)) \\ SN_{C2} &= 0 + (a_0 + \frac{2}{3}(a_2 + b_2 + d_2)) \\ SN_{C3} &= c_2 + c_1 + (a_0 + \frac{2}{3}(a_2 + b_2 + d_2)) \end{aligned} \tag{2.106}$$

The terms between brackets are the same for all three average signal to noise ratios and therefore do not influence which factor level is optimal for the factor C. Comparing equations (2.105) and (2.106), the equivalence between an optimum of the underlying parameter curve and the optimum obtained using the Taguchi method becomes clear. If the maximum signal to noise level is reached when the factor C is at the lowest level, it means that the corresponding variable in the polynomial model must be -1. Substituting the value -1 into the equation for the parameter curve, the expression $c_2 - c_1$ is obtained, which is exactly equal to the variable part in the equation for the average signal to noise ratio. Essentially, the average signal to noise levels for a given level correspond to the unique value for that level on the parameter curve, plus a constant. This is the case because the array is orthogonal and interactions were assumed to be negligible. Because there are no interactions, the complete polynomial model is equal to the sum of all the parameter curves, minus a multiple of the constant term. Separately optimising all the parameter curves for their respective factors is therefore equivalent to optimising the entire polynomial model.

It has now been shown that using the Taguchi method for a deterministic problem is perfectly the same as optimising a polynomial model which has been fitted to the same orthogonal array. Separately optimising the factors is only allowed if there are no interaction terms. The absence of interaction terms is therefore absolutely essential, as this is required to avoid aliasing and to optimise each factor separately.

The relative importance of the different factors can be investigated by comparing the range over which the average signal to noise values vary for each, as shown in equation (2.107) for the factor C.

$$\Delta_C = max(SN_{Ci}) - min(SN_{Ci}) \tag{2.107}$$

By performing this subtraction, the constant terms in equation (2.106) cancel, and only the varying part of the parameter curve is retained. This range is therefore equal to the difference between the largest and the smallest value of the parameter curve (2.105) for the factor. Due to the underlying assumption that there are no interaction effects, the range for every factor is independent of the values of the other

factors. It is important to note that the range depends not only on the dependence of the quantity of interest on the factor, but also on the range over which this factor was allowed to vary. Comparing the ranges of the different factors therefore does not directly say something about the relative effect of the different factors on their own. Instead, it compares the relative importance of the variation of the factors *over their corresponding ranges*.

The advantage of the Taguchi method is that it is very flexible as different levels for each factor can be used by choosing an appropriate orthogonal array. However, it is important to keep in mind that each choice of the orthogonal array corresponds with certain assumptions on the underlying polynomial model, which is assumed to be representative of the system which is optimised using the Taguchi method. If these implicit assumptions are not valid, the Taguchi analysis gives incorrect results. The aliasing pattern of the Taguchi method is quite complicated, interaction factors are aliased with several main effects at once with different multiplicative factors and different signs. The absence of interaction effects is therefore absolutely essential, because the principle of investigating each factor independently from the others is also invalid if interaction effects are present.

2.7.5 Multi-objective optimisation

2.7.5.1 Dominated points and the Pareto front

Two main options can be distinguished for the optimisation of heat exchangers. Either a single PEC such as the VG-1 or the JF criterion is used as the goal functions, or multiple objectives are distinguished. In the case of a single goal function, the optimisation problem results in a single optimal value. For the multi-objective problem, the optimum is given by a surface (or a curve in two dimensions). Figure 2.8 shows a schematic representation of an optimisation problem where there are two objectives, G1 and G2, which should both be minimised.

For any point in the design space P1, if there is some other point P2 which performs better with respect to one of the objectives without any of the other objectives being worse, then P1 is said to be dominated by P2. Any point in the hatched region of the design space is dominated by one of the three indicated points. The Pareto front is a set of points which cannot be dominated by any other feasible design. It is indicated by the dashed line in the figure. The Pareto front is the theoretical optimum of the multi-objective optimisation problem. In general multi-objective algorithms generate a set of non-dominated points which converges to the Pareto front in the limit. The curve defined by the hatched region is the approximation of the Pareto front given a limited amount of data.

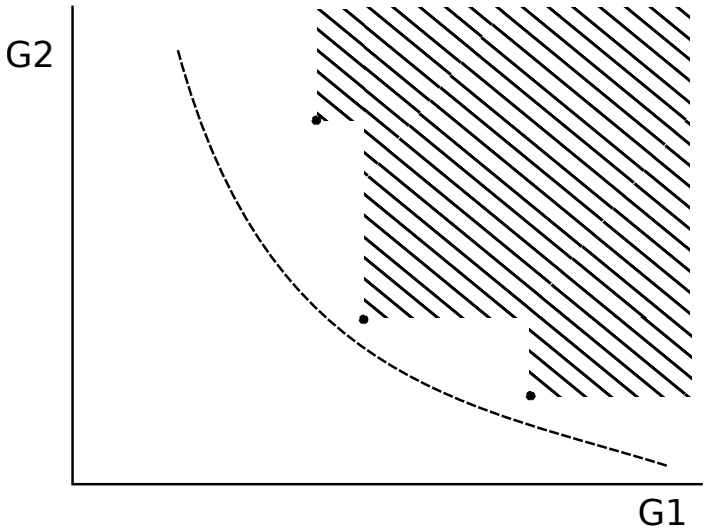

Figure 2.8: Two-dimensional optimisation problem with three indicated known points. The hatched region is dominated by the known points, the Pareto front is indicated by the dashed line.

2.7.5.2 Multi-objective optimisation using Kriging surrogate models

A possible multi-objective optimisation algorithm is given by efficient global optimisation (EGO). Consider a given set of designs which has been calculated so that the locations in the objective space are known. A distance weighting function can be defined, which maps a given test location in the objective space to the distance from the set of non-dominated points if the test location is not dominated and to zero if it is. This function is called the improvement function, since if it is larger than zero for a certain evaluated point, the current estimate of the Pareto front is improved. Kriging surrogate models can now be used to map a test design in the design space to a location in the objective space, which results in a probability density in the objective space. The expected improvement in the set of non-dominated points can then be obtained by integrating the product of the probability density with the improvement function over the entirety of the objective space. This defines the objective improvement function as a function which maps a design to a scalar expected improvement value. The function can then be optimised using any single-objective optimisation algorithm. In this work, a genetic algorithm will be used for this purpose. Figure 2.9 shows the distance weighting function of a given set of known data as well as the probability densities for several feasible designs.

It is clear that even though the uncertainty on one of the designs is very large, the surrogate model has enough data to conclude that evaluating this design will most probably not result in an improvement of the current estimate for the Pareto

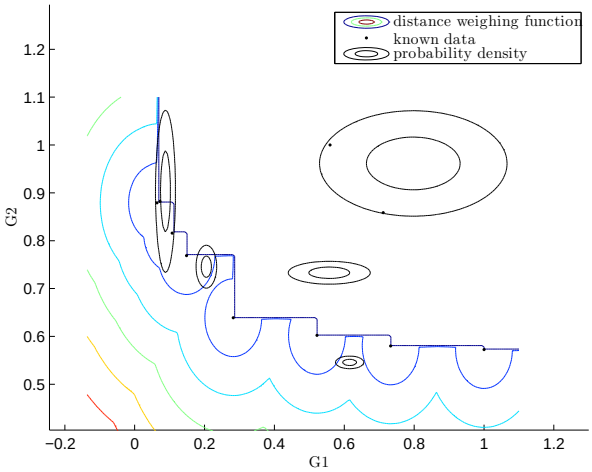

Figure 2.9: Distance weighting function and probability densities for five different designs.

front. On the left-hand side, there is another design with a rather large uncertainty on the second objective. This would be a good design to evaluate, as there is a reasonable probability that the design will result in a better approximation of the Pareto front. This would be an exploration of the design space, as a new calculation is done in a region where little data is available. However, designs which are similar to good designs which have already been evaluated have much smaller uncertainty on the surrogate model. Close to the available data, the impact of the variables in the design space on the objectives is known. This results in the possibility of obtaining a modest improvement, but with large probability. One such example is the point on the bottom right of the figure. Evaluating this design is called exploitation, as new designs are evaluated in a region which is already known to be good. If the algorithm would be limited to exploitation only, it would find a local optimum. In order to find the global optimum, a balance between exploitation and exploration is required. By optimising the expected improvement, the balance is obtained. The same principle can also be applied in a single dimension. The estimate of the Pareto front is then defined by a single value, which is just the current best value for the objective function. The distance weighting function is zero if the new design is worse, and proportional to the difference between the predicted objective and the previous best value otherwise.

A significant problem with the application of EGO is that the selection of new designs is only as good as the predicted probability density function. If the Kriging model does not fit the actual problem well, much is wasted by placing overdue

importance on balancing or exploring, or even exploring and exploiting the wrong regions of the design space entirely.

2.7.6 Conclusions

For louvred fin heat exchangers, significant interaction effects with the louvre angle can be expected on physical grounds. For example, in the limiting case that the louvre angle is zero, the louvred fin is reduced to the plain fin. No other louvre parameters will have any effect. As the disturbance of the primary flow is increased by increasing the louvre angle, other louvre parameters such as the louvre pitch can also be expected to become important. For vortex generators, interactions between vortex generator parameters are also likely. Methods which are unable to resolve two-factor interactions are therefore not to be recommended, such as fractional factorial designs with a resolution lower than V. Taguchi orthogonal designs of strength 2 likewise should be avoided, unless the aliasing pattern is carefully investigated to ensure there is no aliasing with two-factor interactions which are expected to be present. In this work, either full factorial or resolution V fractional factorial designs will be used in conjunction with polynomial surrogate models due to the relative simplicity with which the aliasing pattern can be determined. When Gaussian process models are used, a Latin hypercube sampling plan will be used to provide the initial data.

3

State of the art in heat exchanger optimisation

3.1 Introduction

In this chapter, an overview is presented of the current state of the art in heat exchanger optimisation. First, studies relating to heat exchanger geometries are investigated. Three different geometry groups are considered: the louvred fin with flat tubes, the rectangular louvred fin with round tubes and the X-shaped louvred fin. A distinction is made between experimental and numerical studies. The experimental studies are further subdivided into black box studies and investigations of the flow physics. For the numerical studies, the emphasis is on the models and the boundary conditions which are used. For a detailed discussion of the flow physics using numerical simulations, the reader is referred to chapter 7.

3.2 Louvred fins

3.2.1 Introduction

As discussed in chapter 2, the friction factor f and the Colburn j-factor as a function of the Reynolds number characterise the fin geometry. Together with a fin efficiency correlation and an effectiveness-NTU relation for the stream configuration, they fully determine the heat exchanger for given boundary conditions. Therefore, it is no surprise that many authors have determined correlations for louvred fin

surfaces. These can be determined from black box measurements of heat transfer rate and pressure drop measurements. However, this does not allow understanding why the friction factor and j-factor functions behave as they do, with altered fin geometry. This requires observing the flow physics, which can only be done if measurements can be made inside the heat exchanger. This can be done experimentally, for example, in water tunnel studies of a scale model of a part of the heat exchanger. Alternatively, numerical studies allow obtaining the pressure drop, heat transfer rate and high-resolution information about the flow field inside the heat exchanger all at once.

Two main types of louvred fin heat exchangers exist. The first type is plate-fin heat exchangers with louvred fins. These are also known as louvred fin and flat tube heat exchangers. This type of heat exchanger is very common in automotive applications. The second type is round tube and fin heat exchangers, which are often used in residential HVAC applications when heat is exchanged between a refrigerant and air. In this work, only the second type with round tubes will be discussed.

3.2.2 Experimental studies

3.2.2.1 Louvred fin and flat tube heat exchangers

Heat transfer and pressure drop correlations

Several authors have investigated louvred fin and flat tube geometries. Chang and Wang [17] define five basic topologies, making a distinction between whether the channel is triangular or rectangular and whether a splitter plate is present between the tubes or not. Each of these types is further characterised using eight different geometrical parameters, grouped into seven dimensionless groups. They determined the correlation based on a combination of linear regression and a trial-and-error process using 91 heat exchanger geometries measured by various authors.

Kim and Bullard [18] used the same basic form of the correlation as Chang and Wang and refitted the exponents using 45 heat exchanger samples of two basic topologies. The Reynolds number based on the core velocity and twice the fin pitch was in the range of 120 to 1 000, the corresponding frontal air velocity range was from 0.7 m/s to 3 m/s. The louvre angle was varied between 15° and 29°, the fin pitch between 1 mm and 1.4 mm. They also varied the length of the heat exchanger and found that the louvre angle which corresponded to the maximum heat transfer coefficient was a function of the heat exchanger length. Dong et al. [19] created another correlation, still using the same basic expression, but based on 20 measured heat exchangers of their own. They investigated the flow at a much higher Reynolds number, in the range of 650 to 14 000, with a frontal air velocity

of up to 19 m/s.

Investigation of the flow physics

Other authors have focused on the flow physics in louvred fin heat exchangers. Davenport [20] investigated the heat transfer and fluid flow in louvred fin and flat tube heat exchangers. He noticed that for low Reynolds numbers based on the louvre pitch, the flow tended to be aligned with the duct, whereas for higher Reynolds numbers it was aligned more with the louvres.

Webb and Trauger [21] built a 1:10 scale model in a water tunnel and investigated the flow patterns using a dye injection technique. They defined the flow efficiency as the ratio between the actual transverse distance travelled along a streamline to the ideal transverse distance if the flow would perfectly follow the louvres. They found that to correlate the flow efficiency it was better to use the louvre pitch than the hydraulic diameter as a characteristic length scale for the Reynolds number. They confirmed that the flow efficiency was low for low Reynolds numbers, corresponding to duct-directed flow. As the Reynolds number increased, so did the flow efficiency, until a critical Reynolds number was reached. They found a very significant effect of the louvre angle on the flow efficiency, increased louvre angles resulted in increased flow efficiency for all Reynolds numbers under the critical Reynolds number.

Springer and Thole [22] focused on the entry region in a scale model which is 20 times larger than the real heat exchanger. This scale model was put in a wind tunnel and laser Doppler velocimetry was used to determine the velocity field. They compared the mean velocity angle with the geometric louvre angle and noticed that as the fin pitch increased, the average flow angle decreased. They also noticed that the flow angle reached a constant value after three to five louvres, depending on the fin pitch to louvre pitch ratio.

DeJong and Jacobi [23] investigated the flow, heat transfer and pressure drop. Heat transfer data was obtained using a naphthalene sublimation technique in a wind tunnel. They noticed a very small increase in the mass transfer rate due to vortex shedding, which was within their experimental uncertainty of 5%. They concluded that vortex shedding did not contribute much to the heat transfer enhancement due to the louvres and that steady-state computational models might therefore be expected to provide accurate predictions. The flow was investigated using dye injection in a scale model placed in a water tunnel, this allowed them to detect the presence of the vortex shedding. The lowest Reynolds number for which their observed vortex shedding anywhere in their model was 500, defined on the louvre pitch. Approximating the hydraulic diameter for the two-dimensional case as twice the fin pitch, this corresponds to a Reynolds number of $1\,100$ on the approximated hydraulic diameter, since their fin pitch to louvre pitch ratio was 1.09.

They noticed that flow efficiency, pressure drop and heat transfer coefficient all increased with increasing louvre angle from 18 to 28 degrees.

3.2.2.2 Louvred fin and round tube heat exchangers

Heat transfer and pressure drop correlations

Very few experimental investigations of the louvred fin and round tube geometry exist. Only Wang and his co-workers investigated this, considering seven different louvred fin geometries in 1998 [24]. They continued this research by investigating the effect of the number of tube rows and the fin pitch in a second study in 1998, this time using 17 different geometries [25]. The fin pitch was varied between 1.49 mm and 2.08 mm, the number of tube rows from one to six. The different geometries were investigated for frontal velocities ranging from 0.25 m/s to 7 m/s. Figure 3.1 shows the dependence of the friction and j-factors on the number of tube rows. From the theoretical discussion in chapter 2 on fully developed flow, it is expected that the j- and the f-factors have a similar behaviour as a function of the Reynolds number. Furthermore, as the number of tube rows increases, the friction and j-factor characteristics should converge to a single curve corresponding to fully developed periodic flow.

For the number of tube rows equal to one or two, the j- and f-factors indeed show a similar behaviour in function of the Reynolds number. Furthermore, for the friction factor, the effect of the number of tube rows is small. However, the j-factor exhibits what Wang et al. called a 'level-off' phenomenon. For the lower Reynolds numbers, the j-factor does not increase as the Reynolds number decreases. They speculated that this might be due to the interaction of thermal wakes between two successive louvres. However, this might also be explained by measurement error. As will be shown in paragraph 4.5.3.2, for low Reynolds numbers and a number of tube rows larger than three, the sensitivity of the j-factor with respect to the measured heat transfer rate becomes very large. Shah [8] showed that the measured j-factor could level off at low Reynolds numbers, purely due to measurement errors. He calls this the 'rollover' phenomenon. Small air leaks, heat loss to the ambient and radiation effects on the measured thermocouple temperature all contribute to this effect. Since Wang et al. do not show any error bars on their measurements, it is impossible to say whether this 'level-off' phenomenon is an actual physical occurrence or not. This can be solved by performing numerical simulations, since they do not suffer from the aforementioned measurement problems for low Reynolds applications.

In 1999, Wang et al. published a correlation for louvred fin and round tube geometries [3], using 49 different fin geometries. They considered six different topologies of the louvred fin, but did not include the topology type in the correlation. As a result it is effectively considered as a noise factor. The independent

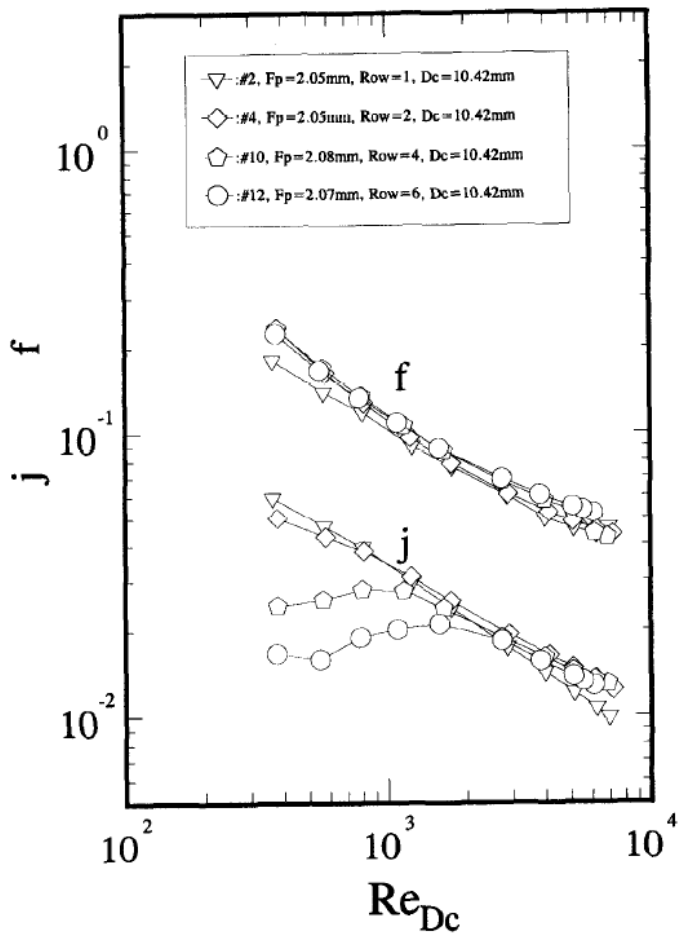

Figure 3.1: Effect of the tube row on the j- and f-factors according to the experimental results of Wang et al. [25]

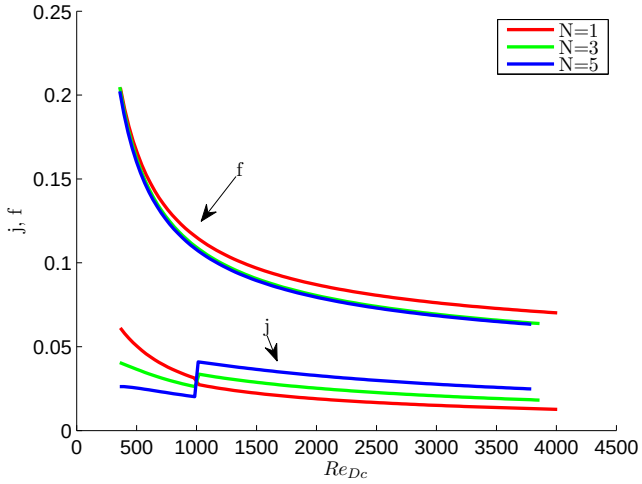

Figure 3.2: Effect of the tube row on the j- and f-factors according to the correlation of Wang et al. [3]

parameters which were taken into account were the outer tube diameter, the transversal and longitudinal tube pitches, the louvre angle and the number of tube rows. The louvre angle was varied by changing the louvre height and the louvre pitch, but these were not included as independent parameters. In total this makes for 6 geometric parameters. The number of levels varied from parameter to parameter, but at least four levels were used for every parameter. Assuming that each variable has a quadratic effect on the j- and f-factors, the theory of fractional factorial designs would require $3^{6-2} = 81$ experiments for a resolution III design which confounds main effects with interactions. This indicates that 49 different geometries are rather few to treat six geometric parameters, especially given that a strong noise effect due to different topologies is present.

From the previous study by Wang and based on the physical reasoning of chapter 2, there is some physical intuition about the physical behaviour of the j- and f-factors as a function of the number of tube rows. Figure 3.2 shows the j- and f-factors as a function of the Reynolds number for a varying number of tube rows, with the data obtained from the correlation.

The friction factor shows a behaviour that can be explained on physical grounds. For a single tube row, the friction factor is higher than for three tube rows, due to the importance of the entrance and exit effect as well as the contribution of the developing flow. If the number of tube rows is increased further to five tube rows, the change is negligible, as can be expected for fully developed periodic flow.

The curves for the Colburn j-factor, on the other hand, are unrealistic. As the

number of tube rows is increased from one to three, the change is of the same order of magnitude as when it is increased further from three to five. This is unreasonable, as convergence to a fully developed flow which is independent of the number of tube rows is expected, as is the case for the friction factor. Furthermore, the effect of the number of tube rows depends on the Reynolds number. Before the discontinuity at the Reynolds number of $1\,000$, increasing the number of tube rows results in a decrease of the j-factor. However, for Reynolds numbers larger than the discontinuity, the j-factor would increase by adding additional tube rows. This is the opposite effect as for the friction factor and cannot be explained by flow development.

Since the louvre topology was not included in the correlation, it is treated as an uncorrelated error term during the development of the correlation. The louvre topology has a very significant impact; Wang et al. note a deviation of up to 100% in the friction factor if only the topology is changed. Since the effect of the topology is not estimated in the correlation, it is aliased with the effects of the other parameters. It is possible that the effect of the number of tube rows in the Wang correlation was not only due to changing the number of tube rows, but also due to changing the topology. The same is true for the effect of the other parameters.

In conclusion, the Wang correlation provides unreasonable physical behaviour for the number of tube rows. Because topology effects were not taken into account during the development of the correlation, effects due to the correlation parameters are aliased with the variation of the topology in the design space. As such, the correlation is not suitable to optimise fin geometries.

Investigation of the flow physics

Studies of the plain fin geometry such as the one by Romero-Méndez et al. [26] have shown that if the distance between the fins relative to the tube diameter and the Reynolds number is sufficiently large, a horseshoe vortex develops around the tube. The flow obstruction caused by the tube results in an increase of the static pressure at the stagnation point. As a result, an adverse pressure gradient is present in front of the tube. The adverse pressure gradient causes the boundary layer in front of the tube to separate and roll up into a vortex. The vortex is then advected with the flow and wraps around the tube. The horseshoe vortex enhances the heat transfer coefficient due to local impingement of the flow on the fin surface. A schematic representation of a horseshoe vortex around a tube is given in figure 3.3.

Very few experimental studies regarding the flow physics in louvred fin heat exchangers exist. Huisseune et al. [28] investigated the horseshoe vortex system in a louvred fin heat exchanger. They noticed that the strength of the horseshoe vortex is different on the top and on the bottom of the fin, which they attribute to the flow

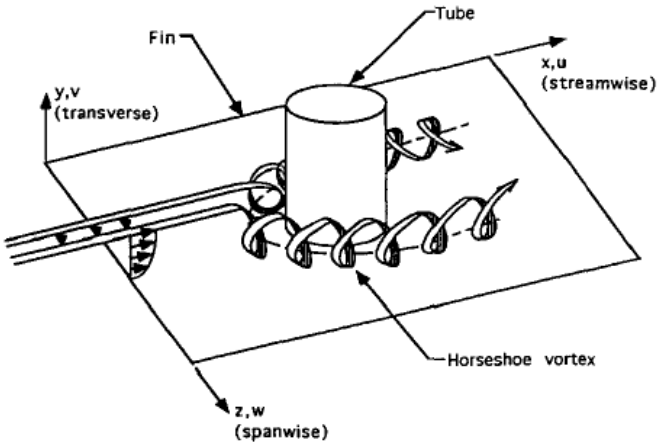

Figure 3.3: Laminar horseshoe vortex at a tube-fin junction [27]

deflection by the louvres. These horseshoe vortices are said to be destroyed in the louvres downstream of the turnaround louvre. They also noticed the presence of a vortex system on the bottom of the fin at the transition between the louvre and the flat landing, a flow feature which has also been noted in numerical studies of louvred fin and flat tube geometries, which will be discussed next.

3.2.3 Numerical studies

For numerical studies, it is important to determine whether the flow is physically steady or unsteady, laminar or turbulent. This strongly impacts the computational effort which is required to simulate the problem. By comparing the flow in the heat exchanger to an equivalent channel flow, the Reynolds number gives a reasonable indication of which kind of flow can be expected. However, different authors define their Reynolds numbers in different ways. For the length scale, the fin pitch, twice the fin pitch, the collar diameter, the hydraulic diameter and the louvre pitch are common choices. The characteristic velocity is sometimes the frontal velocity and sometimes the core velocity. The difference in reference length scales and velocities makes it difficult to compare the operating conditions between different studies. Where it was possible to do so based on the data provided in the papers, the Reynolds number was recalculated based on the hydraulic diameter and the core velocity. The characteristic velocity and length scale were then evaluated for an equivalent channel located in the heat exchanger core. Failing this, the Reynolds number was instead calculated based on twice the fin pitch and the inlet frontal velocity, which approximately corresponded to an equivalent channel based on the heat exchanger inlet if the width of the flow channel was much wider than the

height.

3.2.3.1 Louvred fin and flat tubes

Tafti [29] noted that the develoment of the first instabilities develop in louvred fin and flat tube heat exchangers was due to wake instabilities and Kelvin-Helmholtz instabilities. They investigated these effects using two-dimensional simulations by directly solving the Navier-Stokes equations (DNS). However, as the Reynolds number defined on the hydraulic diameter is around $2\,500$ to $3\,000$, secondary three-dimensional instabilities became important. These were investigated by Cui and Tafti [30]. They used a very fine grid to solve the flow around a single louvre in three dimensions using DNS, periodic boundary conditions were used for all the boundaries of the computational domain. They investigated the effect of the flat landings and the transition region and discovered large streamwise velocities in this region, as well as the formation of a vortex jet on the bottom surface. The shear layers on the top and on the bottom of the louvre surface separated, resulting in the shedding of vortex structures. They concludde that the flow could be characterised as unsteady laminar to chaotic.

Zhang and Tafti [31] performed two-dimensional numerical simulations of a louvred fin array and investigated the flow efficiency. They compared their results with the experimental results of DeJong and Jacobi [23] and found a deviation of around 6% for the Nusselt number and 2% for the flow efficiency. They confirmed the earlier findings that flow efficiency increased as the Reynolds number and louvre angle increased. The flow efficiency also increased as the fin pitch was decreased, but this effect was found to be less important than the effect of the louvre angle.

Perrotin and Clodic [32] considered a three-dimensional model of a louvred fin and flat tube geometry. They used a laminar and steady model for Reynolds numbers based on twice the fin pitch and the inlet velocity varying from 410 to $1\,450$. Symmetrical boundary conditions were used in the transversal direction, the transition zones to the flat landings were neglected. The computational domain is shown in figure 3.4. The average cell size which they used was roughly equal to the fin thickness. With respect to experiments, the deviation on the heat transfer coefficient was 13%.

3.2.3.2 Rectangular louvred fin and round tubes

Leu et al. [34] studied the louvred fin and round tube geometry with rectangular louvres in the frontal velocity range from 0.5 m/s to 2.6 m/s. The corresponding Reynolds number range based on the hydraulic diameter was 150 to 780. They investigated the effect of the louvre pitch (2.08 mm to 3.75 mm) and the louvre angle (10° to 46°) using fully factorial sampling. With respect to the heat transfer

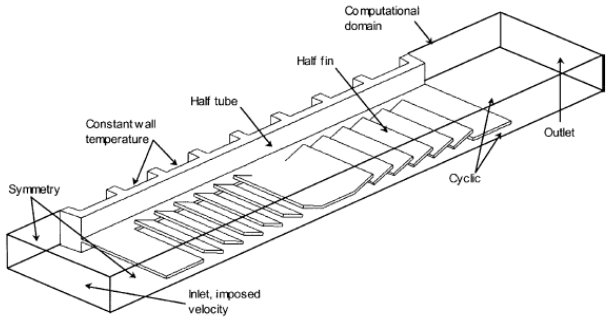

Figure 3.4: Computational domain used by Perrotin and Clodic [33]

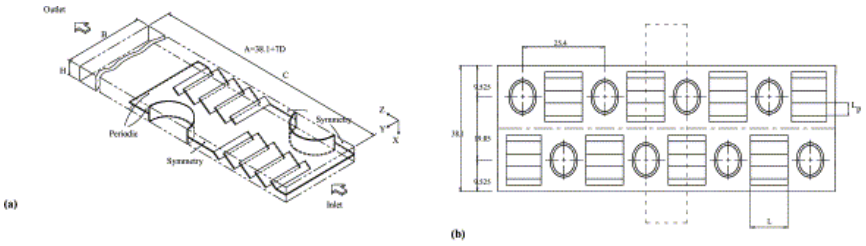

Figure 3.5: Computational domain used by Leu et al. [34]

coefficient, an optimal louvre angle was observed, which was a function of the louvre pitch. As the louvre pitch decreased, the heat transfer rate and the optimal louvre angle both increased. This is important to note as it is an example of an interaction effect between two parameters which was revealed by their study.

A steady and laminar computational model was used, which seems reasonable based on the Reynolds number range. The conduction in the fin material was calculated and coupled to the fluid domain, which corresponded to a conjugate heat transfer simulation. The transition region of the louvres was neglected. They imposed symmetrical boundary conditions in the transversal direction and periodic boundary conditions in the direction normal to the fin. This is indicated on the computational domain, which is shown in figure 3.5. For the outlet of the flow domain, located seven tube diameters downstream of the heat exchanger exit, the pressure was specified. At the inlet of the heat exchanger a constant velocity and temperature is imposed. This does not take the flow contraction upstream of the heat exchanger into account. The computational grid consisted of 720k cells, the cell size normal to the fin surface is was half of the fin thickness. They compared their results with an experimental validation of a geometry with the same geometrical parameters and obtained an approximately systematic error of 20% to 30%, which was deemed an excellent agreement.

3.2.3.3 X-shaped louvred fin and round tubes

Hsieh et al. [35] recently (2012) calculated the X-shaped louvred fin for a variety of geometries. They based the Reynolds number on the inlet frontal velocity and the collar diameter. The lowest reported Reynolds number was $1\,700$, the largest was $18\,000$. Based on the core velocity and the hydraulic diameter, this corresponded to a range of 800 to $8\,800$. They used a $k - \epsilon$ turbulence model. The Reynolds number under consideration ranged from the laminar region to the transition region and the fully turbulent region, the choice of turbulence model might therefore not be appropriate for every Reynolds number. Nevertheless, the authors compared their simulations with experiments and obtained a deviation lower than 3.5% for the j- and f-factors, which was an order of magnitude better than the deviation observed by Leu et al. [34]. Their geometrical parameters were very similar to the ones used by Leu et al., the only difference was the use of X-shaped louvres and a slightly larger fin thickness. The computational grid consisted of only 400k cells. The only difference with respect to the boundary conditions were that the inlet velocity was specified one tube diameter upstream of the heat exchanger, the outlet is located five tube diameters downstream of the exit. A Taguchi method was used to investigate the effect of eight different parameters using 18 different geometries on the JF performance evaluation criterion. The authors used a dynamic Taguchi analysis to optimise the geometry with respect to the JF criterion, considering the Reynolds number as a signal factor. They determined the signal to noise factor for every design by performing a summation over the different Reynolds numbers. Effectively, they therefore considered the Reynolds number as noise, as it is the noise factor for which the summation happened in the signal to noise ratio of a Taguchi analysis. As explained in paragraph 2.7.4, a dynamic Taguchi analysis does not make sense for heat exchanger applications in the first place.

3.3 Vortex generators

3.3.1 Introduction

A vortex generator consists of an obstruction to the flow, which is introduced with the objective of generating a vortex. In 1995, Jacobi and Shah [27] presented a review on the use of longitudinal vortex structures to enhance heat transfer. They summarised four common types of vortex generators, which are shown in figure 3.6.

For the winglet type of vortex generator, a surface is presented at an angle to the flow. As a consequence, a lift force is generated on the surface as the flow curves around the surface. This is exactly the same as the flow around a symmetrical airfoil placed at an angle to a flow. The curvature of the streamlines results in a pressure gradient normal to the streamlines, since the pressure gradient must

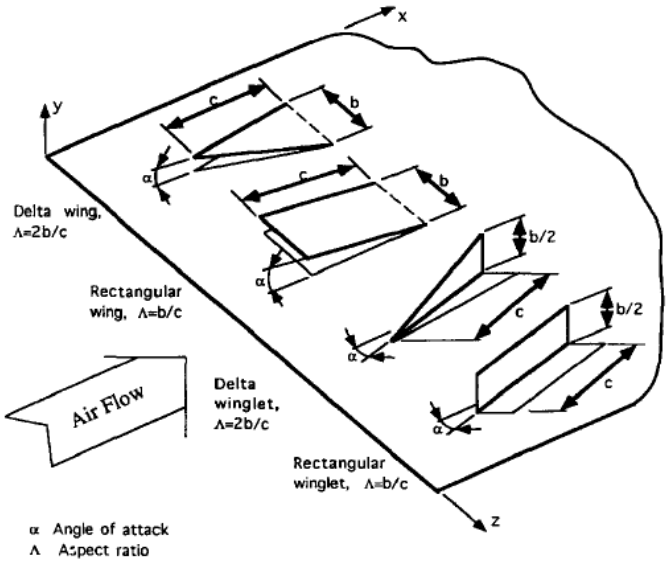

Figure 3.6: Common vortex generator types [27]

balance the centripetal acceleration due to the curvature. This results in one side of the surface having a higher pressure than the other side of the surface, which is also the case for airfoils. Since the obstruction is finite in length, a flow from the high-pressure side to the low-pressure side is present at the tip. In essence, the vortex shed from a winglet type vortex generator is very similar to the wingtip vortices shed from an airfoil of finite length, which is caused by the same phenomenon. As opposed to the horseshoe vortex, this mechanism does not require a boundary layer in order for vortices to be generated. For the wing type of vortex generator, Fiebig [36] explains that the mechanism of generation is due to unstable detached shear layers which roll up, following separation along their leading edges. No matter how it is generated, the resulting vortex is then convected further downstream with the bulk flow.

In general, vortex generators are placed in pairs. Two cases can then be identified, common inflow (also known as common-flow-down) and common outflow (or common-flow-up). This refers to the direction of the flow in between the two vortex generators. The common-flow-down case is shown in figure 3.7. The common-flow-down towards the fin surface results in a thinning of the boundary layer, which increases the shear stress and the heat transfer coefficient at this location. Outside the vortex pair, the boundary layer is thickened.

Each vortex induces a velocity at the location of the other vortex. For a common-flow-down pair, the induced velocity is oriented towards the fin surface,

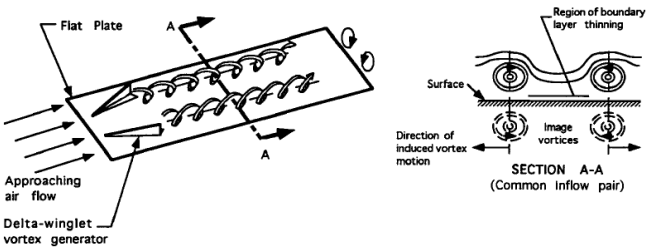

Figure 3.7: Vortex system caused by a common-flow-down delta winglet pair [27]

which results in a tendency of the vortices to stick to the surface. The vortices also interact with the fin surface, the interaction can be treated by using the method of images. The method of images implies that the flow field caused by the interaction between a vortex and a wall is exactly the same as the flow field caused by the interaction between a vortex and its mirror image around the surface. The mirror images of the vortices result in an induced velocity which causes both vortices to move further apart. This is clearly shown by the experimental results of Pesteei et al. [37] from 2005, shown in figure 3.8.

Since the review paper of Jacobi, many more studies with respect to vortex generators have been conducted, both experimentally and numerically. In what follows, a brief overview will be given of recent literature (1998 or later).

3.3.2 Experimental studies

Fiebig [36] investigated vortex generators in channel flow, which corresponds to plate-fin heat exchangers. His main conclusions were that longitudinal vortices enhanced the heat transfer both locally and globally, as opposed to transverse vortices which did not result in an enhancement of the global heat transfer coefficient for steady flow. The longitudinal vortices were found to be very persistent, resulting in an enhancement over an area 100 times larger than the vortex generator area. He also found that the winglet type of vortex generator resulted in a superior enhancement of the heat transfer coefficient in comparison with the wing type. He stated that for laminar flow, the heat transfer enhancement increased with the Reynolds number. It was also noted that the vortex generators destabilised the flow, leading to an onset of unsteadiness and turbulence at lower Reynolds numbers.

Torii and Kwak [38] performed a wind tunnel experiment with a round tube and plain fin geometry, enhanced by delta winglets in a common-flow-up configuration. They varied the frontal air velocity from 0.5 m/s to 3.5 m/s. The corresponding Reynolds number range was from 600 to $4\,000$, due to the rather large fin pitch of 5.6 mm. Remarkably, they found that by adding the vortex generators,

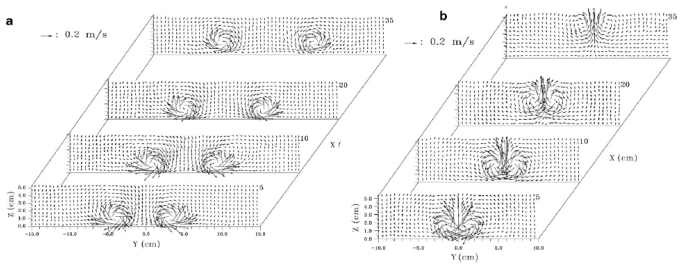

Figure 3.8: Secondary velocity vectors downstream of a vortex generator pair: a) common-flow-down, b) common-flow-up [37]

the heat transfer was augmented by 30%, whereas the pressure drop was actually reduced by 55% for the lowest Reynolds number. For the largest Reynolds number, the heat transfer increase was 10%, the pressure drop again decreased by 34%. They also tried a common-flow-down configuration proposed by Fiebig and obtained increases in both the pressure drop and the heat transfer of 35% and 25% respectively for the lowest Reynolds number. They speculated that the common-flow-up configuration resulted in nozzle like flow passages downstream of the tube, which reduced the form drag on the tube by delaying the separation.

Pesteei et al. [37] studied the heat transfer coefficient and the flow field caused by a delta winglet vortex generator pair in a wind tunnel. Thermochromatic liquid crystals subjected to a uniform heat flux were used to obtain heat transfer coefficients, the velocity field was measured using pressure probes. The velocity field is shown in figure 3.8. It is clear that for the common-flow-down configuration, the vortices remained close to the surface but separated from each other. The opposite was true for the common-flow-up pair, which remained close to each other but separated from the fin surface. The highest heat transfer enhancement was observed for an angle of attack of 45°. The common-flow-down configurations outperformed the common-flow-up designs. They also varied the placement of the vortex generator and concluded that the optimal position was for the leading edge to be positioned one tube radius in the longitudinal and transversal direction away from the tube centre.

Allison and Dally [39] made a compared a louvred fin and a vortex generator fin for a flat tube heat exchanger. The vortex generators were placed in a common-flow-up configuration in front of the tubes. A water tunnel experiment was conducted in order to visualise the flow, whereas a metal prototype was constructed and used in a wind tunnel to obtain pressure drop and heat transfer measurements. The frontal velocity was varied between 2.9 m/s and 6.2 m/s, which according to the authors, were velocities more suited towards radiator applications than HVAC applications. For their lowest velocity, the j-factor is 63% of the louvre surface j-factor, whereas the friction factor is only 48.5% of the louvre surface friction

factor. They contended that as the friction factor was reduced more than the j-factor, the overall effectiveness of the surface was significantly improved. The frontal surface area of the vortex generator fin is indeed only 87% of the louvred fin design. However, if the VG-1 criterion discussed in chapter 2 is used to compare the volume ratio instead, it is seen that the design using vortex generators requires 150% of the volume of the louvred fin design. This is a rather high price to pay for a reduction in the frontal surface area of 13 percentage points. The authors' claim that their geometry has been the best arrangement published in the literature since 2007 should therefore be nuanced.

In 2008, Joardar and Jacobi [40] investigated a round tube and fin heat exchanger with vortex generators using a full-scale heat exchanger in a wind tunnel. A heat exchanger with seven in-line tube rows was enhanced using common-flow-up vortex generators. Three different cases were compared, the baseline configuration, placement of vortex generators on the first tube row and placement of vortex generators on the first, third and fifth tube row. Except for very low flow rates, the configuration using three enhanced tube rows exhibited better performance with respect to the volume goodness criterion.

3.3.3 Numerical studies

Many authors have investigated vortex generators using numerical simulations. In this overview, much emphasis will be placed on the numerical methods used to solve the problem. It is remarkable that a very large amount of work has been done on the combination of vortex generators with oval tubes.

Tiwari et al. [41] investigated a plain fin and single oval tube configuration, enhanced with delta winglet vortex generators. Whereas most studies have only used a single vortex generator pair per tube, they investigated the effect from one up to four pairs of vortex generators around the tube. They neglected the thickness of the fin and the vortex generators and did not include a punched hole. The computational domain was not extended upstream or downstream of the heat exchanger. The Reynolds number based on the frontal velocity and twice the fin pitch was $2\,700$, the flow was solved using an unsteady laminar model. They considered an entire periodic element of the heat exchanger, but instead of using periodic boundary conditions for the transversal side walls, they imposed symmetry conditions at this location, without any physical justification. They solved the problem using a structured computational grid of 72k cells and compared the result with the results on grids of 107k and 166k cells, which resulted in a deviation of 4% for local heat transfer coefficients. Given the modest increase in the number of cells this seems a relatively large deviation. The ratio of the number of cells is only 1.5, for a three-dimensional domain this corresponds to a ratio of only 1.15 in each dimension. They noted that as the angle of attack increases, the strength of the

longitudinal vortices and the enhancement of the heat transfer coefficient also increased. Adding more vortex generator pairs always led to further increases of the heat transfer coefficient. They did not consider the effect on the pressure drop.

Leu et al. [42] performed numerical simulations and water tunnel experiments for a round tube and fin geometry consisting of plain fins and rectangular vortex generators, for an in-line tube layout. No punched holes were present in either the experiment or the simulation. The Reynolds number based on the core velocity and the hydraulic diameter was varied from 700 to $5\,200$ and a $k - \epsilon$ turbulence model was used. As opposed to other authors who performed steady-state simulations, they used periodic boundary conditions in the transversal direction instead of using the symmetry. The flow fields which they obtained were in fact symmetrical. They used the VG-1 criterion to evaluate the performance of the fin geometry and concluded that a volume reduction of up to 25% could be obtained with respect to the plain fin. As this enhancement decreases as a function of the Reynolds number, they concluded that the enhancement strategy was mainly useful for low to moderate Reynolds numbers. They noted that the performance enhancement was not just due to the production of vortices, but also due to the introduction of fluid into the wake zone behind the tubes. They varied the angle of attack of the vortex generator while keeping the position of the leading edge constant at 0.4 tube diameters translated transversally and 0.68 tube diameters longitudinally downstream of the tube centre. They found that the largest heat transfer enhancement was obtained for an angle of $45°$.

Wu and Tao [43] considered a combination of a plain fin with common-flow-down delta winglets and round tubes in an in-line arrangement. They extended the computational domain 10 times the fin pitch upstream and 30 times the fin pitch downstream of the heat exchanger. They varied the inlet frontal velocity from 1.5 m/s to 5.5 m/s. Using the inlet frontal velocity as the reference velocity and twice the fin pitch as the length scale, the corresponding Reynolds number range was 800 to $2\,000$. The authors used this Reynolds number to conclude that the flow was laminar and steady. They used an unstructured quadrilateral mesh of around 4 million cells for a heat exchanger consisting of three tube rows, but did not give any indication of the average cell size nor of the grid convergence. They confirmed earlier results that the heat transfer enhancement increased with increasing angle of attack of the vortex generator. For an angle of attack of 30%, they obtained a reduction in the pressure drop of 10% with respect to the baseline geometry. Given the relatively large fin pitch of 3 mm and tube diameter of 10.2 mm which the authors used, it is remarkable that the flow remains steady for Reynolds numbers up to $2\,000$. At the very least, the flow in the wake of the heat exchanger behind the final tube row should be unsteady.

Herpe et al. [44] also considered a single tube row of an oval tube and common-flow-down vortex generator fin heat exchanger. Based on the inlet velocity and

twice the fin pitch, the Reynolds number was 600. They solved the problem using an unsteady laminar model. From their results, it was clear that the tube wake behind the heat exchanger was unsteady. Unlike the results of Wu et al., this is also what can be physically expected. The grid convergence was checked by analysing the results for three different grids, the fine grid consisted of 4.5M cells. The ratio of cell sizes between the coarsest and the finest was 2.6, the deviation in the Nusselt number is 1%. The region around the vortex generators was meshed using an unstructured tetrahedral grid, the rest of the computational domain was meshed with hexahedral elements.

Another study of a common-flow-down vortex generator fin and oval tube was conducted by Chu et al. [45], for a staggered tube layout consisting of three tube rows. They took the thickness of the fin and the vortex generator into account and performed conjugate heat transfer simulations. The inlet velocity was varied from 1.3 m/s to 5.5 m/s, the corresponding Reynolds number based on the core velocity and the hydraulic diameter ranged from 500 to 2 000. The computational domain was extended 10 times the fin pitch upstream and 30 times the fin pitch downstream of the heat exchanger. They used three different grids, consisting of 500k, 1M and 1.5M cells, the deviation in the heat transfer coefficient was less than 3%. Even taking into account that three tube rows were used, this is significantly more cells than used by Tiwari et al. and significantly less than by Herpe et al.. The region around the vortex generators was again meshed using an unstructured tetrahedral grid, the rest of the domain with hexahedral elements. They used a symmetrical boundary condition for the transversal boundaries of the computational domain and used a laminar and steady model for the flow, just like Wu et al. did for a comparable Reynolds number range. Given the unsteadiness observed by Herpe et al. for a Reynolds number of only 600, the choice for a steady model for Reynolds numbers of up to 2 000 is remarkable. They compared their numerical results with experiments and obtained an average deviation for the Nusselt number of 10%. This deviation increased as the Reynolds number increases, being equal to 16% for the largest Reynolds number.

The authors investigated several possibilities for the placement of the vortex generators. Comparing a placement upstream or downstream of the tubes, they concluded that the downstream case was superior as it enhanced the heat transfer in the tube wakes. Keeping the position of the leading edge constant in the downstream configuration, they proceeded to vary the angle of attack from 15° to 60°. Their result is shown in figure 3.9, the case with the angle of attack equal to zero actually corresponds to the unenhanced plain fin.

There was an optimum angle of attack of 30 degrees for the Nusselt number which was independent of the Reynolds number. The authors explained this by noting that at first increasing the angle of attack increased the strength of the longitudinal vortices, but eventually the combined effect of vortex breakdown and

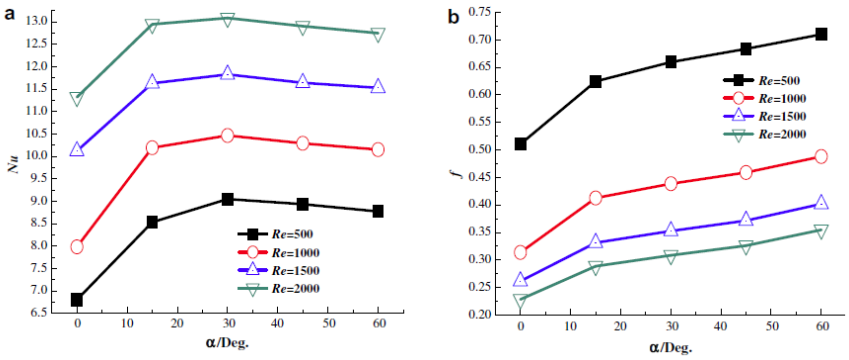

Figure 3.9: Influence of the angle of attack α on Nu (a) and on f (b) [45].

transversal vortices generated by the vortex generator resulted in a decrease of the heat transfer enhancement. The friction factor only increased as a function of the angle of attack, this was attributed purely to the form drag on the vortex generators. As a consequence, it was pointless to increase the vortex generator angle above thirty degrees in this case.

A second aspect investigated by the authors was the effect of the number of tube rows, which they varied from two to five. Figure 3.10 shows their results. As the number of tube rows increases, both the Nusselt number and the friction factor decrease for all Reynolds numbers. As the number of tube rows increased, the effect of adding an additional tube row decreased. This is expected as the characteristics should converge towards fully developed periodic flow. Even for four tube rows, the effect of adding a tube row was comparable to the effect of changing 15% in the vortex generator angle. The flow was therefore not yet fully developed.

Lemouedda et al. [46] investigated a round tube and vortex generator fin of three tube rows in both in-line and staggered configuration. The Reynolds number range based on the inlet velocity and twice the fin pitch was from 400 to 2 400, this corresponded to a range of 440 to 2 660 based on the core velocity and hydraulic diameter. An unsteady laminar model was used for an entire periodic element, using periodic conditions for the transversal boundaries of the computational domain. Their results show that for a Reynolds number in the middle of their range, the tube wake of the final tube row was clearly unsteady. To a lesser extent, some unsteadiness could be observed in the tube wake of the second tube row. An unstructured grid with polyhedral cells was used for the entire computational domain. The grid discretisation error was assumed to be satisfactory based on an investigation on three grids, of 1.26M, 1.35M and 1.45M cells, for which the deviation of the heat transfer rate was less than 0.1%. However, the grid refinement ratio

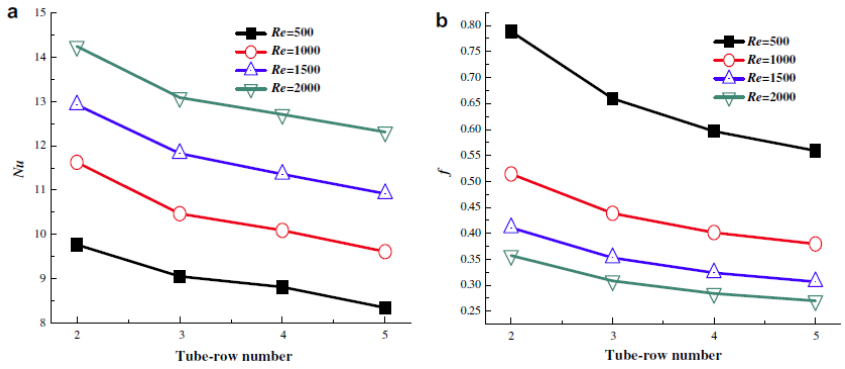

Figure 3.10: Influence of the number of tube rows on Nu (a) and on f (b) [45].

between these grids was also very small. The error on the heat transfer coefficient for a given error on the heat transfer rate also depended on the effectiveness of the heat exchanger, which made it difficult to compare the grid discretisation error of this study with other studies. With respect to their experiments, they obtained a maximal deviation of 11% on the heat transfer coefficient and 13% for the pressure drop. They investigated the effect of the angle of attack of the vortex generator, but as opposed to Chu et al., they kept the position of the centre of the vortex generator constant. Figure 3.11 shows that there was no maximum for the heat transfer rate as a function of the angle of attack. Up until the maximum angle of attack of 90 degrees, the heat transfer rate increases with the angle of attack, although the difference between the larger angles of attack was very small. The staggered arrangement was found to be superior to the in-line arrangement, both with and without vortex generators.

The authors performed a multi-objective optimisation of the fin geometry, using the fan power per unit volume and the heat transfer rate per unit volume as objectives. The parameters which they considered were the inlet fluid velocity (and therefore the Reynolds number) and the vortex generator angle. In order to do this, they trained a Kriging surrogate model with an exponential correlation function on an initial sampling plan of 78 points. The sampling plan was constructed using a full factorial sampling plan of 13 levels for the angle of attack and six levels for the inlet velocity. This surrogate model was then optimised using a genetic algorithm. The surrogate model was not updated as the optimisation proceeded. The resulting optimum was therefore the optimum of the surrogate model, which was not necessarily the same as the optimum of the original problem. The authors recognised this and performed a few verification simulations of arbitrarily selected designs on the Pareto front after the optimisation was finished. They found errors

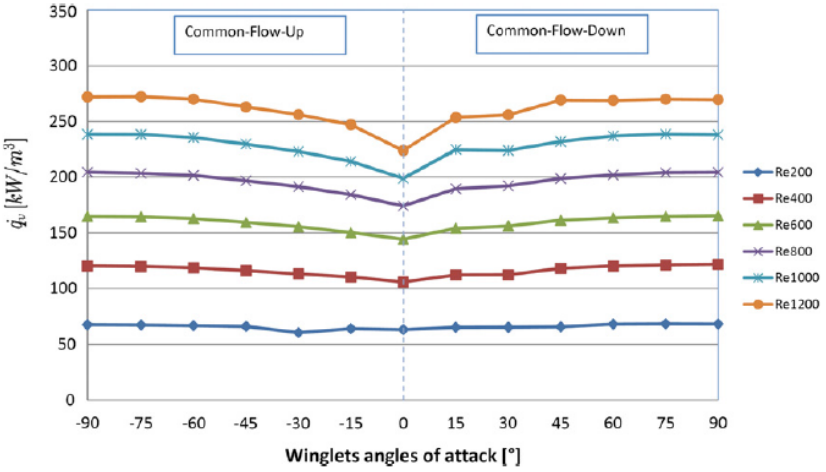

Figure 3.11: Influence of the angle of attack on the heat transfer rate normalised with the heat exchanger volume [46].

of up to 21.5% on the required fan power between the predicted performance by the surrogate model and the verification simulation.

No clear trend for the optimal vortex generator angle as a function of the Reynolds number could be discerned based on their results, the optimal angle varied between 30 and 75 degrees in common-flow-up configuration for the staggered layout, uncorrelated with the Reynolds number. A single outlier predicted a point on the Pareto front at 18 degrees in common-flow-down orientation. It is remarkable that the common-flow-up configuration is preferred to the common-flow-down configuration, which was studied by most authors. For the in-line geometry, with the exception of three outliers, common-flow-down orientations were predicted to be Pareto optimal.

Zeng et al. [47] investigated a round tube and common-flow-down vortex generator fin for six tube rows. The Reynolds number defined on the core velocity and the hydraulic diameter was varied from 1 900 to 6 300. The $k-\epsilon$ turbulence model is used to obtain a steady model. Three grids were used to establish grid independence, namely one consisting of 151k cells, 265k cells and 350k cells. The ratio of the number of cells for the last two grids was 1.35, corresponding to a refinement ratio of 1.10 along every dimension. The corresponding deviation on the Nusselt number for these grids was 1.7%. Compared with experiments, they obtained an average deviation of the friction factor of 12.6% and 7.1% for the Nusselt number.

They investigated the effect of several parameters on the Nusselt number and the friction factor. The first thing they looked into was the effect of the fin material, which is shown in figure 3.12. For all Reynolds numbers except the highest, they

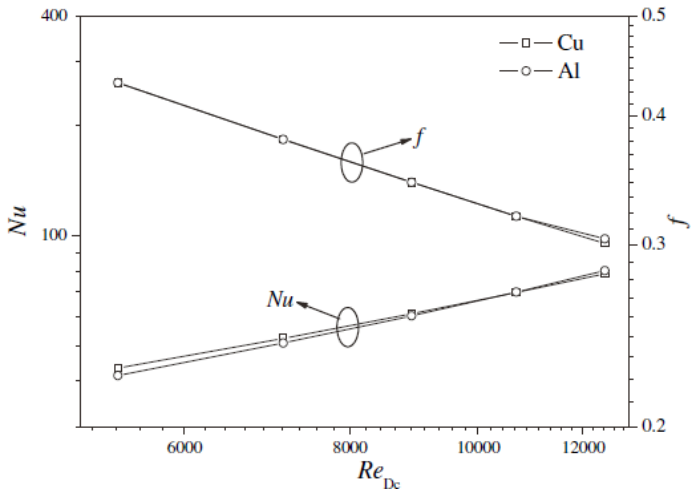

Figure 3.12: Influence of the material on Nu and f [47].

found that the friction factor was independent of the fin material, as should be the case if the temperature dependence of the fluid properties was not taken into account. However, for the largest Reynolds numbers they observed a difference of 1.5% in the friction factor due to the material, which cannot be explained on physical grounds.

The Nusselt number also showed a dependence on the material, which was possible if it was defined on the product of surface efficiency and the heat transfer coefficient. For Reynold numbers defined on the collar diameter smaller than 11 000, the Nusselt number for copper is higher than that for aluminium, as could be expected due to the higher fin efficiency due to the better conductivity of copper. However, for the highest Reynolds number, the situation was reversed, which is again unphysical. They also investigated the impact of the vortex generator height, length and angle of attack. All of these were found to increase both the friction factor and the Nusselt number. It was unclear how the positioning of the vortex generator was constrained as these parameters varied. As the longitudinal pitch or the fin pitch increased, both the friction factor and the Nusselt number decreased. Increasing the transversal tube pitch was found to result in a reduction of the Nusselt number but an increase of the friction factor.

Like Hsieh et al. [35] the authors used a Taguchi analysis with the JF criterion as the performance evaluation criterion. Also like Hsieh et al., they mistakenly used the Reynolds number as a noise factor, even though they said it was used as a signal factor.

Using this objective function they found that the fin pitch should be as large as possible, that there was a local optimum for the vortex generator length and the

longitudinal tube pitch, and that the height of the vortex generator should be as small as possible. However, from equation (2.85) discussed in chapter 2, a priori it would be expected that the hydraulic diameter, and therefore the fin pitch, should be as small as possible, since it has a first-order impact on the required heat exchanger volume for a fixed fan power. In what aspect the heat exchanger performance is improved by using a large fin pitch was not discussed by the authors. Furthermore, the assumption that there were no interaction effects between the vortex generator height, length and angle is questionable at best.

Very recently (September 2013), Jang et al. [48] used a conjugate gradient method to optimise the transversal location and the angle of attack of a rectangular vortex generator and round tube geometry. They were therefore able to take interaction effects between these two parameters into account. They optimised the VG-1 PEC for various fixed Reynolds numbers, from 660 to 2 000 defined on the hydraulic diameter and the core velocity. The simulations were performed under the assumption of steady and laminar flow. They used 126k cells in the computational mesh for a geometry with a fin pitch of 2.77 mm, a longitudinal tube pitch of 27.5 mm, a transversal tube pitch of 31.5 mm and three tube rows. Grid convergence was claimed by noting that the temperatures on a fine grid of 255k cells had a relative deviation of 3% with respect to the used grid.

3.4 Compound designs

Finally, several authors have also investigated the combination between louvres and vortex generators. Already in 2001 Lozza and Merlo [49] conducted an extensive experimental investigation of 15 different fin geometries for a round tube and fin heat exchanger. They used a full-scale heat exchanger cores placed in a wind tunnel. All the fin geometries had the same hydraulic diameter. Several rectangular and X-shaped louvred fin geometries were assessed, as well as a compound vortex generator and rectangular louvres design. They varied the inlet frontal velocity from 1 to 3 m/s, which corresponded to a maximum Reynolds number based on the hydraulic diameter of 600. They noted that the actual fin efficiency of interrupted fins could not be estimated easily and that any deviation of the actual fin efficiency from the fin efficiency estimated with the correlation was therefore attributed to the heat transfer coefficient. They noted that the X-shaped louvred design performed exceptionally well, having a significantly higher Colburn j-factor than the other designs, with only a slightly higher pressure drop than for the rectangular louvred fin. The compound louvres and winglet design was found to have a higher pressure drop than the rectangular louvred fin, without any significant improvement in the j-factor. The placement of the vortex generator was not optimised: the authors noted that it was therefore not possible to definitively assess the merit of the compound design.

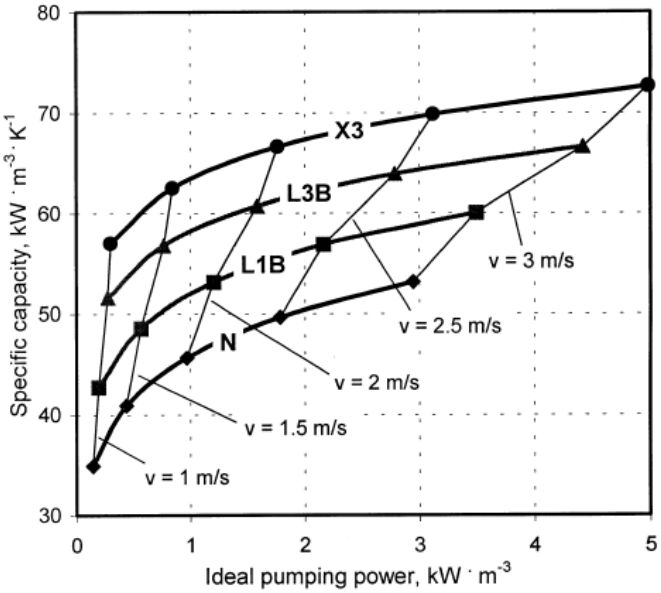

Figure 3.13: Performance comparison between different fin geometries [49].

The authors compared the performance of the different fin geometries using a comparison between the specific capacity (heat transfer rate per unit volume and unit temperature difference) and the pumping power per unit volume. This is a dimensional variation on the J- and F-factors discussed in paragraph 2.6.3. Their result is shown in figure 3.13 for the X-shaped geometry (X3), two variations on the rectangular louvred geometry(L3B and L1B) and the wavy fin (N). The L3B variant of the rectangular louvres had a larger louvre height and therefore larger j- and f-factors for the same Reynolds number.

First, the enhanced geometries seem to achieve a higher specific heat capacity than the less enhanced geometries. The X-shaped geometry performs best of all, as for a given volume and heat transfer rate, it has the lowest pumping (or fan) power. Secondly, in order to achieve the same pumping power per unit volume for the different fin geometries, the frontal velocity must be different. This is an important conclusion, which will be investigated extensively in paragraph 5.2.2.

Tang et al. [50] also studied several fin geometries for fin and round tube heat exchangers in a wind tunnel, including a combination of a slit fin with delta winglet vortex generators. For this compound design, the first tube row was enhanced using vortex generators, whereas the second tube row consisted of a slit fin geometry. For higher Reynolds numbers, the slit fin performed best, whereas for lower Reynolds numbers, the vortex generator fin showed the best performance. The

mixed design was always outperformed by one of these two designs, depending on the Reynolds number. The authors also performed an optimisation of the vortex generator geometry using numerical simulations. Six tube rows were used to ensure that the fully developed periodic flow was attained. The Reynolds number based on twice the fin pitch and the inlet frontal velocity ranged from $1\,300$ to $3\,300$. They used three different $k-\epsilon$ turbulence models, namely the standard model, the realisable model and the renormalisation group model. They opted for the standard model as it agreed best with the experimental results. They varied the vortex generator angle, height and length and found that both the j- and f-factor increased as the angle was increased over the range of $30°$ to $60°$. It was not mentioned how the position of the vortex generator was varied as the angle changed. They fitted an exponential regressive correlation based on 27 numerical calculations, using the Reynolds number, the vortex generator angle and the height over length ratio as variables. The correlation fitted the simulated data with an error of less than 10%. Using the JF criterion and a genetic algorithm, they found that the vortex generator angle should be as high as possible, whereas the height over length ratio should be as small as possible. However, concerns can be raised about the sense of optimising variables with respect to a regression model. Investigating the variation of the friction factor of the correlation due to changes in the geometry, it is seen that the friction factor varies between 0.941 and 0.979 multiplied by a function which only depends on the Reynolds number. This is a change of merely 4% from the average value, which is smaller than the maximum error of 10% between the correlation and the simulation results. It is clear that the correlation does not accurately capture the impact of the geometry on the friction factor. Nevertheless, the optimised vortex generator fin was said to perform better than the slit fin, for all Reynolds numbers.

In 2013, Huisseune et al. [51] investigated a compound combination of a rectangular louvred fin with delta winglet vortex generators. The frontal velocity was varied from 0.63 m/s to 5.25 m/s, which corresponds to a Reynolds number range of 140 to $1\,220$. The computational domain was extended downstream and upstream of the heat exchanger. For a Reynolds number lower than 200, even the wake behind the heat exchanger was found to be steady. For higher Reynolds numbers, laminar and unsteady calculations were performed. Grid independence was verified on two meshes, one of 14M cells and one of 4.3M cells. The deviation between both grids was found to be 2%. They noted that the vortices result in a net enhancement of the heat transfer due to the thinning of thermal boundary layers and due to mixing of the flow. The authors contended that the vortices were destroyed by the louvres and the deflected flow in the downstream louvre bank. The horseshoe vortices were also said to be destroyed by the louvres. The destruction of vortices in a louvred fin heat exchanger will be discussed in chapter 7. Due to the reduction of the tube wake, the form drag of the tubes was decreased. The

overall pressure drop was nevertheless increased, which was attributed to increased frictional pressure drop and flow blockage. Using the J- and F-factor comparison, they showed that the total performance of the compound design was better than that of the rectangular louvred fin.

In a second study, Huisseune et al. [4] used the Taguchi method to investigate the performance of the compound fin design. The computational method was the same as in their previous study. Unlike Zeng et al. and Hsieh et al., they did not consider the Reynolds number a noise factor, but instead conducted separate Taguchi analyses for different Reynolds numbers. This allowed them to study the effect of the Reynolds number separately from all the other factors. They found that at high inlet velocities, the performance was mainly determined by the louvres. It was only for the lower inlet velocities (lower than 1.26 m/s) that the delta winglet geometry contributed significantly.

3.5 Conclusions

An overview of the Reynolds numbers used in numerical studies was given in table 3.1. Based on the results of Leu et al. and Herpe et al., it can be expected that the flow in the heat exchanger core remains approximately steady up to at least a Reynolds number of around 600. In this work, the same baseline parameters for tube diameter, fin and tube pitches will be used as in the work of Huisseune et al. [4]. A Reynolds number range of 120 to 600 then corresponds to a velocity range of 0.5 m/s to 2.6 m/s. This is the same range as used by Leu et al., several other authors investigated the fin performance in a range of around 1 to 3 m/s, so this is an appropriate range for air-conditioning applications. Steady and laminar models can be used for the low Reynolds numbers which correspond to these velocities. For higher Reynolds numbers unsteady laminar models should be used. This greatly increases the computational effort required to evaluate a given flow to the point where optimisation becomes unfeasible with the available computational infrastructure. Several authors use a $k - \epsilon$ turbulence model from Reynolds numbers as low as 700. Since the flow in the heat exchanger core was physically laminar and unsteady, it was decided not to investigate these higher Reynolds number flow by using a turbulence model, as questions could be raised regarding the applicability of turbulence models in this Reynolds number range.

From the literature, it is also apparent that delta winglets are superior to wing type of designs. Wing type vortex generators will therefore not be included in this work. Huisseune et al. [4] showed that the combination of rectangular louvres with vortex generators performed better than the baseline case of rectangular louvres. However, Lozza and Merlo [49] indicated that the X-shaped louvred fin design was significantly superior to the rectangular louvred design. In this study the compound design combining louvres with vortex generators will therefore be

Who?	Reynolds number	Steadiness	Turbulence model
Leu et al. (2001)	150-780	steady	laminar
Hsieh et al. (2012)	830-8 800	steady	$k-\epsilon$
Tiwari et al. (2003)	2 000 (u_{in} and $2F_p$)	unsteady	laminar
Perrotin and Clodic (2003)	410-1 450 (u_{in} and $2F_p$)	steady	laminar
Leu et al. (2004)	700-5 100	steady	$k-\epsilon$
Wu and Tao (2007)	800-2 000 (u_{in} and $2F_p$)	steady	laminar
Chu et al. (2009)	500-2 500 (u_{in} and $2F_p$)	steady	laminar
Herpe et al. (2009)	600 (u_{in} and $2F_p$)	unsteady	laminar
Lemouedda et al. (2010)	440-2 660	unsteady	laminar
Zeng et al. (2010)	1 900-6 300	steady	$k-\epsilon$
Huisseune et al. (2013)	140-1 220	unsteady	laminar
Jang et al. (2013)	660-2 000	steady	laminar

Table 3.1: Overview of the Reynolds number ranges and viscosity models in literature

compared with the X-shaped louvred fin. Different authors used different grid refinement ratios and obtained different deviations between the grids. Some kind of systematic procedure is required in order to compare the different errors due to the grid discretisation. This will be discussed in chapter 4. The optimisation methods which have been used in the scientific literature show some issues. The Taguchi analysis used by several authors neglected the impact of interaction effects, which could be expected to be important on physical grounds. Furthermore, the Reynolds number was either seen as a noise factor or was held constant for different fin geometries. Some authors optimised a surrogate model constructed out of an initial sampling plan instead of using CFD calculations during the optimisation routine. It is also remarkable that some authors found an optimum vortex generator angle of attack, such as Chu et al. [45] and Pesteei [37], whereas other authors like Lemouedda et al. [46] found that increasing the vortex angle further to 90 degrees resulted in additional improvements of the heat transfer rate. The performance evaluation and the optimisation of fin geometries will be treated in chapter 5. The optimum positioning and angle of attack of the vortex generator will also be discussed in this chapter. Lozza and Merlo [49] also indicated that there were issues in determining the fin efficiency for interrupted fin designs. The current common practice and a new method will be discussed in chapter 6. Finally, Huisseune et al. [4] indicated that vortices were destroyed by louvres, whereas they persisted much longer in plain fin designs. The presence and behaviour of the vortices in louvred fins and compound designs will therefore be looked into in chapter 7.

One issue which has been identified that will not be dealt with in this work is the need for a more reliable louvred fin correlation. The correlation of Wang

et al. [3] shows unphysical behaviour for the Colburn j-factor as a function of the Reynolds number and as a function of the number of tube rows. Neither the impact of the different topologies nor the measurement error was taken into account. Another issue is that in order to obtain the heat transfer coefficient from experimental results, a fin efficiency correlation is required. As already indicated by Lozza et al. [49], a reliable fin efficiency correlation for interrupted fin designs does not yet exist. Finally, it is not clear whether it is justified to use turbulence models such as the $k - \epsilon$ for the flow in a heat exchanger core when the laminar and steady model fails, such as in the Reynolds number range between 600 and 4000.

4 Numerical simulation

4.1 Introduction

In order to evaluate the performance of a fin geometry, the modified Colburn j-factor and the friction factor f are required as functions of the Reynolds number. These functions need to be determined for a variety of fin geometries. Since building a new heat exchanger for each possible fin geometry would be prohibitively expensive, the j- and f-factors will be calculated by using computational fluid dynamics (CFD) simulations. A small program is written that accepts geometrical parameters and a Reynolds number and outputs the friction factor and the modified Colburn j-factor for this case. This computational unit can then be coupled to an optimisation routine to investigate optimal fin geometries.

4.2 Characterisation of the materials

4.2.1 Fluid

As in many practical applications, the fluid on the fin side is air. An equation of state needs to be provided to describe the fluid, as well as equations for thermophysical properties such as the viscosity as a function of the thermodynamic properties. In general, air close to atmospheric conditions can be modelled using the ideal gas law. In equation (4.1) the density is expressed as a function of the pressure and the temperature. In this equation, R is the gas constant on a mass basis for air.

$$\rho = \frac{P}{RT} \tag{4.1}$$

Using equation (4.1) results in the full compressible behaviour of air. Since the pressure drop over the heat exchanger is small compared with the atmospheric pressure P_0, the absolute pressure does not vary much throughout the heat exchanger. Therefore, it is possible to neglect the dependence of the density ρ on the pressure, resulting in the incompressible ideal gas equation (4.2).

$$\rho = \frac{P_0}{RT} \tag{4.2}$$

The influence of the temperature on the density is taken into account, resulting in acceleration of the flow as the temperature increases. Using the incompressible ideal gas model therefore takes the pressure drop due to flow acceleration into account.

The dynamic viscosity μ is calculated using the Sutherland viscosity law (4.3) in order to capture the temperature dependence of the viscosity.

$$\mu = \mu_0 \left(\frac{T}{T_0}\right)^{\frac{2}{3}} \frac{T_0 + T_1}{T + T_1} \tag{4.3}$$

$$\mu_0 = 1.716\text{e-}5 \, \frac{\text{kg}}{\text{ms}} \quad T_0 = 273.11\,\text{K} \quad T_1 = 110.56\,\text{K} \tag{4.4}$$

For the thermal conductivity k and the specific heat capacity at constant pressure c_p, constant values are used.

$$c_p = 1006 \, \frac{\text{J}}{\text{kgK}} \tag{4.5}$$

$$k = 0.02637 \, \frac{\text{W}}{\text{mK}} \tag{4.6}$$

4.2.2 Fin material

The fin is constructed from aluminium. The density, heat capacity and conductivity are constant.

$$\rho = 2719 \, \frac{\text{kg}}{\text{m}^3} \tag{4.7}$$

$$c_p = 871 \, \frac{\text{J}}{\text{kgK}} \tag{4.8}$$

$$k = 202.4 \, \frac{\text{W}}{\text{mK}} \tag{4.9}$$

4.3 Geometry

4.3.1 General geometrical parameters

In this work, two main geometries will be used. The first is the X-shaped louvred fin, half of a periodic unit cell is shown in figure 4.1. The louvres are extended upstream and downstream of the round tubes, forming the X-shape. Several important geometrical parameters can be distinguished for the louvred fin, most of which are indicated in the figure. If the contribution of the tube surface to the total heat transfer surface is small, the hydraulic diameter D_h is mainly determined by the fin pitch F_p. Due to the impact of the tubes, the hydraulic diameter is also influenced by the transversal tube pitch P_t. The contraction factor σ is determined by the fin pitch, the tube collar diameter D_c and the fin thickness t_f. Other parameters are specific to the louvre geometry, such as the louvre angle θ and the louvre pitch L_p. Together with the number of louvres N_l which is not indicated in the figure, the louvre pitch determines the total louvred length L_l.

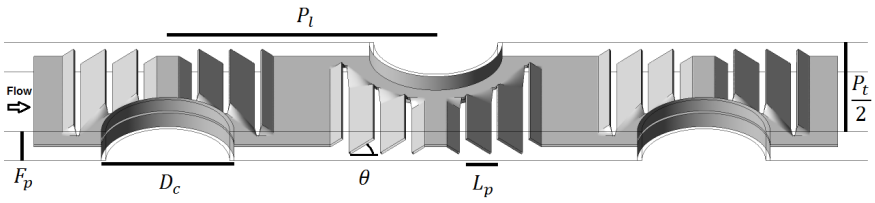

Figure 4.1: X-shaped louvre geometry

In order to combine louvred fins and vortex generators, some space must be available to place the vortex generators. This is possible if the rectangular louvre is considered, following Huisseune et al. [4]. Figure 4.2 shows a close-up of the rectangular louvre geometry and a delta winglet vortex generator (VG). The delta winglet VG consists of a triangle, which is punched out of the fin material. The height of the VGs in this study is always kept equal to 90% of the fin spacing. The base of the VG then determines the aspect ratio Λ. The positioning is expressed relative to the corresponding tube centre and is indicated with ΔX and ΔY. The angle of attack with respect to the inlet frontal velocity is indicated with α. The region where the louvres change geometry to connect with the rest of the fin is called the transition area. For this region, the same geometry was used as by Huisseune et al. [4].

By varying the parameters discussed in this section, different fin geometries can be constructed and simulated using CFD.

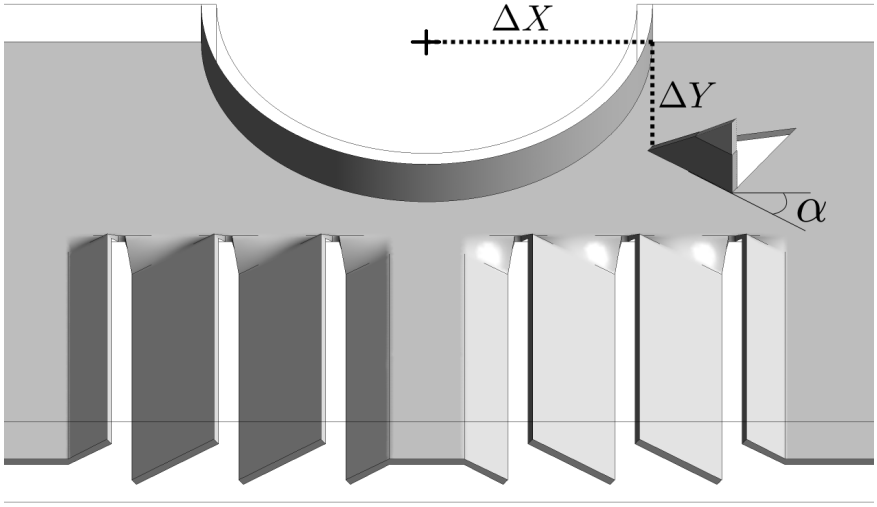

Figure 4.2: Rectangular louvre geometry and delta winglet vortex generator

4.3.2 Computational mesh

An important aspect of numerical finite volume simulations is the computational mesh. In this work, the mesh is generated using the commercial Gambit software (Ansys Inc.). The numerical grid for the fluid domain is divided into two main parts: the louvres and vortex generators are meshed using unstructured tetrahedral cells, for the other regions prismatic cells are used. The solid domain consists of the fin and tube material and is also meshed using tetrahedral cells. The main advantage of the tetrahedral cells is that they can easily be changed in size throughout the domain. It is also easier for the meshing software to generate unstructured tetrahedral grids than it is to generate structured grids. Using tetrahedral grids allows for a greater variation in the geometric designs which can be meshed. The downside of using tetrahedral cells is that they cannot be aligned with the expected flow, which allows obtaining the same results with a lower number of cells. However, vortex structures are expected to be present in the flow around the louvres, which makes it difficult to predict the local flow direction and align the cells with the flow. Furthermore, due to the flow efficiency which is in general not equal to unity, the flow does not exactly follow the louvre orientation even if no vortex structures would be present. Due to these two reasons, the flexibility advantage of the tetrahedral cells was deemed to be larger than the disadvantage of not being able to align the cells in a preferred direction.

The maximum dimension of any cell is equal to the fin thickness, the size is reduced to one third of the fin thickness in regions where important flow features are expected, such as the leading and trailing edges of the louvres. A structured boundary layer mesh is used around the tube walls, since preliminary simulations indicated a small boundary layer thickness in the unseparated region of the flow around the tubes. The prismatic cells outside the louvres have a triangular base. These features are visible in figure 4.3, which shows the mesh on the fin surface.

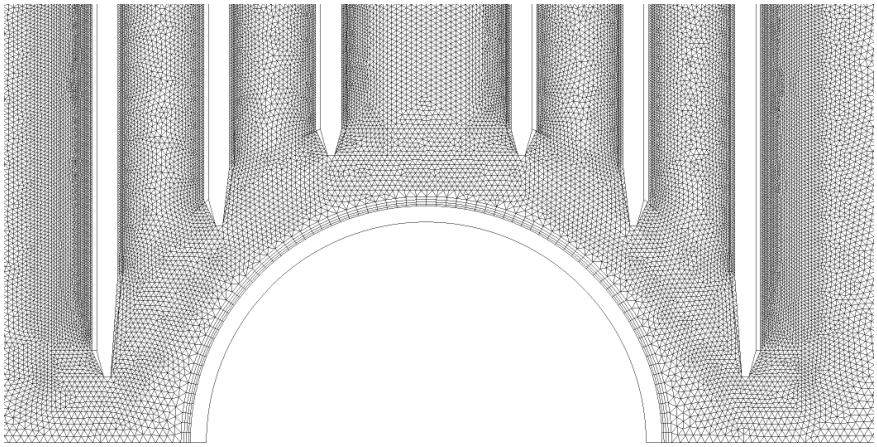

Figure 4.3: Mesh on the fin surface

Figure 4.4 shows the mesh in one of the symmetry planes. The unstructured mesh around the louvres and the prismatic mesh outside them are clearly visible. Prismatic cells are also applied around the louvres, in order to properly resolve the boundary layers. The height of the first layer is approximately one fourth of the fin thickness. These prismatic cells are smaller at the leading edge to better capture the initiation of the boundary layer. The stagnation point is resolved by using smaller cells in front of the leading edge. The size of the tetrahedral cells grows larger further away from the louvres. No prismatic layer was used around the inlet and exit louvres, as it was found this led to problems in the meshing software for larger louvre angles.

For the flow outside the louvres, the height of the cells is again approximately one fourth of the fin thickness close to the fin surface. At first, this may seem useless since the boundary layer will be quite thick if it is not interrupted, as is the case for flow outside the louvres. However, local impingement of vortex structures will locally severely reduce the boundary thickness. Since it is not known a priori where this will occur, small cell heights were used over the entire surface of the fin. Further away from the fin surface, the cell size increases to the fin thickness, in order to limit the total number of cells which is required.

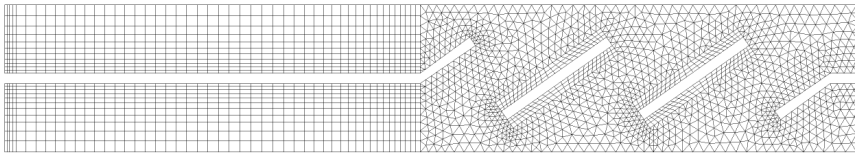

Figure 4.4: Mesh in the symmetry plane

For geometries where vortex generators are present, a tetrahedral mesh was used around the vortex generator and the corresponding punched hole. A distance of two times the fin thickness was used as a buffer to match the tetrahedral grid to the surrounding prismatic grid at the boundary. The cells have a size of one third of the fin thickness close to the vortex generator surface, this size increases slowly further away from the surface.

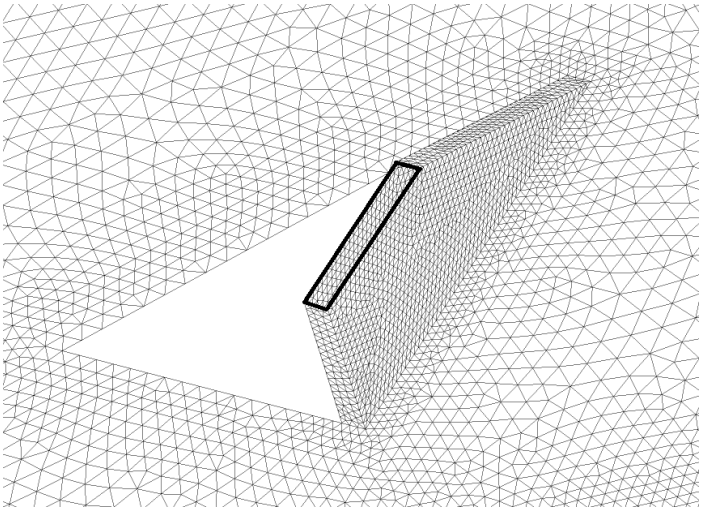

Figure 4.5: Surface mesh around a vortex generator. The vortex generator is intersected by the boundaries of the computational domain at the location of the indicated face, for which a periodic boundary is used

For the periodic boundaries, a conformal mesh is used. This means that both periodic boundaries share the same surface mesh, directly enforcing the equality of all quantities at this boundary. This avoids interpolation errors once the discretised equations are solved.

4.4 Boundary conditions

Any CFD simulation requires boundary conditions for the calculation domain. The velocity and temperature are fixed two tube diameters upstream of the heat exchanger. Uniform velocity and temperature profiles are imposed. The inlet temperature is always 20 °C. Two tube diameters are a sufficient distance for the flow to adapt to the contraction at the heat exchanger inlet.
The top and bottom faces of the computational domain are chosen to be halfway between the fins. Periodic boundary conditions are imposed. Conformal meshing is used to avoid interpolation errors on the interface.
The left and the right side of the computational domain are also periodic with conformal meshes. However, in the case that the flow is steady, the flow is also symmetrical for all cases investigated in the literature. This allows using a domain which is half as wide and in this case, symmetrical boundary conditions are used.
At the interface between the fluid and the fin material, wall boundary conditions are imposed. This requires the heat flux and the temperature to be continuous at the interface. Furthermore, the flow velocity at the interface is equal to zero.
The exit of the computational domain is located 10 tube diameters behind the heat exchanger exit. The pressure on the exit is fixed to the atmospheric pressure. The pressure in the domain is expressed relative to the atmospheric pressure.
For the fin material which is not adjacent to the fluid, additional boundary conditions are required. Everywhere the fin material intersects with the limits of the computational domain, periodic boundary conditions with conformal meshes are used. Only in the case of steady-state flow, symmetrical boundary conditions are used where possible. For the inner-tube walls, a fixed temperature of 50 °C is imposed. This means that the bulk temperature of the fluid inside the tubes is assumed to be constant and that the convective thermal resistance is zero. Neglecting the thermal resistance is an approximation of evaporating/condensing flow of a refrigerant and is required in order to avoid having the optimal geometry depend on the value of the thermal resistance on the secondary fluid side. This is consistent with the approximations and assumptions used in the Cowell method for the performance evaluation.

4.5 Unsteady heat exchanger flow

4.5.1 Physically unsteady flow

In general, the flow behind a fin and tube heat exchanger is almost always unsteady, except for extremely low Reynolds numbers. This is caused by the round tubes, behind which a Von Karman vortex street occurs for Reynolds numbers which are larger than 40, based on the tube diameter. In the heat exchanger core,

the vortex streets are suppressed by the flow contraction of the downstream tube rows. Unsteadiness in the heat exchanger core occurs at larger Reynolds numbers. According to Tafti and Zhang [52], instabilities first appear in the wake of the exit louvre and propagate upstream for higher Reynolds numbers. Behind the final tube row, no downstream flow contraction is present, resulting in unsteady flow behind the heat exchanger even for Reynolds numbers as low as 100.

As long as the flow in the heat exchanger core remains steady, the wake unsteadiness only influences the flow behind the heat exchanger and in the wake zones of the final tube row. In this case, the influence of the unsteadiness on global heat exchanger parameters such as pressure drop and heat transfer rate can be assumed to be small. At higher Reynolds numbers, the wakes of obstructions in the flow such as the tube wakes, vortex generator wakes and the louvre wakes become unsteady. DeJong en Jacobi [23] noted that the flow in a louvred fin and flat tube heat exchanger core was steady for Reynolds numbers up to 670 based on the louvre pitch. They also found that when vortex shedding occurred, it only causes small increases in heat transfer and pressure drop over the Reynolds number range of interest. They concluded that steady-state approximations could be expected to give good results. For a plain fin and tube heat exchanger of two tube rows, He et al. [53] verified that the difference between the steady and unsteady numerical models was only 1.54% for a Reynolds number of $2\,000$.

4.5.2 Timescale problem

As previously noted, some authors do perform unsteady conjugate gradient simulations. However, this requires very long calculation times, as this is a stiff problem where largely different timescales occur. The fastest timescale is determined by the flow oscillations behind the vortex generators and the louvre and tube wakes. An estimate of the order of magnitude of these fluctuations can be made using the Strouhal number (4.10) for cylinders, which is approximately equal to 0.2 for a wide range of Reynolds numbers. Tafti and Zhang [52] showed that a Strouhal number based on the local velocity and a corrected louvre height was appropriate for louvre unsteadiness, corresponding to Strouhal numbers between 0.3 and 0.5.

$$T = \frac{L}{uSt} \tag{4.10}$$

The fluctuations with the smallest period will occur behind the bodies with the smallest characteristic length scale. Since the tube diameter is larger than the louvre height and the fin thickness, the high-frequency oscillations can be expected to be caused by the louvres and the vortex generators. To obtain a very rudimentary estimate of the period of these fluctuations, the characteristic velocity is chosen to be the inlet frontal velocity and for the characteristic length scale, the fin thickness

is used. The Reynolds number based on the fin thickness is approximately 20; based on the VG height, it is 300. For a frontal velocity of 2.6 m/s, this results in an estimate of 250 μs for the smallest period. In the unsteady simulation, which will be discussed in paragraph 4.5.3.2, the period of the fluctuations in the louvre wake was found to be 400 μs for the same frontal velocity, which was indeed the same order of magnitude.

The largest timescale is determined by the thermal equilibrium between the fin material and the fluid. If some kind of average fin temperature can be introduced, the problem can be simplified as a resistor-capacitor system, where the capacitance is determined by the thermal mass of the fin $\rho_{fin} V_{fin} c_{p,fin}$. The resistance is determined by convection between the air and the fin and conduction between the tube walls and the fin material. Since determining a justifiable value for the average temperature and the conductive resistance is difficult, a numerical approach will be used, described in the next paragraph.

For the solution to any unsteady problem, initial conditions are required. In order to solve the unsteady fluctuating heat transfer coefficient, an approximate steady-state solution to the problem is used. The steady-state formulation of the Navier-Stokes equation is entered to the flow solver and it is attempted to find a solution using an iterative algorithm. Since the problem is physically unsteady, it is highly likely that no steady-state solution can be found and the steady-state Navier-Stokes equations are therefore only approximately satisfied. This unconverged approximate solution is used as the initial condition for the transient formulation of the Navier-Stokes equations. Solving the unsteady problem over a sufficiently long interval to obtain statistically steady values for the averaged flow quantities results in an equivalent steady-state heat transfer coefficient.

Now a simple model is made to estimate the time required to obtain the steady-state solution for the fin temperatures. It is assumed that as soon as the unsteady simulation is started, the equivalent time-averaged heat transfer coefficient is immediately imposed. In reality, some time is required to establish a developed flow regime, such as Von Karman streets. Neglecting this timescale results in a step function for the heat transfer coefficient, which can be applied to the fin model used in paragraph 2.4.4.2.

The one-dimensional equation for the fin efficiency (2.60) is modified to include the transient term, resulting in equation (4.11).

$$\frac{\partial^2 T}{\partial x^2} = \frac{2h}{k t_f}(T - T_\infty) + \frac{\rho c_p}{k}\frac{\partial T}{\partial t} \tag{4.11}$$

A constant temperature is imposed on one side, the other side is subject to adiabatic boundary conditions. These are the same boundary conditions that were

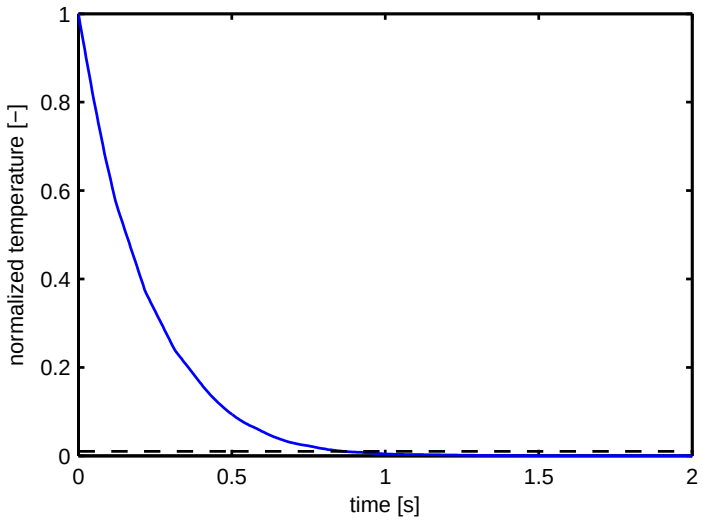

Figure 4.6: Response in fin temperature to step in heat transfer coefficient. 1 corresponds to initial value, 0 to steady-state solution

used for equation (2.60), but now they are valid for every time instance. The initial condition for the temperature is the temperature profile corresponding to the unphysical initial heat transfer coefficient value. At the start of the calculation, the step input for the heat transfer coefficient is imposed. For the length of the fin, the equivalent fin length established by Schmidt is used. The equation is solved numerically, the result is shown in figure 4.6. After 0.85 seconds, the fin temperature difference with respect to the new steady-state solution is smaller than 1%. If a difference of 10% is tolerated, approximately 0.5 seconds is needed, which is the same order of magnitude.

The time required to flow through the region of interest once is 16 milliseconds. By the time thermal equilibrium is obtained, the flow has passed through the region of interest approximately 50 times. In this time, around $3\,400$ periods of the small-scale oscillations have passed. The required time step is determined by the phenomena with the smallest period, but the duration which needs to be simulated is governed by the slowest occurring phenomenon. Since these timescales differ three orders of magnitude, a large amount of computational effort is required to obtain the fully developed solution.
If the fin is not in equilibrium with the heat transfer coefficiennt, taking flow unsteadiness into account, this results in an error on the fin efficiency. The magnitude of this error can be obtained by differentiating the fin efficiency equation (2.63). For a fin efficiency of 90%, the sensitivity with respect to the heat transfer coefficient is 25%. Since this is a significant effect, it is necessary to perform simulations

until sufficient equilibrium between the fin and the fluid is obtained. Only if the impact of the unsteady oscillations on the heat transfer coefficient is small, the initial condition forms a good approximation and the change in fin efficiency as the fin reaches equilibrium with the correct heat transfer coefficient will be small. However, if the impact of the oscillations is small, it would be better if it could be avoided to resolve them at all.

4.5.3 Steady flow approximation

4.5.3.1 Forcing steady-state flow

It is possible that the difference between the heat transfer coefficient for the full transient calculation and a steady approximation is quite small, for instance if all the flow unsteadiness occurs behind the heat exchanger. Since obtaining correct time resolved flow solutions is computationally quite expensive, a steady-state approximation will be used. This has the additional benefit that the flow field is then symmetric, halving the required size of the computational domain.
To achieve steady flow in the simulations, an artificial viscosity profile is established behind the heat exchanger. Starting from behind the heat exchanger to the exit of the flow domain, the viscosity increases linearly to 1000 times its physical value. This damps out all unsteady fluctuations behind the heat exchanger, allowing a solution to the steady-state equations. Furthermore, the viscosity causes a mixing of the flow momentum, bringing the flow profile back to a uniform profile. This emulates the turbulent mixing of the fluid to a uniform profile which occurs in reality. This allows coarsely approximating the static pressure recovery at the exit of the heat exchanger core. Since there are no walls in this region, no extra momentum is lost due to the increase in viscosity. The pressure recovery depends only on the change of momentum between the exit of the heat exchanger core and the exit of the computational domain. Since no momentum is lost, the pressure recovery is not impacted by the viscosity profile. However, there will be some influence of the viscosity on the velocity profile at the exit of the heat exchanger core, which impacts the pressure recovery.
Another option would be to use a turbulence model in the region behind the heat exchanger. The turbulence model imposes a different viscosity profile, which is calculated from mean flow quantities. A turbulence model requires greater computational effort and the results are very similar.

4.5.3.2 Estimating the error due to the steady-state approximation

In order to verify whether the steady calculation using the viscosity profile provides an adequate approximation, it is necessary to perform an unsteady calculation. Since for a conjugate heat transfer simulation this requires too many time steps, an isothermal unsteady simulation is performed instead. To avoid damping

of physical oscillations due to numerical diffusion, a bounded central discretisation scheme was used for the convection of momentum. The energy equation was discretised using a second-order upwind scheme. An implicit bounded second-order time discretisation was used. By setting the fin temperature to a constant value, the slowest timescale is no longer a concern. Now the calculation needs to proceed for long enough so that the wake oscillations behind vortex generators, louvres and tubes are fully developed. This is monitored by observing the time-dependent behaviour of the heat transfer rate and the pressure drop over the heat exchanger. Additionally, the velocity and temperature are monitored in two points in the wake of the vortex generator of the second tube row. The calculation is performed for the highest inlet frontal velocity which will be considered in this work, which is 2.6 m/s.
Since the estimated period of the oscillations with the highest frequency was 250 µs, the time step is chosen so that 20 samples are taken per period, resulting in a value of 12.5 µs. An initial flow solution was obtained by first solving the steady-state equations and then performing 500 coarse time steps of 125 µs. After that, $3\,000$ iterations are performed using the final time step.

Clear oscillations are observed in the pressure drop over the heat exchanger, with an amplitude of 0.1% of the average value. For the heat transfer rate, the amplitude of the oscillations is 0.08% of the average value.
The average pressure drop over the heat exchanger is 111.06 Pa, the average heat transfer rate is equal to 2.785 W. The calculation took more than one month on two hex-core Intel X5690 processors with a clock speed of 3.47GHz.
This is compared with the same geometry which that calculated using symmetrical boundary conditions on a computational domain which is half as wide and using the viscosity profile. The discretisation of the convective terms is second-order upwind. The pressure drop is 110.97 Pa, the heat transfer rate is 2.794 W. The calculation was completed after five hours using the same computational resources.
The error on the heat transfer coefficient can be estimated from the heat exchanger effectiveness-NTU relation (4.12), since the error on the heat transfer coefficient is proportional to the error on the number of transfer units.

$$\frac{dj^*}{j^*} = \frac{\partial NTU}{\partial \epsilon}\frac{dQ}{Q} = \frac{1}{1-\epsilon}\frac{dQ}{Q} \tag{4.12}$$

For a heat exchanger with a high effectiveness, very large increases in the NTU are required to get the effectiveness marginally closer to unity, as the effectiveness has an asymptotic behaviour as a function of the number of transfer units. For the investigated heat exchanger, the effectiveness is 96.44%.
The corresponding error on the j-factor is $\frac{1}{1-0.9644}\frac{2.794-2.785}{2.785} = 28 * 0.1\% = 3\%$.
Even though the error on the heat transfer rate is quite small, the resulting error on the j-factor is still 3%. This is due to the high effectiveness of the heat exchanger,

which corresponds to a high sensitivity of the heat transfer coefficient with respect to the heat transfer rate. The error on the pressure drop is 0.08%.
In conclusion, the steady-state approximation offers a good approximation in a fraction of the time required to solve the full unsteady heat transfer problem. This is in agreement with the findings of DeJong and Jacobi. Furthermore, using the steady-state approximation easily allows performing conjugate heat transfer simulations for which the fin is not isothermal. This allows taking fin efficiency effects into account.

4.6 Data reduction

4.6.1 Verifying iterative convergence

As the system of discretised Navier-Stokes equations is solved iteratively, it is necessary to have some sort of criterion which determines when the iterations can be stopped and the final solution is obtained. The pressure drop over the heat exchanger and the heat transfer rate were monitored as a function of the number of iterations. Residuals are defined by the CFD software (Fluent, Ansys Inc.) as the sum of the absolute values of the imbalance of the conservation equations over all computational cells. These values are scaled with the maximum residual occurring in the first five iterations. It was seen for a couple of simulations that after a value of 1e-4 for the residuals on the continuity equation and 1e-7 for the energy equation, the pressure drop and the heat transfer rate become independent of further iterations. Therefore, iterations were chosen to end after a residual of 1e-5 on the continuity equation and 1e-8 on the energy equation. Since the CFD simulations are used in an optimisation loop, it is not possible to manually check iterative convergence of every single simulation. Nevertheless, for some simulations which were suspected to be difficult, the values of the heat transfer rate and the pressure drop were investigated as a function of the iteration number. For all simulations iterative convergence was observed. Furthermore, the heat balance and momentum balance in the flow direction were checked.

4.6.1.1 Momentum balance in flow direction

The forces in the mean flow direction on the tube and fin surface are determined. Part of the force is due to the net pressure force on the surface, which is also called the form drag. The net force due to the viscous friction at the surface is called the friction drag. These forces on the flow are shown in table 4.1 for one specific simulation. According to Newton's third law, these forces are balanced by equal but opposite forces on the flow. This total force on the flow corresponds to a momentum sink.

Surface	Form drag (N)	Friction drag (N)	Total drag (N)
Tubes	4.903e-4	2.361e-5	5.139e-4
Fin	8.063e-4	3.488e-4	1.155e-3
Total	1.297e-3	3.724e-4	1.669e-3

Table 4.1: Forces on the wetted surfaces

For this simulation, the density was held constant to avoid a flow acceleration term. In this case the same uniform velocity profile as upstream of the heat exchanger is obtained far behind the heat exchanger, due to conservation of mass. This implies that the momentum of the flow is also unchanged. Since momentum has been lost due to the forces in the heat exchanger core, this lost momentum must be compensated for from some other source. This other source is the pressure force on the cross-sectional section of the flow.
The net force due to the pressure is equal to $A_c \Delta P$ and is given by equation (4.13).

$$\Delta P A_c = 1.669\text{e-}3\text{N} \tag{4.13}$$

The imbalance on the momentum is therefore 0.05%, which is reasonably small. Therefore, the global momentum balance is satisfied, which indicates that the convergence criterion for the momentum balance is reasonable.

4.6.1.2 Energy and mass balance

The total heat transfer rate can be obtained by integrating the local heat flux over the entire wetted surface. The contributions by the tubes and the fin are given in table 4.2.

Surface	Heat transfer rate (W)
Tubes	5.959e-2
Fin	1.337
Total	1.397

Table 4.2: Heat transfer rates on the wetted surfaces

According to the conservation of energy, this total heat transfer rate must be equal to the change in bulk temperature multiplied by the heat capacity rate of the fluid, given by equation (4.14).

$$Q = \dot{m} c_p \Delta T_{bulk} = 1.397\text{W} \tag{4.14}$$

Up to four digits, there is no difference between the heat transfer rates. Using higher accuracy, the error on the heat balance is determined to be 6e-6%. This

is an excellent closure of the global heat balance, which gives confidence in the chosen convergence criterion for the heat equation.

The global mass balance is checked by calculating the mass flow rate from the velocity profile at the inlet and the outlet. The error on the mass balance is 2e-4%. Since all balances close quite well, this is an indication that the solution to the set of discretised Navier-Stokes equations is obtained within a quite small error due to the iterative convergence. Now the quantities of interest can be obtained from the simulation data. Afterwards, it will be investigated how well the quantities of interest of the discrete solution can be expected to agree with the quantities of interest of the solution of the continuous Navier-Stokes equations.

4.6.2 Friction factor

In order to obtain the pressure drop over the heat exchanger, the pressure on the inlet face is averaged over the cross-sectional area. This pressure is equal to the pressure drop over the heat exchanger, including all the simulated losses discussed in paragraph (2.5), since it is expressed relative to the outlet pressure. The pressure drop due to flow acceleration can easily be determined theoretically and is subtracted from the overall pressure drop. Since it is very difficult to separate the irreversible pressure drops due to contraction and expansion from the overall pressure drop, they are included in the core friction. The friction factor is defined as in equation (4.15).

$$f = \frac{A_c}{A_s}\frac{\rho_m}{\rho_i}\left(\frac{2\Delta P \rho_i}{G_c^2} - (1+\sigma^2)\left(\frac{\rho_i}{\rho_e}\right) - 1\right) \tag{4.15}$$

Strictly speaking, this is not correct, as the friction factor is assumed to be independent of the length of the heat exchanger. The core friction pressure drop does in fact scale linearly with the heat exchanger length, but the entrance and exit effects are constant. The overall effect is a slight dependence of the friction factor according to equation (4.15) on the heat exchanger length and thus the number of tube rows. Wang et al. [24] showed that for louvred fins this effect was small, as the number of tube rows varied from 1 to 6, the friction factor only changed by 5.2%. Therefore, they recommended using equation (4.15), which is be done in this work.

4.6.3 Modified Colburn j-factor

First, the heat capacity rate of the fluid $C = \dot{m}c_p$ is calculated. The effectiveness is then obtained by dividing the heat transfer rate Q by the maximum possible heat transfer rate $Q_{max} = C(T_{max} - T_{min})$. Using equation (2.55) for the

effectiveness-NTU relation, the number of transfer units NTU is found. Multiplying the NTU with the heat capacity rate results in the thermal conductance UA_s. Since the total surface area is known geometrically, the thermal transmittance U is then known.
Neglecting the thermal resistance due to conduction through the tube walls, the thermal transmittance is equal to the product of the surface efficiency η_o and the overall heat transfer coefficient h.

$$U = \eta_o h \tag{4.16}$$

It is important to note that from the energy balance alone, it is not possible to determine the heat transfer coefficient separately from the surface efficiency. Therefore, the modified Colburn j-factor is used, which is equal to the product of the regular Colburn j-factor and the surface efficiency (2.17).

4.7 Grid discretisation error

4.7.1 Introduction

When CFD calculations are done, there are many possible reasons why the result does not correspond to reality. First and foremost, the correct models must be used. Physically unsteady flow must be modelled using unsteady equations, or an appropriate turbulence model can be applied to simplify the calculations. Furthermore, correct material models for physical properties such as density, viscosity and conductivity are necessary. Finally, the correct boundary conditions must be applied to the computational domain so that the situation is similar to the real-world case. Reasonable approximations were used for the physical properties and the boundary conditions were applied sufficiently far from the region of interest to assume that the error caused by them is negligible. In this work, the physically unsteady flow was solved using a steady-state model, which is a modelling error. The impact was analysed in paragraph 4.5.3.2.

The second possible source of errors is caused by the iterative algorithm used to solve the equations. In general, it is only in the limit that the actual solution is obtained if the iterative algorithm converges. When the algorithm is ended prematurely or the algorithm stalls or diverges, the solution to the equations is not found. The impact of this error can be estimated by observing quantities of interest as a function of the iterations, checking whether the residuals are sufficiently low and verifying the global balances of energy, momentum and mass. In paragraph 4.6.1, it was shown that this error is small.

In computational fluid dynamics, the Navier-Stokes equations are solved for complicated geometries. As opposed to the relatively simple cases of laminar flow over a plate and in a circular tube, it is not possible in general to solve the equations analytically. Therefore, the equations are solved by discretising the continuous equations and solving them numerically. The space is divided into computational cells, which form the computational grid. The result is a discrete set of equations which form an approximation to the original Navier-Stokes equations. However, it still remains to be verified that the discrete problem is a sufficiently close approximation to the original problem. The third and final possibility of errors is therefore due to the influence of the computational grid used to discretise the flow domain. Quantities of interest derived from the discrete solution to the original problem are a function of the computational grid used to calculate them. The error caused by the discrete approximation of a grid with a finite number of cells can be estimated using the grid convergence index (GCI) proposed by Roache [54].

4.7.2 Roache's GCI

If grids of a geometrically similar shape are compared, any quantity of interest which follows from the simulation is a function of the grid spacing, indicated by h. A Taylor series expansion around the theoretical solution with an infinitely small grid spacing ($h = 0$) can be performed.

$$f(h) = f(0) + \left.\frac{\partial f}{\partial h}\right|_{h=0} h + \frac{1}{2!}\left.\frac{\partial^2 f}{\partial h^2}\right|_{h=0} h^2 + O(h^3) \tag{4.17}$$

If the discretisation of the continuous equations is done by means of a p^{th}-order accurate discretisation scheme, local quantities of the discrete solution theoretically converge with the p^{th}-order of the grid spacing. It is now assumed that global quantities converge at the same rate and that the grid spacing is sufficiently small so that the higher-order terms $O(h^{p+1})$ can be neglected. These are strong assumptions, which will be compensated for by using a safety factor.

$$f(h) \approx f(0) + \frac{1}{p!}\left.\frac{\partial^p f}{\partial h^p}\right|_{h=0} h^{p+1} \tag{4.18}$$

This forms an equation with two unknowns, namely the theoretical value at zero grid spacing and the value of the second derivative at zero grid spacing. By performing a calculation on two separate grids with different grid spacings, these coefficients can be determined and an estimate for the grid discretisation error can be made. If a third calculation is used, the actual order of convergence p can also be determined. Due to local grid deformations, local error propagation throughout the computational domain or the higher order terms which are not negligible, the actual order of convergence can be different from the theoretical one.

By evaluating equation (4.18) on a coarse grid with spacing rh and on a fine grid with spacing h, an error estimate on the coarse grid is obtained, given by equation (4.19).

$$E_{rh} = \frac{f(rh) - f(0)}{f(0)} \approx \frac{f(rh) - f(h)}{f(h)} \frac{r^p}{r^p - 1} \tag{4.19}$$

The estimate of the error between the coarse grid solution and the theoretical continuum solution is given by a product of two factors. The first factor is the relative error between the coarse grid and the fine grid. If both grid spacings are quite similar, this relative error will of course be very small. It is not sufficient that the relative error between the coarse grid and the fine grid be sufficiently small, as this might be caused due to an insignificant difference in the computational grids. The second factor weighs the difference between the solutions with the difference between the grids. As the difference between both grids becomes small, the impact of any small observed difference in the outcomes of both grids becomes more important.
As previously mentioned, since several strong assumptions were made, a safety factor F_s is required to obtain a reliable estimate of the error due to the discretisation on a grid with a non-zero grid spacing. This results in the grid convergence index (GCI), given by equation (4.20).

$$GCI = F_s E_{rh} \tag{4.20}$$

Roache suggests estimating the order of convergence as an extra unknown by doing calculations on a third grid, while maintaining the same grid spacing ratio. If the actual order of convergence is within 10% of the theoretical order, the safety factor is recommended to be 1.25. In other cases or in case only two calculations were used and the actual convergence order was unknown, a safety factor of 3 is recommended.

4.7.3 Results of the GCI study

In order to estimate the grid discretisation error on the j- and f-factors for the calculations used in this work, the GCI was computed for the worst case scenario. The worst case scenario consisted of a louvred fin with the highest number of louvres which would be considered in this work. Every louvre except for the entrance louvres has a corresponding leading edge where the boundary layer restarted. The boundary layer thickness was infinitesimally small close to the leading edge (equation (2.7)). Evaluating the boundary layer in this region with a finite number of cells with a finite volume introduced grid discretisation errors. This fin geometry was evaluated at the highest velocity considered in this work, i.e. 2.6 m/s, in order

to obtain the smallest boundary layers. The fin material was considered isothermal, corresponding to a fin efficiency of one. This results in the largest possible heat transfer rate and therefore a large effectiveness and a large sensitivity of the Colburn j-factor to the calculated heat transfer rate.

Calculations were done on a coarse grid of 8 million cells and a fine grid of 64 million cells and the results are given in table 4.3. The fine grid calculation required 16 hours on 18 dual-socket quad-core Intel Xeon L5420 processors with a clock speed of 2.4 GHz.

	Q (W)	Δ P (Pa)	j (-)	f (-)
Coarse grid	2.7853	109.941	0.0682	0.1191
Fine grid	2.7830	109.494	0.0672	0.1186
Relative error	0.082%	0.41%	1.39%	0.41%
GCI	0.33%	1.67%	5.55%	1.67%

Table 4.3: grid convergence index

The estimate of the grid discretisation error on the j-factor was 5.55%, on the f factor it was 1.67%. Since the error due to the steady-state approximation on the Colburn j-factor is in the same order of magnitude as the error due to the finite discretisation, the discretisation error is deemed to be acceptable. For other simulations with less louvres, fin efficiencies below unity and lower velocities, the grid discretisation errors can be assumed to be smaller than the values obtained here.

This value can now be compared with the grid discretisation errors in other studies in the recent literature. For example, in the case of the 2010 study of Zeng et al. [47] the error of 1.7% on the Nusselt number for a refinement ratio of 1.10 resulted in a grid convergence index (GCI) of 29.4% for the grid which they selected as grid independent. Compared with the recent study of Jang et al. [48] of a vortex generator fin, the number of cells in this study was 48 times larger, even though the geometry was two times smaller in every direction. As they did not report the error on the heat transfer coefficient or the error on the heat transfer rate, nor the effectiveness of the heat exchanger, it is impossible to determine the grid convergence index methodology. Nevertheless it is possible to conclude that the grid in this study was significantly finer. In the study of Huisseune et al. [4], an error of 2% was obtained for a refinement ratio of 1.48%, the corresponding GCI was 11%. The study of Herpe et al. [44] has a GCI of only 3.04%, but this was for a single tube row. The estimated grid discretisation error of 5.55% in this study compares favourably with the error which is tolerated in other recent studies.

5

Fin geometry optimisation

5.1 Introduction

In this chapter, the optimisation of heat exchangers will be discussed by combining the PEC methodology developed by Cowell with optimisation routines. It will be shown that special attention needs to be paid to the influence of the Reynolds number and the influence of the heat exchanger length. Furthermore, the Cowell methodology compares heat exchangers for a fixed mass flow rate, which is not always a relevant constraint for applications such as condensers for an air-conditioning unit. Therefore, a more general method in which the mass flow rate is also allowed to vary will be discussed. These methods will be applied to the problem of the X-shaped louvred fin to determine the performance which can be achieved using a well-designed X-shaped fin geometry. In the subsequent section, the compound combination of louvres and vortex generators will be investigated. First, the presence of interaction effects is investigated by redoing a case from literature. Next, the importance of the parametrisation of the geometry is discussed. This results in a proposal of a new fin geometry which is able to outperform the baseline X-shaped louvred fin geometry.

5.2 Comparing different fin geometries

5.2.1 Introduction

In order to optimise the fin geometry, it is necessary to quantitatively compare the heat exchanger designs which result from the choice of the fin geometry. As discussed in paragraph 2.6.3, the Cowell method is a good choice. A large number of scalar performance evaluation criteria can be derived from this method, such as the area goodness factor. As discussed in chapter 3, many authors use one of these first law criteria as the goal function of an optimisation scheme.

5.2.2 Accounting for the effect of the Reynolds number

5.2.2.1 Importance of choosing the correct Reynolds number

As discussed in paragraph 2.6.2, there are optimal values for the hydraulic diameter D_h and the contraction factor σ when the objective is to reduce the heat exchanger volume for a given fan power. Additionally, for a given heat exchanger volume and fin thickness, smaller hydraulic diameters correspond to a larger amount of fins and therefore a higher heat exchanger cost. In what follows, fin geometries will always be compared for the same D_h and σ. The performance criteria which will be considered in this work are based on the first law and can be expressed as a function of the j- and f-factors only.

The j and the f-factors are however functions of the Reynolds number. It is not a priori obvious at which Reynolds number they need to be evaluated when different designs are considered. Some authors such as Huisseune et al. [4] and Jang et al. [48] evaluate all designs at a fixed set of Reynolds numbers and discuss the merits of the fin designs as a function of the Reynolds number at which they are evaluated. Other authors such as Hsieh and Jang [35] consider a signal to noise ratio where an average of the performance over different Reynolds numbers is made. All designs are again evaluated at a fixed set of Reynolds numbers, but the optimal fin geometry is now independent of the Reynolds number.

In this work, the parameters of interest are the required heat exchanger volume and the required fan power. The PEC in this case is given by the VG-1 criterion given by equation (2.86). A Reynolds number is required to evaluate the j- and f-factors which appear in this equation. In order to understand the correct approach to determining this Reynolds number, it is helpful to consider the performance evaluation criterion graphically in a fan power-volume plane. Using data from the correlation by Wang et al. [3] to obtain the j- and f-factor data, the required heat exchanger volume given by equation (2.78) can be graphed as a function of the fan power given by equation (2.80). The result is given in figure 5.1.

The performance characteristic of the plain fin and two variations of the louvred fin are shown. Both the fan power and the volume can be interpreted as

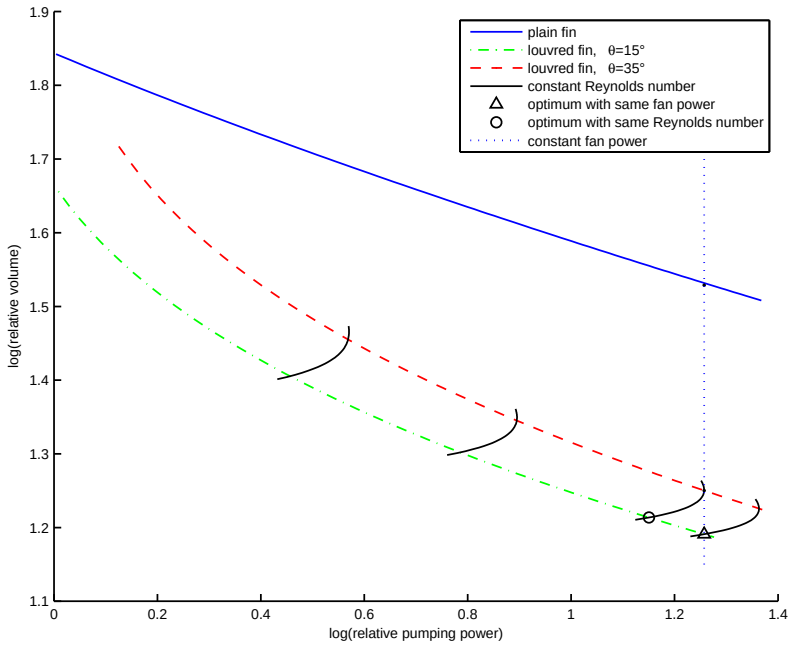

Figure 5.1: Heat exchanger performance in the power-volume plane

parametric functions of the Reynolds number. Every point on one of these curves corresponds to a certain heat exchanger design, with a single Reynolds number, volume, fan power, length and so on. The VG-1 criterion corresponds to the heat exchanger volume for a given constant fan power. This is indicated graphically by a vertical line on the power-volume plane. Only designs which lie on a vertical line can be compared using the VG-1 criterion. The equation (2.86) only represents the heat exchanger volume if designs with the same fan power are compared.

Figure 5.1 also shows curves of constant Reynolds number and varying fin geometry design. It is clear that for these curves, the fan power is not constant. Evaluating the VG-1 equation (2.86) at a fixed Reynolds number for different fin geometries hence has no physical meaning. Even if the equation would still correspond to the heat exchanger volume, optimisation of this equation gives erroneous results. To show this, the heat exchanger volume was optimised under constraint of constant fan power and under constraint of constant Reynolds number. The heat exchanger volumes required by both designs are different. The design with a louvre angle of $15°$ is optimal in both cases. However, this is because there is no trade-off between the heat exchanger volume and the required fan power. Decreasing the louvre angle while keeping the Reynolds number constant results in an improvement in both the volume and the fan power. This is not generally true and in cases where a trade-off exists, the optimal design will be different in both

cases. The curves for a fixed Reynolds number show that every design needs to be evaluated at a different Reynolds number in order to achieve the same fan power.

For the reference indicated by the dot on the plain fin curve on the figure, the Reynolds number is 307.2. If the VG-1 criterion is evaluated at this Reynolds number for the louvred fin with a louvre angle of 15° and of 35°, the VG-1 ratio of these designs is 0.8125. Using the performance curves and evaluating both curves at the same fan power as that of the reference results in a value of 0.8712. Not taking the Reynolds number effect into account predicts an improvement of 18.75% in heat exchanger volume for this variation in louvre angles, whereas the actual improvement is only 12.88%. A difference of nearly 6 percentage points on an improvement of only 12.88% is unacceptable. Clearly, the effect of the changing Reynolds number must be taken into account while evaluating the VG-1 criterion.

5.2.2.2 Determining the correct Reynolds number

The correct Reynolds number to be used follows from the derivation of the VG-1 criterion, as discussed in paragraph 2.6.2. Expressing that the fan power of the heat exchanger under consideration must be the same as some reference heat exchanger, as required by the definition of the criterion, immediately provides an expression for the Reynolds number given by equation (2.83).

$$Re_{Dh} = \sqrt{\frac{f_{ref}}{f}\frac{j^*}{j^*_{ref}}}\frac{D_h}{D_{h,ref}} \qquad \text{(2.83 revisited)}$$

It is this Reynolds number that is then substituted into the expression for relative volume in order to obtain the VG-1 criterion. The Reynolds number no longer appears explicitly in the expression, but since the j- and f-factors are functions of the Reynolds number, the VG-1 criterion does in fact depend on the Reynolds number. Furthermore, it is only valid for one specific Reynolds number, namely the one given by equation (2.83). This single Reynolds number depends on the j- and f-factors of fin geometry under consideration. Since the Reynolds number at which the VG-1 criterion must be evaluated depends on the fin geometry, it is incorrect to compare different fin geometries while evaluating the VG-1 criterion for a single fixed Reynolds number.

The Reynolds number must be determined from equation (2.83) for each fin geometry under consideration. Unless the dependence of the j- and f-factors on the Reynolds number is known analytically, an iterative procedure is needed to solve the equation. It is interesting to note that for laminar thermally and hydraulically fully developed flow in a channel, the ratio of j and f is independent of the Reynolds number, as discussed in paragraph 2.3.4.3. In this case, it is very simple to solve equation (2.83), as the right-hand side is independent of the Reynolds

number. However, the ratio of j and f still depends on the specific shape of the channel geometry. Therefore, even in this simple case, the correct Reynolds number is a function of the channel geometry. With the exception of the area goodness performance criterion which is only a function of the ratio of j and f, it is still necessary to use the correct Reynolds number in the evaluation of any PEC. Additionally, the flow in a compact interrupted fin and tube heat exchanger is not fully developed laminar channel flow. Wake zones are present behind tubes and other flow obstructions and boundary layers periodically restart at every interruption. It comes as no surprise that for this type of flow the ratio of j and f does in fact depend on the Reynolds number, as noted by Wang et al. [24]. For the geometries of interest in this work, it is therefore necessary to solve equation (2.83) iteratively.

5.2.2.3 Optimisation method taking the Reynolds number effect into account

A method to evaluate the VG-1 criterion for a certain fin geometry and a certain reference is now clear. For a given reference case with a certain fan power, volume and Reynolds number, a new fin geometry will be considered, which has a different volume (and Reynolds number), but the same fan power. Optimising the VG-1 criterion then results in the geometry which achieves a smaller volume for the same fan power. First, a reference Reynolds number, j-factor and f-factor must be chosen. Essentially, this determines the reference fan power which the design under consideration must match. The objective is now to determine the volume of the heat exchanger which satisfies the constraints established by Cowell and which requires the correct fan power. Returning to figure 5.1, this corresponds to finding the intersection of the vertical line of constant fan power through the reference heat exchanger and the performance characteristic of the fin geometry under consideration. Of course, this performance curve is not known a priori and must be found by evaluating the j- and f-factors at a certain Reynolds number and computing the corresponding performance. Every evaluation results in knowing a single point on the performance characteristic. In order to evaluate the performance, an initial guess for the Reynolds number of the new fin design must be made. If the j- and f-factors of the reference are determined for a realistic heat fin geometry at the reference Reynolds number, the reference Reynolds number is a good choice. Evaluating the j- and f-factors at this Reynolds number results in the relative volume and relative fan power for the reference Reynolds number. In general, this fan power will not equal the reference fan power. Graphically, this means that the point of the performance characteristic which is found does not lie on the vertical line through the reference heat exchanger. New guesses for the Reynolds number can then be made until the fan power matches that of the reference heat exchanger. Many algorithms exist to efficiently determine these new guesses, such as a trust-region dogleg gradient-based method. Once the Reynolds number is converged,

the VG-1 can be evaluated.

The described method requires a fin geometry and a reference as input and gives the performance of the fin geometry as output. As such, it can be used as goal function for an optimisation method which optimises the fin geometry for a fixed reference. This provides a single point on the optimal performance characteristic in the power-volume plane. Graphically depicted in figure 5.1, this corresponds to finding the point in the design space which achieves the lowest volume, while still being on the vertical line constraining the fan power. In order to find the complete optimal performance characteristic, the optimisation must be performed for different references. This can be done very straightforwardly, by just repeating the described method for a range of references.

However, as the geometry converges to the optimal geometry, the new geometry will be very close to a previously calculated geometry. Intuitively it can be understood that the Reynolds number of this new very similar geometry will be very close to the Reynolds number of the previous geometry. Therefore, it makes little sense to use the reference Reynolds number as an initial guess. The Reynolds number of the previous geometry will be a much better guess if the geometries are similar enough. Additionally, if a certain region in the design space offers optimal performance for a certain reference, then for a slightly different reference, it can be expected that the optimal designs will probably be near the optimal designs for the previous reference in the design space. As an initial guess for the fin geometry to be considered for the optimisation of the new reference, the optimum of the previous reference is a good choice.

This shows that there is a clear need to exchange information between the different loops. The inner loop which determines the Reynolds number clearly benefits from information obtained from previous iterations of the outer optimisation loop. The optimisation loop benefits from information obtained for previous reference Reynolds numbers. This indicates that it is a good idea to use a surrogate model to reduce the number of evaluations of the j and the f-factors, which are quite expensive if they are obtained using CFD computations. Every time values of j and f are necessary in the previously described method, they are calculated from a surrogate model instead of from a CFD calculation. The kriging surrogate model offers an estimate of the error on the prediction of j and f, so additional CFD computations can be performed if this error is larger than a certain threshold. Other surrogate models can be used, the only requirement is some sort of criterion which determines whether the j- and f-factors returned by the surrogate can be trusted or whether an additional CFD calculation is required. The final method for a single reference is shown schematically in figure 5.2.

This method is then repeated for different reference Reynolds numbers in order to obtain the part of the optimal geometry performance characteristic which is of interest. The same surrogate model is used for all calculations.

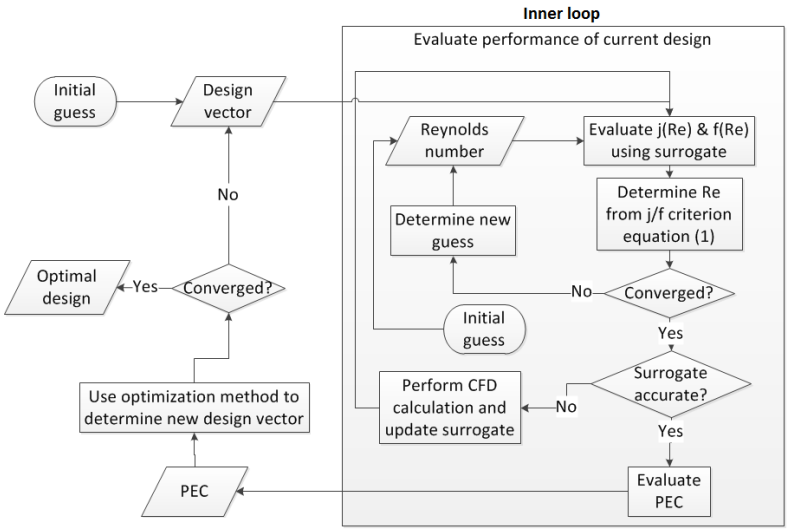

Figure 5.2: Schematic representation of the optimisation method.

5.2.2.4 Application of the optimisation method to the X-shaped louvred fin

As an example, the method described in paragraph 5.2.2.3 is applied to the problem of the X-shaped louvred fin. A simplified geometry neglecting the thickness of the fins for the flow domain is used. The fin temperatures are determined from a two-dimensional conduction problem. As geometrical parameters, the louvre angle, the total louvred length and the number of louvres are chosen. The number of louvres is a discrete parameter, but it is treated as if it were continuous. Every evaluation of a non-integer number of louvres is rounded to the nearest integer. In this way, continuous surrogate models can be used. For the surrogate model, an ordinary kriging surrogate model with exponential variogram is chosen. The models are used to predict the modified j-factor and the f-factor. An initial sampling plan of 32 calculations is determined using the Latin hypercube method. The references are determined from the Wang correlation of the plain fin, with the tube and fin pitches equal to the louvred fin geometry. The reference Reynolds numbers are calculated from an imposed reference velocity range from 0.5 to 2.6 m/s. The optimisation method is a trust-region gradient-based method, searching for a local optimum of the VG-1 criterion in the design space for every reference.

Figure 5.3 shows the power-volume plane after 85 calculations (including the initial sampling plan, indicated with hollow circles). The reference fin geometry performance is indicated by the black line, the dots indicate the 10 reference Reynolds numbers. The curves indicate predictions by the surrogate model. Two louvred fin design performance curves are shown, corresponding to the maximum

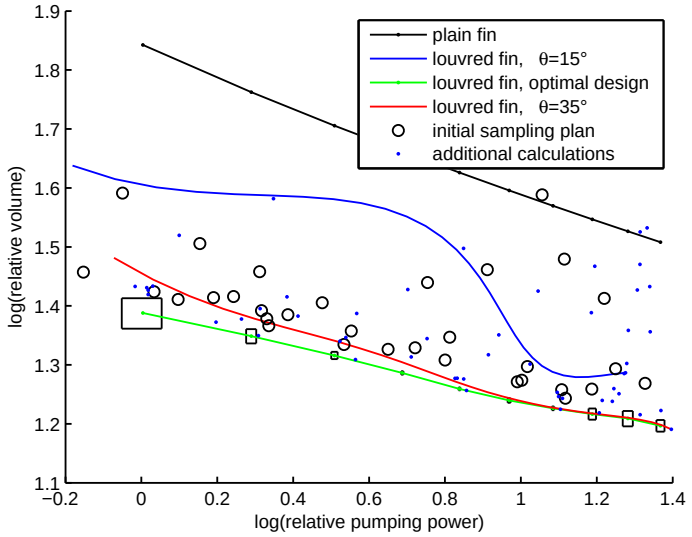

Figure 5.3: The power-volume plane after 85 calculations. Curves show surrogate model predictions

number of louvres and the maximum louvred length. The red curve corresponds to a louvre angle of $35°$, the blue curve to a louvre angle of $15°$. The lower louvre angle curve is clearly unrealistic, showing unphysical oscillations of the performance. This is caused by a lack of data, the optimisation method has not visited this region of the design space. The gradient-based method has identified that a lower louvre angle results in reduced heat exchanger performance and therefore does not request calculations for lower louvre angles. The current estimate of the optimal fin geometry provided by the surrogate model is given by the green curve, the estimated uncertainty for each reference is indicated with black rectangles. This uncertainty is purely an estimate of the accuracy of the surrogate model with respect to the mathematical heat exchanger problem. Deviations between this mathematical model and the physical reality (due to e.g. discretisation error) are not included. It is clear that most additional calculations (indicated by the dots) are concentrated near the estimate of the optimal geometry. Only for the largest fan powers is there a larger spread on the performance of the evaluated designs. This is the result of bad predictions by the surrogate model. At the time of the calculation there was a large discrepancy between the predicted location in the power-volume and the actual location obtained after the calculation.

After 101 calculations, the situation has evolved to the one shown in figure 5.4. The unphysical oscillation of the louvre angle equal to $15°$ design persists, indi-

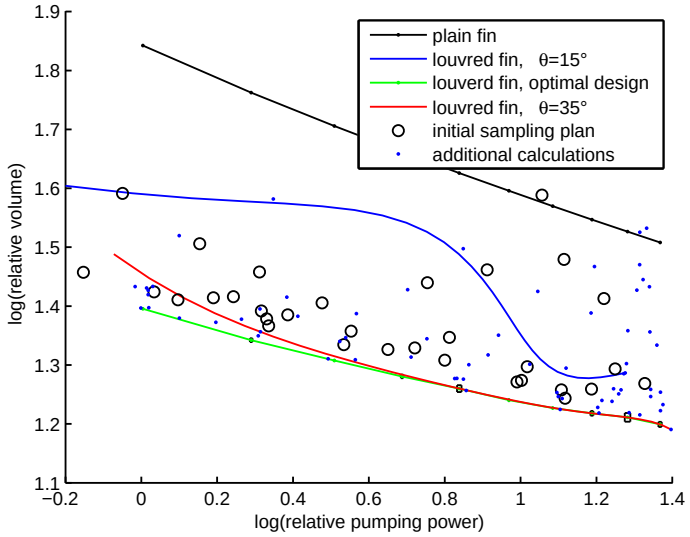

Figure 5.4: The power-volume plane after 101 calculations

cating that no new calculations similar to this design have been done. In contrast, the uncertainty on the optimal design is much reduced. After 101 calculations, the uncertainty on the predictions of the j- and f-factors are lower than 2.5% for all optimal designs.

It is clear that the optimal geometry characteristics coincide with the characteristic for the 35° case for the louvre angle. Only for the lowest fan powers, it appears to be possible to improve on the performance by considering a different design. To evaluate which design this is, the results must be considered in the design space, shown in figure 5.5. All quantities which appear are normalised so that 0 corresponds to the minimum and 1 to the maximum of the design space. The optimal geometries are sorted according to the corresponding reference velocity.

Starting from the reference velocity of 44% (1.4 m/s), the optimal fin geometry is fixed and equal to that of the case with a louvre angle of 35° and the louvred length and the number of louvres are equal to the maximum allowed values. Only for the lower reference velocities, the optimal louvre angle is slightly smaller. For all reference velocities the louvred length and the number of louvres are as large as possible. Clearly as much of the fin surface as possible needs to be covered with louvres, and preferably with a low louvre pitch so that many louvres can be used. Note that this corresponds to a louvre pitch which is neither the minimum, nor the maximum. An apparent optimal louvre pitch is found, namely the ratio of the maximum louvred length limit and the maximum number of louvres. The value of

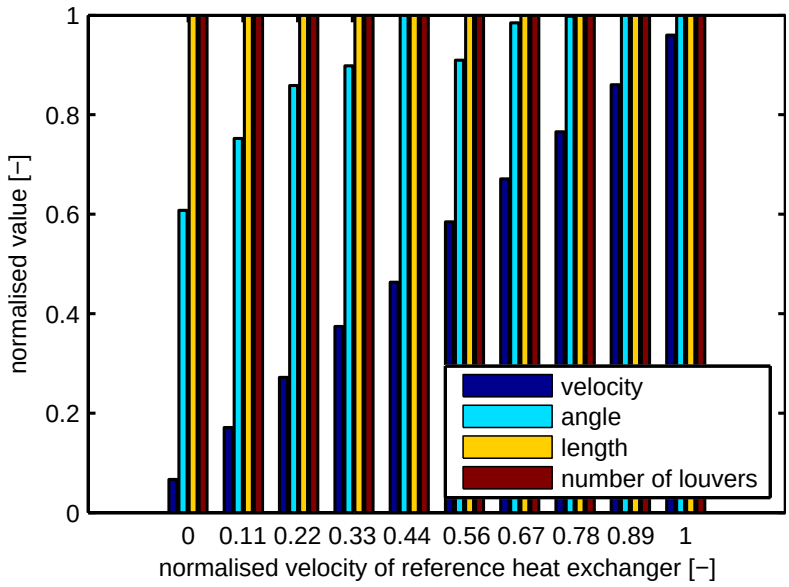

Figure 5.5: Optimal heat exchangers in design space. All quantities are normalised

this optimal louvre pitch is nothing more than an artifact of the limits imposed on the louvred length and the number of louvres. The fin efficiency will be low due to the many surface interruptions near the tubes, but the increase in the heat transfer coefficient compensates for this effect.

Furthermore, it is interesting to note that for the lowest reference velocity, the velocity of the optimal heat exchanger is larger than that of the reference (0.05 instead of 0). On the other hand, for the largest reference velocity, the velocity of the optimal heat exchanger is slightly smaller than that of the reference heat exchanger. This clearly illustrates the dependence of the Reynolds number (proportional to the velocity since the hydraulic diameter is constant) on the fin geometry. As long as the effect of the changing Reynolds number is properly accounted for, optimisation with respect to the VG-1 criterion allows determining the optimal geometry performance characteristic. If the fan power and the volume are considered as separate objectives, the optimal geometry performance characteristic is equal to the Pareto front.

5.2.2.5 Alternative multi-objective approach

The downside of the method described in paragraph 5.2.2.3 is that a gradient-based optimisation method is used. Gradient based methods find a local optimum, which can be different from the global optimum. As discussed in paragraph 2.7.5.2,

efficient global optimisation methods such as EGO exist, but they require an estimate of surrogate model uncertainty. Determining the uncertainty on the VG-1 due to the surrogate model estimate is, however, not straightforward. The j- and f-functions are uncertain, and require the input of a Reynolds number which is also uncertain. The combined resulting uncertainty is difficult to determine.

If several reference Reynolds numbers are used, the final result of the VG-1 method is a part of the Pareto front. Therefore, if the goal is to find the VG-1 optimum for a large number of reference heat exchangers, it is also possible to approach this problem from a multi-objective point of view. This has the advantage that convergence to the global optimum can be guaranteed (in the limit of an infinite number of calculations). The downside of this approach is that there is no longer a clear optimisation towards a single performance criterion, as there are now multiple competing objectives, namely the fan power and the volume. The evaluation of the performance criterion for a given reference Reynolds number has to occur as a post-processing step based on these objectives. Furthermore, the entire Pareto front corresponding to the design space has to be explored, which requires significantly more computational effort than determining one point on the Pareto front, corresponding to a fixed reference heat exchanger design. By approaching the problem in a multi-objective way, the constraint to the fan power is no longer necessary as it becomes the second objective. This eliminates the need for propagating the uncertainty of the Reynolds number through the uncertain j- and f-functions. The uncertainty on the objectives can be calculated, and methods like EGO can be used to perform the global multi-objective optimisation.

As an example, the same problem as in paragraph 5.2.2.4 is optimised using the EGO method. The fin thickness is no longer neglected for the flow domain. The objective function for the multi-objective optimisation algorithm is the expected improvement. The improvement function in the power-volume plane is defined as the distance between a test point in the power-volume plane and the closest point in the data set if it is not dominated by any point in the data set. If the test point is dominated, the distance is set to zero. Two kriging surrogate models are used, one for the modified j-factor and one for the friction factor. The output of each of these models is a univariate Gaussian distribution. This is converted into a multivariate Gaussian distribution by noting that both kriging models are independent. Based on the uncertainties on j and f, the uncertainties on the fan power and the volume can be obtained. This allows calculating the expected value of the improvement by integrating the product of the probability distribution function and the improvement function over the entire power volume plane. This is done numerically by using Gauss-Hermite quadrature on a two-dimensional tensor grid. As a result, the expected improvement function is known for the entire design space and it is optimised using a genetic algorithm. Every optimum is calculated and added to the data set, after which the kriging models are updated. The initial sampling plan is

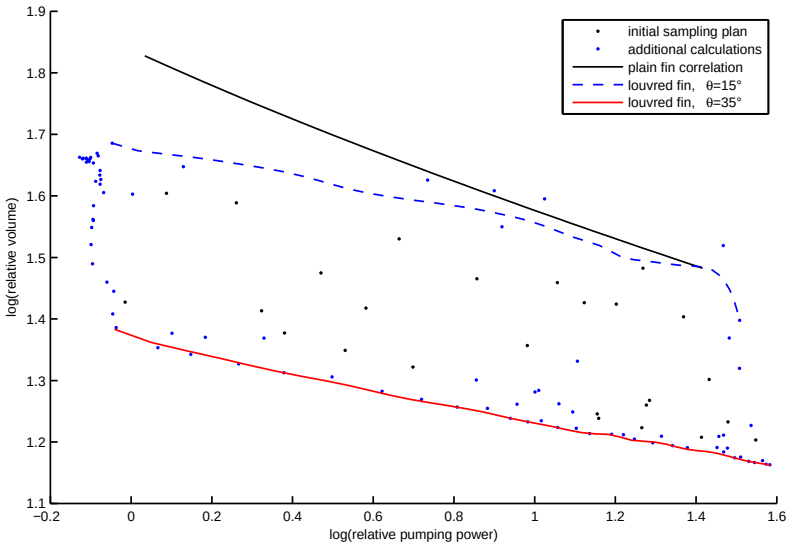

Figure 5.6: Multi-objective optimisation of the X-shaped louvred fin geometry, result after 111 calculations

the same as for the previous optimisation, except for four designs which could not meshed using geometry of finite thickness. A total of 111 heat exchanger designs are evaluated. Figure 5.6 shows the result.

The plain fin heat exchanger performance characteristic is just shown for reference purposes, it is not actually used in the method. The most obvious difference with respect to the result of the VG-1-based optimisation is that a significant number of calculations are clustered in the region of low fan power and a variety of heat exchanger volumes. This section of the Pareto front was not found using the previous method. It corresponds to low heat exchanger velocities and a variety of different geometries. It is purely an artifact of the arbitrary limitation of the velocity in the design space. If the lowest velocity would be higher, a similar near-vertical section of the Pareto front would be found for higher fan powers. Aside from being an artifact of the limits of the design space, it is also a thoroughly uninteresting region in the design space, since very large increases in heat exchanger volume are necessary for marginal decreases in the fan power.

The contour curves of maximum louvred length and maximum number of subdivisions are shown for two louvre angles, they are derived from the surrogate models. The maximum louvre angle contour matches the Pareto front quite nicely, except for very low fan power. This is the same result as was obtained for the zero thickness model used in the VG-1 based optimisation of paragraph 5.2.2.3. The simple zero thickness model gives the same qualitative result. Only for the low velocities, the zero thickness model incorrectly predicts a better performance for

a lower louvre angle. The contour curve of the low louvre angle again exhibits unphysical oscillations, which are due to a lack of data. Generally, the multi-objective optimisation results in a better concentration of the calculations near the Pareto front. The downside is that the entire Pareto front is explored, including the artifact caused by the lower velocity limit. The VG-1-based optimisation method allows finding a new and better heat exchanger with respect to a single reference heat exchanger and has the advantage that no artifacts occur due to limits on the allowed frontal velocities.

A considerable improvement can be made to the multi-objective method by removing all heat exchanger designs with a fan power below that of a reference heat exchanger. The reference fan power must be chosen sufficiently high so that the set of heat exchangers corresponding to the lowest velocity and varying fin geometries all have a lower fan power and are therefore eliminated. Since the performance of this set is not a priori known, accurately determining this minimum fan power is not possible. The fan power required by the plain fin operating at the minimum allowed frontal velocity is a good approximation. This limits the lowest fan power of the Pareto front to the value which can be obtained using the VG-1-based method. The removal of these designs can easily be implemented by setting the improvement function to zero for test points in the power-volume plane which predict a fan power that is lower than the limit. This removes the incentive of the method to exploit the uninteresting region of the Pareto front.

A second improvement is to train surrogate models for the UA and the $F1$ parameter introduced in equation 5.1 instead of directly for the j- and f-factors. If the hydraulic diameter, contraction ratio and the heat transfer area are held constant, the thermal conductance UA is proportional to the product of the j factor and the Reynolds number. Since the j-factor and the f-factor exhibit similar behaviour as a function of the Reynolds number, the $F1$ parameter is defined in order to get a similar behaviour as the thermal conductance as a function of the Reynolds number. For fully developed laminar flow in a cylindrical channel, both the conductance and the $F1$ parameter would be constants [8].

$$F1 = fRe_{Dh} \tag{5.1}$$

In order to reuse the CFD calculation data, surrogate models are trained on the entire CFD data set of 111 calculations. The optimisation method is then repeated including both improvements, but whenever CFD data is requested, it is entered from the separate surrogate models trained on the entire data set. Additional CFD calculations are of little value, since the actual optimum has already been found using the VG-1 method. The result of the improved multi-objective method after 111 calculations is shown in figure 5.7.

It is clear that very little calculations have been done with a fan power smaller than that of the lowest value of the reference plain fin. The few calculations which

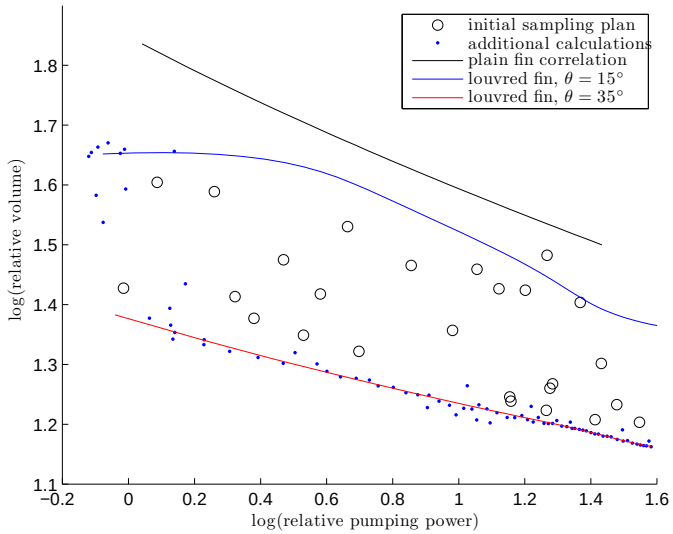

Figure 5.7: Improved multi-objective optimisation of the X-shaped louvred fin geometry, result after 111 calculations

have been done in this region are caused by high uncertainty on the surrogate models. Secondly, the clustering of the calculations near the Pareto front is much better than in the case of the unimproved method shown in figure 5.6. This is caused by the use of surrogate models for UA and $F1$ instead of for j and f. This results in much more reliable predictions of the fin geometry performance. The spacing of the calculations on the Pareto front is nicely spread out, the apparent clustering for higher fan powers is caused by the logarithmic scale for the axes. A cluster of calculations, which seems to perform better than the optimum found using the VG-1 method, appears for larger fan powers. This region is not physical, it is caused by the surrogate models which are used to provide the data instead of the CFD calculations. This shows that there can be a difference between the optimum of the surrogate and the optimum of the physical problem. In order to keep this from happening, the surrogate needs to be updated with actual simulations.

5.2.3 Accounting for the heat exchanger length

5.2.3.1 Behaviour of the heat exchanger length in the Cowell method

An essential assumption in the method of Cowell discussed in paragraph 2.6.2 is that the length varies continuously, without changing the Colburn j- and the f-factors. In practice, there are two ways of changing the heat exchanger length for

a constant hydraulic diameter: either by varying the longitudinal tube pitch, or by varying the number of tube rows. Changing the longitudinal tube pitch changes the heat exchanger geometry and therefore the surface efficiency, the Colburn j and the friction factor. Changing the heat exchanger length for constant j- and f-factors is not possible by changing the longitudinal tube pitch. For fully developed flow, the j- and f-factors are independent of the number of tube rows N. However, in practice this is a discrete parameter. For air-conditioning and heat pump applications, the refrigerant circuit must also be taken into account in determining the number of tube rows and the tube pitches. It is clear that a comparison between fin surfaces for a constant length has significant practical importance. However, using the methodology of Cowell, this is not possible without varying the hydraulic diameter or the contraction ratio. The performance criteria derived from the Cowell methodology are only functions of the geometry and therefore only have one degree of freedom. Imposing an additional constraint removes this single degree of freedom.

In what follows, the effect of the changing heat exchanger length on the j- and f-factors will be taken into account. The required length for a given fin geometry is obtained from the Cowell methodology by dividing the volume by the frontal area as given by equation (2.81).

$$L = \frac{\mathbf{D_h}}{\mathbf{j}^*} \frac{NTUPr^{\frac{2}{3}}}{4} \qquad \text{(2.81 revisited)}$$

By introducing specific values for all the quantities required in equation (2.81) such as the Reynolds number and the NTU, a specific length is obtained. This length is a single global reference value, it is fully determined by the requirements which all heat exchangers under consideration must satisfy. By introducing the global reference length into equation (2.81) and imposing that the hydraulic diameters of all fin geometries under consideration must be equal, the length of any heat exchanger can be expressed as in equation (5.2). The heat exchanger length is inversely proportional to the modified Colburn j-factor, if the hydraulic diameter is held constant. As the fin geometry and the Reynolds number change during the optimisation, so does the j-factor and therefore the required heat exchanger length.

$$L = \frac{j^*_{ref}}{j^*} L_{ref} \qquad (5.2)$$

The heat exchanger length is also uniquely defined by the geometry. It is equal to the product of the longitudinal tube pitch and the number of tube rows, as expressed by equation 5.3. For the global reference heat exchanger, this requirement is satisfied. The required length to achieve the same heat transfer rate, mass flow rate, temperatures and hydraulic diameter as a given heat exchanger is the geometrical length of that heat exchanger.

$$L = \frac{j_{ref}}{j} L_{ref} = N P_l \tag{5.3}$$

It is clear that the number of tube rows and the longitudinal tube pitch cannot both be independent parameters. This is exactly the same as for the Reynolds number, which is also a dependent variable, as discussed in paragraph 5.2.2.2. Three important issues can be identified.

First of all, in the previously considered cases, the reference quantities could always be eliminated by studying relative values. However in this case, the length of the global reference heat exchanger L_{ref} appears explicitly, which is a dimensional quantity. The j- and f-factors of any heat exchanger under consideration (and thus its performance) also depend on this dimensional length of the reference heat exchanger. However, this is also physically the case. As revealed by e.g. Chu et al. [45], the j- and f-factors of compact heat exchangers do in fact depend on the number of tube rows. It should therefore not be surprising that the optimal fin geometry is influenced by the length of the reference heat exchanger.

Secondly, equation (5.3) gives a single constraint for two variables. For each discrete value of the number of tube rows, there is a corresponding longitudinal tube pitch which satisfies the equation. An additional criterion is required to obtain a single solution. This also depends on the global reference heat exchanger. Consider a small modification to the fin geometry of the global reference heat exchanger, resulting in a change to the required heat exchanger length. In a first-order approximation, this change can be expressed as a function of the change in the longitudinal tube pitch and in the number of tube rows, as given by equation (5.4).

$$\frac{L_{ref} + \Delta L}{L_{ref}} = 1 + \frac{N_{ref} \Delta P_l + \Delta N P_{l,ref}}{N_{ref} P_{l,ref}} = 1 + \frac{\Delta P_l}{P_{l,ref}} + \frac{\Delta N}{N_{ref}} \tag{5.4}$$

A given relative change in the heat exchanger length can therefore always be accomplished by the same relative change in the longitudinal tube pitch. Since the smallest change in the number of tube rows ΔN is one, the number of tube rows N_{ref} must be sufficiently large if a change in number of tube rows is to result in a sufficiently small change in the required heat exchanger length. For air-conditioning applications with only two or three tube rows, changing the number of tube rows immediately has a very large impact on the heat exchanger length. Changing the tube pitch is unavoidable in order to satisfy the constraint.

Finally, the results depend on how other parameters are scaled with the longitudinal tube pitch. For example, for a louvred fin heat exchanger, increasing the longitudinal tube pitch results in more space for louvres. This space could be filled by a plain finned surface if the number of louvres and the louvre pitch are kept constant, or the louvre pitch could be scaled with the tube pitch, or more louvres of

the original louvre pitch could be introduced. Each strategy results in a different behaviour of the j- and f-factors as a function of the longitudinal tube pitch. This strategy will impact the optimal fin geometry. This is also to be expected. If a new optimal fin geometry is said to reduce the required volume by reducing the heat exchanger length, it must be specified how this length reduction will be achieved.

5.2.3.2 Accounting for the effect of the length on heat exchanger performance criteria

From the previous discussion, it is clear that for heat exchangers with a limited number of tube rows, the longitudinal tube pitch is a variable which depends on the chosen fin geometry. Performing heat exchanger optimisation or comparisons while keeping the longitudinal tube pitch constant is not physically sound. Instead, the constraints on the Reynolds number (2.83) and on the heat exchanger length (5.3) must be taken into account.

Since the length constraint only gives a single equation for two variables, an additional rule is required to select the longitudinal tube pitch and the number of tube rows for a given length. Several options are available to determine N and P_l for a given length:

- Keep the number of tube rows fixed and vary the longitudinal tube pitch.
- Minimise or maximise the longitudinal tube pitch between two acceptable limits while varying the number of tube rows in discrete steps.
- Select the number of tube rows and longitudinal tube pitch such that the heat exchanger performance is optimal while still meeting the length constraint.

By considering the Reynolds number, the number of tube rows and the longitudinal tube pitch as dependent variables, an algorithm can be devised to determine the performance of a fin geometry while also meeting every constraint. This algorithm is given in figure 5.8. Note that it is very similar to the inner loop of the algorithm to optimise taking the Reynolds number effect into account. This performance evaluation algorithm can likewise be extended to an optimisation algorithm.

5.2.3.3 Application to the performance evaluation of the X-shaped louvred fin

Problem statement

This new algorithm is now applied to the same problem as in paragraph 5.2.2.4. The design vector consists of only the louvre angle. The longitudinal tube pitch is allowed to vary from 11.9 mm to 18.7 mm. The louvre pitch and number of louvres remain constant when the longitudinal tube pitch is changed and the louvres stay

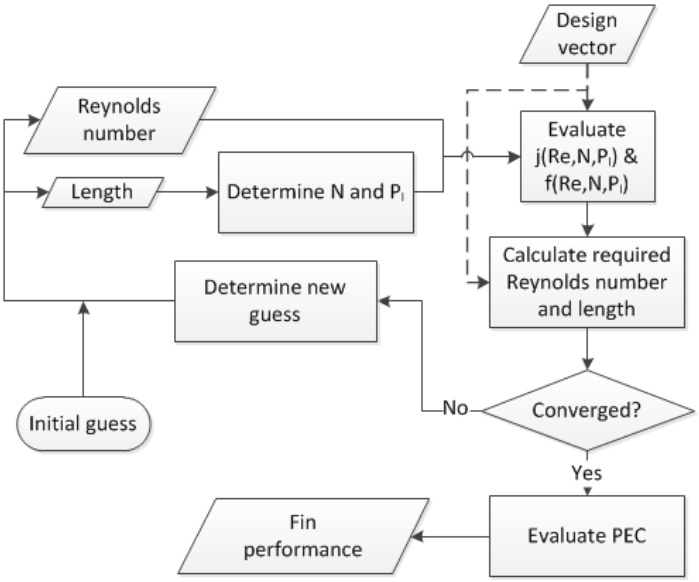

Figure 5.8: Schematic representation of a performance evaluation method which takes length effects into account

grouped around the tubes. The lower limit is the smallest tube pitch for which the louvres still fit on the fin. There is no structural upper limit on the tube pitch. However, for a given louvre area and a large longitudinal tube pitch, significant areas of the fin are just plain flat fin surfaces and the design becomes "unreasonable". In this case it would be more sensible to increase the number of louvres or the louvre pitch. Therefore, an arbitrary limit of 18.7 mm is imposed, which is 37.5% larger than the default of 13.6 mm. For the simulations, the number of tube rows is held constant. However, it is interesting to consider the effect of the number of tube rows on the required longitudinal tube pitch as indicated by equation (5.4). This requires evaluating heat exchanger designs with a changing number of tube rows. In order to lower the computational effort, it is assumed that there is no influence of the number of tube rows on the Colburn j- and f-factors. This simplification also allows investigating the effect of the longitudinal tube pitch without confounding it with effects due to the number of tube rows.

A Kriging surrogate model is constructed based on a full factorial sampling plan. Three levels for the velocity and the longitudinal tube pitch and two levels for the louvre angle are used. The resulting behaviour for a louvre angle of 35° is given in figure 5.9. Since there is a small dependence of the hydraulic diameter on the longitudinal tube pitch, the collar diameter is used for the characteristic length scale in the figure.

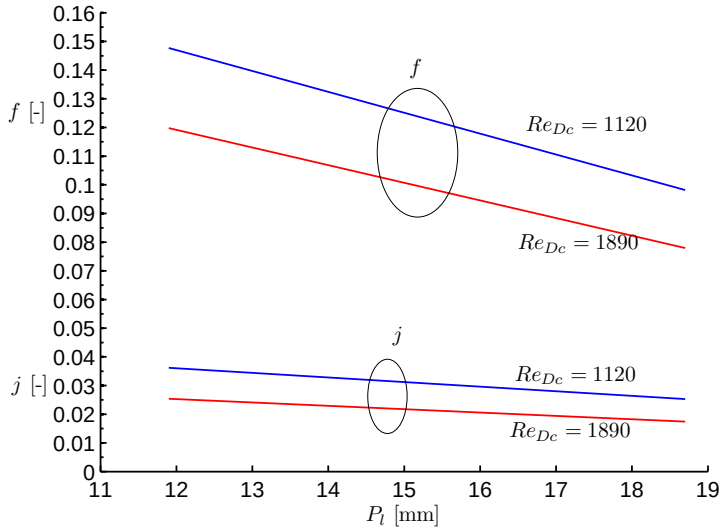

Figure 5.9: j and f factors for a louvre angle of 35° as a function of the Reynolds number and the longitudinal tube pitch

Both the friction factor and the modified j-factor decrease as a function of the Reynolds number and as a function of the longitudinal tube pitch. Hsieh and Jang [35] also saw a decrease of the friction factor with increasing tube pitch. However, in contrast to figure 5.9, they found an increase of the j-factor for their simulations of isothermal fins. This can be explained by noting that in this work, the fin efficiency effects are taken into account and that the fin efficiency decreases with increasing tube pitch. Furthermore, for constant louvre parameters and in the limiting case of very large tube pitches, the louvred fin starts to behave like a plain fin. Since the j-factor of the plain fin is lower than that of the louvred fin for the same Reynolds number, a region in which the j-factor decreases with increasing tube pitch must exist. In this region, the modified Colburn j-factor definitely decreases with increasing longitudinal tube pitch. Zeng et al. [47] considered a fin surface with mounted vortex generators and observed a decrease of the Nusselt number (based on a constant collar diameter) with increasing longitudinal tube pitch, which is in agreement with the findings here.

Additional constraints

In order to investigate the effect of the longitudinal tube pitch on the heat exchanger performance, a choice for the global reference heat exchanger is needed

due to the dimensional nature of the heat exchanger length. The extent to which the longitudinal tube pitch varies as the fin geometry is changed depends on the number of tube rows of the reference heat exchanger. In this section, the global reference heat exchanger is a heat exchanger with three tube rows, the default tube pitch of 13.6 mm and a louvre angle of 35° and a frontal inlet velocity of 1.45 m/s. The requirements of the mass flow rate, inlet fluid velocity and heat transfer rate are chosen such that this specific heat exchanger satisfies them. For all other heat exchangers under consideration, the same requirements must be met. For this single global reference heat exchanger, all the relative quantities of the Cowell methodology introduced in paragraph 2.6.2 are equal to one.
To determine the number of tube rows for a given required length, it is assumed that the longitudinal tube pitch must be at least 11.9 mm, which is the minimum tube pitch. The upper limit for the tube pitch is 22 mm, which is larger than the tube pitches used in the calculations, so extrapolation is used through the surrogate model. The number of tube rows is changed to meet these limits, if possible. If multiple solutions are possible, the solution with the smallest tube pitch is retained. This corresponds to the second option for determining N and P_l, where P_l is minimised while constrained between two limits. As will be shown later, this results in the best heat exchanger performance in this case. Solutions which require a tube pitch larger than the calculation limit of 18.7 mm should be regarded as very poor designs, but are still shown because in some cases no solution can be found if the tube pitch is limited to 18.7 mm.

Performance for the minimum tube pitch, neglecting length effects

The performance curves in the fan power-volume plane for different cases are shown in figure 5.10. The global reference heat exchanger is located in the origin of the plot, as it is a logarithmic scale and all other designs are expressed relative to the reference. The dashed lines show the limiting case for an infinite number of tube rows, when the heat exchanger length can be varied without changing the longitudinal tube pitch. They are shown for the minimum longitudinal tube pitch, for which the best performance is reached. The velocity along these curves varies from 0.5 m/s for the largest volume to 2.6 m/s for the smallest volume. These curves show a clear trade-off between the required volume and the required fan power for the heat exchanger.

Performance for the default tube pitch, neglecting length effects

A second set of curves in figure 5.10 is indicated by the hollow symbols. These represent the fin performance when the effect of the longitudinal tube pitch is not taken into account. The j- and f-factors are calculated using a constant default

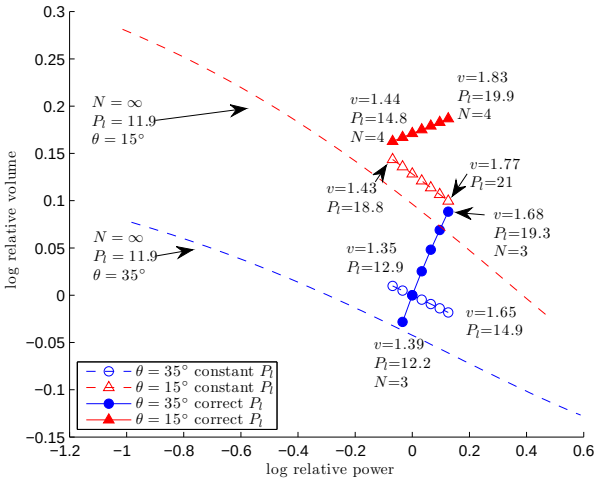

Figure 5.10: Fin performance compared with a reference heat exchanger with three tube rows. Constant P_l refers to the j- and f-factors being calculated for a constant P_l. The P_l-values indicated in the figure are the geometrically required values to satisfy the length constraint.

value of the longitudinal tube pitch. This corresponds to the case with an infinite number of tube rows and a longitudinal tube pitch equal to the default pitch. Seven baseline heat exchangers are defined, indicated by the hollow circles, for a velocity ranging from 1.35 m/s to 1.65 m/s. The baseline heat exchangers correspond to the default geometry, evaluated at several different Reynolds numbers. The method of paragraph 5.2.2.2 is then used to determine heat exchangers which satisfy the same constraints on mass flow rate, heat transfer rate and inlet fluid temperature and which require the same fan power as the baseline heat exchangers, but with a louvre angle of $15°$. These are indicated by the hollow triangles. By comparing both groups of open symbols with the dashed curves corresponding to the smaller longitudinal tube pitch, it is clear that a smaller tube pitch corresponds to better heat exchanger performance, independent of the louvre angle. For the first and the last heat exchanger in each curve, the velocity and the longitudinal tube pitch which are required to satisfy the required heat exchanger length without changing the number of tube rows are indicated. Note that the required longitudinal tube pitch is different from the tube pitch for which the j- and f-factors were obtained.

Since the hollow circles correspond to the baseline heat exchangers, the velocities here are equal to the baseline velocities. For the baseline heat exchanger which corresponds to the reference heat exchanger, the relative volume and relative fan power are equal to one and the longitudinal tube pitch is equal to that of

the reference case, i.e. 13.6 mm. For lower velocities than that of the reference heat exchanger (i.e. 1.45 m/s), the required tube pitch is smaller (12.9 mm instead of 13.6 mm) and for higher velocities the tube pitch is larger.

For the heat exchangers with a louvre angle of $15°$, which satisfy the constraints, the velocities are higher than those of the baseline heat exchangers with a louvre angle of $35°$ (1.43 m/s instead of 1.35 m/s and 1.77 m/s instead of 1.68 m/s). The longitudinal tube pitch required to meet the constraints is also significantly longer, up to 21 mm instead of the 13.6 mm for which the performance was calculated. This means that for a given fan power, the heat exchangers with the louvre angle of $15°$ are longer and operate at a higher frontal velocity than the corresponding heat exchangers with a louvre angle of $35°$. Again, the required longitudinal tube pitch increases with increasing frontal inlet velocity. However, the impact of the different longitudinal tube pitch has not been taken into account.

Taking the effect of the longitudinal tube pitch into account

By re-evaluating the j- and f-factors until the geometrical longitudinal tube pitch matches the required longitudinal tube pitch, the curves with the full symbols in figure 5.10 are obtained. For the baseline heat exchanger with the smallest velocity, no solution was found for a louvre angle of $35°$. If the number of tube rows is equal to three, the required longitudinal tube pitch is smaller than 11.9 mm, which is not possible. To overcome this problem, the number of tube rows can be decreased to two, however, then the required longitudinal tube pitch is larger than 40 mm. This is too far from the largest calculated tube pitch to trust the surrogate model. Furthermore, this is a bad fin design, where there is more surface without louvres than with louvres. It is therefore not shown in figure 5.10. For the global reference heat exchanger, the correct solution coincides with the solution with a longitudinal tube pitch equal to the default value. Indeed, the global reference heat exchanger is defined as the heat exchanger which meets all the constraints with a longitudinal tube pitch equal to that of the default case. As the fan power of the baseline heat exchanger increases (due to a higher Reynolds number), the required tube pitch is increased. Re-evaluating the fin performance at this new required tube pitch shows that the fin performs worse for this larger tube pitch, and even larger tube pitches are required. For the largest baseline velocity, the new method proposed in this work shows that the final tube pitch is 19.3 mm. This tube pitch is larger than the initial estimate of 14.9 which was obtained by neglecting the effect of the tube pitch. Neglecting the tube pitch effect predicted that the volume of the new heat exchanger would be $10^{-0.0182} = 96\%$ of the volume of the reference heat exchanger, with a fan power of $10^{0.126} = 133\%$. However, applying the method proposed in this work shows that for the same increase in fan power, there is no reduction in heat exchanger volume at all. Instead, the heat exchanger volume is $10^{0.088} = 122\%$ of the reference heat exchanger. This is because operating at a

higher velocity requires a longer heat exchanger. Since it is not possible to change the number of tube rows while maintaining a reasonable tube pitch, the tube pitch must be changed while maintaining the number of tube rows constant. The new heat exchanger hence requires a larger tube pitch. Any improvement in the heat exchanger volume by operating at a higher Reynolds number is lost because the modified Colburn j-factor is smaller at this larger longitudinal tube pitch. For the louvre angle of $15°$, the result is even more pronounced. If the number of tube rows remains constant, the longitudinal tube pitch again severely exceeds the maximum allowed tube pitch. However, it is possible to increase the number of tube rows by one and maintain a reasonable tube pitch. This new tube pitch is still larger than the default case, resulting in a worse performance than predicted while not taking the effect of the tube pitch into account. Again, the tube pitch increases with increasing baseline velocity and this effect dominates the expected improvement of the heat exchanger volume due to the increased Reynolds number.

5.2.3.4 Conclusions

For short heat exchangers with three tube rows, the qualitative behaviour of the heat exchanger performance in the power-volume plane changes fundamentally if the tube pitch effect is taken into account. Neglecting the influence of the tube pitch predicts a decrease of the heat exchanger volume as the Reynolds number increases. However, taking the tube pitch effect into account shows that the opposite is true, due to the required increase in the longitudinal tube pitch.

For the discussed case, it is better to use shorter longitudinal tube pitches and therefore shorter heat exchangers. As the required heat exchanger length is inversely proportional to the Colburn j-factor, this provides an additional incentive to use geometries with large Colburn j-factors.

The downside of the proposed method is that it is necessary to introduce a global reference heat exchanger with a dimensional length. Additionally, the results depend on how the other fin parameters are changed as the tube pitches are changed. Furthermore, it is important how the number of tube rows and the longitudinal tube pitch are changed as the required heat exchanger length changes. Neglecting the impact of the heat exchanger length corresponds to the limiting case of infinitely many tube rows.

5.2.4 Performance comparison under fixed heat exchanger length constraint

5.2.4.1 Performance evaluation criteria for fixed heat exchanger length

As discussed in the previous paragraphs, both the length and the hydraulic diameter must be chosen as small as possible. However, there are only two degrees

of freedom for a given fin geometry. It is not possible to fix both the length and the hydraulic diameter as this fully determines both the fan power and the volume. It is then impossible to match the fan power of the heat exchanger to a reference fan power. Optimisation under constraint of fixed hydraulic diameter was discussed extensively in the previous paragraphs. In this paragraph, the heat exchanger length will be fixed. This requires the hydraulic diameter to be variable in order to have the degree of freedom which is necessary to match the fan power for different fin geometries. The equality of the heat exchanger length to the reference length is expressed by equation 5.5.

$$\frac{D_h}{j^*} = \frac{D_{h,ref}}{j^*_{ref}} \tag{5.5}$$

This equation can be solved for the hydraulic diameter D_h as shown in equation (5.6).

$$D_h = D_{h,ref} \frac{j^*}{j^*_{ref}} \tag{5.6}$$

Just as the VG-1 criterion resulted in a single Reynolds number as a function of the fin geometry, now a single hydraulic diameter is obtained as a function of the fin geometry (both for a given reference). The relation for the hydraulic diameter (5.6) can now be substituted in the relations for the volume (2.78) and the fan power (2.80) and the ratio with the reference quantities can be calculated. For the relative power under constraint of fixed length, this results in equation (5.7). The relative volume under the same constraint is given by equation (5.8). This is proportional to the frontal area since the length is fixed.

$$\frac{\mathcal{P}}{\mathcal{P}_{ref}} = \frac{f}{f_{ref}} \left(\frac{j^*_{ref}}{j^*} \right)^3 \left(\frac{Re_{Dh}}{Re_{Dh,ref}} \right)^2 \tag{5.7}$$

$$\frac{V}{V_{ref}} = \frac{j^*}{j^*_{ref}} \frac{Re_{Dh,ref}}{Re_{Dh}} \frac{\sigma_{ref}}{\sigma} \tag{5.8}$$

It is now again possible to specify that the fan power must be equal to that of a reference heat exchanger. This results in an equation for the Reynolds number, given by equation (5.9)

$$Re_{Dh} = \left(\frac{j^*}{j^*_{ref}} \right)^{\frac{3}{2}} \left(\frac{f_{ref}}{f} \right)^{\frac{1}{2}} Re_{Dh,ref} \tag{5.9}$$

Substituting equation (5.9) into equation (5.8) results in the equation for the relative volume under constraint of the same fan power and the same heat exchanger length, given by equation (5.10).

$$\frac{V}{V_{ref}} = \left(\frac{j^*_{ref}}{j^*}\right)^{\frac{1}{2}} \left(\frac{f}{f_{ref}}\right)^{\frac{1}{2}} \frac{\sigma_{ref}}{\sigma} \tag{5.10}$$

Since the length is constant, the relative volume ratio is also equal to the relative frontal area ratio. Equation (5.10) is then exactly equal to the area goodness criterion given by equation (2.84).

$$\frac{A_{front}}{A_{front,ref}} = \frac{1}{\sqrt{\frac{f_{ref}}{f}\frac{j^*}{j^*_{ref}}}} \frac{\sigma_{ref}}{\sigma} \tag{2.84 revisited}$$

This is to be expected, since it is assumed that the j- and f-factors are independent of the hydraulic diameter. Since the area goodness factor which represents the relative frontal area ratio at constant fan power, is a function of these two quantities, it is also independent of the hydraulic diameter. Therefore, it does not matter whether the equation was obtained while allowing the hydraulic diameter to vary or not. However, it is important to note that the Reynolds number at which the equation needs to be evaluated is different. The exponent of the j-factor in the Reynolds number for the constant hydraulic diameter constraint is 1/2, for the constant heat exchanger length constraint, it is 3/2. Even though the equation for the relative frontal area ratio is the same, the results do in fact depend on whether the hydraulic diameter or the length of the heat exchanger is held constant.

5.2.4.2 Performance curves in the power-volume plane

There are two options to find the performance curves. The first and easiest method is to assume all geometrical parameters are scaled with the hydraulic diameter as it varies. This has the advantage that the contraction factor σ remains constant and that the j- and f-factors are independent of the hydraulic diameter. Once the pressure drop and heat transfer characteristic of a fin geometry is known as a function of the frontal velocity for a single hydraulic diameter, the performance at different hydraulic diameters can be extrapolated. However, this supposes that the tube diameters are also scaled, which is not a realistic assumption for air-conditioning applications.

The second method is to use a single geometric parameter in order to vary the hydraulic diameter, such as the fin pitch. Both the hydraulic diameter and the contraction factor now change with the geometrical parameter. This is no problem, as there are still two degrees of freedom, namely the fin pitch and the frontal velocity. The fin pitch is then fixed by calculating it from the hydraulic diameter (5.6) by using the geometrical relation between the fin pitch and the hydraulic diameter. Since the j-factor depends on the fin pitch, an iterative solution procedure is required. The same approach as for determining the Reynolds number for the VG-1

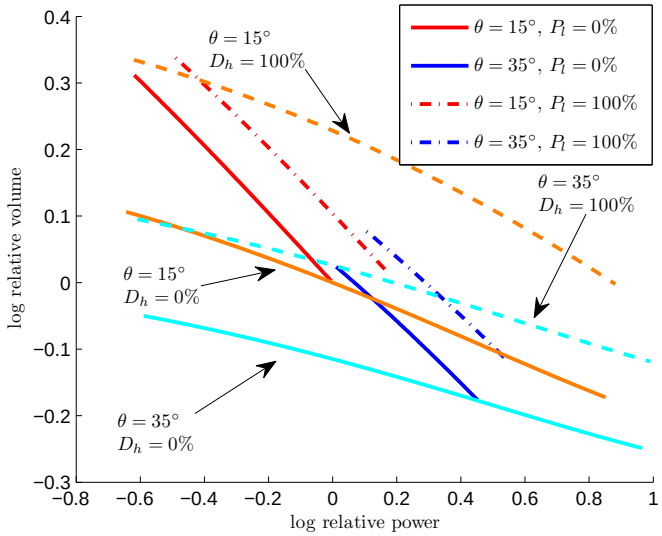

Figure 5.11: Performance curves for constant heat exchanger length. Tube pitch and hydraulic diameter are expressed relative to their limits in the design space.

criterion is used. This results in performance evaluation curves such as shown in figure 5.11.

The data is obtained from a full factorial sampling plan with three levels for the velocity, two levels for the louvre angle, two levels for the fin pitch and two levels for the longitudinal tube pitch. The frontal velocity is varied from 0.5 to 2.6 m/s, the fin pitch from 1.51 to 1.91 mm, the longitudinal tube pitch from 11.9 to 15.3 mm and the louvre angle from $15°$ to $35°$. The requirements on the mass flow rate, temperatures and heat transfer rate are chosen so that the heat exchanger with minimum longitudinal tube pitch, minimum fin pitch, minimum louvre angle and a dimensionless frontal velocity of 25% meets them. This heat exchanger will be referred to as the global reference heat exchanger.

The performance curves for constant hydraulic diameter are also indicated on the figure as a reference. The curves for constant hydraulic diameter are shown for the minimum longitudinal tube pitch, which is considered in the design space, as this corresponds to the optimal performance. For both louvre angles, the curves of both the minimum and maximum hydraulic diameter are shown. From paragraph 5.2.3, it is clear that these curves should be interpreted as theoretical limits, since it is assumed that the length can be changed without any influence on the j- and f-factors. The choice of the global reference heat exchanger meeting the requirements determined the relative positions of the curves of constant hydraulic diame-

ter and the curves of constant length. The global reference specifies the velocity for which the performance curves corresponding to the design with minimum louvre angle, longitudinal tube pitch and fin pitch intersect.

As mentioned earlier, the hydraulic diameter varies for the performance curves with constant heat exchanger length. The performance curve for a certain louvre angle is therefore limited by the performance curves corresponding to the minimum and the maximum hydraulic diameter. The dash-dot lines show the effect of the longitudinal tube pitch. As expected, the performance deteriorates if the length is fixed to a value corresponding to the maximum longitudinal tube pitch.

It is interesting to note that the design with a louvre angle of 15° slightly outperforms the design corresponding to a louvre angle of 35°, if the performance curves are extrapolated. This can also be seen without needing to extrapolate in figure 5.12, where the analysis is repeated for a larger range of fin pitches. This is to be expected, since the relative volume follows the behaviour of the area goodness factor. If the louvre angle is increased, the corresponding increase in the j-factor is smaller than the corresponding increase in the f-factor. For an increase in the louvre angle from 15° to 35° for a fixed frontal velocity of 2.6 m/s, the j-factor increases 33% for an increase in the f-factor of 57%. Since the exponents of the j-factor and f-factor are equal for the area goodness factor, this results in a deterioration of the performance. It should be noted that this reasoning is approximate, since the frontal velocity will not be the same for both designs, but instead needs to be determined from equation (5.9).

The increase in hydraulic diameter with increasing louvre angle can be understood from the equation for the heat exchanger length (2.81). Since the modified Colburn j-factor is larger for the larger louvre angle, the length would need to be smaller for the same frontal velocity. This is not possible as the length is fixed, the hydraulic diameter in the numerator must therefore be increased to satisfy the length constraint. Increasing the hydraulic diameter to avoid reducing the length makes physical sense if the required length would be smaller than it is possible to construct, or if the longitudinal tube pitch would become too large if the length would be reduced by removing a tube row.

$$L = \frac{\mathbf{D_h}}{\mathbf{j}^*} \frac{NTUPr^{\frac{2}{3}}}{4} \qquad \text{(2.81 revisited)}$$

If the constraints on the fin pitch and the longitudinal tube pitch correspond to actual physical constraints, for instance, due to manufacturability, the limited extent of the performance curves for fixed heat exchanger length in the fan power-volume space also has physical meaning. For the same limited range of fin pitches, tube pitches and velocities, choosing a larger louvre angle allows constructing designs with a smaller heat exchanger volume but a larger fan power.

For the same relative fan power of one (the logarithm is then 0), the design

with $\theta = 15°$ corresponds to the minimum hydraulic diameter. This was imposed by fixing the global reference heat exchanger at this point. The $\theta = 35°$ design corresponds to the maximum hydraulic diameter. If the global reference heat exchanger would be chosen to have the maximum hydraulic diameter for $\theta = 15°$, the $\theta = 35°$ design would require hydraulic diameters larger than the maximum. Physically, this means if the requirements of the heat exchanger are such that the maximum hydraulic diameter is required for the $\theta = 15°$ design, it is impossible to improve performance by using a larger louvre angle and still maintain the same length.

5.2.4.3 Influence of the fin pitch

In paragraph 5.2.4.2, the fin pitch was varied from 1.51 to 1.91 mm. The performance curves were shown for a constant hydraulic diameter corresponding to the minimum fin pitch of 1.51 mm. Just like in paragraph 5.2.2.4, where the fin pitch was constrained to 1.71 mm, the louvre angle $\theta = 35°$ is the superior design for the entire range of considered velocities. In theory, there could be a local optimum for the louvre angle between the limits of $\theta = 15°$ and $\theta = 35°$. As this was not the case in the extensive optimisation performed in paragraph 5.2.2.4, this possibility is not further investigated.

For the performance curves corresponding to fixed length, the range of fan powers for the two different louvre angles barely overlaps. This can be remedied by increasing the range over which the fin pitch is allowed to vary. Increasing the fin pitch further results in an increase of the maximum Reynolds number if the same maximum frontal velocity is obtained. This would lead to less reliable CFD simulations, as unsteadiness in the heat exchanger core becomes important. Therefore, the range of the fin pitch is increased by decreasing the minimum fin pitch to 1.21 mm. The same requirements for the global reference heat exchanger are maintained. The resulting performance curves are shown in figure 5.12.

The performance curves for an increased longitudinal tube pitch are not shown for the sake of clarity. Increased longitudinal tube pitch still results in a performance deterioration which is well approximated by a similar translation of the performance curves for both louvre angles. It is now clear that the louvre angle $\theta = 15°$ design is superior if the length is constrained. Decreasing the fin pitch improves the performance at constant hydraulic diameter for both designs, but significantly more so for the design with the smaller louvre angle. As a result, even if the hydraulic diameter is constrained, the optimal louvre angle is also $\theta = 15°$, except for very low velocities. This is a clear example of an interaction effect between the fin pitch and the louvre angle. The optimal louvre angle depends on the fin pitch: for the fin pitch equal to 1.51 mm and 1.71 mm the larger louvre angle is optimal, whereas for the fin pitch of 1.21 mm, the smallest louvre angle results in the best performance.

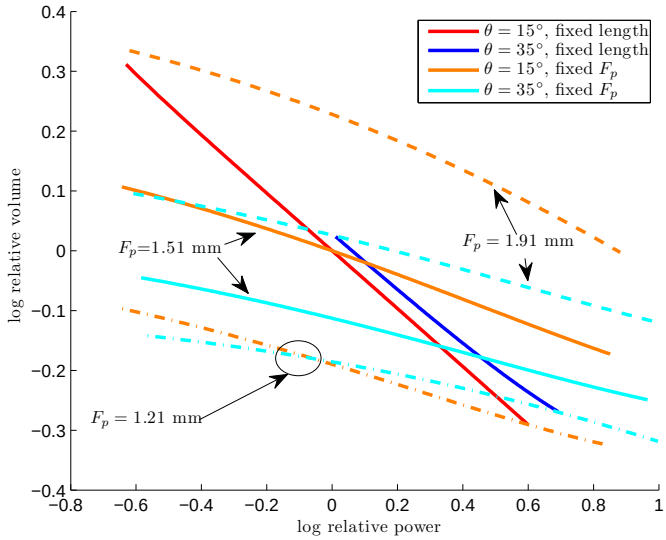

Figure 5.12: Performance curves for constant heat exchanger length with minimum fin pitch equal to 1.21 mm

In conclusion, the optimal louvre angle depends on the boundary conditions for the optimisation, i.e. fixed hydraulic diameter or fixed heat exchanger length. Furthermore, clear interaction effects are observed between the louvre angle and the fin pitch. This is in agreement with the findings of Leu et al. [34], who also identified an interaction between these parameters. Optimisation methods such as the Taguchi method which assume there is no interaction between the louvre angle and the fin pitch can be expected to give misleading results.

5.2.5 General optimisation under fixed mass flow rate constraint

In paragraph 5.2.3, the effect of the heat exchanger length on the performance was shown to be very significant for air-conditioning applications. However, the downside of that approach is that the performance of the fin design depends on the chosen global reference and the manufacturing limits on the longitudinal tube pitch. For example, if the reference corresponds to the minimum longitudinal tube pitch and the modification would result in a lower heat exchanger length, it is then necessary to decrease the number of tube rows and increase the tube pitch. The total effect can be a reduction in the heat exchanger performance. On the other hand, for a different choice of the global reference, it could be possible to achieve the required reduction in heat exchanger length by reducing the tube pitch.

Any improvement in performance due to the fin modification on its own is further improved upon by the effect of being able to reduce the longitudinal tube pitch.

In paragraph 5.2.4, the length was then fixed to avoid the dependence of the performance on the global reference for the application. As a result, any tendency to reduce the heat exchanger length in the previous method now results in an increase in the hydraulic diameter, which is detrimental to the performance.

Since the longitudinal tube pitch and the fin pitch should be as small as possible for the X-shaped louvred fin, it makes sense to consider this as the reference case. Now suppose a modification is applied to the fin geometry which increases the modified Colburn j-factor. If the hydraulic diameter would be kept constant at its minimum value, the heat exchanger length would need to be reduced. This can be done by reducing the number of tube rows and increasing the longitudinal tube pitch, but this incurs a performance penalty which depends on the number of tube rows. For an infinite number of tube rows, the penalty is infinitesimally small, whereas for air-conditioning applications with few tube rows, it may be unacceptably large. However, it is always possible to increase the hydraulic diameter from the minimum value, which also incurs a performance penalty. This latter performance penalty is independent of the number of tube rows.

Optimisation under constraint of constant and minimum hydraulic diameter while neglecting heat exchanger length effects can be interpreted as optimisation of the best possible case. The performance penalty due to variation in D_h and P_l is assumed to be zero and it is not possible to do better than this optimum. However, in real-life applications, it is probable that the predicted performance cannot be attained due to the performance penalties associated with the need to change the geometry to match the required length.

On the other hand, optimisation while keeping the heat exchanger length constant and minimum is independent of the number of tube rows. The hydraulic diameter is changed from the optimal value during the optimisation, incurring a performance penalty. However, the heat exchangers under consideration are all feasible and can be constructed independently of the specific application. Some regions in the power-volume plane can be unreachable due to limits on the hydraulic diameter.

5.3 Generalised method to compare heat exchanger performance

In the Cowell methodology, the mass flow rate was constrained. In practical applications, this might not be necessary. Varying the mass flow rate for constant inlet temperature of the flow results in changing the outlet temperature of the flow. For the condenser of an air-conditioning unit, the air temperature leaving the con-

denser unit is not of interest. The only thing that matters is that the heat transfer rate can be attained for the given inlet temperatures of the air and of the refrigerant. This shows that it is a good idea to relax the mass flow rate constraint. As a consequence, the number of transfer units is no longer constant, complicating analytical treatment of the problem. This has the advantage that both the heat exchanger length and hydraulic diameter can be fixed during the optimisation of the fin geometry.
It is now assumed that the j- and f-factors are known as a function of the local flow characteristics and the fin geometry. They can be determined either from correlations, or by performing CFD simulations. A periodic unit cell of the heat exchanger with a finite number of tube rows is considered. For a given fin geometry and inlet frontal velocity, the heat transfer rate and the pressure drop corresponding to the periodic unit cell can be determined. The influence of the number of tube rows can be handled by continuous interpolation between the discrete values of the number of tube rows. This allows taking the effects of flow development in the heat exchanger core, as well as entrance and exit losses into account. Alternatively, it can be assumed that the j- and f-factors are independent of the heat exchanger length and the performance of the periodic unit cell can be calculated using this assumption, as is done in the Cowell methodology. The heat exchanger length is represented by indicating the continuous value of the number of tube rows: in order to obtain the actual length, this value must be multiplied with the longitudinal tube pitch $P_l = 13.6mm$.
The total heat exchanger can now be pieced together by placing a number of unit cells in parallel. The number of cells is determined by the ratio of heat transfer rates between the total heat exchanger and the periodic unit cell, as indicated by equation (5.11).

$$N_{cells} = \frac{\dot{Q}}{\dot{Q}_{cell}} \tag{5.11}$$

The pressure drop over the total heat exchanger is equal to the pressure drop over any unit cell, assuming a uniform velocity profile. The total heat exchanger mass flow rate, thermal transmittance, fan power, frontal area and volume are equal to the product of the corresponding quantity per unit cell and the number of unit cells.

The following global quantities are constrained to fixed values for all heat exchangers under consideration: the heat transfer rate $\dot{Q}$, the inner-tube wall temperature T_{tube}, the inlet temperature of the air flow T_{in}, the hydraulic diameter D_h and the contraction ratio σ. This leaves three degrees of freedom for the heat exchanger, namely the inlet frontal velocity v, the heat exchanger length L and the fin geometry. All other possible quantities of the global heat exchanger are then a function of these two degrees of freedom, such as frontal area A_{front}, volume

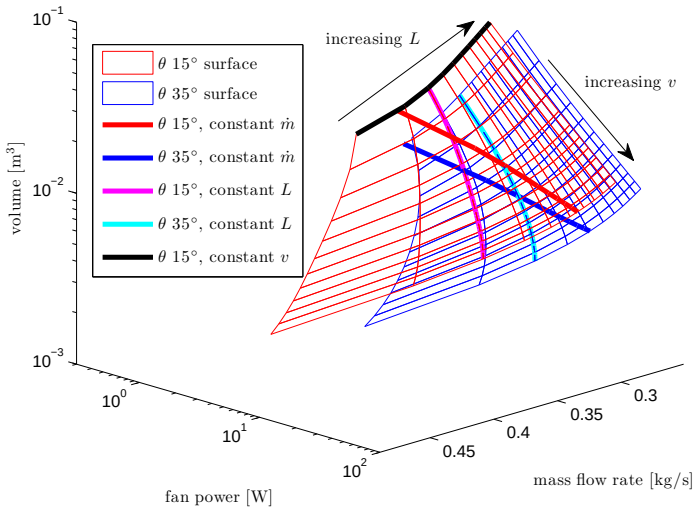

Figure 5.13: Three-dimensional heat exchanger performance

V, mass flow rate $\dot{m}$, outlet temperature T_{out}, number of transfer units NTU, pressure drop ΔP and fan power $\mathcal{P}$.

For two different louvred fin geometries indicated with $\theta = 15°$ and $\theta = 35°$, the performance is evaluated for different velocities and heat exchanger lengths. The data is obtained from numerical simulations, all of which were calculated for three tube rows. In order to vary the length of the global heat exchanger, the simplifying assumption is made that the j- and f-factors are independent of the heat exchanger length, as was done for the Cowell method. Since the j- and f-factors depend on the longitudinal tube pitch, this parameter is kept constant for all calculations. This implies that the heat exchanger length must be varied by using fictitious continuous values for the number of tube rows. The result is shown in figure 5.13. All heat exchangers which are considered correspond to a heat transfer rate of 8 kW for a fluid temperature of $20°C$ and a tube temperature of $50°C$.

The quantities of interest were taken to be the heat exchanger volume V, the fan power $\mathcal{P}$ and the mass flow rate $\dot{m}$. Since there are two degrees of freedom per fin geometry, each geometry is represented by a two-dimensional surface. Every point on the surface corresponds to a certain global heat exchanger, with one fixed frontal velocity, fin geometry, length and so on. Each surface is spanned by two families of parameter curves, which are indicated by the thin lines in the figure.

The first family are curves of constant frontal velocity and changing heat ex-

changer length. One of these curves is indicated in black. The direction in which the length increases along this curve is shown on the figure. As the length of the heat exchanger increases for a constant frontal velocity, the fan power and the required volume increase. Since the mass flow rate and the maximum temperature difference are constant, this means that the maximum heat transfer rate is also constant. Imposing a constraint of fixed heat transfer rate then means that the number of transfer units NTU is fixed. For a given frontal velocity, this can be achieved by modifying the geometry to obtain larger heat transfer coefficients, or by increasing the surface area by increasing the heat exchanger length.

The second family is given by curves of constant heat exchanger length and varying frontal velocity. Since this is an interesting comparison to make, one curve has been indicated on each surface. Both of these curves correspond to the same heat exchanger length of three times the longitudinal tube pitch, but for a different fin geometry. Along a curve of constant heat exchanger length, increasing the velocity results in increased fan power and decreased heat exchanger volume. These curves depend on the choice of the heat exchanger length. To analyse the behaviour of these type of curves, it is interesting to write the heat transfer rate as in equation (5.12).

$$\dot{Q} = C_p A_{front} \rho_i u_i \epsilon (NTU) \Delta T_{max} = \dot{m} C_p (1 - exp(-NTU)) \Delta T_{max} \quad (5.12)$$

Consider an arbitrarily chosen velocity u_i. Since the heat transfer rate, the inlet conditions and the maximum temperature difference are fixed, this means that the product of the effectiveness and the frontal surface area is constant. The effectiveness is determined by the number of transfer units NTU. The effectiveness is a dimensionless representation of the outlet temperature, which is the same for the entire heat exchanger and for a single periodic unit cell. The NTU is therefore the same for the entire heat exchanger and for a single periodic unit cell. The NTU is only determined by the fin geometry and the length constraint. If a modification to the fin geometry results in an increase of the heat transfer coefficient, this means the NTU and therefore the effectiveness also increase. As a result, the frontal surface area (and therefore the volume since the length is constant) decreases. This is valid for any velocity. The impact on the fan power has two components. On the one hand, the modification of the geometry results in an increased pressure drop, which increases the fan power per unit mass flow rate. On the other hand, the decreased frontal surface area results in a lower mass flow rate, which reduces the fan power.

The comparison according to the Cowell method can easily be obtained from the three-dimensional performance surfaces by finding the intersection between the fin performance surface and a surface of constant mass flow rate. Since the mass flow

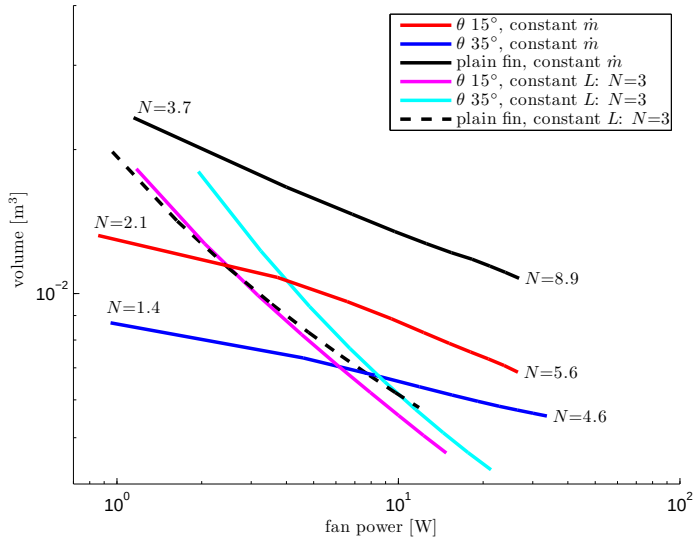

Figure 5.14: Projection of the curves at constant mass flow rate (0.28 kg/s) and constant length (N=3) on the power-volume plane

rate was chosen as the third dependent variable, a surface of constant mass flow rate is simply a plane. The resulting intersections are two curves and are also indicated in the figure for a mass flow rate of 0.28 kg/s. Depending on the choice of the mass flow rate, the position of the curves changes. For a fixed mass flow rate, equations (2.78) and (2.80) show that the mass flow rate only appears in a product. Since all quantities are expressed on a logarithmic scale, choosing a different mass flow rate corresponds to a translation of the curves at constant mass flow rate in the three-dimensional space.

These curves can also be projected on the power-volume plane as shown in figure 5.14. One design is better than another if a smaller heat exchanger volume can be attained while not requiring more fan power. The curves are shown for frontal velocities ranging from 0.5 m/s to 2.6 m/s. The end points of the curves correspond to these velocities. By comparing the ends of the curves, it is seen that the required volume of the plain fin is the highest, followed by the louvred fin with $15°$ louvre angle.

For the designs with fixed mass flow rate, the number of tube rows N of the corresponding heat exchanger is indicated for the lowest and highest velocity designs. This is calculated by dividing the length of the heat exchanger by the longitudinal tube pitch. The lowest velocity corresponds to the small number of tube rows and the lowest fan power. The mass flow rate for the heat exchangers with

fixed mass flow rate is 0.28 kg/s. This does not impact the relative performance of the heat exchanger designs, but it does change the required number of tube rows. This mass flow rate is chosen so that all heat exchanger designs require a number of tube rows between one and nine for the chosen frontal velocity range of 0.5 m/s to 2.6 m/s. As can be seen in figure 5.13, larger mass flow rates correspond to a lower number of tube rows.

It is clear that the plain fin designs require a much larger number of tube rows (and therefore heat exchanger length) than the louvred designs. For the same heat exchanger volume and mass flow rate, the plain fin requires a significantly higher heat exchanger length and velocity than the louvred design with a louvre angle of $\theta = 15°$. Enhanced fin designs therefore correspond to shorter heat exchangers operating at a lower frontal velocity. For the louvre angle of $\theta = 35°$, the velocity range is not large enough to find a solution where the louvred fin and the plain fin require the same heat exchanger volume.

However, for shorter heat exchangers the assumption that the j- and f-factors are independent of the heat exchanger length breaks down. In real-life applications, the number of tube rows cannot be varied continuously. Therefore, non-integer number of tube rows must be implemented by changing the longitudinal tube pitch. Since the total heat exchanger length is equal to the product of the longitudinal tube pitch and the number of tube rows, the change in tube pitch is small as long as the number of tube rows is large. In this case, neglecting the impact of the change in tube pitch on the j- and f-factors can be justified, since the change in tube pitch is small. For short heat exchangers with a low number of tube rows, this simplification is no longer valid. Changes in heat exchanger length require larger changes in the tube pitch, making it necessary to take the impact on the j- and f-factors into account.

For the heat exchanger designs with fixed heat exchanger length, the number of tube rows is equal to three. The difference in performance between the different fin geometries is much smaller if the hydraulic diameter and the heat exchanger length are fixed. If the mass flow rate is constrained, the fin design with $\theta = 35°$ is better with respect to the trade-off between fan power and required volume. However, if the length is constrained, the other design with $\theta = 15°$ performs better.

The heat exchanger performance surfaces are dependent on the heat transfer rate and the temperatures. This is a downside, but also an unavoidable consequence of allowing the mass flow rate to vary. It is only for constant mass flow rate and inlet temperatures that the heat transfer rate is proportional to the thermal conductance UA. As a consequence, the relative performance between two fin types at constant heat exchanger length depends on the chosen length. A large length corresponds to a large NTU, additional increases in the NTU due to geometry modifications result in only a small increase of the effectiveness and therefore only a small decrease of the required volume. In contrast, for low NTU values,

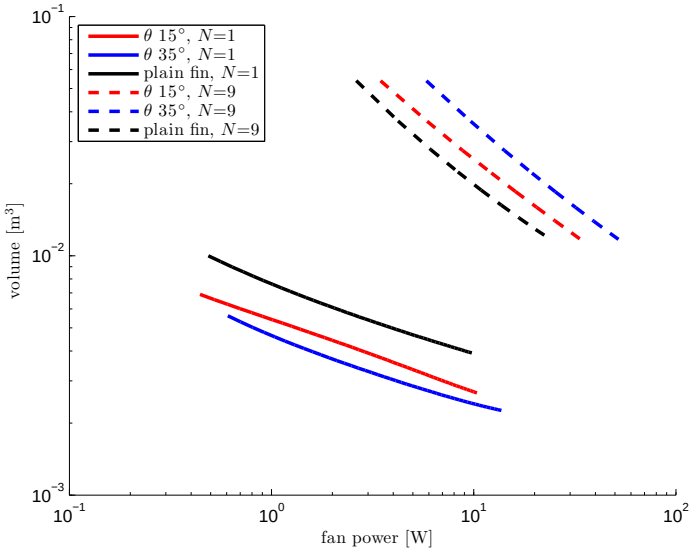

Figure 5.15: The influence of the heat exchanger length in the power-volume plane

the sensitivity of the effectiveness with respect to the NTU is much larger and geometry modifications can result in significant increases in the effectiveness (and therefore a significant reduction of the volume). Figure 5.15 shows the influence of the heat exchanger length on the performance. All heat exchangers were calculated for a length corresponding to three tube rows. The performance at other numbers of tube rows was extrapolated using the assumption that j and f are independent of the heat exchanger length. The smaller length corresponds to a fictitious heat exchanger with a single tube row, the larger length corresponds to nine tube rows.

It is clear that for small heat exchanger lengths, both louvred fin geometries perform better than the plain fin geometry. For the long heat exchangers, the conclusion is reversed. This is explained by noting that both the pressure drop and the thermal conductance in a single periodic unit cell scale linearly with the heat exchanger length. For a fixed flow velocity, the number of transfer units therefore also scales linearly with the length. The relationship between the heat transfer rate and the number of transfer units is given by equation (2.54). For large heat exchanger lengths (and thus large NTUs), the additional increase in heat transfer rate (due to increased effectiveness) with increased heat exchanger length becomes quite small (due to the low sensitivity at larger NTU values) and does not weigh up against the increased pressure drop. This depends on the fin geometries. For louvred fin heat exchangers, the thermal conductance and pressure drop are larger

than for plain fin heat exchangers with the same length and flow velocity.

In conclusion, the actual best fin geometry depends on the application (heat transfer rate, temperatures and mass flow rate), if the heat exchanger length and the hydraulic diameter are fixed a priori. This is the case, for example, if the hydraulic diameter must be sufficiently large to avoid fouling constraints and if the tube pitches are determined due to manufacturing constraints.

5.4 Performance screening of the compound fin design

5.4.1 Introduction

Performance evaluation and optimisation have been discussed extensively and applied to the X-shaped louvred fin. In what follows, the compound vortex generator fin will be discussed. Since the impact of vortex generator parameters was shown to be small, simpler polynomial surrogate models are used instead of the kriging surrogates. This allows identifying the main trends with much less computational effort.

First, it will be shown that interaction effects between the geometrical parameters of the vortex generator are significant, by repeating a case from literature. The parametrisation of the vortex generator placement is then discussed. The interaction between the louvre angle and the vortex generator parameters is then revealed. By studying the optimal value of the vortex generator angle for two different parametrisations of the geometry, it is shown that the optimal angle depends on the placement of the vortex generator. Finally, since the optimisation of the X-shaped louvre fin revealed that as much of the surface as possible should be covered with louvres, a new compound design is introduced. The performance of this new design is shown to be slightly superior to the other designs considered in this work.

5.4.2 Taguchi analysis for a compound louvred fin and vortex generator fin

5.4.2.1 Analysis of the j-factor at a fixed Reynolds number

Chapter 3 revealed that the use of the Taguchi method for the performance screening and optimisation of compact heat exchangers shows some issues. Some authors use only strength one orthogonal arrays, which alias main factor effects, and not a single author has checked whether the very essential assumption regarding the absence of interaction effects is actually satisfied.

Therefore, in this section, a similar problem as that of Huisseune et al. [4] will be investigated using a full factorial sampling plan. In order to perform the full

factorial analysis, only two levels will be used for each variable, as opposed to three levels in the original study. This reduces the required number of calculations from $3^5 = 243$ to a more tractable $2^5 = 32$. Furthermore, the maximum ranges of the levels are changed. For instance, the combination of the maximum fin pitch, height ratio and aspect ratio results in impossible geometries, as the vortex generators can no longer be punched out of the fin material. The range for the fin pitch, height and aspect ratio is therefore halved. It is reasonable to assume that if three levels are sufficient to capture the behaviour of the parameter over the entire range, two levels suffice to capture the behaviour over half of the range. In the original study, the fin pitch ranged from 1.2 mm to 1.99 mm, this is now 1.4 mm to 1.8 mm. Likewise, the aspect ratio varies from 1 to 1.5 instead of from 1 to 2 and the height ratio varies from 0.7 to 0.9 instead of from 0.5 to 0.9. The original ranges of the louvre angle from 22° to 35° and of the VG angle from 25° to 35° are maintained, since no quadratic effects are expected over such a small range.

The average factorial effects of the study for the j-factor for a frontal velocity of 1.26 m/s are shown in table 5.1. As discussed in paragraph 5.2.2, the frontal velocity and Reynolds number should be a function of the geometry if performance evaluations are made. For the impact of the j-factor however, it is justified to conduct the analysis at a constant Reynolds number.

	Level	F_p	θ	α	h^*	Λ
j-factor	1	0.0359	0.034	0.0352	0.0365	0.0349
	2	0.0361	0.0345	0.0334	0.0329	0.0358
	3	0.0323	0.0359	0.0357	0.0349	0.0336
Contribution ratio (%)		27.4	13.6	16.9	26	16.2

Table 5.1: Average factorial effects for the study of Huisseune et al. [4]

Table 5.1 reveals local optima for every variable except for the louvre angle. Except for the height ratio, the new ranges are chosen so these local optima are included in the range. The height ratio according to the original study should be as small as possible to obtain the highest j-factor, which seems counter-intuitive. It was decided to retain the two higher levels for the height ratio, instead of the two lower levels. Using the new full factorial design, a polynomial model is trained, which includes all interaction effects. As discussed in chapter 2, the contribution ratio of the Taguchi design can be interpreted as the maximum difference along a parameter curve for the parameter in question, normalised with the sum of all these differences for all parameters. If interaction effects are present, this difference along a parameter curve is no longer constant. Therefore, for each of the points in the sampling plan, a parameter curve and the corresponding maximum difference were determined. The contribution ratio is reported as the average of these differences, normalised with the sum of the same average differences over

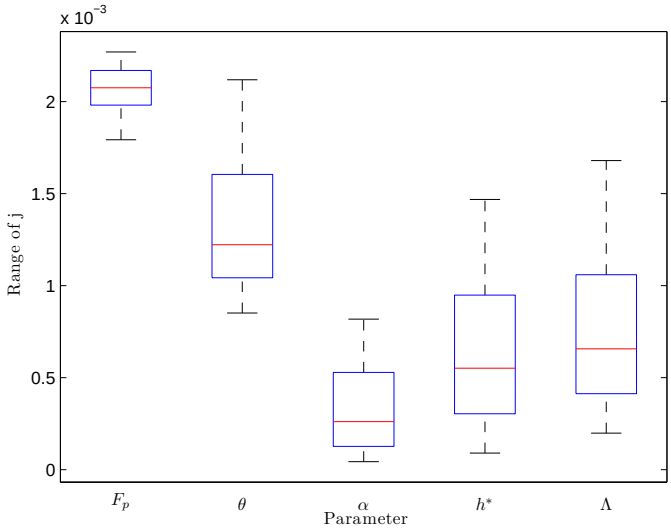

Figure 5.16: Box plot of the range of the j-factor for every set of parameter curves

all factors. The standard deviation can also be calculated, it is normalised with the same sum of average differences.

The result is shown in table 5.2. It reveals that the variation of the vortex generator angle from $25°$ to $35°$ has a much smaller effect than the variation of the other parameters over their ranges, whereas in the study of Huisseune et al. [4] this effect was more important than the effect of the louvre angle. The fin pitch and the height ratio are found to have the most important effect, this is in agreement with the previous study. The standard deviation is quite large compared with the average contribution ratio, which indicates that the deviation along a parameter curve strongly depends on the value of the other parameters. In other words, the interaction effects are significant. This can also be represented graphically by considering the box plots of the range distribution for each set of parameter curves, given in figure 5.16.

The louvre angle, the VG height ratio and the VG aspect ratio especially show strong interactions with the other parameters. It is not possible to determine which interactions are responsible for variation in the range of the j-factor for each of the parameter curves. This information can be obtained by looking at the equation for the polynomial model, given by equation (5.13). If the variables are chosen such that they vary from -1 to 1 over the range of a parameter, the coefficient gives an indication of the importance of the term.

Parameter	Range	Average contribution ratio	$2\,\sigma$
F_p	1.4 mm - 1.8 mm	40.2	5.2
θ	22° - 35°	26.0	14.8
α	25° - 35°	6.4	9.4
h^*	0.7 - 0.9	12.7	16.5
Λ	1 - 1.5	14.8	17.0

Table 5.2: Average contribution ratios and twice the standard deviation determined from the polynomial model

Note that the symbols which appear in equation (5.13) refer to the normalised versions of the variables, not to the dimensional variables.

$$\begin{aligned} j = 0.0356(1 &- 0.03F_p + 0.019\theta + 0.011\Lambda + 0.0091h^* + 0.0046\alpha \\ &+ 0.004h^*\Lambda + 0.0034\theta\Lambda + 0.0033\theta h^* + 0.0021\alpha\Lambda \\ &+ 0.0017\alpha h^* + 0.0014\theta\alpha + 0.0011F_p h^* \\ &+ 0.00085\theta h^*\Lambda - 0.00072F_p\theta h^*\Lambda ...) \end{aligned} \tag{5.13}$$

Only the first 15 terms when sorted in decreasing magnitude of the coefficients are shown, out of a total of 32 terms. The smallest coefficient that is shown is 0.75% of the sum of the absolute values of all coefficients. It is clear that some interaction terms are of the same order of magnitude as the smallest main terms. The interactions which are found to be important are the same interactions that were also identified using the method of the standard deviation of the contribution ratios. The signs of the different terms allow determining that the fin pitch should be as small as possible and the other parameters as large as possible to obtain the highest Colburn j-factor. The same result is also obtained by doing a formal analytical optimisation of the polynomial equation. This is also what can be intuitively expected. In chapter 2, it was shown that smaller hydraulic diameters tend to increase the heat transfer coefficient for laminar flows. The effect of the vortex generator can also be expected to be stronger as its surface area increases, therefore also increasing the heat transfer coefficient.

The interaction between the height ratio and the aspect ratio is shown graphically in figure 5.17. These variables are allowed to vary while all other variables are held fixed at their lowest value. This results in a two-dimensional surface. There are two parameter curves passing through the data for each variable. It is clear that only when the aspect ratio and the height ratio are simultaneously large, a significant effect on the j-factor is present.

Investigating the flow reveals the physical reason for this behaviour. The velocity magnitude at a location 15% of the fin spacing above the fin surface is shown

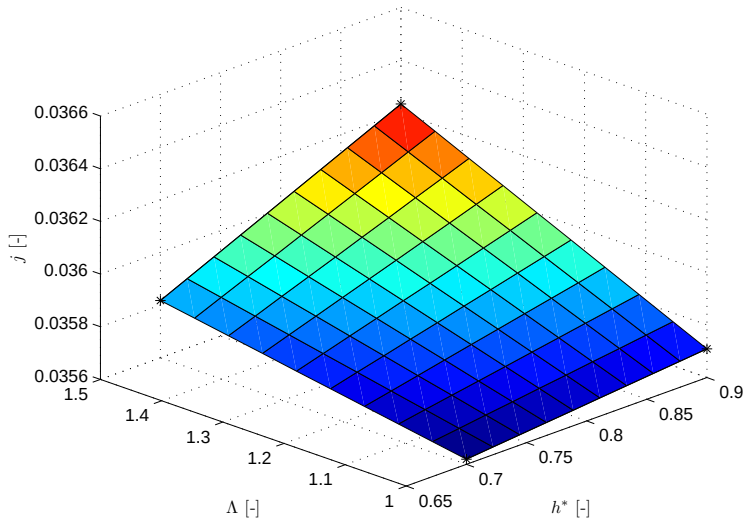

Figure 5.17: The j-factor as a function of the height ratio and the aspect ratio

for all four geometries in figure 5.18. The vortex generator is indicated in white for the first tube row. The velocity contours reveal that the vortex generator is located almost entirely in the tube wake for the lowest value of the height ratio, regardless of the other vortex generator parameters such as aspect ratio and angle. For the larger height ratio, the vortex generator is still largely in the tube wake for the lowest aspect ratio. The j-factor is therefore only slightly higher than for the lowest height ratio. However, if both the height ratio and the aspect ratio are large, the vortex generator protrudes from the tube wake and has an influence on the flow. It is only for this combination when both variables are large that the vortex generator is effective. This interaction effect between the height ratio and the aspect ratio cannot be taken into account by a standard Taguchi analysis, but is clearly quite important.

The transversal distance between the trailing edge of the vortex generator and the tube centre is determined by the interaction between the fin pitch, the height ratio and the aspect ratio. For a given tube wake, the third-order term therefore determines the extent to which the vortex generator protrudes from the tube wake, which very significantly influences the flow disturbance caused by the vortex generator. The transversal extent of the tube wake at the location of the vortex generator is influenced by the louvre angle. A larger louvre angle presents a larger obstruction to the flow through the louvre bank and therefore results in a higher

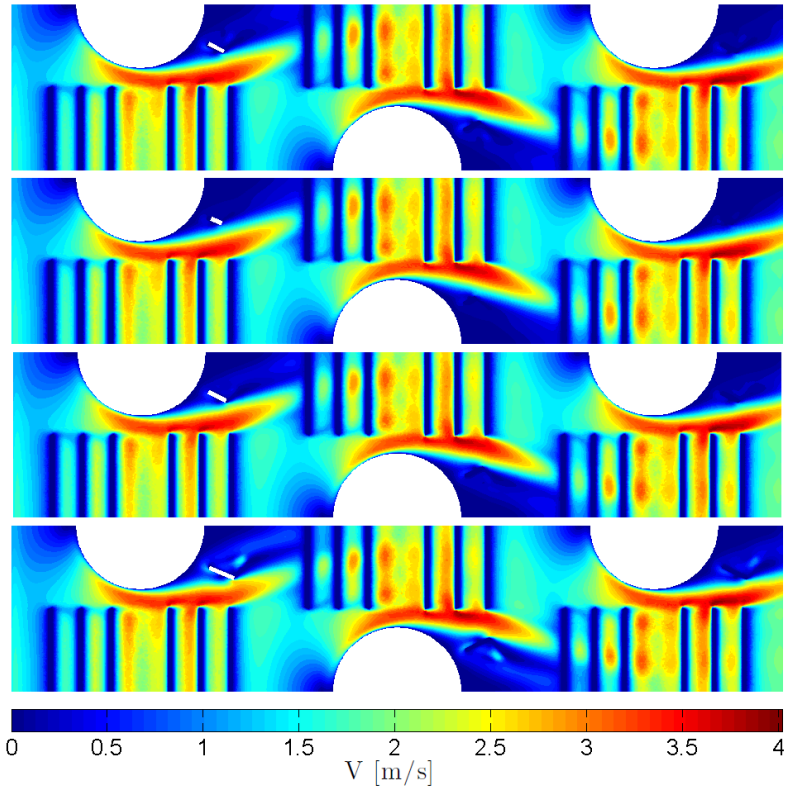

Figure 5.18: Velocity magnitude at a location 15% of the fin spacing above the fin surface. Top to bottom: h^* large, both small, Λ large, both large

velocity bypass jet, reducing the tube wake. As a result, the vortex generator will protrude out of the tube wake for smaller transversal positions of the trailing edge. Even four-factor interactions due to the interaction between the extent of the tube wake and the vortex trailing edge position can therefore be expected on physical grounds. The four-factor interaction between louvre angle, fin pitch, aspect ratio and height ratio has a polynomial coefficient of 0.0007 and is therefore not even two orders of magnitude lower than the most important main factor effect. It is only one third-order effect out of the 10 possible ones and one fourth-order effect out of 5 possibilities that are significant, but it is important that these few interactions are not aliased with other important terms. The design of experiments can reduce the computational effort with respect to a full factorial sampling plan, but only on the condition that the aliasing pattern is investigated a priori. Interaction effects which are expected to be important based on physical intuition of the flow must not be aliased.

In conclusion, interaction effects are quite significant for compound louvred fin and vortex generator designs. The louvre angle interacts with the aspect ratio and the height ratio of the vortex generator. The height ratio and the aspect ratio of the vortex generator also interact strongly. Three- and four-factor interactions are less important, but two of these high order interaction terms are still less than two orders of magnitude smaller than the largest effects. Unless the aliasing pattern is investigated and tailored to avoid aliasing with important high order interactions, an experimental design with reduced resolution can only provide approximate results. Care must be taken when applying Taguchi methods, since there are many two-factor interactions which have been identified as significant. The Taguchi method can cope with these interactions if they are considered as a factor on their own, but this requires larger experimental designs and is never done in the heat exchanger literature. Varying the vortex generator angle over a range of 25 to 35 degrees is found to have the least influence compared with the other modifications to the fin geometry.

5.4.2.2 Analysis of PECs using the Taguchi method

Since significant interaction effects have been identified for the j-factor, it stands to reason that similar interaction effects will be present for the performance of the heat exchanger, evaluated according to some PEC. In order to determine the impact of the parameters on a PEC, it is no longer possible to do the analysis at a constant Reynolds number. Instead, the method discussed in paragraph 5.2.2.3 is used to determine the correct Reynolds number for each geometry such that the fan power is constant. The full factorial sampling plan is extended such that there are four levels of the velocity: 0.59 m/s, 1.26 m/s, 1.93 m/s and 2.6 m/s. The corresponding polynomial models for the j-factor and the f-factor are determined from the data.

The resulting performance curves are shown in figure 5.19. A line of constant

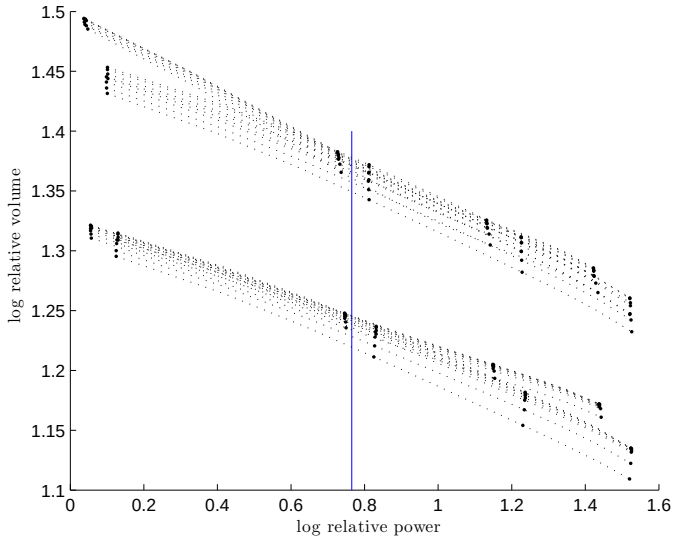

Figure 5.19: Performance of all designs in the design space in the power-volume plane. The large dots indicate available data, the small dots are interpolated by the model

fan power is indicated, chosen such that all the data obtained for a velocity of 1.26 m/s is close to the fan power. For each of the designs, the volume corresponding to this constant fan power is determined, corresponding to the VG-1 criterion. The reference volume of VG-1 is chosen to be the largest volume in the design space for the fan power. A polynomial surface is then constructed to predict the VG-1 criterion for all geometries in the design space. The box plots of the distribution of the range of VG-1 for the different sets of parameter curves are given in figure 5.20.

Figure 5.20 shows that the fin pitch is by far the most important parameter determining the required volume for a fixed fan power. As the fin pitch varies from 1.4 mm to 1.8 mm, the required volume changes by around 25%. This is to be expected, as the fin pitch has a very strong effect on the hydraulic diameter. A smaller hydraulic diameter allows obtaining the same heat transfer surface area for a smaller volume. Even if the change in fin pitch would have no effect on the j- and f-factors, this effect would reduce the required volume, as is shown by equation 2.85.

$$\frac{V}{V_{ref}} = \left(\frac{j^*_{ref}}{j^*}\right)^{\frac{3}{2}} \left(\frac{f}{f_{ref}}\right)^{\frac{1}{2}} \frac{D_h}{D_{h,ref}} \frac{\sigma_{ref}}{\sigma} \qquad \text{(2.85 revisited)}$$

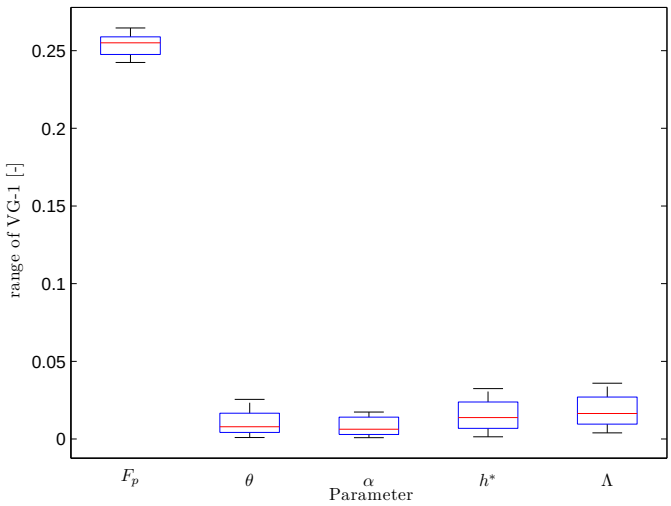

Figure 5.20: Box plot of the ranges of the VG-1 criterion for every set of parameter curves

The impact of the other parameters on the required volume is much smaller. The variation in the heat exchanger volume when the vortex generator angle is varied from 25 to 35 ° is between 0 and 1.7%, depending on the value of the other parameters. The other parameters have a slightly higher impact, between 0 and 3.5%. With the exception of the fin pitch, there is no single parameter which is clearly much more important than the others. The effect of all of the parameters is strongly influenced by interaction terms, as interactions determine whether a parameter influences the required volume or not.

The coefficients of the polynomial model show which interaction terms are present and whether the parameters have a positive or a negative effect on the required volume. Part of the polynomial model is given by equation 5.14. Again, the symbols appearing in this equation refer to the normalised version of the variables, not to the dimensional variables.

$$\begin{aligned}\text{VG-1} = 0.855(1 &+ 0.015F_p - 0.01\Lambda - 0.0088h^* - 0.006\theta - 0.0045\alpha \\ &- 0.0035h^*\Lambda - 0.0034\theta\Lambda - 0.0032\theta h^* - 0.0025F_p h^* \\ &- 0.0022F_p\Lambda - 0.0019\alpha\Lambda - 0.0015\alpha h^* - ...)\end{aligned} \tag{5.14}$$

The positive sign of the fin pitch term indicates that the fin pitch should be

small, as is expected on physical grounds. The other terms all have a negative sign, which means that in order to reduce the required volume they should be as large as possible. The interaction terms are of the same order of magnitude as the smallest main term (the VG angle) and are therefore not negligible. The interaction between the VG height ratio and the VG aspect ratio is the most important, both of these parameters must be large for the vortex generator to protrude significantly from the tube wake. Since the louvre angle determines the extent of the tube wake, there are also interactions between the louvre angle and the vortex generator parameters. The height of the vortex generator is determined by the interaction between the fin pitch and the height ratio, this interaction is also found to impact the performance. Interactions between the angle of attack and the size of the vortex generator are present and also expected, since this angle is only important if a part of the VG actually protrudes from the tube wake.

In conclusion, the assumption that interaction effects are negligible is definitely not valid for vortex generator geometries. Due to the physical interaction between the tube wake and the location of the vortex generator, interactions between the VG angle of attack, the VG height ratio and the VG aspect ratio are all of the same order of magnitude as the main effect of the VG angle. For the combination of vortex generators with louvres, additional interactions with the louvre angle occur. Since two-factor interactions are crucial to the performance of a vortex generator fin, experimental designs with a resolution lower than V should be used with care.

5.4.3 Parametrisation of the vortex generator

In order to evaluate the performance of different compound louvred fin and vortex generator designs, a parametrisation is first required. A unique relationship needs to be established between fin geometries and the design vectors. The choice of the parametrisation is important for two reasons. First of all, the set of realisable designs depends on the parametrisation. Due to the complex geometry, fixing some parameters limits the possible options for other parameters. As the aspect ratio is increased, the possible positions where the vortex generator can be placed are reduced. Depending on whether the aspect ratio or the positioning is chosen first, the range of possible designs is different. Secondly, the choice of the parametrisation influences the observed interaction between parameters. For example, in the previous section, the leading edge of the vortex generator was kept at a constant position, which resulted in the trailing edge position to be determined by the interaction between the height ratio and the aspect ratio. If instead the trailing edge position would be held fixed as the other parameters change, the protrusion of the vortex generator from the tube wake would no longer depend on the other parameters. Depending on whether the leading edge or the trailing edge is kept at a constant position, the design and thus the performance will be different. The

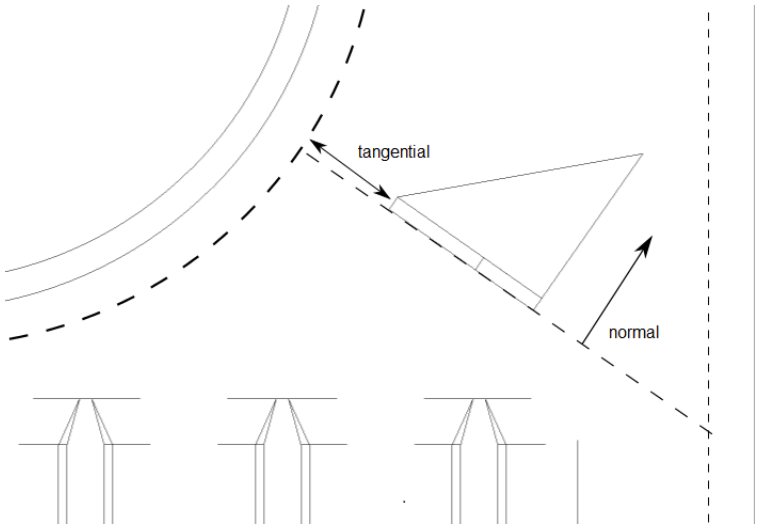

Figure 5.21: Parametrisation of the vortex generator positioning using tangential and normal translation

resulting optimal vortex generator angle will depend on this choice. If the position of the vortex generator is also parametrised, interaction effects with the angle of attack and the aspect ratio can be expected. This is caused by the presence of the louvres, which strongly limits the possible positions depending on the angle of attack and the aspect ratio.

As important parameters for the compound design, the louvre angle, the vortex generator angle of attack and two position parameters are chosen. The fin pitch and the transversal tube pitch are kept fixed in order to maintain a constant hydraulic diameter. The fin thickness, the longitudinal tube pitch and the number of tube rows are also not varied. In order to select the positioning of the vortex generator, tangential and normal translations are used, as indicated in figure 5.21. The forbidden regions are indicated with the dashed lines. Sufficient distance must be kept from the louvres so that there is never any intersection between the vortex generator and the louvres. The distance between the tangential line through the vortex generator and the louvres is therefore fixed at 0.5 mm. Also a minimum distance from the edge of the fin behind the final tube row and a minimum distance from the tube must be respected. The minimum distance is also equal to 0.5 mm. The advantage of this parametrisation is that the aspect ratio can be varied while keeping the positioning of either the leading edge or training edge of the vortex generator constant, without danger of intersection with the louvres.

First, the translation in the normal direction, the angle of attack and the aspect ratio are chosen. The translation in the normal direction is entered as an offset

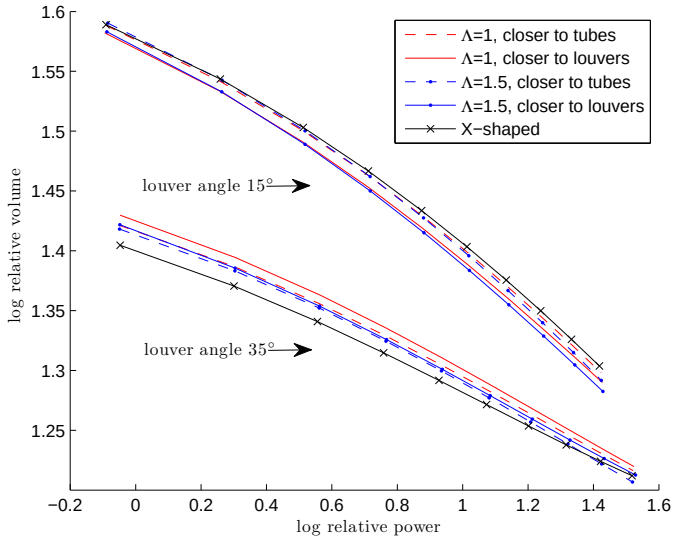

Figure 5.22: The influence of the louvre angle, vortex generator tangential translation and aspect ratio in the power-volume plane

from the dashed line shown in figure 5.21, corresponding to a distance of 0.5 mm between the tangential line through the vortex generator and the louvres. Once these parameters are fixed, the limits for the tangential translation can then be determined. One limit is formed by the minimum distance between the vortex generator and the tubes, the other is formed by the minimum distance between the vortex generator and the fin edge for the final tube row. The final parameter determines the tangential positioning between these two limits.

5.4.4 Effect of the louvre angle on the optimal vortex generator geometry

A full factorial sampling plan is used to investigate the influence of the louvre angle θ, the tangential translation of the vortex generator $d1$ and the aspect ratio Λ. Two levels are used for each of these parameters. The normal offset is kept fixed at 0 mm, the vortex generator angle of attack is fixed at 35°. To account for the influence of the velocity, three levels are used for this parameter. The corresponding polynomial models are built for the UA_s and the $F1$ parameter. Using these models, the heat transfer surface performance can be predicted for the entire design space.

Figure 5.22 shows the resulting performance in the power-volume plane. For

comparison purposes, the X-shaped louvred fin performance is also indicated. It is immediately clear that the louvre angle is by far the most important parameter. Larger louvre angles allow for the construction of more compact heat exchangers for the same required fan power. The aspect ratio has a significantly smaller effect, small improvements can be obtained by using larger aspect ratios, except in the case of low louvre angles and low velocities. The tangential translation is an example of an interaction effect. For the low louvre angle, positioning the vortex generator close to the louvres is beneficial. For the larger louvre angle, however, the fin surfaces with the vortex generators positioned closer to the tubes offer the best performance.

The importance of this interaction effect can be revealed by evaluating the VG-1 criterion. All designs in the design space are compared with the X-shaped louvred fin with a louvre angle of 15° and operating at a frontal velocity of 2.6 m/s. It is important to note that it is the velocity (and thus Reynolds number) of the *reference* heat exchanger which is fixed. For each design under consideration, the appropriate frontal velocity is determined according to the method of paragraph 5.2.2.2. The required volumes are evaluated for each design in the full factorial sampling plan and the corresponding polynomial interpolation model is determined. The polynomial is given by equation (5.15). The tangential translation is indicated with the symbol x_t, the aspect ratio by Λ and the louvre angle by θ. These variables are normalised to vary between -1 and 1. The factor 0.91 in front is the predicted VG-1 criterion for the design where the design variables are all in the middle of their limits. The sign and magnitude of each coefficient show the impact of every factor. The products of different factors are called the factor interactions.

$$\begin{aligned} VG\text{-}1 = 0.91(1 &- 0.002x_t - 0.008\Lambda - 0.07\theta \\ &+ 2\text{e-}05x_t\Lambda + 0.007x_t\theta - 0.0002\Lambda\theta + 0.0006x_t\Lambda\theta) \end{aligned} \tag{5.15}$$

A contribution ratio is defined as the ratio of the absolute value of the coefficient divided by the sum of the absolute values of all coefficients except for the constant term. The contribution ratios of each variable are given in table 5.3. The contribution ratios show that the louvre angle is by far the most important parameter and that the interaction effect between the tangential translation and the louvre angle is of the same order of magnitude as the effect of the aspect ratio. The same analysis can be done comparing the X-shaped heat exchanger with a louvre angle of 15°, but operating at the lowest velocity of 0.5 m/s. In this case the contribution ratio of the louvre angle is 91%, the translation interaction contributes 4% and the aspect ratio interaction 2%.

It is clear that the louvre angle is by far the most important parameter of the compound design. Note that the louvre angle was much less important during the

Variable	Contribution ratio	Polynomial coefficient
Louvre angle	79.5%	-0.072274
Aspect ratio	9.1%	-0.0083022
Interaction translation and louvre angle	8.1%	0.0073825
Tangential translation	2.3%	-0.0021224

Table 5.3: Contribution ratios to VG-1 of tangential translation, aspect ratio and louvre angle

analysis of section 5.4.2. In that case the vortex generator parametrisation was such that it could be placed entirely in the tube wake or not, which is no longer the case for this parametrisation. It was therefore to be expected that the effect of the vortex generator parameters is smaller with respect to the effect of the louvre angle in this case. For the lowest velocity, the louvre angle and its interactions are the only significant contributors to the fin performance. The equation for the VG-1 criterion (5.15) is optimised, constraining the design parameters within the limits used for the calculations. The design requiring the lowest heat exchanger volume while still achieving the same heat transfer rate and fan power as an X-shaped louvred fin with a louvre angle of $15°$ is then revealed. The aspect ratio and the louvre angle should be equal to the maximum considered values, 1.5 and $35°$ respectively. The optimal tangential positioning is closer to the tubes and further away from the louvres. This results in a heat exchanger design which requires 83% of the volume of the X-shaped louvred fin with a louvre angle of $15°$.

5.4.5 Effect of the vortex generator angle

5.4.5.1 Using tangential-normal parametrisation for the positioning

Since the louvre angle is by far the most important parameter, it is now kept fixed at its optimal value of $35°$. In order to estimate the effect of the vortex generator angle, a full factorial sampling plan is calculated where the vortex generator angle is changed from $35°$ to the fixed value of $55°$. Three levels for the velocity and two levels for the aspect ratio and the tangential translation are used. The comparison is made with the previously found optimum design, for the same constraints. If the vortex generator angle is $55°$, the optimal tangential positioning is closer to the louvres, the aspect ratio is again optimal for the largest value. However, this design takes 0.4% more volume than the optimum with vortex generator angle of attack equal to $35°$. Apparently, the lower vortex generator angle is to be favoured slightly. This result takes interaction with one-dimensional tangential positioning into account.

The design is shown in figure 5.23. The positioning with respect to the louvres is limited by the constraint that the punched area of the vortex generator is not

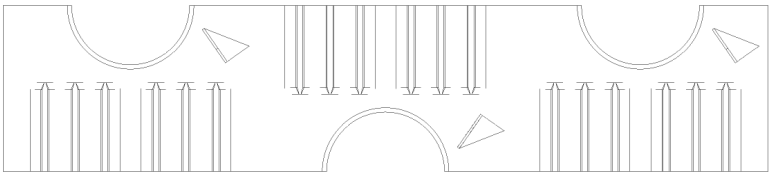

Figure 5.23: Optimal compound geometry with a vortex generator angle of $55°$

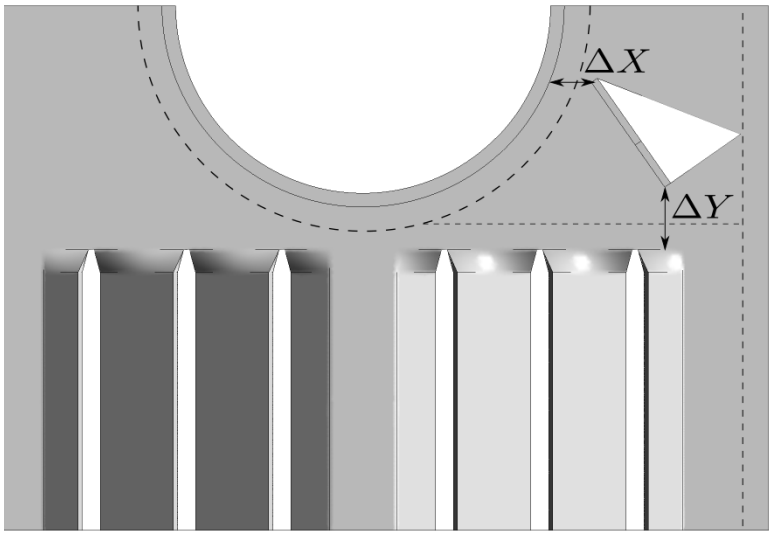

Figure 5.24: Parametrisation of the vortex generator geometry according to the x*- and* y*- axes*

allowed to be closer to the end of the fin. Because of the large vortex generator angle and the limitation of only tangential translations, this results in a rather large distance between the louvres and the vortex generator. Designs where the vortex generator is positioned closer to the louvres are not considered in the design space.

5.4.5.2 Using a different parametrisation for the vortex generator positioning

The aspect ratio is effectively limited by the requirement that the vortex generator must fit on the fin at the final tube row. Furthermore, tangential translations in the downstream direction which move the vortex generator past the louvre arrays are impossible for the same reason. Therefore, the constraint that during tangential translations the vortex generator cannot intersect the louvres does not occur

in practice. Additionally, for large vortex generator angles, the region of possible placements is severely limited. Therefore, it is a good idea to abandon the tangential and normal coordinate system and parametrise the vortex generator positioning in a different way, illustrated in figure 5.24. First, the distance between the vortex generator and the louvres along the Y-axis ΔY is chosen. The closest distance allowed is 0.5 mm, which is necessary for the unstructured region around the vortex generator. From a manufacturing point of view, the distance cannot be made arbitrarily close in any case, so the restriction due to the grid generation is tolerable. The positioning along the X-axis is then limited by the distance between the vortex generator and the tube and by the distance from the end of the fin for the final tube row, which must be at least 0.5 mm in all cases. The limits are indicated with dashed lines on the figure. The limit on the X-position depends on the chosen ΔY. The positioning along the X-axis ΔX is therefore chosen as a percentage, where 0% corresponds to a positioning as close as possible to the tube row and 100% corresponds to a positioning as far away from the tube as possible. As the distance from the louvres ΔY or the aspect ratio Λ increases, the range for the positioning along the X-axis decreases.

A full factorial sampling plan is constructed for the new parametrisation, using two levels for the vortex generator angle α, ΔX and ΔY. The vortex generator angle varies between 35° and 55°, ΔY between 0.5 and 0.8 mm and ΔX between 0% and 100%. Optimising the corresponding polynomial model shows that both ΔY and ΔX should be minimum, resulting in a design which requires 98% of the volume of the optimal compound design with a vortex generator angle of 35°. For the different parametrisation of the positioning, an improvement of 2% instead of a deterioration of 0.4% with respect to the case of an angle of 35° is seen. This is again an illustration of interaction effects between the vortex generator positioning and the its angle of attack. The interaction is also apparent from the contribution ratios given in table 5.4. Only the four most important contributions are shown, the remaining contributions are due to the main effect of the X-translation and the interaction between all factors.

Variable	Contribution ratio	Polynomial coefficient
Vortex generator angle α	39.3%	-0.0078924
Interaction α and ΔY	23.6%	0.004748
Translation ΔY	19.2%	0.0038532
Interaction ΔY and ΔX	8.2%	-0.0016503

Table 5.4: Contribution ratios to VG-1 of α, ΔX and ΔY

The interaction effect between the vortex generator angle and the positioning along the Y-axis is of the same order of magnitude as the main effect of the vortex generator angle. The interaction effect between the ΔY and ΔX translation is

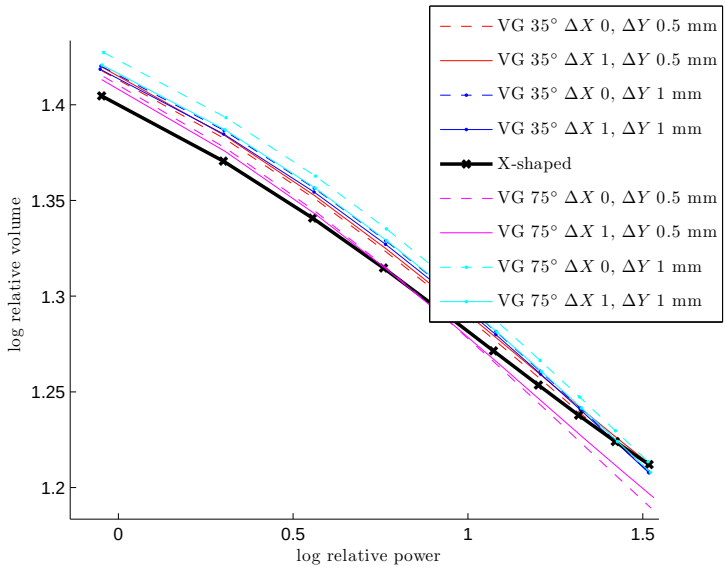

Figure 5.25: The influence of the vortex generator angle and positioning in the power-volume plane

more important than the main effect of the ΔX translation. This is logical, since the X-translation is entered as a percentage and the limits are a strong function of ΔY. Now that a different parametrisation is used, the most important main effect indicates that the vortex generator angle should be larger to reduce the VG-1 criterion. Therefore, two more levels for the vortex generator angle are added to the design, corresponding to angles of $75°$ and $95°$. Figure 5.25 shows the performance curves in the power-volume plane for an angle of $35°$ and $75°$. The curves corresponding to an angle of $55°$ lie in between both set of curves but are not shown for the sake of clarity. A vortex generator angle of $75°$ and a positioning as close as possible to the louvres (minimum ΔY) and to the tubes (minimum ΔX) results in the best performance for every velocity under consideration. The effect of the vortex generator angle is dominant for the performance. For all positions, the designs with the larger angle outperform the designs with the smaller angle.

By considering the contribution ratios it can be seen that the ΔX positioning has a relatively small effect. If the fin geometry is optimised with respect to the VG-1 criterion, it is found that the optimal ΔX positioning is minimum. Therefore, this parameter is held fixed at the minimum value. This allows making a 2D representation of the VG-1 criterion as a function of the vortex generator angle α and the Y positioning ΔY. The representation is shown in figure 5.26. It is confirmed that the performance does indeed improve with increasing angle of attack,

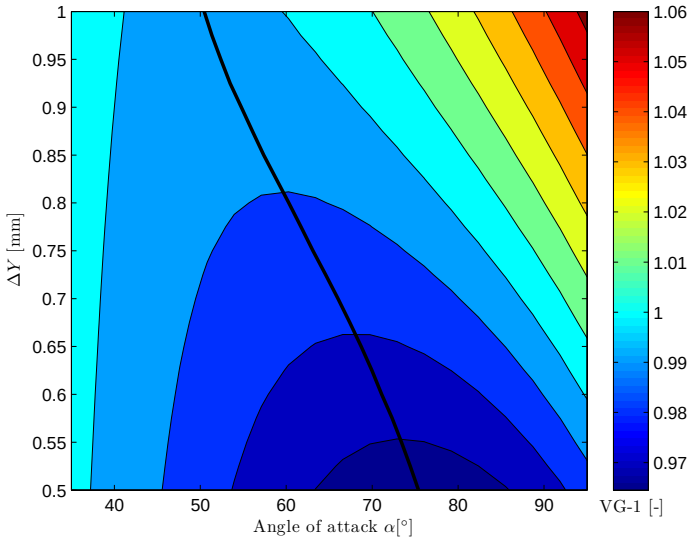

Figure 5.26: The influence of the vortex generator angle and positioning on the VG-1 criterion. The black line indicates optimal vortex generator angles

but two important remarks need to be made. First, the increase does not continue indefinitely. After a certain angle of attack is reached, the performance deteriorates again as the angle of attack increases further. Hence there is an optimal angle of attack. Secondly, this optimal angle of attack depends on the positioning of the vortex generator. As the positioning of the vortex generator is closer to the louvres (smaller ΔY), the optimal angle of attack is larger. The relative volume is 97% with respect to the compound fin design with a vortex generator angle of attack of $35°$, a louvre angle of $35°$ and positioning using the tangential-normal parametrisation.

With respect to the X-shaped louvres with an angle of attack of $35°$, the relative volume is 96.1% for the investigated reference frontal velocity.

5.4.6 Proposal of a new geometry: the Y-shaped louvred and vortex generator fin

From the results of the optimisation of the X-shaped louvred fin, it is found that adding more louvred surfaces is beneficial. This inspires a proposal for a new geometry where the part of the louvred fin upstream of the tube centre is replaced with an X-shaped fin. The downstream part remains a rectangular louvre in order for space to be available for the positioning of the vortex generator. This is called

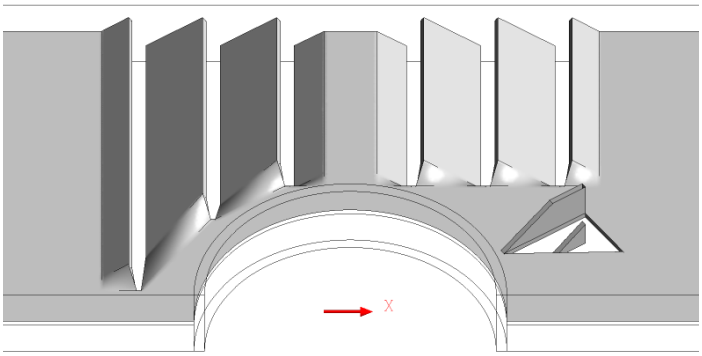

Figure 5.27: The Y-shaped louvred and vortex generator fin

the Y-shaped louvres and vortex generator fin design, show in figure 5.27.

The performance of the geometry is screened by using the same ΔX and ΔY parametrisation, the vortex generator angle is varied from $35°$ to $95°$ in four steps. The resulting performance curves corresponding to the vortex generator angles of $35°$ and $75°$ are shown in the power-volume plane by figure 5.28. The legend for the coloured curves is the same as in figure 5.25. The dashed black line indicates the optimal geometry for the combination of rectangular louvres and vortex generators.

It is clear that all Y-shaped designs outperform the previous design. Even more remarkable is that the Y-shaped design performs better than the X-shaped louvred case. The relative performance increases with increasing fan power, which indicates that the largest advantages with respect to the X-shaped louvres are obtained at higher Reynolds numbers. By comparing the different variations of the Y-shaped design, it is clear that the same optimal vortex generator geometry as in the previous case is recovered. The vortex generator angle should be $75°$, the distance from the louvres in both the X- and Y-directions should be as small as possible.

This is confirmed in figure 5.29 which shows the contours of the VG-1 criterion as a function of the Y positioning and the vortex generator angle. The reference for the VG-1 criterion is the previously found optimum for the rectangular louvres and vortex generator combination. Using the Y-shape allows using a volume of 96.5% of this design for the chosen reference fan power. This corresponds to 92.7% of the volume of the reference X-shaped louvred fin with a louvre angle of 35%. The shape of the curve is very similar to figure 5.26 for the rectangular louvres. This indicates that the optimal vortex generator geometry is little influenced by the shape of the louvres upstream of the tube centre.

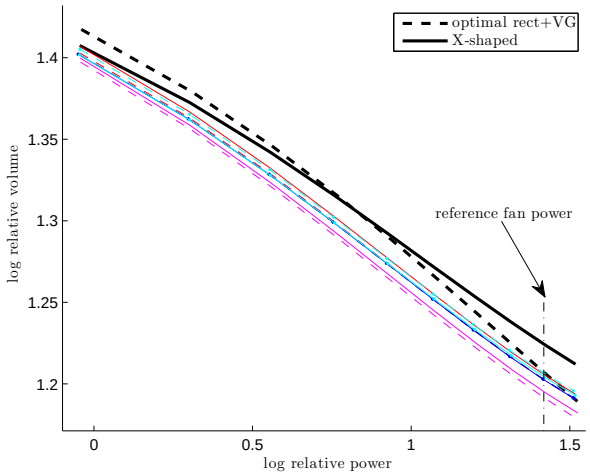

Figure 5.28: The performance in the power-volume plane of different variations on the Y-shaped design compared with the optimal compound rectangle louvres and vortex generator design and the X-shaped design. The legend for the coloured curves is the same as in figure 5.25

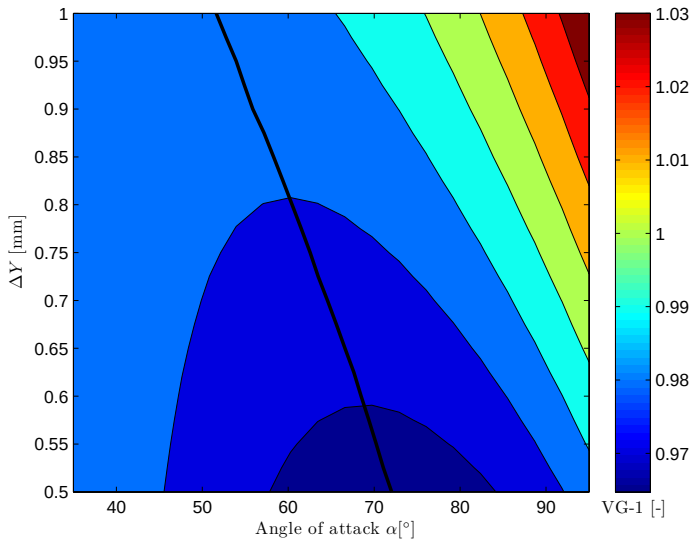

Figure 5.29: The influence of the vortex generator angle and positioning on the VG-1 criterion for the Y-shaped design. The black line indicates optimal vortex generator angles

5.5 Conclusions

Several methods were developed to optimise fin geometries under different boundary conditions. If a comparison is made between heat exchangers with the same mass flow rate, hydraulic diameter, inlet fluid temperature and fan power, it is important to take into account that the Reynolds number is different for each fin geometry. Using data from the Wang correlation, errors in the order of 45% resulted if this effect was neglected. A new method combining a gradient-based solver with a surrogate model is proposed to efficiently evaluate the fin performance while taking the Reynolds number influence into account. This method was applied to the optimisation of the X-shaped louvred fin geometry. It was shown that this method could be used to find the Pareto optimal fin geometry design. Alternatively, a multi-objective method could be used to determine the Pareto front, using EGO. However, this resulted in the exploration of an uninteresting region of the Pareto front, which was an artifact of the arbitrarily chosen limit on the velocities in the design space. Imposing a minimum fan power could resolve this issue. The optimal louvred fin design was found to be largely independent of the reference velocity. A louvre angle of 35°, a large louvred length and a large number of louvres was found to be optimal for the entire range of velocities from 0.5 to 2.6 m/s.

It was shown that the optimisation of a heat exchanger under the conditions for the VG-1 criterion implied that the heat exchanger length could vary significantly without affecting the Colburn j and friction factors. This was only possible for very large number of tube rows. For a realistic number of tube rows for air-conditioning applications in the order of three, variations of length must be accomplished by changing the longitudinal tube pitch. A method was developed to take this variation into account during optimisation. It was shown that if this effect was taken into account, an increase in the Reynolds number did not lead to a reduction in the heat exchanger volume as predicted if this effect was neglected.

As an alternative, optimisation under constraint of constant heat exchanger length and varying hydraulic diameter was presented. It was shown that the relative volume at constant fan power was given by the same equation as the area goodness factor. The dependence of the Reynolds number on the design was different from the case of constant hydraulic diameter. A louvre angle of 15° resulted in better performance than the design with a louvre angle of 35°.

A discussion on the optimisation of heat exchangers if the constraint on the mass flow rate was abandoned as presented. It was shown how the VG-1 criterion followed from parameter curves of constant mass flow rate in this more general method. An optimisation method of heat exchanger geometries for constant heat exchanger length and varying mass flow was is developed. The optimal geometry was shown to depend on the particular application. If a large heat exchanger length

was required, the plain fin performed quite well. On the other hand, for short heat exchangers the louvred fin geometry performed better. Depending on the actual constraints in industrial practice, the optimal fin geometry is different. This indicates that the optimal fin geometry found by a PEC analysis is therefore not necessarily optimal in practical applications.

Interaction effects on the modified Colburn j-factor were investigated for a compound rectangular louvres and vortex generator geometry. The louvre angle interacted with the aspect ratio and the height ratio of the vortex generator. The height ratio and the aspect ratio of the vortex generator also interacted strongly. If orthogonal arrays or fractional factorial designs are used, it is crucial to verify that these interactions are not aliased with main factor effects.

A performance screening of the compound louvred fin and vortex generator heat exchanger design was done. It was again confirmed that interaction effects were very important. These interaction effects could be present in two ways. The first was implicitly, due to the choice of the vortex generator positioning if other parameters such as angle of attack or aspect ratio changed. Even if no explicit positioning parameters were chosen, the result would depend on which part of the vortex generator was held fixed in position as other parameters changed. A second way occured if the positioning was explicitly taken into account as parameters. A clear dependence of the optimal vortex generator of attack on the minimum transversal distance between the vortex generator and the louvres was seen. The importance of the interaction was of the same order of magnitude as the primary effect of the angle of attack, it was also significantly more important than the positioning in the longitudinal direction. Using a full factorial sampling plan, which took all interaction effects into account, and polynomial surrogate models, the optimal compound louvred fin and vortex generator design was found. A reduction of 4% in heat exchanger volume could be obtained when compared with the X-shaped louvred fin. A new Y-shaped louvred and vortex generator fin design was proposed, which allowed reducing the volume by 7% with respect to the X-shaped louvred fin. The compound design performed increasingly better with respect to the X-shaped fin as the Reynolds number increased.

6

Fin efficiency in interrupted fin heat exchangers

6.1 Introduction

6.1.1 Overview

One of the results indicated in chapter 5 was that the thermal conductance was improved by increasing the number of and the area occupied by the louvres. Intuitively, it can be expected that the fin efficiency will decrease due to these modifications, as more interruptions are introduced close to the tubes. This decreases the available surface area for heat transfer in the fin material. For the same heat transfer rate, the heat flux and therefore the magnitude of the temperature gradient in the fin material increase. A greater conductive temperature drop in the fin material results in a decreased fin efficiency. Clearly, a quantitative investigation of the fin efficiency is required. Therefore, in this chapter, a discussion of fin efficiency in interrupted fin heat exchangers is presented.

First, a brief discussion on some practical issues in determining the fin efficiency is given. Next, a review of the scientific literature is given to reveal the different ways of dealing with fin efficiency. The review reveals that many authors use fin efficiency incorrectly when performing CFD simulations. Therefore, a thorough discussion on the meaning of fin efficiency in a heat exchanger is presented. The difference between the general definition of fin efficiency of paragraph 2.4.4 and the application in heat exchangers is highlighted. Some essential assumptions

are also explicitly addressed. A post-processing method is then proposed to determine the fin efficiency from CFD simulations without requiring extra calculations. This new method is applied to two different fin geometries and compared to an another approximate method requiring an additional CFD calculation.

6.1.2 Practical issues with fin efficiency

The performance of heat exchangers as a black box is often analysed by means of the LMTD (paragraph 2.4.2) or the effectiveness-NTU method (paragraph 2.4.3). The heat transfer rate is determined from the (numerical) experiment and using either method, the total thermal conductance UA is obtained. In the simple case where the heat transfer coefficient is infinitely large for one fluid and the thermal resistance due to conduction in the tube walls is neglected, the thermal conductance is given by equation (2.58).

$$UA = \eta_f h_{fin} A_{fin} + h_{base} A_{base} \qquad \text{(2.58 revisited)}$$

There are three unknowns in this equation: the fin efficiency η_f, the heat transfer coefficient for the fin h_{fin} and the heat transfer coefficient for the tube walls h_{base}. As was discussed in chapter 2, the fin efficiency corrects for the fact that the entire fin surface area is not at the base temperature, due to conductive temperature differences in the fin material itself. It was also discussed how the fin efficiency for a given surface could be obtained, if the heat transfer coefficient and temperature of the surrounding fluid were both known. However, in a practical heat exchanger application, the surrounding fluid temperature varies in space and the heat transfer coefficient is not known.

The heat transfer rate can be obtained from simulations or experiments, but it only allows determining the thermal conductance UA and not the contributing terms. Even if the simplifying assumption is made that the heat transfer coefficients are the same for the wall and for the fin surface, it is only possible to determine the product of the surface efficiency and the heat transfer coefficient. However, as the fin geometry is changed, both the heat transfer coefficient and the conductive path through the fin material change. In order to analyse the thermal impact of changes to the fin geometry, it is interesting to separate the fin efficiency effect from the heat transfer coefficient effect.

6.2 Fin efficiency in scientific literature

In the scientific literature, many authors have used a correlation to determine the fin efficiency. Wang et al. [3] used the Schmidt correlation [10] to determine the fin efficiency for a variety of louvred fin heat exchangers. As long as the same ex-

perimental conditions and correlation are used in later problems, the same thermal conductance can be recovered, even if the correlation is be inappropriate.

Tang et al. [50] used the Schmidt correlation for a variety of different fin geometries ranging from the plain fin to the compound louvred fin and delta winglet vortex generator designs. The fact that for a given heat transfer coefficient, the fin efficiency will be different for all these geometries is not taken into account. For fin designs where the Schmidt correlation overpredicts the actual fin efficiency, the heat transfer coefficient is underpredicted and vice versa.

Huisseune et al. [51] investigated the performance enhancement which could be obtained for the compound louvres and vortex generator fin design with respect to the regular louvred fin. The Schmidt correlation was again used to determine the fin efficiency. The fin performance was calculated based on the pure heat transfer coefficients. Physically, this corresponds to comparing heat exchangers with the same heat transfer coefficients as those obtained in the numerical experiment, but with an infinitely conducting fin. However, this can potentially lead to misleading results. Assume, for instance, that moving the vortex generator further away from the tubes does not change the heat transfer coefficient to any significant degree. The actual fin efficiency is increased because the punched hole in the fin surface is moved further away from the high heat flux region close to the tubes. As a result the thermal conductance UA is increased. As the Schmidt correlation does not predict the increase in fin efficiency, the heat transfer coefficient, which is obtained from the Schmidt correlation, is increased. The fin performance criterion therefore predicts an increase in the heat transfer rate for an infinitely conducting fin if the vortex generator is moved further away from the tubes. In reality, the fin efficiency increase does not occur for the infinitely conducting fin and the heat transfer is unchanged by moving the vortex generator.

In general, modifications to the fin geometry will change both the heat transfer coefficient and the fin efficiency and the total effect for an infinitely conducting fin will not be easy to determine. Artifacts caused by the fin efficiency can be avoided by basing the performance evaluation on the modified heat transfer coefficient, which predicts the heat transfer performance for a fin made of the same material and of the same thickness. This is a limitation on the scope of the performance criterion. Other researchers avoided this problem by performing numerical experiments directly for infinitely conduction fins, such as He at al. [53] and Hsieh and Jang [55]. The downside of this approach is that for a real fin, it is important to take the effect of the geometry on the fin efficiency into account. If a certain fin geometry results in a worse fin efficiency for a given material and fin thickness, more material will be required to obtain the same fin efficiency as a fin geometry which results in a better fin efficiency for the same conditions. In the opinion of the author, it is better to take the effect of the fin efficiency into account and evaluate the fin performance based on the modified heat transfer coefficient.

It has been established by several authors that the Schmidt correlation shows deficiencies for interrupted fin and round tube fin geometries. In these fin types, the surface is divided into smaller elements, which break up the thermal boundary layer. The local behaviour of the heat transfer coefficient is according to the thermal boundary layer: it decreases in value when moving away from the leading edge. As a result, the assumption of constant heat transfer coefficient used in the derivation of the fin efficiency correlation is clearly violated. Furthermore, in a fin and tube heat exchanger with air on the fin side, the objective is to exchange heat, resulting in a temperature change of the air stream as it passes over the fin. The assumption that the surrounding bulk temperature in a heat exchanger is constant is also not valid.

Huang and Shah [56] investigated the influence of the assumptions used in the Schmidt correlation and noted that a varying heat transfer coefficient can result in significantly lower values for the actual fin efficiency. For a particular linear profile of the heat transfer coefficient, deviations of up to 24% were seen. On the other hand, for fin efficiencies greater than 80%, the assumption of constant bulk temperature was shown to only have a very small influence if the heat transfer coefficient was constant. According to Teertstra et al. [57], this small effect on the fin efficiency can be treated by defining the driving temperature difference for convection as the difference between the fluid inlet temperature and the fin base temperature. However, it is unknown whether the influence of the bulk temperature remains small if the heat transfer coefficient is not constant.

Another assumption in the Schmidt correlation is that the heat conduction is one-dimensional and radial. Perrotin and Clodic [33] studied the effect of the interruptions on the conductive resistance. They applied a constant heat transfer coefficient and a constant bulk temperature as boundary conditions on an interrupted fin. Due to the interruptions in the fin material, the conductive resistance was increased and the fin efficiency decreased. They found that the Schmidt correlation overestimated the fin efficiency by up to 5%, as it did not take this effect into account. Since the varying heat transfer coefficient was also shown to decrease the fin efficiency by Huang and Shah, it is expected that taking both effects into account will result in an even lower value for the actual fin efficiency.

Song et al. [58] experimentally obtained the heat transfer coefficients on the fin surface using the naphthalene sublimation technique and the heat and mass transfer analogy. These values were then applied as boundary conditions to a numerical simulation, allowing for the calculation of the fin efficiency. In contrast to the previous studies, they found that the correlation underestimated the actual fin efficiency by up to 19.6%.

In computational fluid dynamics (CFD) studies of heat exchangers, the fin wall temperature is known at every point, which is very rarely the case for experimental studies. Furthermore, the entire flow field is also known. This allows for actually

calculating the fin efficiency, instead of having to rely on a correlation. It is also not necessary to impose invalid assumptions like constant surrounding fluid temperature, radial conduction or constant heat transfer coefficient. Wang et al. [59] calculated the fin efficiency as the ratio of the heat transfer rate of two separate simulations, one for the actual geometry and fin parameters and another one with an isothermal fin:

> *"The non-conjugate numerical method uses a uniform temperature on the fin surface, thus which is equivalent to unit fin efficiency, while other conditions that fin thermal conductivities combined with different flow conditions (Re) are equivalent to different fin efficiencies. Based on such think way, the numerical fin efficiency is determined as* $\eta_f = \frac{Q_{cou}}{Q_{non}}$ *where* Q_{cou} *is the heat transferred from fin to air using conjugate numerical method without considering conjugate heat transfer of the tubes and fluid flows inside the tubes,* Q_{non} *is the heat transferred from fin to air using non-conjugate method."*

This approach was also followed by Gao et al [60]. An and Choi [61] define the fin efficiency for a wavy fin and tube heat exchanger as follows:

> *"... defined as the ratio of actual heat-transfer rate, to the ideal maximum rate."*

These definitions correspond to the definition given in paragraph 2.4.4, where the fin efficiency was given for an application where the temperature of the surrounding fluid is constant. In the next paragraph, it will be shown that this definition is fundamentally wrong for determining the fin efficiency of heat exchangers.

6.3 Meaning of fin efficiency in a fin and tube heat exchanger

The fin efficiency is commonly defined as the ratio of the actual heat transfer rate of a fin to its ideal heat transfer rate if the entire fin were at the same temperature as its base [62]. It is important to note that the definition is for a fin where the temperature of the surrounding fluid is a constant. Specifically, the temperature of the surrounding fluid is independent of the heat transfer rate from the fin. In a heat exchanger, the bulk temperature does in fact change due to the transferred heat. Nevertheless, some authors still define the fin efficiency in this way for heat exchangers, such as Wang et al., Gao et al. and An and Choi. It will now be shown that this approach can provide quite erroneous results.

When sizing a heat exchanger using correlations with a convective resistance for a single fluid and a constant base temperature, the thermal transmittance is

equal to the product of the heat transfer coefficient of the fin surface and the fin efficiency. If the heat transfer rate from the tubes is neglected, the heat transfer rate for the fin can be determined from the effectiveness-NTU method. For the sake of simplicity, the temperature of the tube wall is held constant. This corresponds to evaporating or condensing flow inside of the tubes, with the fluid of interest flowing over the tubes and the fin surface. It is this fluid of interest which changes in temperature.

$$\begin{aligned} \dot{Q}_{fin} &= C\Delta T_{max}(1 - exp(-\frac{U_{fin}A_{fin}}{C})) \\ &= C\Delta T_{max}(1 - exp(-\frac{\eta_f h_{fin}A_{fin}}{C})) \end{aligned} \tag{6.1}$$

Since there is only one fluid, the subscript min is omitted from the heat capacity rate C. U is the thermal transmittance, equal to the product of the heat transfer coefficient for the fin h_{fin} and the fin efficiency η_f. ΔT_{max} is the temperature difference between the constant tube wall (or base) temperature and the fluid at the inlet of the heat exchanger. In this work, it will always be assumed that η_f is defined in such a way that equation 6.1 is correct for a case where the heat transfer coefficient is constant. Consider a given surface area, fin geometry, fin material, fin base temperature as well as a flow with a given heat capacity rate and inlet temperature. If the heat transfer coefficient is known, it is possible to compute the heat transfer rate. The symbol η_f, which corresponds to the concept of fin efficiency is then fully defined by equation 6.1. Physically this implies that the fin efficiency must be equal to the ratio of the thermal transmittance of the real fin to the thermal transmittance of the ideal perfectly conducting fin.

Now, the fin efficiency will be determined using the definition used by An and Choi [61] based on the ratio of heat transfer rates. This requires evaluating the ideal maximum heat transfer rate. The heat transfer rate for the case of infinitely conducting isothermal fins can easily be obtained by setting the fin efficiency equal to unity in equation (6.1). The fin efficiency as defined by Wang et al. or An and Choi can then be obtained by taking the ratio of the actual heat transfer rate given by equation (6.1) and the ideal maximum rate obtained by setting the fin efficiency to one in the same equation. The result is given by equation (6.2). This calculation should result in η_f, which is the fin efficiency as defined to be compatible with equation 6.1.

$$\frac{\dot{Q}_{fin}}{\dot{Q}_{fin,isothermal}} = \frac{1 - exp(-\frac{\eta_f h_{fin}A_{fin}}{C})}{1 - exp(-\frac{h_{fin}A_{fin}}{C})} \tag{6.2}$$

It is clear, however, that this expression is not equal to the fin efficiency η_f. Regardless of the actual fin efficiency used in the thermal transmittance relation, the ratio goes to one if the number of transfer units (NTU) for the fin $\frac{h_{fin}A_{fin}}{C}$

goes to infinity. Consider, for example, the case where a very inefficient fin is used, so that changing the fin material to a perfectly conducting material would result in a doubling of the thermal conductance UA. According to equation 6.1, the fin efficiency of this fin is then only 50%. However, if one would calculate the fin efficiency of the fin by applying equation 6.2, defining the fin efficiency as the ratio of heat transfer rates between the actual and the perfectly conducting case, the result depends on the NTU. If the NTU goes to infinity, this corresponds to an infinitely large heat exchanger making use of this inefficient fin. In this case, both the actual heat transfer rate $\dot{Q}_{fin}$ and the theoretical isothermal heat transfer rate $\dot{Q}_{fin,isothermal}$ converge to the maximum possible heat transfer rate $Q_{max} = C\Delta T_{max}$. The ratio given by equation 6.2 then converges to one, regardless of the thermal performance of the fin. It makes sense that a fin efficiency of 50% should be obtained by the method which is used to determine the fin efficiency, as the real fin has exactly half of the thermal conductance of the ideal fin.

The physical reason for this discrepancy is elucidated by considering the LMTD method. This also allows conducting the analysis without having to neglect the heat transfer from the tubes. The total heat transfer in the heat exchanger is separated into two contributions, corresponding to the tube and the fin respectively. The tube wall temperature is assumed to be constant, the corresponding cross-flow factor F is then equal to one.

$$\dot{Q}_{total} = \dot{Q}_{tube} + \dot{Q}_{fin} = (h_{tube}A_{tube} + h_{fin}A_{fin})\, LMTD \tag{6.3}$$

The fin efficiency as used in the LMTD method is given by equation (6.4) [8].

$$\eta_f = \frac{\dot{Q}_{fin}}{h_{fin}A_{fin}LMTD} \tag{6.4}$$

Applying the equation for the LMTD (2.45) to this specific case with a single fluid in contact with a constant temperature T_{base} results in equation (6.5).

$$LMTD = \frac{(T_{base} - T_{fluid,in}) - (T_{base} - T_{fluid,out})}{ln(\frac{T_{base}-T_{fluid,in}}{T_{base}-T_{fluid,out}})} \tag{6.5}$$

If the heat transfer coefficient is constant, the LMTD is also given by integrating the local temperature difference over the entire fin surface (6.6) [8]. The bulk temperature is another name for the adiabatic mixing cup temperature. It is assumed that the LMTD remains the same whether this integral is performed only over the fin surface area or over the entirety of the heat exchanger surface. This is a reasonable assumption since equation (6.5) is valid regardless of the surface used to integrate the temperature difference over, hence there is only a single LMTD. Essentially, this boils down to assuming that the fin surface is smeared out uniformly over the tube surface and that integrating over a certain percentage of the

tube surface corresponds to integrating over the same percentage of the fin surface. If this is not a reasonable simplification, then the temperature profile is not exponential and equation (6.5) is not valid.

$$LMTD = \frac{1}{A}\int_{A_{total}} T_{base}(A) - T_{bulk}(A)dA \tag{6.6}$$

The bulk temperature changes in the heat exchanger due to the heat transfer from the fin and from the tubes, as expressed by the energy balance equation, are given by the first equation of (2.43).

$$d\dot{Q} = \dot{m}_1 C_{p1} dT_1 = \dot{m}_2 C_{p2} dT_2 \tag{2.43 revisited}$$

The heat transfer from the tube walls will change the bulk temperature, and therefore also the exit temperature and the LMTD, independently of the heat transfer from the fin surface. By using the LMTD instead of the effectiveness-NTU relation, no assumptions regarding the contribution of the tubes to the total heat transfer rate are required. The local heat transfer coefficient on the tube surface can be different from the local heat transfer coefficient of the fin. Only the fin is examined and the balance equation (2.43) will not be used, as the tube heat transfer rate is not of interest.

The LMTD is not the actual driving temperature difference between the fin and the bulk fluid, as the fin temperature in general differs from the base temperature. The fin efficiency is defined to compensate for this temperature difference between the fin body and base. If a single constant heat transfer coefficient is assumed for the entire fin surface, the heat transfer rate of the fin is given by equation (6.7).

$$\dot{Q}_{fin} = \int_{A_{fin}} h_{fin}(T_{fin}(A) - T_{bulk}(A))dA = \eta_f h_{fin} A_{fin} LMTD \tag{6.7}$$

If a second calculation is done where the entire fin is at the base temperature (isothermal ideal fin), the heat transfer rate to the fluid changes. As a consequence, the bulk temperature and the LMTD change as well. If the fluid properties are not constant, the increased heat transfer also changes the density, the velocity as well as the fluid viscosity at the wall and therefore also the heat transfer coefficient. Neglecting the temperature dependence of the fluid properties, the heat transfer coefficient is unchanged if the fin is made isothermal. The heat transfer rate is given by equation (6.8).

$$\dot{Q}_{fin,id} = \int_{A_{fin}} h_{fin}(T_{base}(A) - T_{bulk,id}(A))dA = h_{fin} A_{fin} LMTD_{id} \tag{6.8}$$

The LMTD is not equal to the LMTD used in the definition for the fin efficiency in equation (6.4). Since the heat transfer rate has increased, the outlet

temperature has also increased, changing the LMTD according to equation (6.5). As a consequence, the ratio of the actual heat dissipation and the ideal dissipation is not in general equal to the definition of the fin efficiency for heat exchangers as given by equation (6.1).

$$\frac{\dot{Q}_{fin}}{\dot{Q}_{fin,id}} = \eta_f \frac{LMTD}{LMTD_{id}} \tag{6.9}$$

This difference is especially visible for high effectiveness heat exchangers. Consider, for example, the very simple case of figure 6.1. A plain fin is heated from both sides by a base surface at a fixed temperature. Colder fluid flows above and below the fin surface. The walls of the base surface in contact with the fluid are assumed to be adiabatic. For each position in this rudimentary heat exchanger, the surface area seen by the bulk flow can be determined. This area is simply twice the fin width multiplied by the x distance from the inlet. For each position, the bulk temperature can also be determined, which allows plotting the bulk flow temperature as function of the heat transfer surface area. For a fixed x-position and thus a fixed area, the fin temperature still varies in the y-direction. At the base surface, the fin temperature is equal to the temperature of the base surface, further away from the base surface, the fin temperature changes due to the conductive temperature drop in the fin material. Nevertheless, a single fin temperature can be associated with every surface area position by averaging transversally.

As the surface area encountered by the flow increases, the bulk temperature increases. As a consequence, the heat transfer rate between the flow and the base surface decreases. The decreased heat transfer rate results in a lower heat flux in the fin material and therefore a smaller conductive temperature drop. Therefore, just like the bulk flow temperature, the fin temperature approaches the base temperature as the surface area encountered by the flow increases.

The theoretical temperature profiles as a function of the surface area for a heat exchanger with 90% effectiveness are shown in figure 6.2. The dimensionless temperature is defined in equation (6.10).

$$\Theta = \frac{T - T_{fluid,in}}{T_{base} - T_{fluid,in}} \tag{6.10}$$

The baseline case is a heat exchanger where the dimensionless fin temperature at each location is the average of the local bulk temperature and the base temperature. The tube heat transfer rate is neglected. The heat exchanger is quite large, so that the effectiveness is equal to 90%, as can be seen from the dimensionless bulk temperature at the outlet. The fin is then changed to an infinitely conducting fin. The fin temperature then becomes equal to the base temperature at each point. The heat transfer rate is only slightly increased (plus 9 percentage points), to an effectiveness of 99%, which is quite close to the theoretical maximum of 100%. In

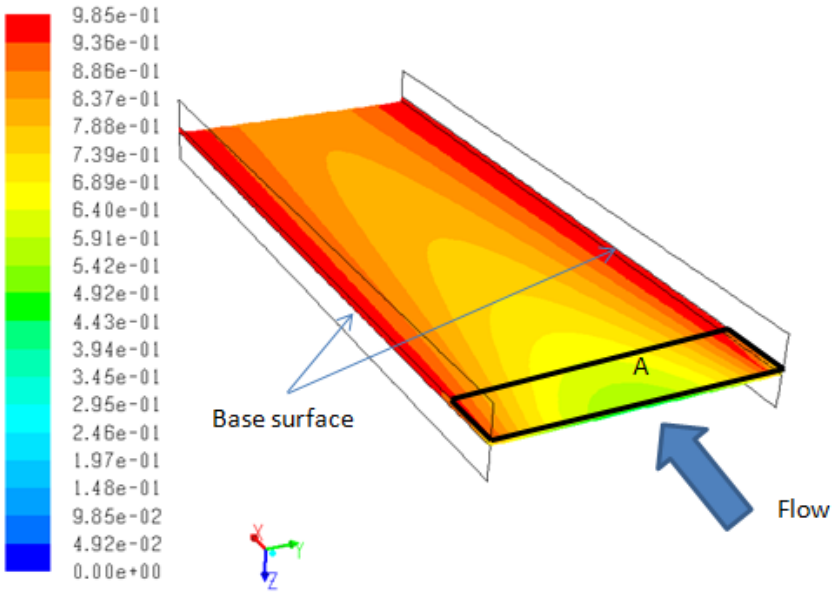

Figure 6.1: Schematic example of the fin temperature

the first case, the LMTD is equal to 0.39. In the case of the perfectly conducting fin, the outlet bulk temperature is increased due to the increased heat transfer rate, reducing the LMTD to 0.215.

If the influence of the changing LMTD would be neglected by just taking the ratio of the actual heat transfer rate to the ideal heat transfer rate for an isothermal fin, the obtained fin efficiency would be $90\%/99\% = 91\%$. However, by including the LMTD terms, the actual fin efficiency was 50%. This is a logical result, as the fin temperature was exactly halfway between the original bulk temperature and the base temperature at every position in the heat exchanger. It will be shown later that under certain conditions, the fin efficiency can be interpreted as the dimensionless fraction $\frac{T_{fin}-T_{bulk}}{T_{base}-T_{bulk}}$. This is the same definition as used by Tao et al. [63] for the local fin efficiency.

To avoid the ratio of LMTDs appearing in equation (6.9), the ideal heat transfer that is required as a reference is the *fictitious ideal heat transfer if the entire fin were at the same temperature as its base, and if the driving temperature difference were still the same*. In order to keep the driving temperature difference from changing, the bulk temperature must be held constant. To maintain the bulk temperature at its original value at each point in the heat exchanger, a fictitious heat transfer rate is required to remove the additional heat transferred due to the now uniform fin temperature. The total fictitious ideal heat transfer is the sum of the

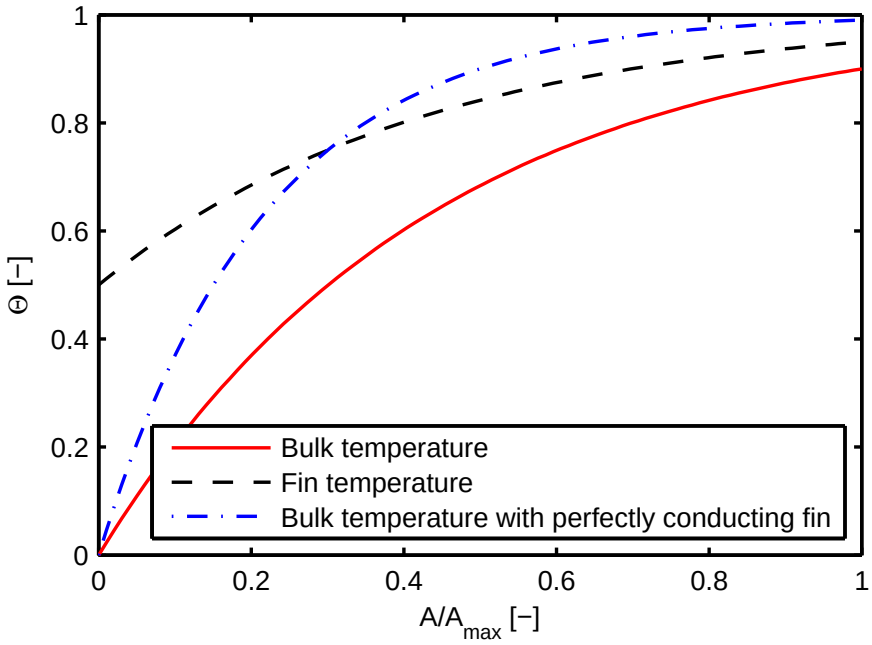

Figure 6.2: Theoretical dimensionless temperature profiles for heat exchanger with 90% effectiveness

actual heat transfer from the fin and all the fictitious heat transfer that would be required in order to maintain the bulk temperature at its old temperature (in absolute values). This fictitious ideal heat transfer rate is exactly the same reference heat transfer rate used for the definition of the fin efficiency in paragraph 2.4.4, since the bulk temperature was assumed constant in that case. The only difference is that the bulk temperature is physically not constant in the case of a heat exchanger application. The reference ideal heat transfer rate is therefore not a physical quantity but a fictitious one.

The driving temperature difference for this fictitious heat transfer rate is the difference between the original bulk fluid temperature and the fin base temperature. This corresponds to the LMTD used in the definition of the fin efficiency. The corresponding fictitious heat transfer rate can be obtained by replacing the local fin temperature by the base temperature at every point of the heat exchanger in equation (6.7). The resulting fictitious reference heat transfer rate is given by equation (6.11).

$$\dot{Q}_{fin,id,fict} = \int_{A_{fin}} h_{fin}(T_{base}(A) - T_{bulk}(A))dA = A_{fin}h_{fin}LMTD \tag{6.11}$$

In this equation, the driving temperature difference is the difference between the fin base temperature and the old bulk temperature obtained for a non-ideal fin. With this definition of the ideal heat transfer, the ratio of the actual heat transfer rate (6.7) and the ideal heat transfer rate (6.11) becomes the fin efficiency as defined for heat exchangers shown in equation (6.12).

$$\frac{\dot{Q}_{fin}}{\dot{Q}_{fin,id,fict}} = \frac{\eta_f A_{fin}h_{fin}LMTD}{A_{fin}h_{fin}LMTD} = \eta_f \tag{6.12}$$

Note that when the bulk temperature of the fluid is constant as is done for the definition of the fin efficiency given in paragraph 2.4.4, the logarithmic mean temperature differences of the real case and the ideal case are the same. Both are equal to the temperature difference between the constant base temperature and the constant bulk temperature, the ratio of LMTDs is therefore equal to unity. In this case, the ratio of the heat transfer rates is in fact equal to the ratio of thermal transmittances and therefore compatible with the fin efficiency as defined using equation (6.1). Equation (6.13) gives an alternative form as a function of the local temperatures.

$$\eta_f = \frac{\dot{Q}_{fin}}{\dot{Q}_{fin,id,fict}} = \frac{\int_{A_{fin}} h_{fin}(T_{fin}(A) - T_{bulk}(A))dA}{\int_{A_{fin}} h_{fin}(T_{base}(A) - T_{bulk}(A))dA} \tag{6.13}$$

If, instead of taking the ratio of the total heat transfer rate and the total fictitious ideal heat transfer rate, the same ratio is made on a local heat flux basis, the local fin efficiency is obtained.

$$\eta_{f,local}(A) = \frac{d\dot{q}_{fin}}{d\dot{q}_{fin,id,fict}} = \frac{h_{fin}(T_{fin}(A) - T_{bulk}(A))}{h_{fin}(T_{base}(A) - T_{bulk}(A))} \tag{6.14}$$

This is the definition used by Tao et al. [63]. It can be argued that the term *local fin efficiency* is a misnomer, since the supposedly local value depends on conditions of the entire fin. For example, a temperature drop between the base surface and the fin due to a bad connection results in lower values of the local fin efficiency everywhere. There is no simple link between the local fin efficiency and the regular fin efficiency, unless the local fin efficiency is constant. In that case, the local values are equal to the global fin efficiency. Indeed, the integrand of the numerator is proportional to the integrand of the denominator in equation (6.13). The proportionality constant is equal to the local fin efficiency. Equation

(6.14) can also be interpreted as a thermal resistance network, following a heat flux line from the tube at base temperature to a point on the fin surface. The total temperature difference along this line $\Delta T(A)$ consists of two contributions: a conductive temperature drop in the fin material, and a convective temperature drop in the convective boundary layer. These temperature drops are the product of a thermal resistance and the heat transfer rate, whhis is expressed by equations (6.15) and (6.16).

$$\begin{aligned}\Delta T(A) &= T_{base}(A) - T_{bulk}(A) \\ &= (T_{base}(A) - T_{fin}(A)) + (T_{fin}(A) - T_{bulk}(A))\end{aligned} \tag{6.15}$$

$$\Delta T(A) = R_{total}\dot{Q} = (R_{conductive,fin} + R_{fin,convective})\dot{Q} \tag{6.16}$$

The convective resistance per unit of heat transfer rate is the numerator of equation (6.14), whereas the denominator is the total resistance per unit of heat transfer. The local fin efficiency expresses the fraction of the total heat transfer resistance, which is due to the convective resistance. If the fin efficiency is one, the entire thermal resistance is due to the convective resistance, corresponding to a perfectly conductive fin.

In conclusion, it is incorrect to say that the fin efficiency for a heat exchanger is equal to the ratio of the heat transfer rate of a real fin to the heat transfer rate of the ideal perfectly conducting fin. Instead, the ratio of thermal transmittances must be used. It is only in the case of the bulk fluid temperature being independent of the heat transfer rate that both definitions agree.

Nevertheless, it is still possible to express the fin efficiency as a ratio of heat transfer rates. However, the ideal case to be compared with in the definition of the fin efficiency is not a physical case. It is not the heat transfer rate in the case of isothermal fins, but a fictitious heat transfer rate, which would occur if the bulk temperature remained unchanged by the change in fin material. The assumption of constant heat transfer coefficient is absolutely crucial in the development of the theory presented above. It is what allows the fin efficiency definition to be compatible with the LMTD (and effectiveness-NTU) method for the design of heat exchangers. In that case, the local fin efficiency has a physical interpretation as the ratio of convective heat transfer resistance to the total heat transfer resistance. If this ratio is constant for the entire fin surface, the interpretation is also valid for the global fin efficiency. In what follows, the assumption of constant heat transfer coefficient is abandoned and a definition of the fin efficiency in the case of varying local heat transfer coefficient is proposed.

6.4 Accounting for a variation in the heat transfer coefficient

In real heat exchangers, the heat transfer coefficient is not constant over the fin surface area. Even in plain fin heat exchangers, there is variation due to the presence of horseshoe vortices shed by the tubes or the formation of a wake zone. Complex interrupted fins have a strongly varying heat transfer coefficient due to the constant restarting of the boundary layers. The variation of the heat transfer coefficient significantly complicates matters. The local heat transfer coefficient is defined by equation (6.17), where $\dot{q}$ is the local heat flux.

$$h_{local}(A) = \frac{\dot{q}}{T_{fin}(A) - T_{bulk}(A)} \tag{6.17}$$

By integrating over the fin surface, the total heat transfer rate given by equation (6.18) is obtained.

$$\begin{aligned} \dot{Q}_{fin} &= \int_{A_{fin}} h_{local}(A)(T_{fin}(A) - T_{bulk}(A))dA \\ &= \int_{A_{fin}} h_{local}(A)\eta_{f,local}(A)(T_{base}(A) - T_{bulk}(A))dA \end{aligned} \tag{6.18}$$

Under the assumption that the product of the local heat transfer coefficient and the local fin efficiency is constant, the expression reduces to the well-known LMTD result.

$$\begin{aligned} \dot{Q}_{fin} &= h_{local}\eta_{f,local} \int_{A_{fin}} (T_{base}(A) - T_{bulk}(A))dA \\ &= U_{fin}A_{fin}LMTD \end{aligned} \tag{6.19}$$

However, in real interrupted fin heat exchangers, neither the local heat transfer coefficient nor the local fin efficiency is constant. In general, the product of the two is not constant either. Separately averaged values for the heat transfer coefficient and the local fin efficiency can be reported as was done by Tao et al. [63], but it is important to note that their product is not equal to the thermal transmittance U_{fin}. The thermal transmittance is the average of the product, which is not in general equal to the product of the averages.

A second issue is that due to the strong fluctuations in the heat transfer coefficient, the bulk temperature does not have an exactly exponential profile. Hence, the LMTD method is no longer the surface-averaged temperature as described by equation (6.6). The difference between the actual driving temperature difference and the assumed logarithmic mean temperature difference is another issue when

using the thermal transmittance idea. Furthermore, if the thermal transmittance is not constant, there is interaction between it and the temperature profile. If high regions of thermal transmittance correspond to areas of large driving temperature difference, the total heat transfer rate is greater than if they correspond to areas of low driving temperature difference. The problem is now to define reasonable characteristic values for the fin efficiency and the heat transfer coefficient, given that there is interaction between the local behaviour of the temperature profile, the heat transfer coefficient and the local fin efficiency.

In realistic cases where neither the local fin efficiency, the heat transfer coefficient nor their product are constant, it is no longer possible to separate the heat transfer coefficient from the temperature profiles, since both are functions of the local position. The thermal transmittance can still be obtained from equation (6.20), using the LMTD method. Errors due to the mismatch between the assumed exponential temperature profile and the actual temperature profile are lumped into the thermal transmittance.

$$U_{fin} = \frac{\dot{Q}_{fin}}{A_{fin} LMTD} \tag{6.20}$$

The thermal transmittance now needs to be separated into a global heat transfer coefficient and a global fin efficiency. Taking the difference between the bulk temperature and the local fin temperature as driving temperature difference and the actual local values for the heat flux, local values of the heat transfer coefficient h_{local} can be obtained from equation (6.17). With these local values, the total fictitious ideal heat transfer rate in case of varying heat transfer coefficient can be calculated from equation (6.21).

$$\dot{Q}_{fin,id,fict} = \int_{A_{fin}} h_{local}(A)(T_{base}(A) - T_{bulk}(A))dA \tag{6.21}$$

Now the global heat transfer coefficient can be defined as the *fictitious constant heat transfer coefficient, which gives the same fictitious ideal heat transfer rate as the real local heat transfer coefficients, if the fin temperature is constant and equal to the base temperature*.

$$h_{fin} = \frac{\dot{Q}_{fin,id,fict}}{A_{fin} LMTD} \tag{6.22}$$

Note that the driving temperature difference here is the LMTD. This assumes an exponential profile for the bulk temperature. This is only valid if the heat transfer coefficient is constant. In general, the real bulk temperature profile deviates from the exponential profile. The local heat transfer coefficients were determined by comparison with the real local bulk temperature. Also note that this heat transfer coefficient is not equal to the surface average of the local heat transfer coeffi-

cients, due to interaction between the temperature profile and the local heat transfer coefficients.

The fin efficiency is still defined as the ratio between the actual heat transfer rate and the ideal fictitious heat transfer rate (equation (6.23)), where the heat transfer coefficient h_{fin} is now obtained from equation (6.22).

$$\begin{aligned}\eta_f &= \frac{\dot{Q}_{fin}}{\dot{Q}_{fin,id,fict}} = \frac{\int_{A_{fin}} h_{local}(A)(T_{fin}(A) - T_{bulk}(A))dA}{\int_{A_{fin}} h_{local}(A)(T_{base}(A) - T_{bulk}(A))dA} \\ &= \frac{\dot{Q}}{h_{fin}A_{fin}LMTD}\end{aligned} \tag{6.23}$$

The global heat transfer coefficient h_{fin} accounts for the interactions between the local heat transfer coefficient and the temperature profile, as well as deviations from the exponential bulk temperature profile. It is a fictitious constant heat transfer coefficient which gives the same heat transfer rate as the real varying one, if the LMTD is used instead of the actual driving temperature difference. The fin efficiency accounts for the deviation of the fin temperature from the base temperature. The thermal transmittance can be determined from equations (6.20) and (6.23).

$$U_{fin} = \frac{\dot{Q}_{fin}}{A_{fin}LMTD} = \frac{\eta_f h_{fin} A_{fin} LMTD}{A_{fin}LMTD} = \eta_f h_{fin} \tag{6.24}$$

With these definitions, the fin efficiency becomes 1 if the fin temperature is equal to the base temperature at every point and 0 if the fin temperature is equal to the bulk temperature at every point. This is the same behaviour as in the theoretical case of a constant heat transfer coefficient. Furthermore, these definitions are compatible with the commonly used LMTD and effectiveness-NTU methods and the constraint that the product of the thermal transmittance is equal to the product of fin efficiency and heat transfer coefficient is respected. These definitions are necessary because of the strong fluctuations in heat transfer coefficient and local fin efficiency in interrupted fin and tube heat exchangers, which interact with each other and with the locally varying bulk temperature. These definitions will be used in the remainder of this work.

6.5 Determining the fin efficiency as a post-processing step for conjugate heat transfer CFD simulations

The previously described theory can now be applied to obtain fin efficiency data from a CFD simulation as a post-processing step.

The fin efficiency is given by equation (6.23). Every factor can be determined in a straightforward manner from the CFD data, with the exception of the global

heat transfer coefficient h_{fin}, which needs to be calculated from equations (6.21) and (6.22). In order to do this, the bulk temperature and the local heat transfer coefficient are required for every point on the fin surface. Using equation (6.17), the latter can be obtained from the bulk temperature and known quantities. Once the bulk temperature has been found, the fin efficiency can be calculated from the aforementioned equations. The local bulk temperature is defined as in Wang et al. [59], by taking the adiabatic mixing cup temperature over cross-sections perpendicular to the inlet velocity vector and assuming fluid properties are constant. If the X-axis is aligned with the inlet velocity vector, this corresponds to equation (6.25). The mixing cup temperature is evaluated at 200 discrete positions in the heat exchanger along the X-axis. In the equation, u is the component along the X-axis of the fluid velocity vector.

$$T_{bulk}(x_i) = \frac{\int\int T(x_i, y, z)u(x_i, y, z)dydz}{\int u(x_i, y, z)dydz} \tag{6.25}$$

A piecewise linear continuous approximation is used to know the bulk temperature in each position of the heat exchanger. This allows evaluating the heat transfer coefficient at every point on the fin surface.

$$h(x, y, z) = \frac{\dot{q}(x, y, z)}{T_{fin}(x, y, z) - T_{bulk}(x)} \tag{6.26}$$

The ideal fictitious heat flux can now be determined for each point. The total fictitious heat transfer rate can then be determined by applying equation (6.21) and integrating this ideal flux over the entire fin surface.

$$\dot{Q}_{fin,id,fict} = \int\int_{A_{fin}} h(x, y, z)(T_{base} - T_{bulk}(x))dA \tag{6.27}$$

By applying equation (6.23), the fin efficiency is obtained. This method can be applied as a post-processing step to any CFD conjugate heat transfer calculation as it only requires information which can be readily obtained from a single simulation. The entire process is shown schematically in figure 6.3.

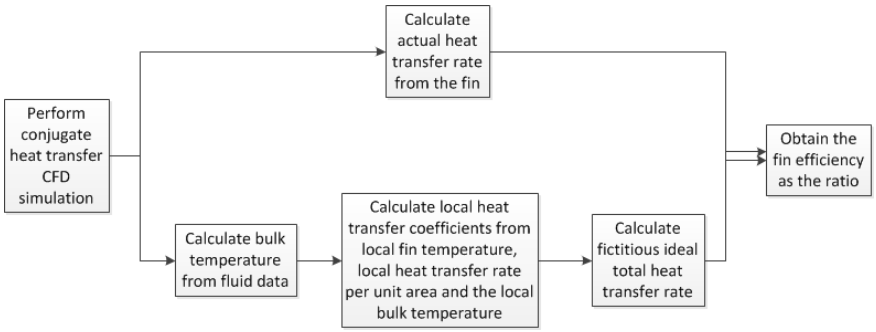

Figure 6.3: Schematic representation of the post-processing method

6.6 Application to the rectangular louvred fin

6.6.1 Results of the post-processing method

The method will now be applied to the case of a rectangular louvred fin heat exchanger with three tube rows operating with a frontal velocity of 2.69 m/s. Table 6.1 shows the geometrical parameters for this fin.

Parameter name	value
Outer-tube diameter	6.75 mm
Fin thickness	0.12 mm
Fin pitch	1.71 mm
Transversal tube pitch	17.6 mm
Longitudinal tube pitch	13.6 mm
Louvre pitch	1.5 mm
Louvre angle	28°

Table 6.1: Geometrical parameters

Figure 6.4 shows the dimensionless temperature Θ on the fin surface. It is clear that the fin conduction is not one-dimensional in the radial direction, as assumed in the Schmidt correlation. This was already noted by Perrotin and Clodic [33]. The conduction in the fin material is perpendicular to isotherms and shows a strong alignment with the louvres. The fin temperature increases with increasing tube rows. This is to be expected, since the bulk temperature increases, resulting in a decrease of the driving temperature difference with respect to the base temperature. As such, the heat transfer rate through the fin is lower for the more downstream tube rows, which causes a lower temperature drop through the fin.

The local fin efficiency is shown in figure 6.5. The local fin efficiency tends to decrease with increasing distance from the tube rows. The influence of the bulk

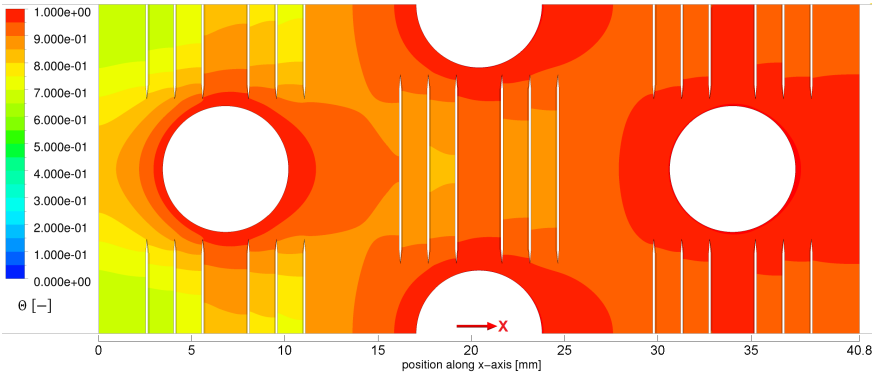

Figure 6.4: Dimensionless fin temperature

temperature is removed, which reveals that the behaviour of the local fin efficiency is quite similar for all tube rows. Small differences are caused by the development of the flow and the temperature dependence of the fluid properties.

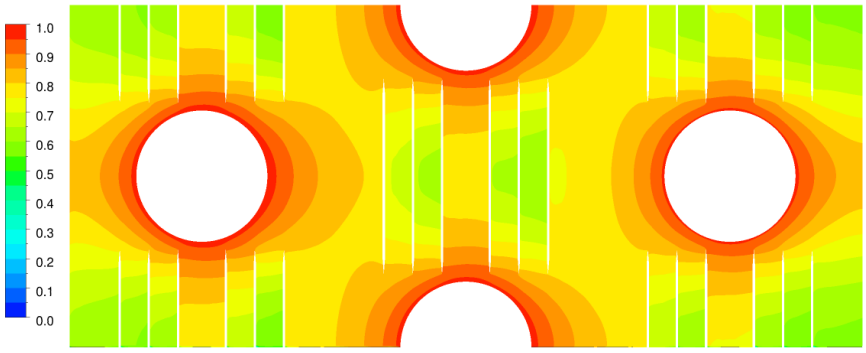

Figure 6.5: Local fin efficiency of Tao et al. [63]

In figure 6.6, the different temperatures in the heat exchanger are displayed as a function of the X-axis, which is parallel to the free-stream inlet velocity in front of the heat exchanger. The fin temperature T_{fin} is averaged transversally to represent it on a two-dimensional graph. The exponential bulk temperature T_{LM} is defined as the exponential temperature profile which, attains the same temperatures as the real temperature profile at the inlet and exit of the heat exchanger. The deviation with the real adiabatic mixing cup temperature T_{bulk} obtained by transversal averaging is small. Using the LMTD instead of the actual driving temperature difference gives only a small deviation. The theoretical fin temperature $T_{fin,theo}$ is defined as the fin temperature, which has a constant local efficiency

as defined by Tao et al. [63] as well as a constant heat transfer coefficient over the entire fin surface and which transfers the same amount of heat as the real fin. The fin temperature T_{fin} increases as the bulk temperature T_{bulk} increases. This was already identified based on figure 6.4.

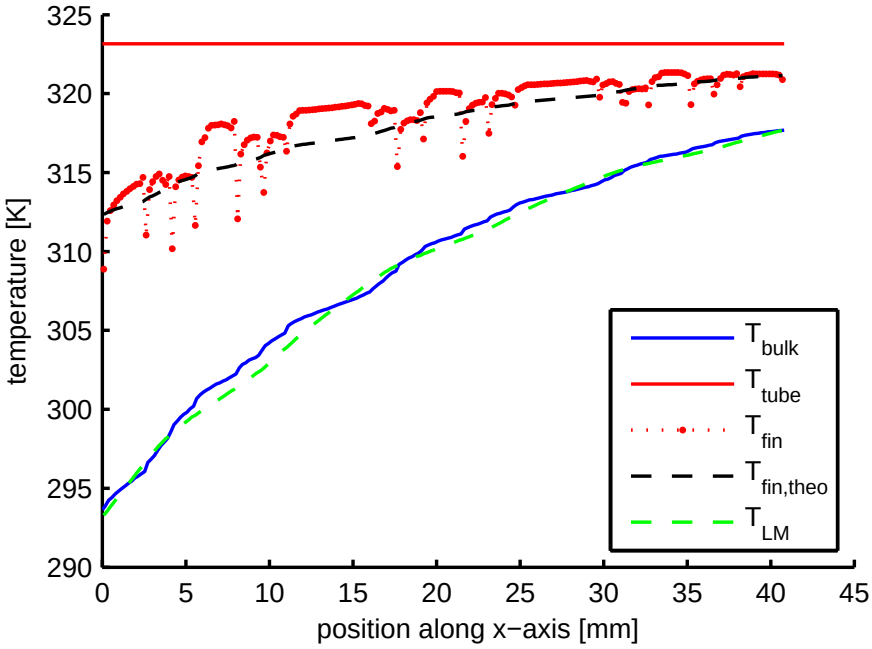

Figure 6.6: Transversally averaged temperature profiles in the heat exchanger

Figure 6.7 shows the distribution of the local heat transfer coefficient h_{local} on the bottom of the fin surface, according to the definition of equation (6.27). The growing temperature boundary layer at the leading edge of the fin at the entrance of the heat exchanger core is clearly seen by the decrease in the heat transfer coefficient. Due to restarting boundary layers at the leading edge of each louvre, the heat transfer coefficient is again very high at this location. This can best be seen in the louvres around the first tube row, as the flow at the inlet of these louvres is much more uniform in temperature than for the downstream louvres. The flow around the louvres of the first tube row is shown in figure 6.8. The growing thermal boundary layers are clearly visible. In the subsequent tube rows, the flow has been disturbed by the presence of the upstream tubes and louvres. Part of the flow bypasses the louvres in a high-velocity jet, and is therefore colder than the average flow temperature at that location. For the first tube row this is indicated in figure 6.7. This colder fluid flows through the downstream louvres of the second tube

row, causing a higher heat transfer rate on the fin surface than on the parts of the louvres which are in thermal contact with the warmer flow that has passed through the previous louvres. Since the bulk temperature is the same for all parts of the louvres at the same x-coordinate, this higher heat transfer rate is translated into a higher heat transfer coefficient. A second reason for these regions of high heat transfer coefficient adjacent to the tube wakes is that the velocity of the bypass jet is significantly (50%) larger than the velocity of the surrounding fluid. The increased velocity results in an increased local heat transfer rate and thus in an increased heat transfer coefficient. The tube wakes are clearly seen to be areas of very low heat transfer coefficient, due to the slow-moving fluid in this region. Again, the tube wakes are local regions of high temperature with respect to the bulk temperature, further lowering the obtained value of the heat transfer coefficient. In between the louvres and the tubes, the heat transfer coefficient is noticeably lower. This is due to the recirculation downstream of the last louvre, which causes a thicker thermal boundary layer and therefore a lower local heat transfer coefficient.

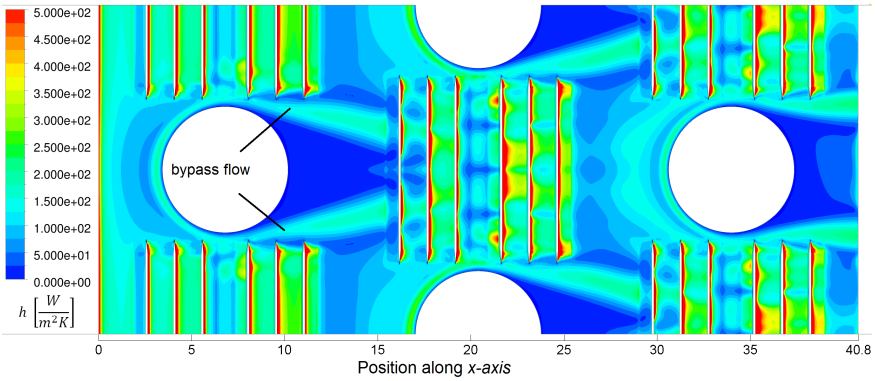

Figure 6.7: Heat transfer coefficient on the bottom of the fin

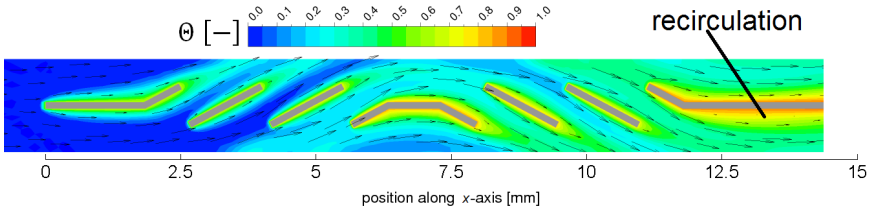

Figure 6.8: Dimensionless temperature and flow in the louvres around the first tube row

From the logarithmic mean temperature and the fin heat transfer rate, the ther-

mal transmittance U_{fin} is determined equal to 121.34 W/m^{2}K. According to the previously discussed method, the fin efficiency η_f is equal to 75.14%. The corresponding global heat transfer coefficient h_{fin} is 161.49 W/m^{2}K. With this global heat transfer coefficient, the Schmidt correlation predicts a value of 81.8% for the fin efficiency. This is 8% higher than that of the calculated fin efficiency.

6.6.2 Comparison with an alternative method

Another possibility of evaluating the fin efficiency is by using equation (6.9). Two simulations are performed, the actual case and a case with the isothermal fin. By taking the two logarithmic mean temperatures into account, the fin efficiency can be obtained. This method assumes that exponential temperature profiles are valid, whereas the post-processing method uses the actual temperature profiles to determine the local heat transfer coefficients. Any interaction between the bulk temperature profile and the heat transfer coefficient profile is also neglected. As a result, a small difference between both methods can be expected.

Equation (6.9) can be solved for the fin efficiency, resulting in equation (6.28).

$$\eta_f = \frac{\dot{Q}_{fin}}{\dot{Q}_{fin,id}} \frac{LMTD_{id}}{LMTD} = \frac{U_{fin} A_{fin}}{U_{fin,id} A_{fin}} \tag{6.28}$$

Evaluating this equation requires a second calculation with isothermal conditions for the fin material, as was done by Wang et al. [59]. An additional simulation is performed with isothermal boundary conditions for the fin walls. The results of both simulations are shown in table 6.3.

	$\dot{Q}_{fin}$	Outlet temperature T_{out}	LMTD	U_{fin}
Real fin	2.22 W	317.64 K	14.30 K	122.97 W/m^{2}K
Isothermal fin	2.49 W	319.75 K	12.04 K	162.94 W/m^{2}K
Ratio	89.20%	99.30%	118%	75%

Table 6.2: Heat transfer and outlet temperature for the real and the isothermal X-shaped fin

Calculation of the fin efficiency according to equation (6.28), results in a fin efficiency of 75%. This is an excellent match with the previously described method. The thermal transmittance of the isothermal fin $U_{fin,id}$ matches quite well (less than 1% difference) with the thermal transmittance of the isothermal fin predicted by the post-processing method proposed in this work. Both methods agree that the fin efficiency should be significantly lower than predicted by the Schmidt correlation. As was already noted by Huang and Shah [56], significantly lower values for the fin efficiency can occur if the heat transfer coefficient is not constant. This effect is exacerbated by the additional conductive resistance due to the interruptions

in the fin surface, as was described by Perrotin and Clodic [33]. If the thermal transmittance is determined from the effectiveness-NTU or LMTD method, using the Schmidt correlation for an interrupted fin will result in an underestimation of the heat transfer coefficient. The post-processing method, which is developed in this work, matches the results of the alternative method quite well and has the advantage that it is a post-processing method. Since it does not require an extra CFD calculation to obtain the fin efficiency, it is computationally more efficient.

6.6.3 Comparison with an alternative method in case of significantly interrupted fins

In order to illustrate the impact of the geometry on the fin efficiency, a second geometry is considered. This compound Y-shaped geometry is the same geometry that is discussed in the grid convergence study in paragraph 4.7.3. In front of the tubes, the louvres are extended and vortex generators are used behind the tubes. The same geometrical parameters as in table 6.1 are used. The number of louvres is increased to 12+1 turnaround. The inlet velocity is 2.6 m/s. The local fin efficiency for this case is shown in figure 6.9.

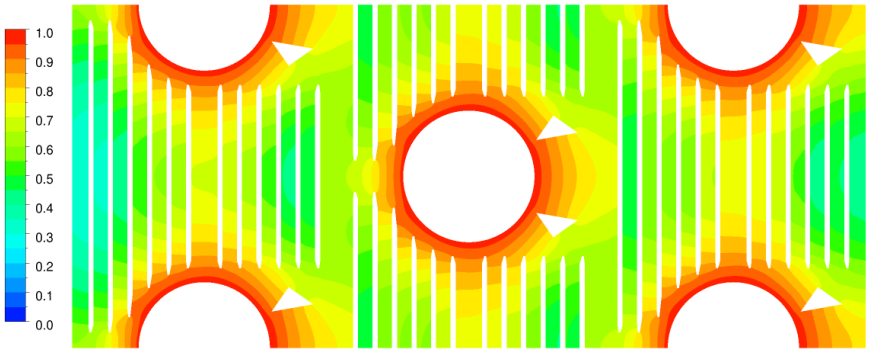

Figure 6.9: Local fin efficiency for the compound Y-shaped fin

It is clear, in general, that the local fin efficiency is lower. By applying the post-processing method, the fin efficiency is predicted to be 64.2%. The results from the simulation for the real fin and the isothermal fin are given in table 6.3.

Based on the method using two calculations, the fin efficiency is predicted to be 65.5%. This is a deviation of 2% relative to the post-processing method, which is deemed to be acceptable. Using the Schmidt correlation to predict the fin efficiency for the given geometric parameters and the given thermal transmittance for the fin of 157.03 W/m^{2}K results in a value of 78.6% for the fin efficiency and 199.89 W/m^{2}K for the heat transfer coefficient. The fin efficiency is overpredicted by 20% with respect to the method based on two calculations.

	$\dot{Q}_{fin}$	Outlet temperature T_{out}	LMTD	U_{fin}
Real fin	2.57 W	319.85 K	12.10 K	157.03 W/m^{2}K
Isothermal fin	2.79 W	322.03 K	8.78 K	239.72 W/m^{2}K
Ratio	90.29%	99.32%	138%	65.5%

Table 6.3: Heat transfer and outlet temperature for the real and the compound Y-shaped fin

6.7 Conclusions

It was shown that when the heat transfer coefficient needed to be determined from CFD simulations, it was better not to use conjugate heat transfer simulations and a fin efficiency correlation such as the Schmidt correlation. This approach could lead to an incorrect prediction of the behaviour the heat transfer coefficient, which was actually purely due to fin efficiency effects. Instead, the fin efficiency must either be fixed to one a priori by using an isothermal fin in the simulation, or the fin efficiency must be calculated from the CFD data.

Since many of the ideal assumptions on which the Schmidt correlation is based were violated, careful definition of the fin efficiency was necessary. Several authors used the ratio of heat transfer rate from the real case to that of an isothermal case as a way to obtain the fin efficiency. This approach was found to be incorrect when the bulk temperature was not constant, as is the case in heat exchangers. Due to the dependence of the bulk temperature profile on the heat transfer rate in heat exchanger applications, the fin efficiency for high-effectiveness heat exchangers was severely overestimated. It was important to account for the effect of the changing bulk temperature in the calculation of the fin efficiency. This was done by taking the ratio of the thermal conductances of the real fin and the isothermal fin instead of the ratio of the heat transfer rates.

However, calculating the fin efficiency in this way ignored the interaction between the temperature profile and the heat transfer coefficient profile. Additionally, this method required two CFD simulations. Another method was therefore proposed, which allowed evaluating the fin efficiency as a post-processing step in a CFD calculation. Using the simulation results, a fictitious ideal reference heat transfer rate was calculated. The ratio of the actual heat transfer rate to this reference was equal to the fin efficiency.

The proposed post-processing method offered a very good estimate of the fin efficiency. It was compared with the method requiring two CFD calculations. Two different fin geometries were evaluated, which would result in the same prediction for the fin efficiency using the Schmidt correlation if the heat transfer coefficient would be the same. The Schmidt correlation predicted a reduction in fin efficiency from 81.8% to 78.6% due to the increased heat transfer coefficient caused by the

change in the geometry. Both the post-processing method and the method based on two calculations agreed that the fin efficiency reduced from 75% to around 65%. The Schmidt correlation significantly overestimated the real fin efficiency in the considered interrupted fin designs. Therefore, the Schmidt correlation did not give a conservative estimate of the fin efficiency in interrupted fins. If the correlation is applied to obtain the heat transfer coefficient in experimental research, it results in an underestimation of the heat transfer coefficient as the fin efficiency is overestimated.

The reduction in fin efficiency due to the modification of the fin geometry was significant, which showed that it was required to take fin efficiency effects into account while performing optimisation of the fin geometry. The new method did not require the second simulation with an isothermal fin and could therefore be used as a post-processing step to any heat exchanger calculation. Furthermore, the post-processing method properly accounted for the interaction between the heat transfer coefficient distribution and the temperature difference distribution, as apposed to the method using two simulations.

7

Thermohydraulic analysis of selected fin designs

7.1 Introduction

In chapter 5, several optimisation techniques were discussed to optimise the fin geometry. This was done on a black box basis. For every fin geometry and frontal velocity, the j- and f-factors were determined only based on the pressure drop and the heat transfer rate of the flow domain. Using the j- and f-factors as function of the Reynolds number a performance evaluation was carried out. It is also instructive to investigate why the j- and f-factors behave the way they do as a function of the geometry modifications. This will be investigated in this chapter.

The heat transfer rate is a function of the thermal conductance, which is a global parameter and lumps the effect of the heat transfer coefficient and the fin efficiency. In chapter 6, it was discussed how these two parameters could be obtained from local CFD data of a heat exchanger. In a first step, a decomposition of the heat transfer coefficient and the pressure drop into the subcomponents which cause them will be discussed.

In a second step, the local flow fields will be investigated. By studying the local heat transfer coefficient and how it changes as the fin geometry is changed, it can be understood why some geometries perform better than others. The flow features of several important baseline geometries will be analysed by looking at the heat transfer coefficient. In paragraph 2.3.4.3, it was shown that there is an analogy between the friction factor and the heat transfer coefficient for wall-bounded flow.

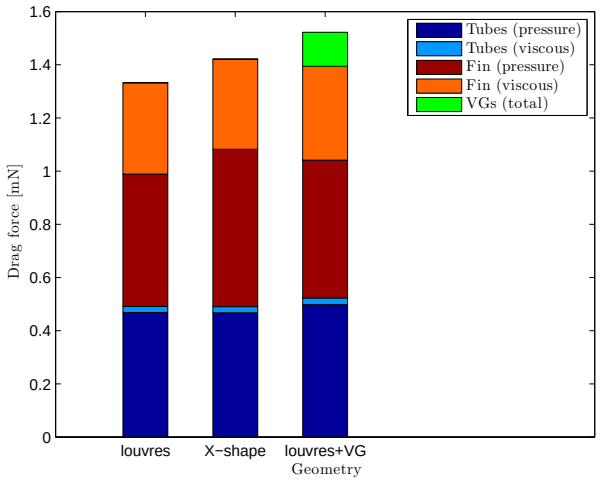

Figure 7.1: Decomposition of the drag force into subcomponents

It is therefore often instructive to also look at the distribution of the shear stress on the fin surface. All geometries will be discussed for a frontal velocity of 2.6 m/s.

7.2 Decomposition of pressure drop and heat transfer coefficient

The contribution of the pressure drop of the different components is obtained by integrating the shear stress and the pressure over the relevant surfaces and projecting the resulting force on the direction of the inlet flow velocity vector. This results in the drag force exerted on the flow by the different surfaces. According to the conservation of momentum, this drag force must be compensated for by a pressure drop over the heat exchanger core (if the momentum remains the same). The result is shown in figure 7.1 for the baseline rectangular louvred fin, the optimal combination of the rectangular louvres with a delta winglet vortex generator revealed in paragraph 5.4.5.2 and the baseline X-shaped louvred fin.

It is clear that the pressure drag is significantly more important than the viscous drag. This is especially true for the drag caused by the tubes, where the viscous drag is nearly negligible compared with the form drag. The drag on the tubes is comparable for all three geometries, it is only for the compound design that the drag on the tubes is slightly higher. This shows that the vortex generator not only introduces secondary flow vortices, but also changes the primary flow around the tubes. This is in contrast to the results obtained by Huisseune et al. [51], who

used a different VG placement and geometry and noted that the VG delays the separation of the flow from the tube and therefore must decrease the form drag on the tubes. The impact of the vortex generator on the flow separation of the tube will therefore be investigated in more detail in paragraph 7.6.

The impact of the vortex generator on the viscous and pressure drag on the fin surface is limited, the total increase in drag due to all surfaces except for the vortex generator is only 4.5%. The vortex generator accounts for an additional 9.8% increase, the total drag of the vortex generator-enhanced fin is 14.3% larger than that of the baseline case. The X-shaped fin has a larger drag than the baseline case purely due to the increased form drag on the fin surface, which is 18.9% larger. This is logical, as a larger portion of the fin surface is presented at an angle to the flow. Taking into account that the contribution of the drag on the tubes is nearly exactly the same for both geometries, the total increase in pressure drop is 6.8%. It is apparent that the vortex generator-enhanced fin has a significantly larger pressure drop than the X-shaped louvred fin, due to the form drag on the vortex generator.

As extensively discussed in chapter 5, the overall performance of the fin geometry is determined by a trade-off between the pressure drop increase and the enhancement of the heat transfer coefficient. This trade-off depends not only on the relative increases of the pressure drop and the heat transfer coefficient, but also on how these quantities change with the flow Reynolds number. If a certain geometry modification increases both the pressure drop and the heat transfer more than another modification for a fixed Reynolds number, a performance criterion analysis is required, taking the effect of the Reynolds number into account. However, if a certain geometry modification results in a larger increase of the heat transfer coefficient for a lower increase of the pressure drop, this geometry will very likely perform better in all cases. Only in the very unlikely case that the behaviour of j and f as a function of the Reynolds number would be vastly different for both geometry variations, would this conclusion not be valid.

By integrating the local heat transfer coefficient over the component surfaces, the thermal conductance for an isothermal fin is obtained. Alternatively, integrating the product of the local fin efficiency and the local heat transfer coefficient over the surface results in the thermal conductance, which takes fin efficiency into account. As discussed in chapter 6, directly integrating the heat transfer coefficient over the surface does not take interactions between the temperature profile and the heat transfer coefficient into account. The result of this integration does not correspond exactly to the product of the global heat transfer coefficient and the surface area, but it is a reasonable approximation. The result is shown in figure 7.2.

In the first instance, the extra contribution in the case of an isothermal fin is disregarded. It is clear that the total contribution of the tube surface to the total thermal conductance is very limited. The contribution is the same for the rectangu-

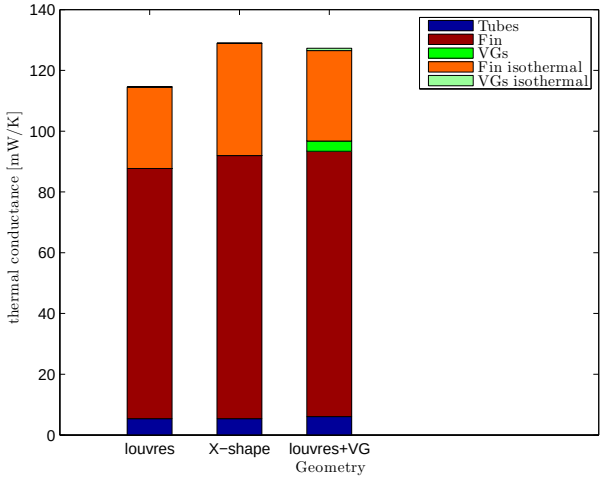

Figure 7.2: Decomposition of the thermal conductance into subcomponents. The isothermal contribution corresponds to the extra conductance in the case of an isothermal fin

lar louvred fin and the X-shaped louvred fin. The shape of the louvres (rectangular or X-shaped) does not have any influence on the heat transfer coefficient of the tubes. This is reasonable, since the pressure and viscous drag were also the same for both of these cases. The vortex generator enhances the heat transfer coefficient of the tubes by 13.2%, but given the limited contribution of the tubes the overall impact is small. The thermal conductance of the X-shaped louvred fin surface is 5.2% larger than for the baseline fin surface. The overall thermal conductance is increased by 4.9%. From the performance evaluation in chapter 5 it is known that the X-shaped louvre has a better performance for all Reynolds numbers. The increase in the pressure drop is clearly more than compensated for by the increase in the overall heat transfer coefficient. For the compound combination of the vortex generator with the louvres, the overall increase in the thermal conductance due to enhancement of the fin and tube heat transfer coefficients is 10.3%. Both the heat transfer enhancement and the pressure drop increase are larger than for the X-shaped fin. The performance evaluation revealed that the compound fin performed better than the X-shaped louvred fin in this Reynolds number range.

However, by directly integrating the heat transfer coefficient and therefore neglecting the fin efficiency effects, the thermal conductance for an isothermal fin is obtained. This reveals that the enhancement of the X-shaped fin in this case is larger than for the compound case. The heat transfer coefficient is larger for the X-shaped fin than for the compound design, but due to fin efficiency losses, the

overall increase in conductance of the compound design is larger. For an isothermal fin, the X-shaped fin achieves a slightly larger heat transfer enhancement for a lower pressure drop penalty and will therefore outperform the compound design. However, the difference in isothermal heat transfer rates is only 1.6%, which is of the same order of magnitude as the deviation between the two methods of determining the fin efficiency. It is therefore hard to say which design will perform best in the isothermal case, taking the actual temperature profiles into account as discussed in chapter 6. Nevertheless, it is possible to say that for the isothermal fin, the heat transfer rates will be very closely matched between the compound geometry and the X-shaped geometry. This reveals that the optimal geometry is not only determined by the flow enhancement, but that effects of the geometry on the fin efficiency are essential to determine the optimal geometry. For an increased fin thickness, smaller tube pitches or better conducting materials, it is entirely likely that the X-shaped fin will be competitive with or even outperform the compound fin. This also indicates that geometry modifications to the X-shaped geometry with the objective of increasing the fin efficiency are beneficial if the penalty on the heat transfer coefficient is not too large. It is also apparent that the contribution of the vortex generator depends very little on whether the fin is isothermal or not. Indeed, due to the close proximity of the vortex generator to the tube, the local fin efficiency for the vortex generator is quite large.

By doing the calculations for the isothermal versions of the X-shaped fin and the compound fin, the difference in thermal conductance is seen to be only 0.5%, whereas for the real fin case, the difference is 5.1%. The difference in thermal conductance between these two designs in the case of non-isothermal fins is therefore to be attributed to the effect of the fin efficiency.

In what follows, the heat transfer coefficient and the viscous drag will be investigated in even more detail, by studying the local distribution over the fin surface for several basic geometries. The flow field will also be investigated, with special emphasis on the presence of vortices. Huisseune et al. [51] indicate that vortices are destroyed in the louvres, so this will also be verified.

7.3 Thermohydraulic analysis of the plain fin

7.3.1 Heat transfer coefficient and surface friction

The simplest fin and tube geometry is the plain fin. It is symmetrical around a plane in the middle of the fin material. For steady-state flow, the flow and therefore the heat transfer coefficient are also symmetrical. The heat transfer coefficient for the plain fin is shown in figure 7.3. The shear stress is given in figure 7.4.

Several important observations can be made. The first is that there are large zones of low heat transfer coefficient behind the tubes, these are the tube wakes.

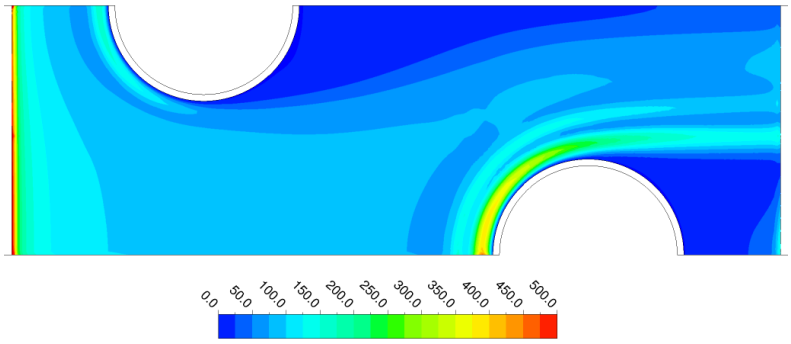

Figure 7.3: Local heat transfer coefficient on the surface of the plain fin

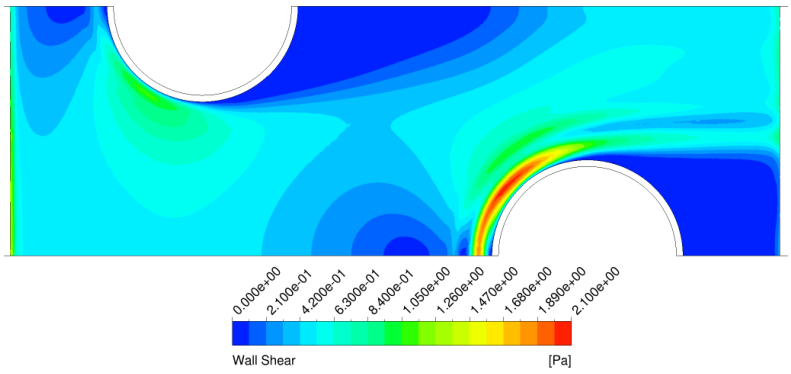

Figure 7.4: Shear stress on the surface of the plain fin

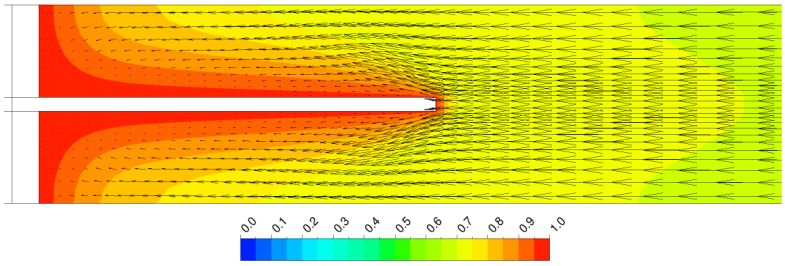

Figure 7.5: Dimensionless temperature and velocity vectors in the symmetry plane of the final tube

In this region, the friction factor is also low, which indicates that it is a region of flow circulation. This is confirmed by looking at the velocity field. The heat transfer coefficient is low in tube wake for two main reasons. First, the circulating fluid moves significantly slower than the surrounding fluid. In some regions of the tube wake it is even slower than 3% of the frontal velocity. As is known from chapter 2, slower-moving fluid results in thicker thermal boundary layers and therefore lower heat fluxes and heat transfer coefficients. Secondly, this recirculating region is effectively isolated from the rest of the flow. The temperature in the wake region is significantly higher than the average temperature at the x-coordinate in the heat exchanger. The bulk temperature is defined as the adiabatic mixing cup temperature, which is lower than the actual local temperature inside the wake region. As a consequence, the actual local driving temperature difference is lower than the reference driving temperature difference between the tube wall temperature and the mixing cup temperature. This again leads to a reduction in the obtained heat transfer coefficient, since the actual local temperature difference is lower than the reference temperature difference used to determine the heat transfer coefficient.

By comparing the heat transfer coefficient with the shear stress distribution, it is observed that the region of recirculating flow indicated by the shear stress is smaller than the region of low heat transfer coefficient. This is again caused by the increased local temperature of the fluid behind the recirculating region in the wake of the tubes with respect to the adiabatic mixing cup temperature. Even if the velocity and the boundary layer thickness are exactly equal, a local increase in the temperature with respect to the mixing cup temperature leads to a reduced heat transfer coefficient.

A remarkable feature of the heat transfer coefficient in the wake of the final tube row is that the heat transfer coefficient is again increased near the fin edge. Even though this seems counter-intuitive, it can be easily explained by observing the fluid temperature and velocity in the wake of the tube, shown in figure 7.5.

A clear recirculation of the flow can be seen, as the local flow is towards to

final tube, instead of away from it. This convects colder fluid from outside the tube wake into the wake near the edge. This reduces the thermal boundary layer thickness and therefore increases the heat transfer coefficient. This phenomenon does not occur behind the other tubes in the heat exchanger core, because of the influence of the downstream tubes. In reality, the flow behind the final tube row is likely to be unsteady, which also increases the heat transfer coefficient in the wake of the final tube.

This is a clear example that the flow is not fully developed periodic, since the features of the final tube row are different from those of tubes deeper in the heat exchanger core. The first tube row is also an exception, since the incoming flow is approximately uniform as it has not been influenced by upstream tubes. The development of the boundary layer can be seen by the strong decrease of the heat transfer coefficient, starting from a very high value at the leading edge of the fin. By looking at figure 7.3, it can be seen that the thermal boundary layer develops very rapidly. Before the flow is influenced by the second tube, the heat transfer coefficient remains constant once the distance from the leading edge of the fin is approximately half the longitudinal tube pitch.

Another example of dependence of the local heat transfer coefficient and shear stress can be observed by looking at the behaviour in front of the tubes. Both tubes show a region of increased heat transfer coefficient and increased friction close to the tubes. For the second tube row, this effect is much more pronounced. This phenomenon is caused by the horseshoe vortex, which is formed due to interaction between the boundary layer and pressure gradient caused by a flow obstruction such as the tube.

Bougeard [64] studied the heat transfer coefficient for a plain fin experimentally, based on a thermographic method. He also observed a stronger horseshoe vortex system for the second tube row as well as the region of increased heat transfer coefficient in the wake of the final tube.

7.3.2 The horseshoe vortex

The horseshoe vortex system of the second tube is shown in figure 7.6. The fin surface is coloured by the heat transfer coefficient using the same colour map as figure 7.3. The dimensionless temperature is shown in a plane perpendicular to the fin surface at an angle of 45° with respect to the free-stream velocity vector. The velocity vectors are also given for the same plane, which reveals the locally circulating nature of the flow. Several streamlines for the flow are also given, which indicate the presence of the vortex. Finally, an iso-surface of the swirling strength vortex core detection criterion [65] is shown in grey. A vortex is clearly present, which wraps around the tube. This is the horseshoe vortex.

It is clear that the vortex results in a strong increase of the heat transfer co-

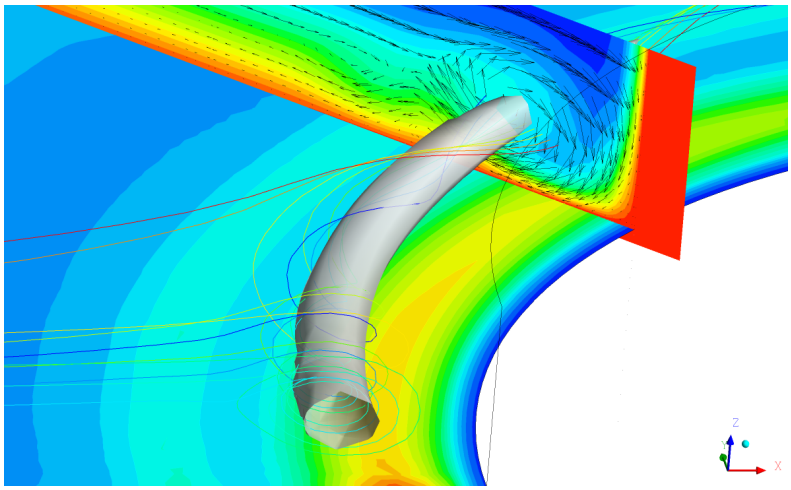

Figure 7.6: Horseshoe vortex around the second tube. Fin surface coloured by heat transfer coefficient, normal plane by dimensionless temperature

efficient. The local downflow induced by the vortex results in a thinning of the thermal boundary layer and thus in an increase of the heat transfer coefficient. In the region where the local flow is away from the fin, the boundary layer is thicker and the heat transfer coefficient is therefore lower. Going even further away from the tube, a second region of improved heat transfer coefficient is observed, which is caused by a smaller secondary vortex. This secondary vortex was also observed experimentally among others by Bougeard using the thermographic technique and by Kim and Song [66] using the naphthalene sublimation technique.

7.4 Thermohydraulic analysis of the rectangular louvred fin

Cui and Tafti [30] investigated a flat tube and rectangular louvred fin heat exchanger numerically. They concluded that the flow in the louvres is nominally two-dimensional with weak three-dimensionality. Only in the transition region where the louvres were connected to the rest of the fin surface, strong three-dimensionality occurred. A vortex jet is formed at this junction, underneath the louvre.

Huisseune et al. [67] considered a combination of rectangular louvres with round tubes. They concluded that it is only for the first tube row that the flow in the louvres can be considered two-dimensional. They noted that the flow in the rest of the heat exchanger should be considered three-dimensional because of the periodic contraction and expansion due to the presence of the round tubes.

In this section, the flow features of the rectangular louvred fin will be investigated further.

7.4.1 The horseshoe vortex system

7.4.1.1 Comparison with the plain fin

Figures 7.7 and 7.8 show the heat transfer coefficient and the shear stress on the bottom and the top of the fin surface respectively. Due to the addition of the louvres, the flow field is no longer symmetrical around the midplane of the fin.

First, the heat transfer coefficient distribution of the plain fin (figure 7.3) is compared with that on the bottom surface of the louvred fin. Focusing on the horseshoe vortex system around the tubes, it is clear that for the first tube row, this is very similar. In both cases, an increase of the heat transfer coefficient is observed, which occurs in a relatively narrow band in front of the tube. After approximately 90° around the tube the heat transfer coefficient enhancement is negligible. In the case of the louvred fin, a second region of high heat transfer coefficient can be observed adjacent to the tube wake. This will be discussed later.

For the second tube row, however, the behaviour is completely different. Whereas in the plain fin case, the heat transfer enhancement in front of the tube is much more pronounced than for the first tube row and concentrated in a narrow band, for the louvred fin, a much wider region of enhanced heat transfer coefficient can be observed. The enhancement is less intense than the horseshoe vortex. For the plain fin tube the heat transfer coefficient is of the same magnitude as for the first tube row.

Secondly, the comparison is made between the top of the louvred fin surface and the plain fin surface. On the top of the fin, the horseshoe vortex system for the first tube row is very similar to that on the bottom surface and that of the plain fin. The heat transfer coefficient in front of the second tube row is similar to that of the plain fin surface. Two separated bands of increased heat transfer coefficient can be observed, which probably correspond to a primary and a secondary vortex.

Finally, the flow in front of the second tube row is considered. Figure 7.9 shows the dimensionless temperature and the velocity field in the symmetry plane of the second tube.

It is immediately clear that the horseshoe vortex system is much stronger on top of the fin than on the bottom. This is in agreement with the findings of Huisseune et al. At the top of the fin, the flow immediately downstream of the exit louvre impinges on the fin surface, which explains the larger heat transfer coefficient and friction stress in this region. Closer to the tube, there is an especially large heat transfer coefficient, which is caused by the impingement of the bypass flow. Even further downstream, the fluid flows upwards, increasing the thickness of the velocity boundary layer. Since horseshoe vortices are developed by the interaction

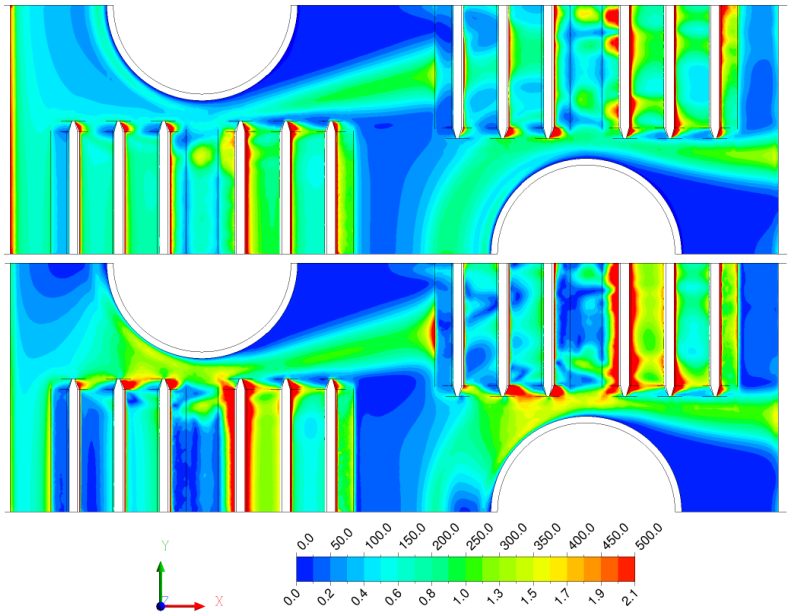

Figure 7.7: Heat transfer coefficient (top figure) and shear stress (bottom figure) on the bottom of the fin surface

between the boundary layer and a flow obstruction, it is therefore not surprising that the largest vortex occurs at the top of the fin where the boundary layer close to the tube is the largest. The strong vortex results in a significant enhancement of the heat transfer coefficient directly in front of the tube. On the bottom of the fin, the opposite is true. A large recirculation zone is present downstream of the exit louvre, which is responsible for the low heat transfer coefficient directly downstream of the louvres on the bottom of the fin surface. Closer to the tube, the flow is aligned towards the fin surface, reducing the boundary layer thickness. It is this impingement of the flow and the resulting decrease in the thermal boundary layer which explains the large region of enhanced heat transfer in front of the tube. Due to the reduced boundary layer thickness, the resulting horseshoe vortex is also much smaller.

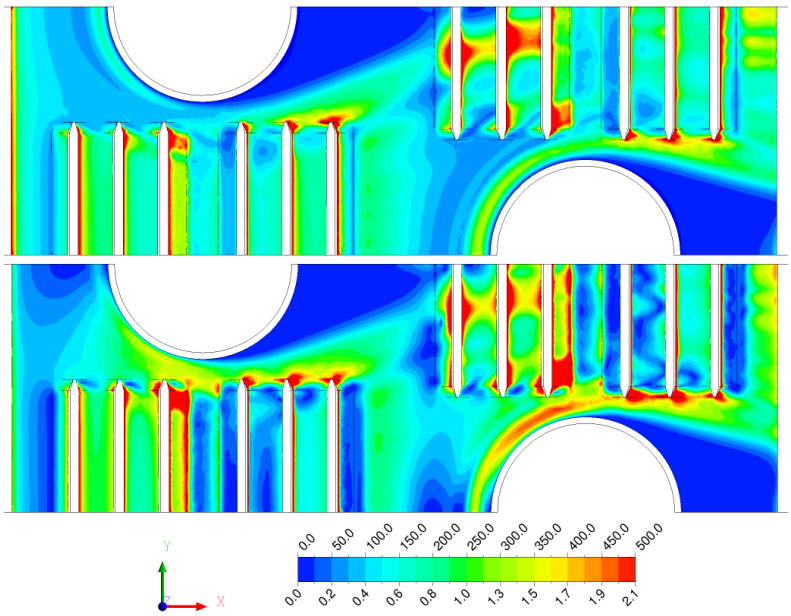

Figure 7.8: Heat transfer coefficient (top figure) and shear stress (bottom figure) on the top of the fin surface

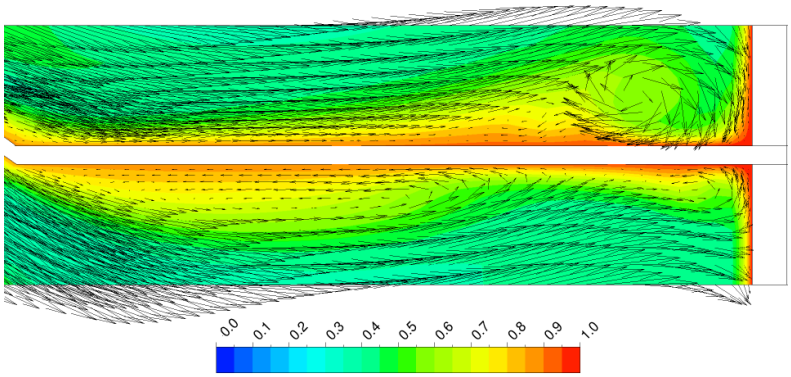

Figure 7.9: Dimensionless temperature and velocity field in the symmetry plane of the second tube

7.4.1.2 Evolution of the horseshoe vortex system

In front of the tube, at the bottom of the fin

Now that it is understood why the formation of the horseshoe vortices is different for the top and bottom of the louvred fin and different from the plain fin case, it is instructive to look at how the horseshoe vortex develops afterwards. The horseshoe vortex for the second tube row will be considered. Figure 7.10 shows the bottom of the fin surface, looking upwards at the fin from below the fin surface. The contours of the heat transfer coefficient are given for this surface. The velocity vectors are also shown for four different planes. The inlet velocity is aligned with the red x-vector shown in the top left. The first plane corresponds with an angle of 45° with the X-axis, the front part of the tube is shown. On the right-hand, side a louvre and a part of the turnaround louvre can be seen.

The horseshoe vortex wraps around the tube. For the large vortex in the first plane from the bottom, it can be seen that the flow at the tube wall is oriented towards the fin. This is the case for the horseshoe vortex, as can be seen from figure 7.9. For the second plane a little more downstream, a second vortex counter-rotating is seen to develop at the junction between the tube and the fin. The horseshoe vortex is convected upwards. In the third plane, the developing counter-rotating vortex has developed further, the flow at the tube wall is now aligned away from the fin. The horseshoe vortex can no longer be seen because the upwards velocity is too large. For the final plane, the new vortex has become even larger. As expected, the region of local downflow correlates well with the region of increased heat transfer coefficient.

A second vortex can be seen to the right of this vortex. The second vortex has been shed by the transition region of the inlet of the turnaround louvre. The presence of the vortex indicates the three-dimensional nature of the flow at the location of the turnaround louvre.

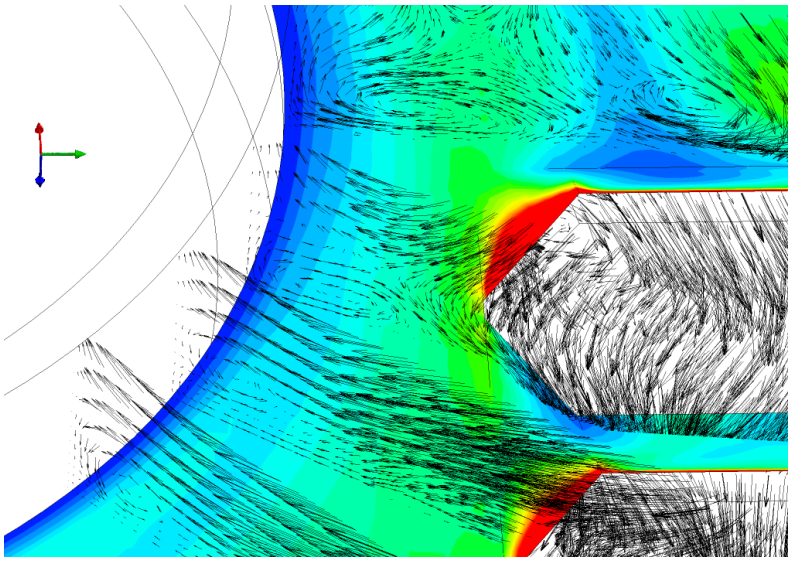

Figure 7.10: Heat transfer coefficient and vortices on the bottom fin surface for the front part of the tube.

At the back of the tube, at the bottom of the fin

Figure 7.11 shows what happens further downstream. The bottom plane, which can be seen, is the same plane as the last plane of figure 7.10. The rightmost vortex of this plane, which is shed from the transition of the turnaround louvre is convected into the rest of the louvre bank. Directly downstream of this vortex on the exit of the turnaround louvre, a region of increased heat transfer can be seen. The downstream louvre also shows an increased heat transfer coefficient. Both of these enhancements are caused by the vortex shed from the transition of the inlet of the turnaround louvre.

The downstream planes show that the large vortex, which developed close to the tube wall, wraps around the tube. The transition zones of the downstream louvres are responsible for a second counter-rotating vortex. Both of these vortices result in a flow which impinges on the fin surface between the louvres and the tube. The primary flow at this location is the high-velocity and low-temperature bypass jet. Since the vortex forces the jet close to the surface, thin boundary layers and large heat transfer coefficients are obtained in this region.

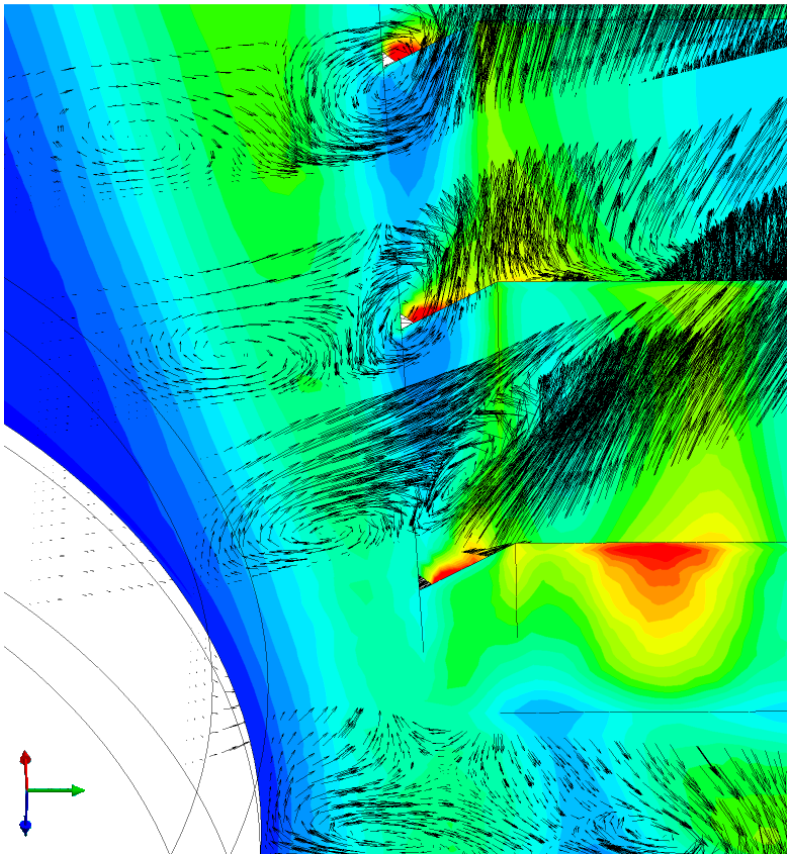

Figure 7.11: Heat transfer coefficient and vortices on the bottom fin surface for the back part of the tube

In front of the tube, at the top of the fin

The horseshoe vortex at the top of the fin was significantly stronger. How it develops as it wraps around the front of the tube is shown in figure 7.12.

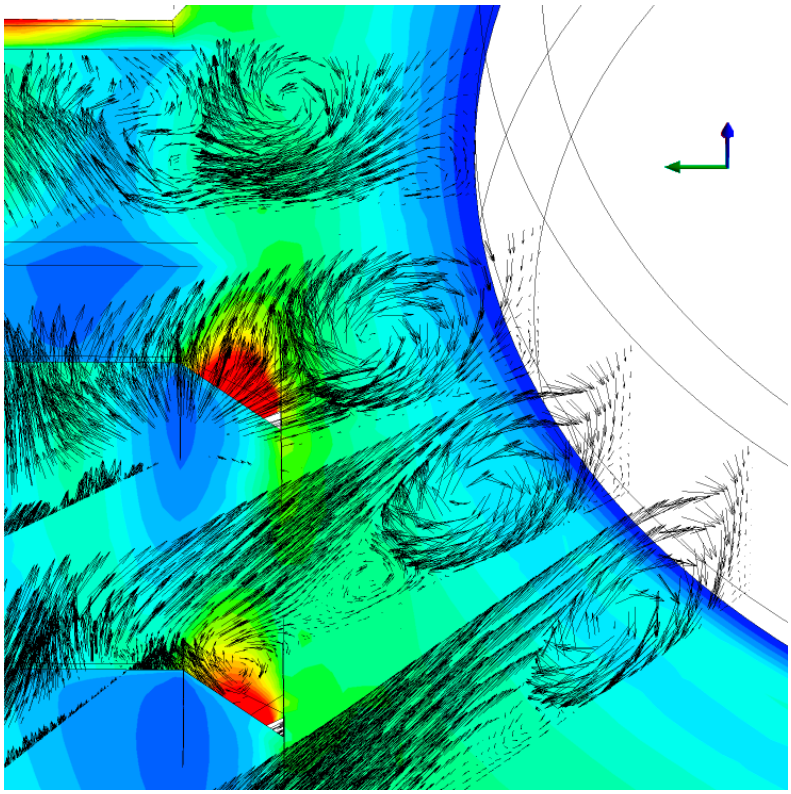

Figure 7.12: Heat transfer coefficient and vortices on the top fin surface for the front part of the tube

The first plane on the bottom of the figure shows the horseshoe vortex and the secondary vortex, which have both wrapped around the tube. One plane further downstream, it can be seen that a third vortex is present behind the transition zone of the louvre. As was the case on the bottom of the fin, a corner vortex develops at the junction between the tube and the fin. The horseshoe vortex is again convected away from the fin surface. However, as opposed to what happens on the bottom of the fin, the horseshoe vortex is sufficiently strong to remain visible in all the subsequent planes. Due to the strength of the horseshoe vortex, the corner vortex does not develop to the same size as the corner vortex on the bottom of the fin. For the last plane, a third vortex is visible, which is shed from the transition of the inlet

of the turnaround louvre, just like on the bottom of the fin.

At the back of the tube, at the top of the fin

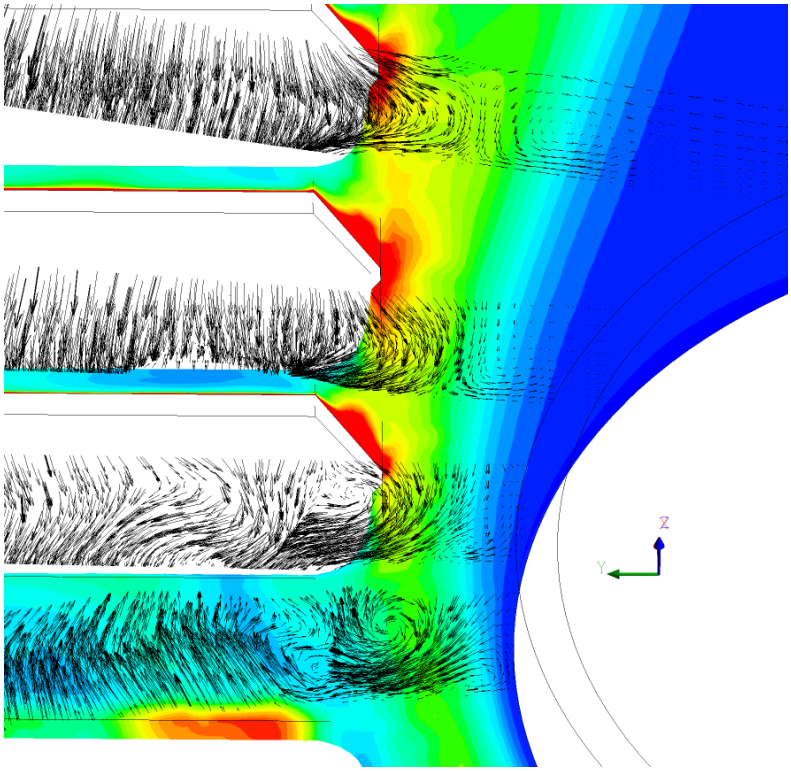

Figure 7.13: Heat transfer coefficient and vortices on the top fin surface for the back part of the tube.

Figure 7.13 shows the situation at the back of the tube. The horseshoe vortex is convected with the flow into the louvres and is no longer visible by the third plane, which is located downstream of the first louvre behind the turnaround louvre. The corner vortex develops further and is the only vortex which is still visible behind the second louvre, as shown by the final plane.

Bypass flow

In order to be able to explain the heat transfer coefficient distribution completely, the presence of the bypass flow must be considered. Figure 7.14 shows the velocity in the middle between two fins, normalised with the inlet velocity. The

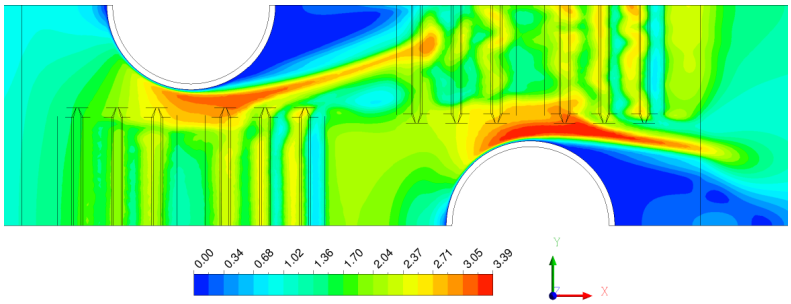

Figure 7.14: Velocity magnitude normalised with inlet velocity for a plane in the middle between two fins

flow which passes between the louvres and the tube is called the bypass flow, as it bypasses the louvres.

It is clear that this flow forms a high-velocity jet, which convects the vortices located between the tube and the louvres. As this flow has bypassed the louvres it is also colder than the local adiabatic mixing cup temperature. The high velocity, the presence of the vortices and the local temperature reduction with respect to the mixing cup temperature all contribute to the large heat transfer coefficient, which is found adjacent to the tube wakes in figures 7.7 and 7.8. The high velocity and the vortices also result in an increased shear stress, which can be seen in the same figures.

7.4.2 Flow inside the louvre bank

7.4.2.1 Influence of the incoming flow

One last aspect of the distribution of the heat transfer coefficient which still needs to be explained is the behaviour on the louvre surfaces. For the first tube row, the inlet and the first two louvres, the heat transfer coefficient depends only on the distance from the leading edge. The flow here is then largely two-dimensional. Only in the transition area deviations are visible. These findings are in agreement with Cui and Tafti [30]. For the subsequent louvres of the first tube row, some small deviations can be seen. Overall, two-dimensional flow is a reasonable approximation for the flow around the louvres of the first tube row, as was noted by Huisseune et al. [51].

For the second tube row, however, the profile of the heat transfer coefficient on the louvre surfaces is strongly two-dimensional. This shows that the flow inside the louvres is strongly three-dimensional and hints at the presence of vortices. In figure 7.8, depicting the heat transfer coefficient on top of the fin, the second louvre shows a region of strongly increased heat transfer coefficient. Figure 7.15a shows

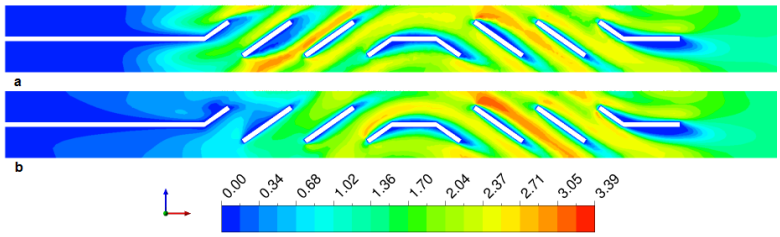

Figure 7.15: Velocity divided by inlet velocity in planes parallel to the symmetry plane: (a) passes through the region of high heat transfer on the top of the second louvre (y=7.54 mm), (b) is the symmetry plane

the dimensionless velocity in a plane parallel to the symmetry plane and through this region. The second panel of the figure shows the velocity in the symmetry plane.

It is clear that the flow up until the turnaround louvre differs significantly. For plane (a), pronounced louvre wakes can be observed behind the inlet louvre and the first louvre. The flow which passes between the wake of the first louvre and the second louvre flows three times faster than the inlet velocity. The high velocity explains why the heat transfer coefficient is so high. The high-velocity fluid comes from the bypass jet, as can be seen in figure 7.14. For plane (b), the louvres are situated in the tube wake. In this case, it is the top surface of the inlet and first louvre which encounters lower fluid velocities. The difference in the local flow velocity explains why differences in the heat transfer coefficient are present for the same distance from the leading edge.

7.4.2.2 Vortices in the flow around the louvres

The first tube row

A second important aspect is the presence of vortices in the flow around the louvres. Figure 7.16 shows the flow at the location of the turnaround louvre of the first tube row. It is clear that two strong vortices are present close to the flat landing, one above and one below the fin surface. These vortices are shed by the transition zones of the upstream louvres. The third vortex, which can be seen in this figure, is the horseshoe vortex, located between the transition region and the tube wall. The vortex below the fin surface is located closer to the fin surface than the vortex above the fin. As can be seen in figures 7.7 and 7.8, on the bottom of the fin, the heat transfer coefficient is strongly enhanced by the locally impinging flow caused by the vortex. Apparently, the vortex on the top of the fin surface does not increase the heat transfer coefficient, which is unexpected.

Taking a closer look at the flow on the top of the turnaround louvre surface, it

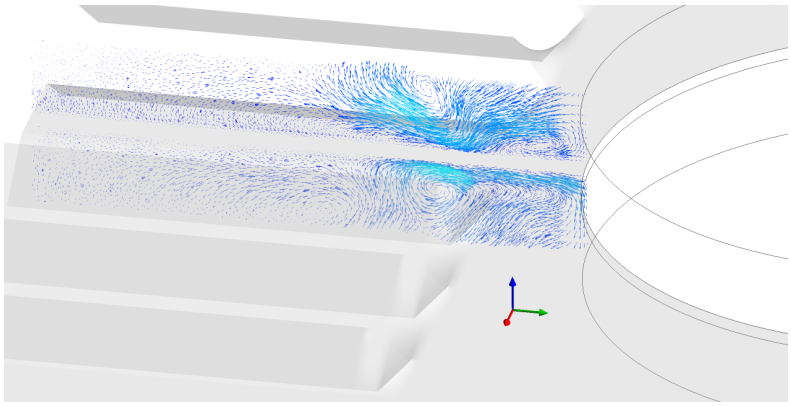

Figure 7.16: Vortices around the turnaround louvre of the first tube row

is revealed that the flow separates slightly from the fin surface. This is shown in figure 7.17. Where the region of decreased heat transfer coefficient starts, the flow has a small upward component very close to the surface. Due to this flow separation, the heat transfer coefficient on the top of the turnaround has a local minimum close to the vortex. It should also be noted that the thermal boundary layer is quite thick directly above this region even though the flow in this region is downwards. This is caused by the incoming flow at this position, which is hotter than the surrounding fluid. In general, a local region of enhanced heat transfer coefficient results in local increased heat transfer rate and therefore in a local increase in fluid temperature. If this hotter fluid is then convected into a region where the velocity field does not enhance the heat transfer coefficient, the local heat transfer rate will be lower. As a result, the calculated heat transfer coefficient will be smaller.

Further to the left, the heat transfer coefficient increases again. This is caused by the presence of a region where the fluid temperature is locally lower. Because the adiabatic mixing cup temperature is used as the reference for the heat transfer coefficient, this local temperature decrease results in an increase of the obtained heat transfer coefficient.

Further away from the flat landing, the velocity vectors are very small. The flow in this region is approximately two-dimensional and aligned with the louvres. As a result, the heat transfer coefficient is approximately independent of the distance from the tube. Clearly, the vortices remain in the neighbourhood of the transition region. This can also be observed by considering the streamlines which pass through the vortices, shown in figure 7.18. The streamlines follow the contraction and expansion imposed by the staggered tube layout. Around the second louvre, the flow is aligned towards the symmetry plane of the louvres. The streamline shows a clear rotation after passing through the transition regions of the first and second louvre. After passing over the transition louvre, the flow moves away again

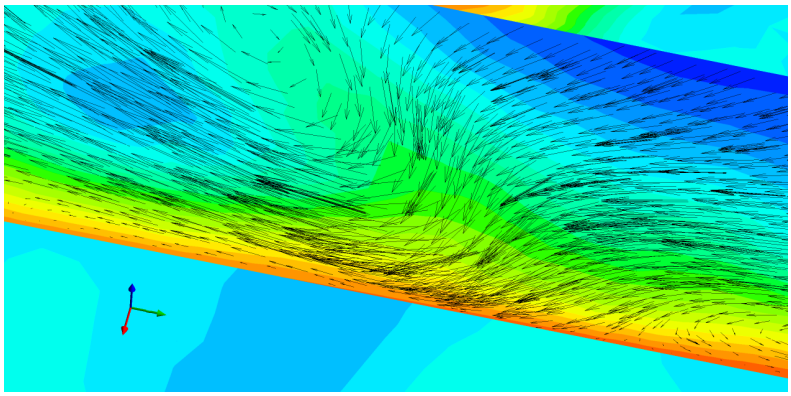

Figure 7.17: Heat transfer coefficient on the louvre surface, as well as velocity vectors and dimensionless temperature in the perpendicular plane

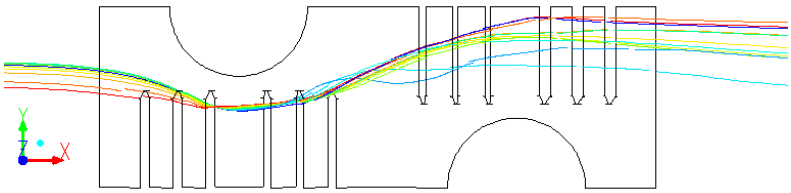

Figure 7.18: Streamlines through a vortex present around the turnaround louvre of the first tube row

from the symmetry plane, due to the flow contraction of the downstream tube. As a result, the vortices are concentrated near the transition zones. Afterwards, this rotating flow passes close to the centre of the louvres of the downstream tube row.

In conclusion, for the first tube row, some vortices are present, which are shed from the upstream flat landings. These vortices are concentrated near the transition region. Further away from the tube, towards the symmetry plane, no vortices are present and the flow is approximately two-dimensional. This is in agreement with the distribution of the heat transfer coefficient in this region, which is approximately only a function of the distance from the leading edge.

The second tube row

For the second tube row, significant variations in the heat transfer coefficient can be seen over the entire louvre surface. A decrease of the heat transfer coefficient can be expected directly behind the tube due to the impingement of the tube wake. This is in fact seen on the surfaces of the inlet louvre and the first two louvres. However, the turnaround louvre shows a significant enhancement in the heat

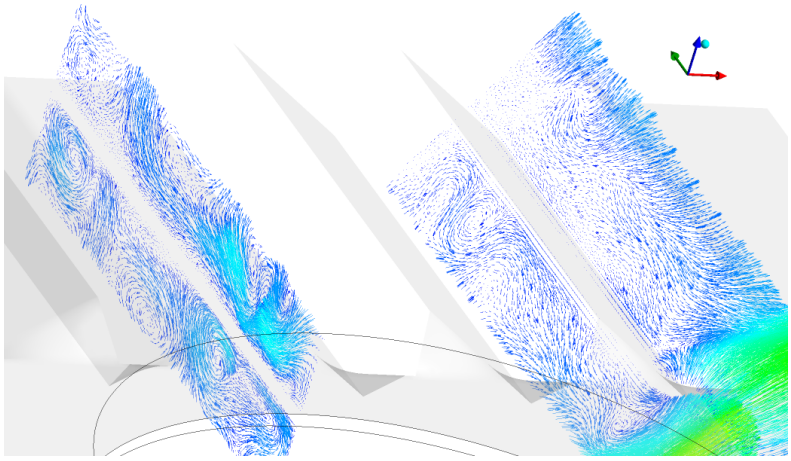

Figure 7.19: Velocity vectors in a plane perpendicular to the turnaround louvre and in a plane perpendicular to the final louvre

transfer coefficient directly behind the tube. This is unexpected, since vortices are only expected near the transition zone, as discussed for the case of the first tube row. However, as figure 7.19 shows, vortices are clearly present near the centre of the louvres.

The leftmost plane of the figure shows the expected vortices near the transition zones, but strong vortices are also present very close to the symmetry plane of the louvres, far away from the tube. Furthermore, these vortices still exist by the time the flow reaches the final louvre, as shown by the right plane on the figure. As shown in figure 7.18, these vortices must be caused by the transition zones of the upstream louvres. Indeed, the streamlines passing through the vortices of the upstream louvre end up near the centre of the downstream louvre. Near the symmetry plane of the louvres, there is a strong impingement of the flow on the bottom of the fin surface. This explains why the heat transfer coefficient is large in this region, even though it is downstream of the tube wake.

According to Huisseune et al. [51], vortices which are shed by vortex generators are immediately destroyed by the upward air flow at the entrance of the louvres. They contend no more vortices can be discerned after the entrance of the louvre bank. However, this work clearly shows that vortices are in fact present in the louvre banks, shed by the transition regions of the louvres of the upstream tube row. The louvres do not destroy vortices, as alleged by Huiseune et al.

The vortices result in significant increases and decreases of the heat transfer coefficient on the tube surface, as can be seen in figures 7.7 and 7.8. Even for the last louvre, the heat transfer coefficient distribution is clearly not two-dimensional.

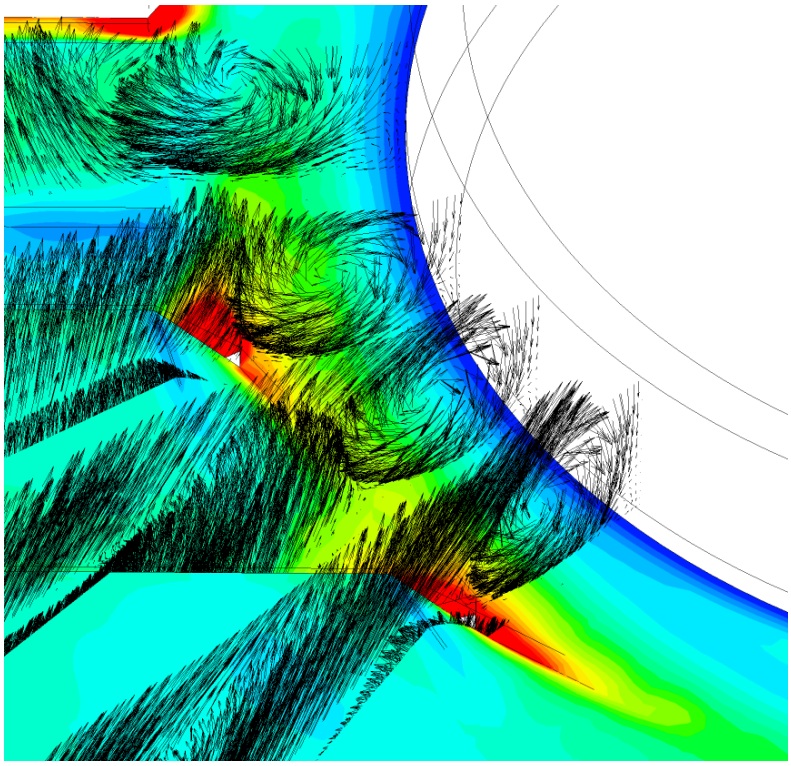

Figure 7.20: Heat transfer coefficient and vortices on the top fin surface for the front part of the tube for the X-shaped fin

7.5 Thermohydraulic analysis of the X-shaped louvred fin

Huisseune et al. [67] also contend that in X-shaped louvred fin and round tube heat exchangers, the horseshoe vortices are destroyed by the louvres. However, figure 7.20 shows the flow on the top of the fin surface in front of the tube, the planes are the same as the ones used in figure 7.12 for the rectangular louvred fin. Clearly, the horseshoe vortex is also generated for the X-shaped louvred fin. Further on, the vortex is again convected into the louvre bank. Since the vortices were not destroyed in the louvre bank for the rectangular louvred fin, they will also not be destroyed for the X-shaped fin. Therefore, it is not necessary to use the rectangular louvred fin to obtain the heat transfer enhancement caused by the horseshoe vortex.

A major difference, however is that the high-velocity bypass jet, which was present for the rectangular louvred fin, is much less pronounced. The dimensionless velocity in the plane halfway between two fins is given in figure 7.14. For the

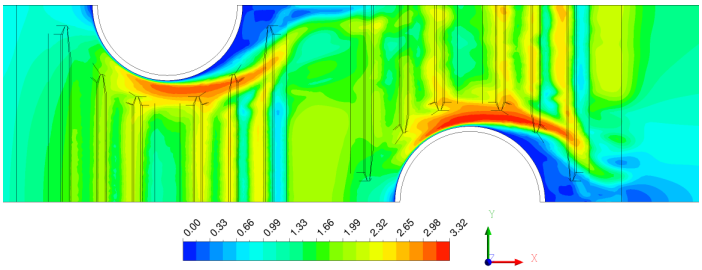

Figure 7.21: Velocity normalised with inlet velocity for a plane in the middle between two fins

rectangular louvred fin, this high-velocity jet remained outside the louvre bank and persisted until the second louvre of the downstream louvre bank. For the X-shaped fin, the high-velocity jet enters the louvre bank downstream of the turnaround louvre. The jet has a larger velocity component towards the tube, causing the jet to impinge on the tube wake. As a result, the tube wake is much less pronounced. The tube wake persists until the entrance of the downstream louvre bank just as in the case of the rectangular louvred fin, however, the velocity in the wake is higher. Furthermore, the extent of the wake in the transversal (y) direction is smaller, the wake is hence narrower.

The consequence for the distribution of the heat transfer coefficient on the fin surface is shown in figure 7.22. Whereas the rectangular louvred fin shows two high heat transfer regions adjacent to a pronounced tube wake on both sides of the fin, this is not the case for the bottom of the X-shaped fin. Only on top of the fin surface, a region of increased heat transfer coefficient can be observed, which is due to the presence of a vortex at this location. The heat transfer coefficient in the tube wake is higher, the region where the heat transfer coefficient is below 25 $\frac{W}{m^2K}$ is much smaller than for the wake in the case of rectangular louvres being used.

A region of high heat transfer coefficient can be seen behind the exit louvres of both tube rows. Investigating the flow field reveals that this is due to impingement of part of the bypass flow at this location (not shown). The distribution of the heat transfer coefficient also indicates that vortices are present in the flow around the louvres of the second tube row. This is confirmed by considering the flow around the second louvre of the second tube row in more detail, as shown in figure 7.23. Where the secondary flow due to the vortex impinges on the fin surface, the heat transfer coefficient is increased, whereas the regions where the secondary flow is away from the fin surface have a decreased heat transfer coefficient.

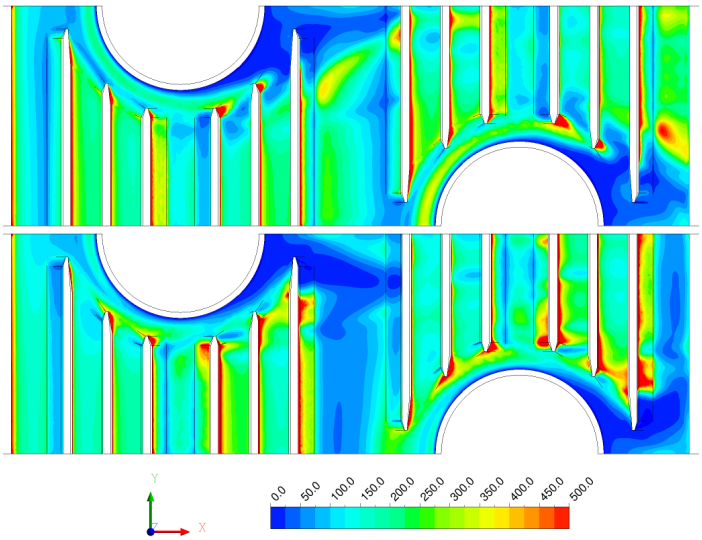

Figure 7.22: Heat transfer coefficient on the fin surface. The top figure corresponds to the top of the fin surface, the bottom figure to the bottom of the surface

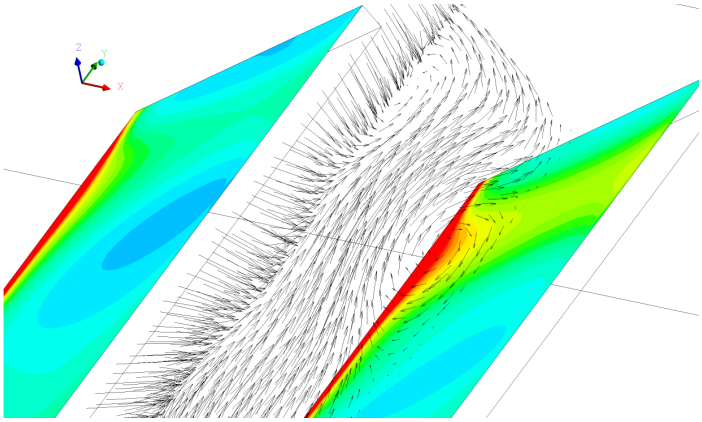

Figure 7.23: Heat transfer coefficient on the top of the second louvre of the second tube row, as well as the local flow field in a perpendicular plane

7.6 Compound rectangular louvred fin and vortex generators

7.6.1 Vortices in the compound fin

The left panel of figure 7.24 shows the heat transfer coefficient on top of the fin and the vortices behind the vortex generator. The right panel shows the flow and the heat transfer coefficient at the same location for the rectangular louvred fin. It is clear that the transition zone of the louvres is responsible for a single vortex. The same vortex can also be found in the case of the compound fin, but four additional vortices can be distinguished. Both to the left and to the right of the vortex generator, two counter-rotating vortices can be seen.

To the left of the transition zone of the inlet louvre, a region of high heat transfer coefficient can be seen in both cases. This is due to the bypass flow, which is a cold high-velocity fluid jet which passes between the louvres and the tube. The impingement of this cold jet on the inlet louvre causes a high heat transfer coefficient. In the case of the vortex generator geometry, this jet is split in two as it impacts on the vortex generator. Part of the jet moves to the left of the vortex generator, enhancing the heat transfer in the tube wake. The other part of the jet again impacts on the louvre surface.

Figure 7.25 shows the flow in the middle of the louvre bank. A plane is constructed perpendicular to the fin surface in the middle of the turnaround louvre of the second tube row. The velocity vectors in this plane and contours of the ratio of the velocity magnitude to the inlet frontal velocity are shown. The top of the figure corresponds to the case of the rectangular louvred fin, whereas the bottom corresponds to the compound fin. The bypass flow is clearly visible at the right of the figure, the velocity reaches up to three and a half times the inlet velocity. It is also apparent that in both cases, a significant number of vortices are present at this location. This again confirms that vortices are not destroyed by the flow in the louvre bank.

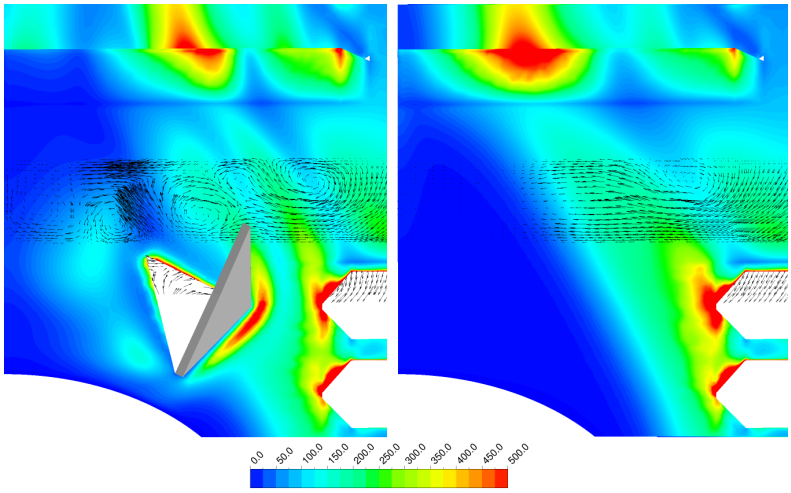

Figure 7.24: Heat transfer coefficient on the top of the fin surface and vortices: left: compound fin, right: rectangular louvred fin

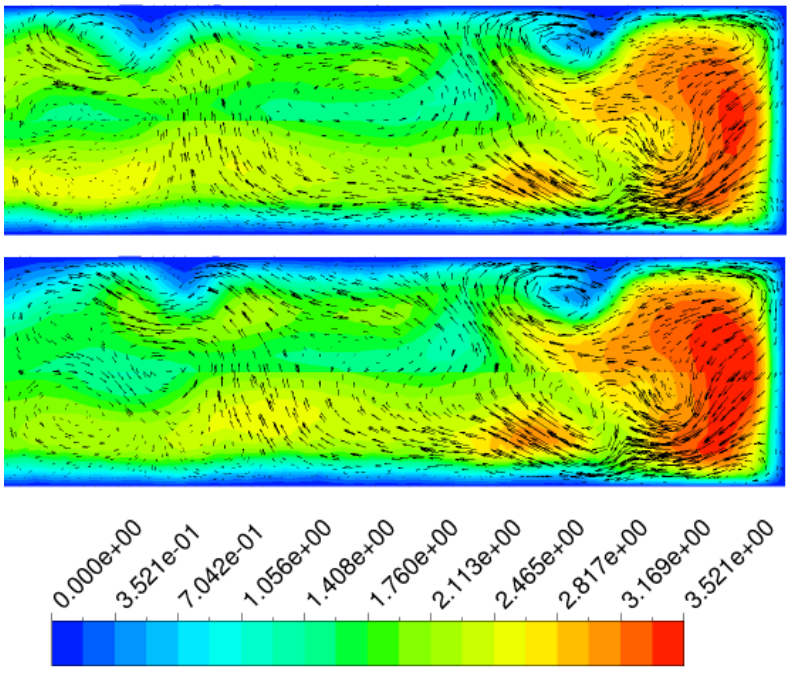

Figure 7.25: Vortices and dimensionless velocity magnitude in a plane perpendicular to the fin in the middle of the turnaround louvre of the second tube row: top: rectangular louvred fin, bottom: compound fin

7.6.2 Effect of the vortex generator angle of attack

In the optimisation of the vortex generator geometry in chapter 5, it has become apparent that the optimal angle of attack is around $70°$. In order to understand why this is the case, the heat transfer coefficient distribution is investigated for four different angles of attack. Figure 7.26 shows the top of the fin, whereas figure 7.27 shows the bottom of the fin. Both figures show that the wake region of the tubes is strongly influenced by the vortex generator angle of attack. However, when one looks at the exit of the turnaround louvre of the second tube row, significant differences in the heat transfer coefficient can be observed. The effect of the vortex generator is not just local, but persists in the downstream louvres.

The heat transfer coefficient in the tube wake on both sides of the fin for the $95°$ case is worse than for the $70°$ case. However, there is a small region of increased heat transfer coefficient directly behind the tube centre for the largest angle of attack, which is not there for the smaller angle of attack. The reason for this is revealed by considering the temperature and velocity field in a plane in the middle between two fins, shown in figure 7.28.

Figure 7.28 confirms what was already apparent in the heat transfer coefficient distribution, namely that the tube wakes are strongly influenced by the angle of attack of the vortex generator. The larger heat transfer coefficient directly behind the centre of the tube for the largest angle of attack is caused by a small part of the cold bypass jet which is deflected to this position. The velocity vectors also reveal that the vortex generator has a wake zone associated with it. However, the temperatures in the wake zone of the vortex generator are not as high as in the wake zone behind the tube in case there is no vortex generator. Therefore, the heat transfer rate penalty caused by the wake zone of the vortex generator is compensated for by the reduction in the tube wake.

The presence of these wake zones is shown more clearly in figure 7.29, which shows the velocity magnitude. The extent of the wake zone behind the vortex generator increases as the angle of attack of the vortex generator increases up to an angle of $70°$.

Even though the heat transfer coefficient distribution, temperature and velocity fields reveal interesting flow features, it remains difficult to assess which of the four geometries results in the best overall heat transfer coefficient. It is therefore interesting to look at the decomposition of the thermal conductance, shown in figure 7.30.

This clearly reveals that as the angle of attack increases, the thermal conductance of the fin increases, up until the angle of attack of $70°$. Based on the heat transfer coefficient distribution in figures 7.26 and 7.27, this is most likely due to the improvement of the heat transfer coefficient in the tube wakes, rather than due to enhancement in other positions on the fin surface. There is also a very slight improvement in the thermal conductance of the tubes, but they contribute little to

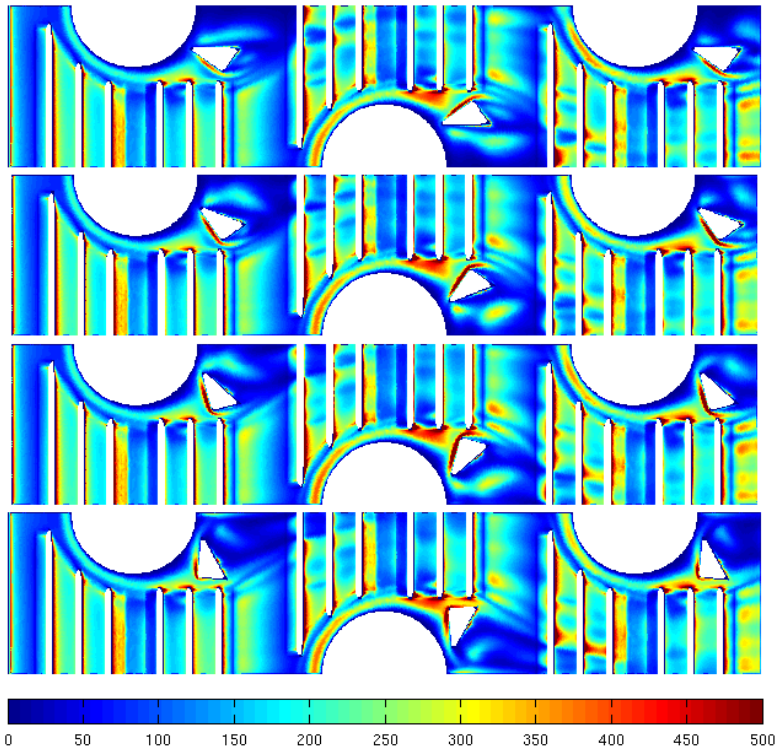

Figure 7.26: Heat transfer coefficient on the top of the fin for the angles of attack $35°$, $55°$, $70°$ *and* $95°$

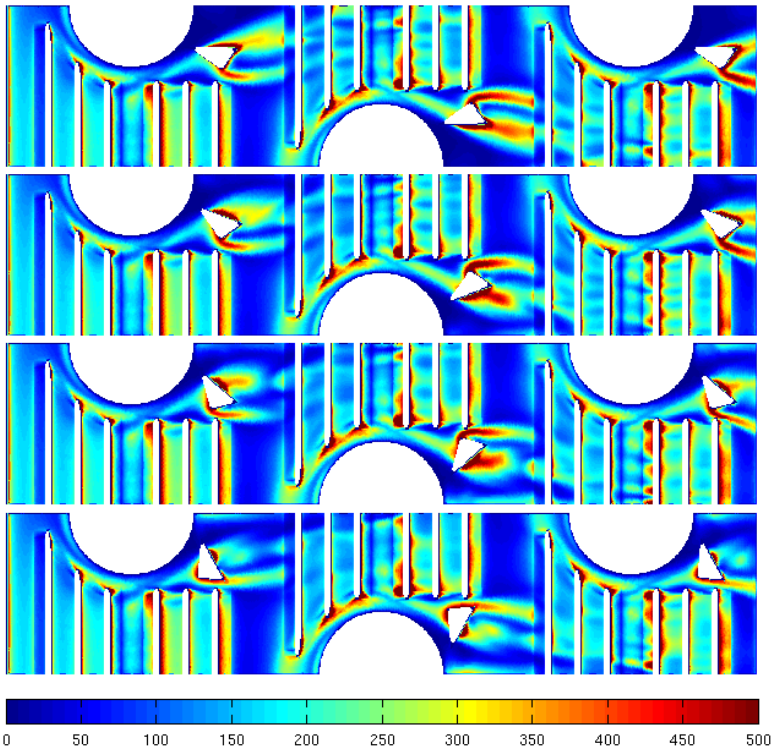

Figure 7.27: Heat transfer coefficient on the bottom of the fin for the angles of attack $35°$, $55°$, $70°$ *and* $95°$

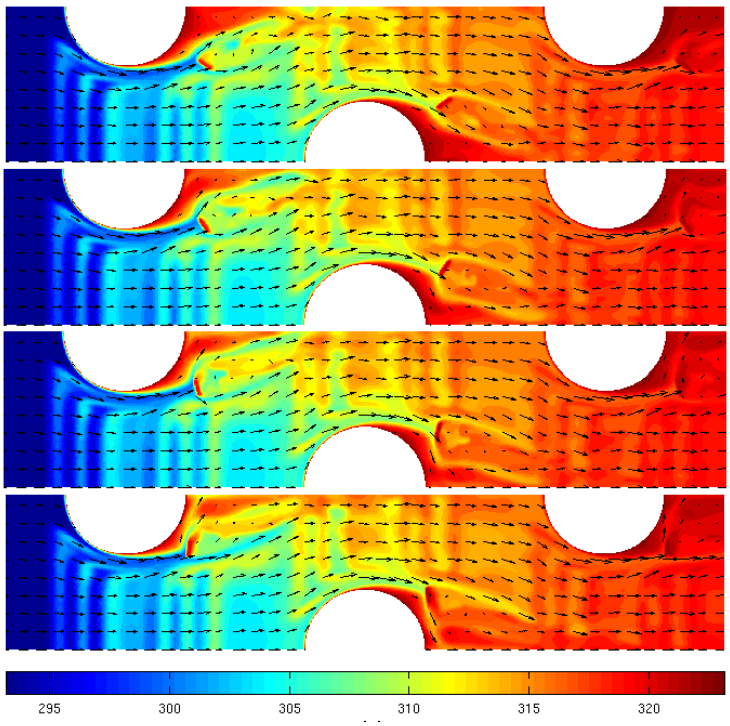

Figure 7.28: Contours of temperature and velocity vectors in a plane halfway between two fins for the angles of attack $35°$, $55°$, $70°$ *and* $95°$

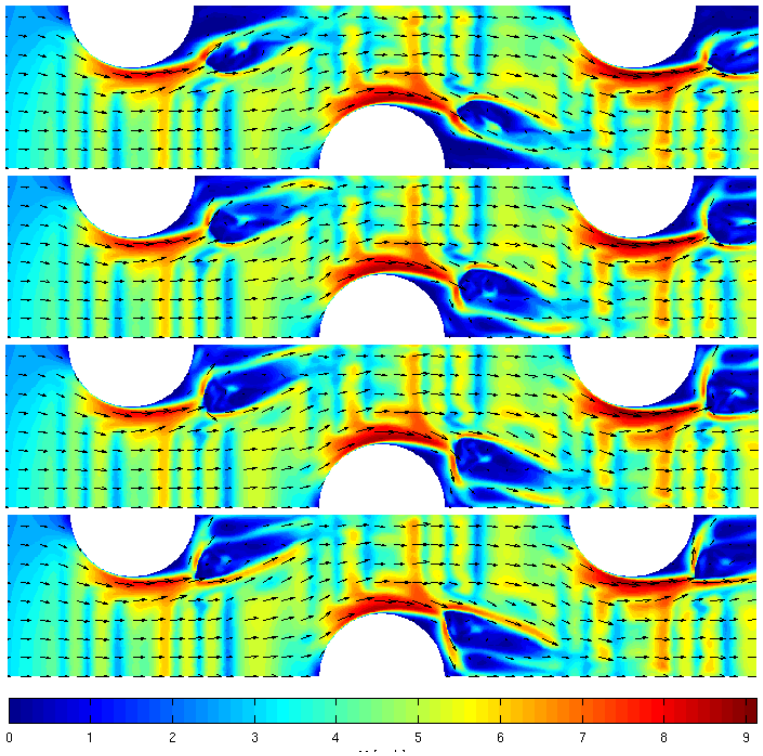

Figure 7.29: Contours of velocity magnitude and velocity vectors in a plane halfway between two fins for the angles of attack 35°, 55°, 70° *and* 95°

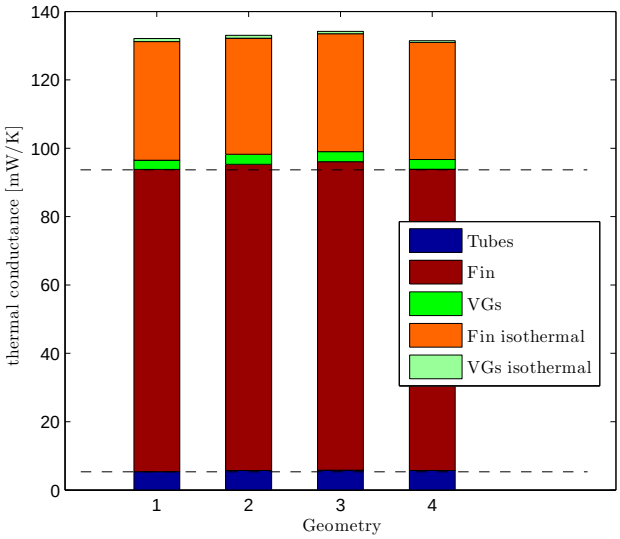

Figure 7.30: Decomposition of the thermal transmittance for the angles of attack $35°$, $55°$, $70°$ *and* $95°$

the total thermal conductance. For the largest angle of attack, the thermal conductance of the fin again deteriorates, which is in accordance with the reduction of the heat transfer coefficient in the tube wakes, which was seen previously.

Since wake zones are identified behind the vortex generators, which become more prominent as the angle of attack increases, it can be expected that there is an associated pressure drag penalty that increases with the angle of attack. This is confirmed in figure 7.31, which shows the drag decomposition for all four geometries.

The drag on the vortex generator increases with the angle of attack up to an angle of $70°$. For the angle of $95°$, the drag on the vortex generator is again reduced. Remarkably, the form drag on the tubes is also slightly reduced, due to the impingement of a part of the bypass flow which is deflected by the vortex generator. Since it is known from chapter 5 that the third geometry corresponding to an angle of $70°$ has the best performance with respect to the trade-off between fan power and volume, this shows that the increase in thermal conductance by the vortex generator is more important for the heat exchanger performance than the pressure drop associated with the wake zones.

As the angle increases from $35°$ to $70°$, the thermal conductance increases by 2.6%, whereas the pressure drop increases by 4%. Recalling that the exponent of the j-factor in the VG-1 criterion was $\frac{3}{2}$ and that of the f-factor only $\frac{1}{2}$, this result

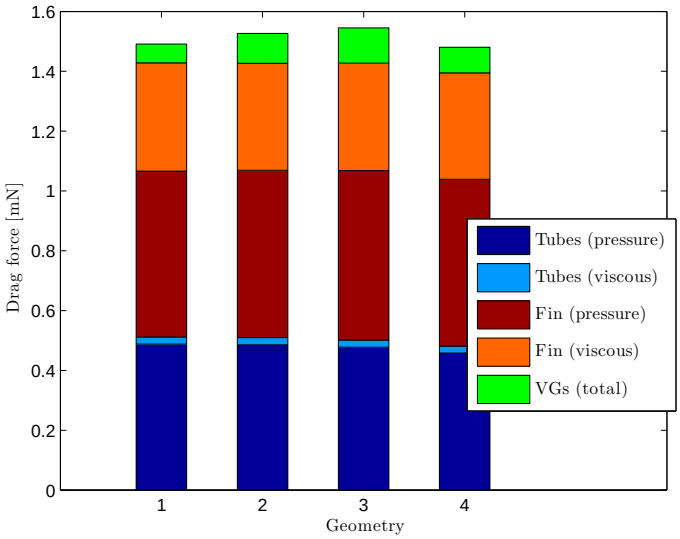

Figure 7.31: Decomposition of the drag force for the angles of attack $35°$, $55°$, $70°$ *and* $95°$.

is reasonable. Neglecting the effect of the Reynolds number, an improvement of the j-factor with a factor 1.026 corresponds to an increase of $1.026^3 = 1.08$ of the f-factor, which can be tolerated in order to maintain constant VG-1.

7.7 Conclusions

Fin efficiency is responsible for the difference in thermal performance between the X-shaped louvres and the compound design. The X-shape performed worse than the compound design purely due to fin efficiency effects. In all cases, the thermal conductance contribution of the fin was much larger than that of the tubes. The compound design achieved a slightly lower heat transfer coefficient but a better fin efficiency, resulting in an overall larger thermal conductance than the X-shaped louvred fin. Making modifications to the X-shaped geometry with the objective of increasing the fin efficiency for a given heat transfer coefficient forms an interesting research path.

An in-depth investigation of the flow patterns in various round tube and fin geometries was presented. In all cases, a high-velocity bypass jet was present between the louvres and the tubes. As expected, there was a strong correlation between the behaviour of the local heat transfer coefficient and the presence of vortices. The vortices were not destroyed in the louvres. Instead, the transition

zones generated vortices which persisted in the louvres. These vortices resulted in a downward flow which kept the high velocity bypass jet close to the fin surface. With or without vortex generators, the flow inside the louvre banks exhibited a strong three-dimensional character and vortices.

The optimum angle of attack of the vortex generator with respect to the VG-1 criterion corresponded to the angle for which the heat transfer coefficient was maximum for a fixed inlet frontal velocity. The increase in thermal conductance was more important for the heat exchanger performance than the pressure drop penalty incurred due to the wake zone which was present behind the vortex generator. The heat transfer coefficient in the vortex generator wake was higher than that in the tube wake. Reducing the tube wakes at the cost of increasing the wakes behind the vortex generator is therefore sensible.

8
Conclusions

The literature study revealed several problem areas in the optimisation of compact heat exchangers. First of all, the performance evaluation criteria were not applied correctly, because they were often evaluated at the same Reynolds number for all geometries. It was shown why this was incorrect and two possible alternatives were proposed. The first option is calculating the Reynolds number as a function of the fin geometry in an iterative loop, which benefits from a surrogate model. Alternatively, a multi-objective approach can be followed. The advantage of the first option is that a fin geometry can be optimised with respect to a single reference case. This allows finding an optimum for a specific application, which requires less computational effort than determining the entire Pareto front. Both methods were applied to the problem of the X-shaped louvred fin. This showed that increasing the louvred area using a large number of louvres resulted in a better performance. Higher louvre angles also performed better than the lower ones. A second issue is that PECs such as the VG-1 criterion assume that the heat exchanger length can be varied without changing the j- and f-factors. It was shown that for HVAC applications where the number of tube rows tend to be small, this assumption is still valid. An approach which varies the geometry of the heat exchanger such that the impact of the length on the performance was correctly taken into account was proposed and applied to the problem of the X-shaped louvred fin. This shows that the idea of decreasing the required volume by increasing the Reynolds number by decreasing the frontal area and increasing the length does not work. Any improvement in the trade-off between heat transfer and pressure drop by increasing the Reynolds number is lost due to the deterioration of the thermal transmittance as the longitudinal

tube pitch increases. The downside of this method is that the results depend on the reference heat exchanger. If it is possible to increase the heat exchanger length by increasing the number of tube rows and decreasing the tube pitch with respect to the reference, a performance improvement can be obtained. If the longitudinal tube pitch of the reference case is already at a geometrical minimum, increasing the length results in a deterioration of the improvement. Neglecting the impact of the heat exchanger length on the j- and f-factors during the optimisation results in an optimisation of the best-case scenario. As the performance of the heat exchanger improves as the hydraulic diameter is reduced or as the longitudinal tube pitch is reduced, both of these should be as small as possible. However, it is not possible to fix both of these quantities and still optimise the fin geometry if the mass flow rate is also constrained. Therefore the case where the hydraulic diameter was allowed to vary by changing the fin pitch and the heat exchanger length was constrained was discussed. In this case the louvred fin with a smaller louvre angle showed a better performance, as it could satisfy the constraints with a smaller fin pitch and therefore greater compactness.

The third issue is that it is not always reasonable to fix the mass flow rate in practical applications. For example, in the case of the condenser of an air-conditioning system, the only thing that matters is that the heat transfer rate can be achieved for a given refrigerant temperature. The fan power and the required volume and surface area must be as small as possible, but the mass flow rate is unimportant. It was shown what the performance curves looked like in a three-dimensional space where the mass flow rate was an additional independent variable. Projecting parameter curves of constant mass flow rate on the power-volume plane resulted in the performance curves of the Cowell method. It was shown that if the heat exchanger length was constrained and the mass flow rate was allowed to vary, the optimal geometry depended on the length constraint. For heat exchangers with a large number of tube rows, the plain fin performs better than the louvred fin, whereas the opposite is true for heat exchangers with a small number of tube rows. This shows that the optimal fin geometry strongly depends on the practical constraints which are specific to the application.

The compound fin geometry combining louvres with vortex generators was then investigated. It was shown that the use of low-resolution experimental designs to analyse this type of geometry requires special care regarding the aliasing of interaction effects. A relatively large number of two-factor interactions with the same importance as main factor effects were identified. Third-order and fourth-order interactions are also significant. These interactions are physically caused by the interaction between the position of the trailing edge of the vortex generator and the extent of the tube wakes around this position. In contrast to the results of a Taguchi analysis which neglected the presence of interaction effects, a variation of the vortex generator angle over a range of 10° was found to have a much smaller

impact than changing the fin pitch from 1.4 to 1.8 mm. The height ratio of the vortex generator should be 0.9.

Since the position of the trailing edge is critical to the impact of the vortex generator, the parametrisation of the vortex generator position is essential. Many previous studies fix the position of the leading edge. This results in the fin pitch, the height ratio, the vortex generator angle and the aspect ratio all determining the trailing edge position, making it impossible to separate the effect of the parameters from the effect on the trailing edge position. The vortex generator geometry is therefore optimised using two different parametrisations of the positioning. The simple PEC-based optimisation, which only takes effects of the Reynolds number into account, was used. This corresponds to an optimisation of the best-case performance, but has the advantage that the results are not dependent on the dimensions of the reference heat exchanger. The impact of each parameter on the VG-1 criterion was investigated.

The parametrisation is determined not by fixing either the leading or trailing edge position, but instead a feasible area in which the vortex generator can be positioned is identified. The vortex generator can then be positioned in this feasible area by translating it along two axes. The first parametrisation allows translations in a coordinate frame attached to the vortex generator, whereas the second parametrisation considers the longitudinal and transversal position relative to the louvres. For the longitudinal-transversal parametrisation, the vortex generator angle should be small (35°). However, for the other parametrisation, the optimal angle is found to be much larger at 75°. The volume of the heat exchanger can be reduced to 96.1% of that of the X-shaped louvred fin geometry. By extending the louvres in front of the tube further, the Y-shaped geometry is obtained. This geometry results in a further reduction of the required volume to 92.7% of the X-shaped louvred fin. This reduction is expected to increase as higher air velocities are used.

In order to investigate the physical reasons why certain geometries perform better than others, it is necessary to consider the behaviour of the fin efficiency. Many authors use correlations or incorrect methods to obtain the fin efficiency from CFD calculations. A new post-processing method to determine fin efficiency was therefore proposed and validated using two different cases. Using this new method, it was revealed that the heat transfer coefficient of the X-shaped louvred fin was very similar to that of the compound design. The improved performance of the latter is to a very large extent due to the greater fin efficiency of the latter design.

Finally, the flow inside the heat exchanger core was studied for several fin geometries. It was revealed that the form drag on the fin and the tubes was the most significant contribution to the pressure drop for all of the cases. Several vortices were present in the flow in the louvre banks, even when no vortex generators were

used. These vortices were generated by the transition regions and the flat landings. Neither these vortices, the horseshoe vortices nor the vortices generated by vortex generators are destroyed by the upward flow in the louvres. At large angles of attack, the vortex generators reduced the extent of the tube wakes by changing the primary flow.

Recommendations for future work

A new louvred fin correlation should be developed, since the existing correlations were shown to be lacking. Experimental uncertainty should be taken into account by using weighted least squares, larger weight for measurements with smaller experimental uncertainties. Furthermore, if different topologies are used, care should be taken that topology effects are not aliased with the effects of the geometrical parameters to which the correlation will be fitted. Finally, it should be ensured that the correlation has a physically correct behaviour, for example, the correlation should exhibit asymptotic behaviour as a function of the number of tube rows. By combining physical experiments with numerical experiments, sufficient data can be obtained while ensuring the numerical model is sufficiently reliable.

In order to ensure that the correlation is also reliable for conditions which differ from the experimental conditions, a fin efficiency correlation should be developed for use with the heat transfer correlation. Given the significant difficulties in experimentally determining the fin efficiency for representative heat exchanger conditions, the post-processing method developed in this work is a good candidate. The numerical data used to determine the heat transfer correlation can be used directly to develop the fin efficiency correlation. Finding appropriate parameters to capture the effect of the fin topology on the fin efficiency is a major challenge.

Furthermore, the Reynolds number range of the correlation needs to be sufficiently large. At Reynolds numbers larger than 600, the flow in the heat exchanger core will no longer be laminar and steady. Whether the flow in the heat exchanger core for moderate Reynolds numbers between 600 and 3000 can safely be modeled as fully turbulent flow for the purposes of heat transfer is still an open question.

The constraints imposed in the first law based PECs are not realistic for practical applications. For example for the evaporator of heat pump, choosing a different fin geometry can allow changes in air mass flow rate, condensing temperature and heat transfer rate. This will have repercussions not only on the fan power, but also on the compressor power. It is the total electrical power required to deliver a certain heat transfer rate at a certain temperature in the condensor which is the quantity of interest. As such, the optimisation of the fin geometry as well as the overall heat exchanger geometry for a specific practical case under constraints with respect to volume and mass is the most relevant for practice in industry. The optimisation of fin geometry with respect to second law based PECs, how well they match with

the requirements of industrial practice and the impact of the different assumptions are interesting options for future work.

Finally, the optimisation of the X-shaped louvred fin geometry still has significant potential. By breaking up the longest louvres by introducing flat regions and transition zones, the fin efficiency will be improved. This removes the most important reason why the X-shaped geometry performed worse than the Y-shaped geometry. Furthermore, the transition zones introduce vortices into the flow, just like vortex generators. By optimally choosing the locations of these transition zones, it is likely that the performance of the X-shaped louvred fin can be improved further.

A Publications

Publications as first author in peer-reviewed international journals

B. Ameel, K. De Kerpel, H. Canière, C. T'Joen, H. Huisseune, and M. De Paepe. *Classification of two phase flows using linear discriminant analysis and expectation maximization clustering of video footage*. International Journal of Multiphase Flow, vol. 40, pp. 106-112, 2012.

B. Ameel, C. T'Joen, K. De Kerpel, P. De Jaeger, H. Huisseune, M. Van Belleghem, and M. De Paepe. *Thermodynamic analysis of energy storage with a liquid air Rankine cycle*. Applied Thermal Engineering, vol. 52, pp. 130-140, 2013.

B. Ameel, H. Huisseune, J. Degroote, C. T'Joen, P. De Jaeger, J. Vierendeels, and M. De Paepe. *On fin efficiency in interrupted fin and tube heat exchangers*. International Journal of Heat and Mass Transfer, vol. 60, pp. 557-566, 2013.

B. Ameel, J. Degroote, C. T'Joen, P. De Jaeger, H. Huisseune, S. De Schampheleire, J. Vierendeels, and M. De Paepe. *Optimization of X-shaped louvered fin and tube heat exchangers while maintaining the physical meaning of the performance evaluation criterion*. Applied Thermal Engineering, vol. 58, pp. 136-145, 2013.

B. Ameel, J. Degroote, C. T'Joen, H. Huisseune, S. De Schampheleire, J. Vierendeels, and M. De Paepe. *Accounting for the effect of the heat exchanger length in the performance evaluation of compact fin and tube heat exchangers*. Applied Thermal Engineering, vol. 65, pp. 544-553, 2014.

B. Ameel, J. Degroote, H. Huisseune, J. Vierendeels, and M. De Paepe. *Interaction effects between parameters in a vortex generator and louvered fin compact heat exchanger*. International Journal of Heat and Mass Transfer (accepted for publication).

Publications as co-author in peer-reviewed international journals

De Jaeger, Peter, Christophe T'Joen, Henk Huisseune, Bernd Ameel, and Michel De Paepe. *An Experimentally Validated and Parameterized Periodic Unit-cell Reconstruction of Open-cell Foams.* Journal of Applied Physics 109 (10), 2011.

De Jaeger, Peter, Christophe T'Joen, Henk Huisseune, Bernd Ameel, Sven De Schampheleire, and Michel De Paepe. *Assessing the Influence of Four Bonding Methods on the Thermal Contact Resistance of Open-cell Aluminum Foam.* International Journal of Heat and Mass Transfer 55 (21-22): 6200-6210, 2012.

Huisseune, Henk, Christophe T'Joen, Peter De Jaeger, Bernd Ameel, Joachim Demuynck, and Michel De Paepe. *Numerical Study of Flow Deflection and Horseshoe Vortices in a Louvered Fin Round Tube Heat Exchanger*. Journal of Heat Transfer-transactions of the Asme 134 (9), 2012.

De Jaeger, Peter, Christophe T'Joen, Henk Huisseune, Bernd Ameel, Sven De Schampheleire, and Michel De Paepe. *Assessing the Influence of Four Cutting Methods on the Thermal Contact Resistance of Open-cell Aluminum Foam.* International Journal of Heat and Mass Transfer 55 (21-22): 6142-6151, 2012.

De Kerpel, Kathleen, Bernd Ameel, Henk Huisseune, Christophe T'Joen, Hugo Canière, and Michel De Paepe. *Two-phase Flow Behaviour and Pressure Drop of R134a in a Smooth Hairpin.* International Journal of Heat and Mass Transfer 55 (4): 1179-1188, 2012.

De Kerpel, Kathleen, Bernd Ameel, Christophe T'Joen, Hugo Canière, and Michel De Paepe. *Flow Regime Based Calibration of a Capacitive Void Fraction Sensor*

for Small Diameter Tubes. International Journal of Refrigeration-revue Internationale Du Froid 36 (2): 390-401, 2013.

De Jaeger, Peter, Christophe T'Joen, Henk Huisseune, Bernd Ameel, Sven De Schampheleire, and Michel De Paepe. 2013. *Influence of Geometrical Parameters of Open-cell Aluminum Foam on Thermohydraulic Performance.* Heat Transfer Engineering 34 (14): 1202-1215, 2013.

De Schampheleire, Sven, Peter De Jaeger, Henk Huisseune, Bernd Ameel, Christophe T'Joen, Kathleen De Kerpel, and Michel De Paepe. *Thermal Hydraulic Performance of 10 PPI Aluminium Foam as Alternative for Louvered Fins in an HVAC Heat Exchanger.* Applied Thermal Engineering 51 (1-2): 371-382, 2013.

Huisseune, Henk, Christophe T'Joen, Peter De Jaeger, Bernd Ameel, Sven De Schampheleire, and Michel De Paepe. *Performance Analysis of a Compound Heat Exchanger by Screening Its Design Parameters.* Applied Thermal Engineering 51 (1-2): 490-501, 2013.

Huisseune, Henk, Christophe T'Joen, Peter De Jaeger, Bernd Ameel, Sven De Schampheleire, and Michel De Paepe. *Influence of the Louver and Delta Winglet Geometry on the Thermal Hydraulic Performance of a Compound Heat Exchanger.* International Journal of Heat and Mass Transfer 57 (1): 58-72, 2013.

Huisseune, Henk, Christophe T'Joen, Peter De Jaeger, Bernd Ameel, Sven De Schampheleire, and Michel De Paepe. *Performance Enhancement of a Louvered Fin Heat Exchanger by Using Delta Winglet Vortex Generators.* International Journal of Heat and Mass Transfer 56 (1-2): 475-487, 2013.

De Schampheleire, Sven, Peter De Jaeger, Robin Reynders, Kathleen De Kerpel, Bernd Ameel, Christophe T'Joen, Henk Huisseune, Steven Lecompte, and Michel De Paepe. *Experimental Study of Buoyancy-driven Flow in Open-cell Aluminium Foam Heat Sinks.* Applied Thermal Engineering 59 (1-2): 30-40, 2013.

De Kerpel, Kathleen, Bernd Ameel, Sven De Schampheleire, Christophe T'Joen, Hugo Canière, and Michel De Paepe. *Calibration of a Capacitive Void Fraction Sensor for Small Diameter Tubes Based on Capacitive Signal Features.* Applied Thermal Engineering (3): 77-83, 2014.

Publications in proceedings of international conferences

Ameel, Bernd, Kathleen De Kerpel, Hugo Canière, Henk Huisseune, Christophe T'Joen, and Michel De Paepe. *Video Based Classification of Two Phase Flows Using Linear Discriminant Analysis and Expectation Maximization Clustering.* In 8th International Conference on Heat Transfer, Fluid Mechanics and Thermodynamics, Proceedings, 250-256. Ghent, Belgium: Ghent University, Department of Flow, heat and combustion mechanics, 2011.

Ameel, Bernd, and Michel De Paepe. *Using Liquid Air as a Way to Store Energy.* In 8th International Conference on Heat Transfer, Fluid Mechanics and Thermodynamics, Proceedings, 464-473. Ghent, Belgium: Ghent University, Department of Flow, heat and combustion mechanics, 2011.

Ameel, Bernd, Joris Degroote, Henk Huisseune, Peter De Jaeger, Jan Vierendeels, and Michel De Paepe. *Numerical Optimization of Louvered Fin Heat Exchanger with Variable Louver Angles.* In Journal of Physics Conference Series, ed. Daniel Petit and Christophe Le Niliot. Vol. 395. Editions Société Française de Thermique, 2012.

Ameel, Bernd, Joris Degroote, Henk Huisseune, Peter De Jaeger, Jan Vierendeels, and Michel De Paepe. *Optimization of a Louvered Fin Heat Exchanger with Individually Variable Louver Angles.* In 9th International Conference: Heat Transfer, Fluid Mechanics and Thermodynamics, Proceedings, ed. Josua P Meyer, 428-433. Hefat, 2012.

B
Miscellaneous

B.1 The energy equation for fluids with constant density

In order to introduce fluid properties into the internal energy equation (B.1), it is assumed that the enthalpy is a function of the pressure and the temperature. This is valid in general as long as these properties are independent, which is the case for single-phase fluids.

$$\rho \frac{Dh(P,T)}{Dt} - \frac{DP}{Dt} = \varphi - \vec{\nabla}.\vec{q} \tag{B.1}$$

By applying the chain rule, this results in equation (B.2), where the first partial derivative is equal to the isobaric specific heat capacity by definition.

$$\rho \left(\underbrace{\left.\frac{\partial h}{\partial T}\right|_P}_{c_p} \frac{DT}{Dt} + \left.\frac{\partial h}{\partial P}\right|_T \frac{DP}{Dt} \right) - \frac{DP}{Dt} = \varphi - \vec{\nabla}.\vec{q} \tag{B.2}$$

The second term representing the pressure dependence of the enthalpy at constant temperature can be evaluated using the Maxwell relation for the partial derivative of the enthalpy with respect to the pressure [68], resulting in equation (B.3).

$$\rho c_p \frac{DT}{Dt} + \rho \left(\frac{1}{\rho} + \frac{T}{\rho^2} \left.\frac{\partial \rho}{\partial T}\right|_P \right) \frac{DP}{Dt} - \frac{DP}{Dt} = \varphi - \vec{\nabla}.\vec{q} \tag{B.3}$$

Simplifying results in equation (B.4), where the coefficient of the total derivative of the pressure is equal to the product of the volume expansivity β and the temperature.

$$\rho c_p \frac{DT}{Dt} \underbrace{+ \frac{T}{\rho} \frac{\partial \rho}{\partial T}\bigg|_P}_{-T\beta} \frac{DP}{Dt} = \varphi - \vec{\nabla}.\vec{q} \tag{B.4}$$

If the volume expansivity of the fluid is zero, the simplified equation is exactly valid. This is the case for an incompressible fluid.

If the density of the fluid does depend on the temperature, the pressure-dependent term must be small compared with the other terms in order for it to be negligible. In this case, the simplified equation is a good approximation. For an ideal gas, the volume expansivity is equal to the reciprocal of the temperature and the coefficient of the pressure term is simply minus one.

B.2 Tip boundary condition for fin efficiency

In order to investigate when it is reasonable to assume an adiabatic boundary condition at the fin tip instead of a convective boundary condition, it is helpful to investigate the case where the heat transfer rate at the tip $\dot{Q}_{tip}$ is imposed.

By solving the differential equation for the temperature and calculating the total heat transfer rate, equation (B.5) is obtained. In this equation, $\mathbf{P}$ is the perimeter of the fin.

$$\dot{Q}_{fin} = \frac{h\mathbf{P}(T_{bulk} - T_{base})}{m} tanh(mL) + \frac{\dot{Q}_{tip}}{cosh(mL)} \tag{B.5}$$

This shows that the heat transfer rate of the fin is equal to the heat transfer rate with the adiabatic boundary condition $Q_{tip} = 0$ plus a correction term. If the heat transfer rate from the fin tip is much smaller than the heat transfer rate from the rest of the fin, the difference between the heat transfer rate from the fin in the case of an adiabatic fin tip and the heat transfer rate with the correct boundary condition is negligibly small. This is the case because the hyperbolic cosine is always at least unity or larger.

For the sake of simplicity, it is now assumed that the fin temperature is higher than the bulk fluid temperature. In this case, there is a conductive temperature drop from the base of the fin to the tip of the fin. The actual heat transfer rate from the fin is then higher than the heat transfer rate if the entire fin would be at the fin tip temperature.

$$\dot{Q}_{fin} = \int_{A_{fin}} h_{fin}(T_{fin} - T_{bulk})dA > \int_{A_{fin}} h_{fin}(T_{fin,tip} - T_{bulk})dA \quad \text{(B.6)}$$

The heat transfer rate from the fin is then much larger than the heat transfer rate from the fin tip (equation (B.7)) if the total fin area is much larger than the area of the fin tip. This is therefore a sufficient (but not a necessary) condition for the adiabatic boundary condition to be valid.

$$\dot{Q}_{fin,tip} = \int_{A_{fin,tip}} h_{fin}(T_{fin,tip} - T_{bulk})dA \quad \text{(B.7)}$$

B.3 Impact of discretisation on performance comparison

The impact of the discretisation error is verified using a coarser mesh, lacking the prismatic cells around the the louvres. As a result, the grid consists of only 4 million cells. Several possible combinations of the rectangular louvres with vortex generators are evaluated, for the coarse mesh and for a mesh which is refined with a factor of 2 in every direction. The GCI of the modified j-factor is 2.1%. Even though the grids considered here are coarser, the GCI is lower than the GCI reported in chapter 4. This is because this case is for the baseline amount of louvers, for which there are less fin interruptions. As a result, the boundary layers are thicker and therefore more easily captured with a coarser grid.

Figure B.1 shows the power-volume plane for the different geometries on the two grids. For the X-shaped louvred fin, the original coarser mesh of 4 million cells is also compared with the final mesh using a prismatic layer described in chapter 4. It is clear that the impact of the grid discretisation is larger for larger pumping power, which corresponds to larger velocities. This is especially apparent for the X-shaped louvred fin, where the prismatic layer has a negligible influence for the lowest velocity.

A second issue which is apparent is that the discretisation error is highly correlated with the flow velocity. For every geometry, the coarser grid results in an underprediction of the volume for the low velocities, whereas for higher velocities the volume is overpredicted. The discretisation error for a specific velocity is nearly independent of the geometry, which indicates that it is approximately a systematic error, which only depends on the velocity and not on the geometry. Assuming an uncorrelated Gaussian noise model for the discretisation error is not correct. This is as expected, since the discretisation error is mainly determined by how well the grid can capture the boundary layers. The thickness of the boundary

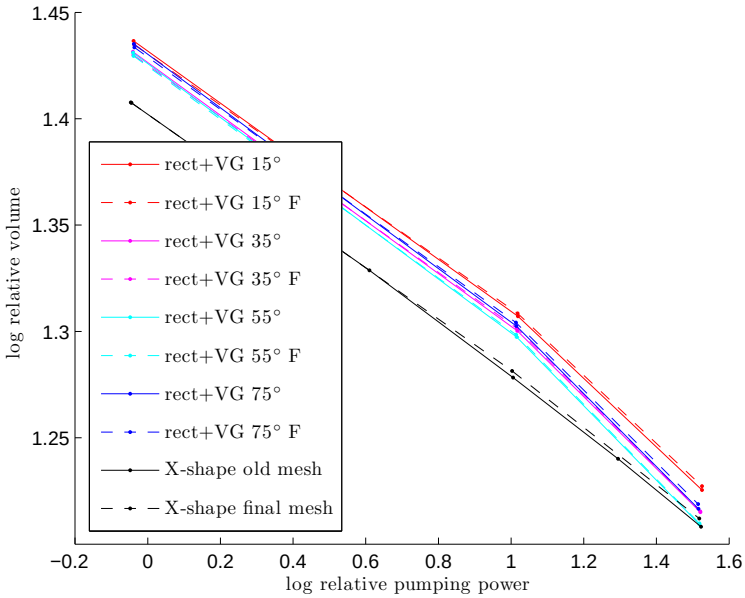

Figure B.1: Results in the power-volume plane for different numerical grids. The suffix F indicates the fine grid, the final mesh refers to the mesh as described in chapter 4

layers is mainly determined by the flow velocity and not so much by the vortex generator angle or other geometrical parameters.

Finally, it is clear that the grid discretisation error is not very important. For the case of a vortex generator angle of $15°$, the impact of the mesh size on the required volume is only 0.3%. The comparison between the different fin geometries is therefore not impacted by the discretisation error to any significant degree.

References

[1] T. A. Cowell. *A General Method for the Comparison of Compact Heat-Transfer Surfaces*. Journal of Heat Transfer-Transactions of the Asme, 112(2):288–294, 1990.

[2] *Ta Chin Chin Co., Ltd*. `www.fin-dies.com`, 16 Januari 2014.

[3] C. C. Wang, C. J. Lee, C. T. Chang, and S. P. Lin. *Heat transfer and friction correlation for compact louvered fin-and-tube heat exchangers*. International Journal of Heat and Mass Transfer, 42(11):1945–1956, 1999.

[4] Henk Huisseune, Christophe T'Joen, Peter De Jaeger, Bernd Ameel, Sven De Schampheleire, and Michel De Paepe. *Performance analysis of a compound heat exchanger by screening its design parameters*. Applied Thermal Engineering, 51(1–2):490–501, 2013.

[5] Ludwig Prandtl. *Über Flüssigkeitsbewegung bei sehr kleiner Reibung*. Verhandl. III. Intern. Math. Kongr. Heidelberg, 1904.

[6] Heinrich Blasius. *Grenzschichten in Flüssigkeiten mit kleiner Reibung*. PhD thesis, 1907.

[7] J.H. Lienhard. *A Heat Transfer Textbook*. Dover Publications, 2011.

[8] R. K. Shah and D.P. Sekulic. *Fundamentals of Heat Exchanger Design*. Wiley, New York, 2003.

[9] K.A. Gardner. *Efficiency of extended surface*. Transactions of the American Society of Mechanical Engineers, 67:621, 1945.

[10] T.E. Schmidt. *Heat transfer calculations for extended surfaces*. Refrigerating Engineering, pages 351–357, 1949.

[11] W.M. Kays and A.L. London. *Compact heat exchangers*. Krieger Pub. Co., 1984.

[12] R. L. Webb. *Principles of Enhanced Heat Transfer*. Wiley, New York, 1994.

[13] P. G. LaHaye, F. J. Neugebauer, and R. K. Sakhuja. *A Generalized Prediction of Heat Transfer Surfaces*. Journal of Heat Transfer, 96(4):511–517, 1974.

[14] J. Y. Yun and K. S. Lee. *Influence of design parameters on the heat transfer and flow friction characteristics of the heat exchanger with slit fins*. International Journal of Heat and Mass Transfer, 43(14):2529–2539, 2000.

[15] Carl Edward Rasmussen and Christopher K. I. Williams. *Gaussian Processes for Machine Learning (Adaptive Computation and Machine Learning)*. The MIT Press, 2005.

[16] C.F.J. Wu and M.S. Hamada. *Experiments: Planning, Analysis, and Optimization*. Wiley, 2011.

[17] Yu-Juei Chang and Chi-Chuan Wang. *A generalized heat transfer correlation for Iouver fin geometry*. International Journal of Heat and Mass Transfer, 40(3):533–544, 1997.

[18] Man-Hoe Kim and Clark W. Bullard. *Air-side thermal hydraulic performance of multi-louvered fin aluminum heat exchangers*. International Journal of Refrigeration, 25(3):390–400, 2002.

[19] Junqi Dong, Jiangping Chen, Zhijiu Chen, Wenfeng Zhang, and Yimin Zhou. *Heat transfer and pressure drop correlations for the multi-louvered fin compact heat exchangers*. Energy Conversion and Management, 48(5):1506–1515, 2007.

[20] C.J. Davenport. *Heat Transfer and Fluid Flow in Louvered Triangular Ducts*. PhD thesis, 1980.

[21] Ralph L. Webb and Paul Trauger. *Flow structure in the louvered fin heat exchanger geometry*. Experimental Thermal and Fluid Science, 4(2):205–217, 1991.

[22] M. E. Springer and K. A. Thole. *Entry region of louvered fin heat exchangers*. Experimental Thermal and Fluid Science, 19(4):223–232, 1999.

[23] N. C. DeJong and A. M. Jacobi. *Localized flow and heat transfer interactions in louvered-fin arrays*. International Journal of Heat and Mass Transfer, 46(3):443–455, 2003.

[24] C. C. Wang, Y. M. Tsai, and D. C. Lu. *Comprehensive study of convex-louver and wavy fin-and-tube heat exchangers*. Journal of Thermophysics and Heat Transfer, 12(3):423–430, 1998.

[25] Chi-Chuan Wang, Kuan-Yu Chi, Yu-Juei Chang, and Yeon-Pun Chang. *An experimental study of heat transfer and friction characteristics of typical louver fin-and-tube heat exchangers*. International Journal of Heat and Mass Transfer, 41(4–5):817–822, 1998.

[26] Ricardo Romero-Méndez, Mihir Sen, K. T. Yang, and Rodney McClain. *Effect of fin spacing on convection in a plate fin and tube heat exchanger*. International Journal of Heat and Mass Transfer, 43(1):39–51, 2000.

[27] A. M. Jacobi and R. K. Shah. *Heat-Transfer Surface Enhancement through the Use of Longitudinal Vortices - a Review of Recent Progress*. Experimental Thermal and Fluid Science, 11(3):295–309, 1995.

[28] H. Huisseune, C. T'Joen, P. De Jaeger, A. Willockx, and M. De Paepe. *Study of junction flows in louvered fin round tube heat exchangers using the dye injection technique*. Experimental Thermal and Fluid Science, 34(8):1253–1264, 2010.

[29] D. K. Tafti. *Time-dependent calculation procedure for fully developed and developing flow and heat transfer in louvered fin geometries*. Numerical Heat Transfer, Part A: Applications, 35(3):225–249, 1999.

[30] J. Cui and D. K. Tafti. *Computations of flow and heat transfer in a three-dimensional multilouvered fin geometry*. International Journal of Heat and Mass Transfer, 45(25):5007–5023, 2002.

[31] X. Zhang and D. K. Tafti. *Flow efficiency in multi-louvered fins*. International Journal of Heat and Mass Transfer, 46(10):1737–1750, 2003.

[32] Thomas Perrotin and Denis Clodic. *Thermal-hydraulic CFD study in louvered fin-and-flat-tube heat exchangers*. International Journal of Refrigeration, 27(4):422–432, 2004.

[33] T. Perrotin and D. Clodic. *Fin efficiency calculation in enhanced fin-and-tube heat exchangers in dry conditions*, 2003.

[34] Jin-Sheng Leu, Min-Sheng Liu, Jane-Sunn Liaw, and Chi-Chuan Wang. *A numerical investigation of louvered fin-and-tube heat exchangers having circular and oval tube configurations*. International Journal of Heat and Mass Transfer, 44(22):4235–4243, 2001.

[35] Ching-Tsun Hsieh and Jiin-Yuh Jang. *Parametric study and optimization of louver finned-tube heat exchangers by Taguchi method*. Applied Thermal Engineering, 42(0):101–110, 2012.

[36] M. Fiebig. *Vortices, Generators and Heat Transfer*. Chemical Engineering Research and Design, 76(2):108–123, 1998.

[37] S. M. Pesteei, P. M. V. Subbarao, and R. S. Agarwal. *Experimental study of the effect of winglet location on heat transfer enhancement and pressure drop in fin-tube heat exchangers*. Applied Thermal Engineering, 25(11-12):1684–1696, 2005.

[38] K. Torii, K. M. Kwak, and K. Nishino. *Heat transfer enhancement accompanying pressure-loss reduction with winglet-type vortex generators for fin-tube heat exchangers*. International Journal of Heat and Mass Transfer, 45(18):3795–3801, 2002.

[39] C. B. Allison and B. B. Dally. *Effect of a delta-winglet vortex pair on the performance of a tube-fin heat exchanger*. International Journal of Heat and Mass Transfer, 50(25-26):5065–5072, 2007.

[40] A. Joardar and A. M. Jacobi. *Heat transfer enhancement by winglet-type vortex generator arrays in compact plain-fin-and-tube heat exchangers*. International Journal of Refrigeration-Revue Internationale Du Froid, 31(1):87–97, 2008.

[41] S. Tiwari, D. Maurya, G. Biswas, and V. Eswaran. *Heat transfer enhancement in cross-flow heat exchangers using oval tubes and multiple delta winglets*. International Journal of Heat and Mass Transfer, 46(15):2841–2856, 2003.

[42] J. S. Leu, Y. H. Wu, and H. Y. Jang. *Heat transfer and fluid flow analysis in plate-fin and tube heat exchangers with a pair of block shape vortex generators*. International Journal of Heat and Mass Transfer, 47(19-20):4327–4338, 2004.

[43] J. M. Wu and W. Q. Tao. *Investigation on laminar convection heat transfer in fin-and-tube heat exchanger in aligned arrangement with longitudinal vortex generator from the viewpoint of field synergy principle*. Applied Thermal Engineering, 27(14-15):2609–2617, 2007.

[44] J. Herpe, D. Bougeard, S. Russeil, and M. Stanciu. *Numerical investigation of local entropy production rate of a finned oval tube with vortex generators*. International Journal of Thermal Sciences, 48(5):922–935, 2009.

[45] P. Chu, Y. L. He, Y. G. Lei, L. T. Tian, and R. Li. *Three-dimensional numerical study on fin-and-oval-tube heat exchanger with longitudinal vortex generators*. Applied Thermal Engineering, 29(5-6):859–876, 2009.

[46] A. Lemouedda, M. Breuer, E. Franz, T. Botsch, and A. Delgado. *Optimization of the angle of attack of delta-winglet vortex generators in a plate-fin-and-tube heat exchanger*. International Journal of Heat and Mass Transfer, 53(23-24):5386–5399, 2010.

[47] M. Zeng, L. H. Tang, M. Lin, and Q. W. Wang. *Optimization of heat exchangers with vortex-generator fin by Taguchi method*. Applied Thermal Engineering, 30(13):1775–1783, 2010.

[48] Jiin-Yuh Jang, Ling-Fang Hsu, and Jin-Sheng Leu. *Optimization of the span angle and location of vortex generators in a plate-fin and tube heat exchanger*. International Journal of Heat and Mass Transfer, 67(0):432–444, 2013.

[49] G. Lozza and U. Merlo. *An experimental investigation of heat transfer and friction losses of interrupted and wavy fins for fin-and-tube heat exchangers*. International Journal of Refrigeration-Revue Internationale Du Froid, 24(5):409–416, 2001.

[50] L. H. Tang, M. Zeng, and Q. W. Wang. *Experimental and numerical investigation on air-side performance of fin-and-tube heat exchangers with various fin patterns*. Experimental Thermal and Fluid Science, 33(5):818–827, 2009.

[51] Henk Huisseune, Christophe T'Joen, Peter De Jaeger, Bernd Ameel, Sven De Schampheleire, and Michel De Paepe. *Performance enhancement of a louvered fin heat exchanger by using delta winglet vortex generators*. International Journal of Heat and Mass Transfer, 56(1–2):475–487, 2013.

[52] D. K. Tafti and X. Zhang. *Geometry effects on flow transition in multilouvered fins - onset, propagation, and characteristic frequencies*. International Journal of Heat and Mass Transfer, 44(22):4195–4210, 2001.

[53] Y. L. He, W. Q. Tao, F. Q. Song, and W. Zhang. *Three-dimensional numerical study of heat transfer characteristics of plain plate fin-and-tube heat exchangers from view point of field synergy principle*. International Journal of Heat and Fluid Flow, 26(3):459–473, 2005.

[54] P. J. Roache. *Quantification of uncertainty in computational fluid dynamics*. Annual Review of Fluid Mechanics, 29:123–160, 1997.

[55] Ching-Tsun Hsieh and Jiin-Yuh Jang. *3-D thermal-hydraulic analysis for louver fin heat exchangers with variable louver angle*. Applied Thermal Engineering, 26(14–15):1629–1639, 2006.

[56] L. J. Huang and R. K. Shah. *Assessment of Calculation Methods for Efficiency of Straight Fins of Rectangular Profile*. International Journal of Heat and Fluid Flow, 13(3):282–293, 1992.

[57] P. Teertstra, M. M. Yovanovich, and J. R. Culham. *Analytical forced convection modeling of plate fin heat sinks*. Journal of Electronics Manufacturing, 10(04):253–261, 2000.

[58] Ke-Wei Song, Ye Wang, Qiang Zhang, Liang-Bi Wang, and Yan-Jun Liu. *Numerical study of the fin efficiency and a modified fin efficiency formula for flat tube bank fin heat exchanger*. International Journal of Heat and Mass Transfer, 54(11–12):2661–2672, 2011.

[59] Ye Wang, Liang-Chen Wang, Zhi-Min Lin, Yu-Huan Yao, and Liang-Bi Wang. *The condition requiring conjugate numerical method in study of heat transfer characteristics of tube bank fin heat exchanger*. International Journal of Heat and Mass Transfer, 55(9–10):2353–2364, 2012.

[60] Yifeng Gao, Ji Song, Jingdan Gao, and Guoliang Ding. *Fin design for fin-and-tube heat exchanger with microgroove small diameter tubes for air conditioner*. In 4th IIR Conference on Thermophysical Properties and Transfer Processes of Refrigerants. IIF-IIR, 2013.

[61] Cheen Su An and Do Hyung Choi. *Analysis of heat-transfer performance of cross-flow fin-tube heat exchangers under dry and wet conditions*. International Journal of Heat and Mass Transfer, 55(5–6):1496–1504, 2012.

[62] A.D. Kraus, A. Aziz, and J. Welty. *Extended Surface Heat Transfer*. Wiley, 2002.

[63] Y. B. Tao, Y. L. He, J. Huang, Z. G. Wu, and W. Q. Tao. *Numerical study of local heat transfer coefficient and fin efficiency of wavy fin-and-tube heat exchangers*. International Journal of Thermal Sciences, 46(8):768–778, 2007.

[64] D. Bougeard. *Infrared thermography investigation of local heat transfer in a plate fin and two-tube rows assembly*. International Journal of Heat and Fluid Flow, 28(5):988–1002, 2007.

[65] Václav Kolář. *Vortex identification: New requirements and limitations*. International Journal of Heat and Fluid Flow, 28(4):638–652, 2007.

[66] Jin-Yoon Kim and Tae-Ho Song. *Microscopic phenomena and macroscopic evaluation of heat transfer from plate fins/circular tube assembly using naphthalene sublimation technique*. International Journal of Heat and Mass Transfer, 45(16):3397–3404, 2002.

[67] H. Huisseune, C. T'Joen, P. De Jaeger, B. Ameel, J. Demuynck, and M. De Paepe. *Numerical Study of Flow Deflection and Horseshoe Vortices in a Louvered Fin Round Tube Heat Exchanger*. Journal of Heat Transfer, 134(9):091801–091801, 2012.

[68] M.J. Moran, H.N. Shapiro, D.D. Boettner, and M. Bailey. *Fundamentals of Engineering Thermodynamics*. John Wiley and Sons, 2010.